Simulations of Glass and Ceramic Systems for Nuclear Waste Applications

A dissertation submitted to the University of London

for the degree of Doctor of Philosophy

and the Diploma of Imperial College

by

M.J.D. Rushton

Department of Materials

Imperial College of Science, Technology and Medicine 2006

The work presented in this thesis is by Michael James Daniel Rushton.

M.J.D Rushton

Abstract

Glass and ceramic materials have been used for the immobilisation of nuclear wastes. A greater understanding of these materials and the way in which they interact will lead to better waste-form design and performance. For this reason, atomic scale simulations were performed on glass, ceramic and glass-ceramic systems relevant to nuclear waste applications.

Here molecular dynamics techniques are used to form models of vitreous silica, alkali silicate, alkali borosilicate and alkali aluminoborosilicate glasses using a melt-quench procedure. The interactions occurring at interfaces between these glass compositions and (100) and (110) surfaces of ceramics exhibiting the rock-salt crystal structure are considered. Three different methods for interface formation are considered and their relative merits explored.

In particular, the changes in the modifier and network structure of glasses, encountered at glass-ceramic interfaces were investigated. Considerable modifier enhancement at interfaces was observed. In addition, considerable differences in the modifier distribution were found between (100) and (110) interfaces. Interfacial energies were calculated for each interface; of the interfaces considered it was found that (110) interfaces consistently gave lower energies than comparable (100) interfaces. A borosilicate waste glass composition was compared to a similar glass which had small additions of aluminium and magnesium. In general, interfacial energies for this aluminoborosilicate glass composition were found to be lower than those corresponding to the borosilicate glass.

Partial ordering of the glass network adjacent to the glass-ceramic interfaces was observed. Borate and silicate polyhedra in the glass close to glass-ceramic interfaces were found to adopt

preferred orientations based on the structure of the ceramic surface. At interfaces with the (100) surfaces of CaO, SrO and BaO, glass anions were found to sit over interstitial sites. By comparison, at interfaces with the (100) surface of MgO, glass anions were associated with cations in the ceramic surface.

The presence of the ceramic interface was found to cause layering of the glass network. Regularly spaced boron/silicon and oxygen rich layers were found parallel to the plane of all glass ceramic interfaces except that formed between SiO_2 and the (100) surface of MgO. The lack of layering in this system was attributed to the absence of network modifiers in this system.

Rare earth pyrochlore materials have been proposed as host materials for nuclear waste applications. A systematic series of calculations on $A_2^{3+}B_2^{4+}O_7$ pyrochlores were performed. In particular the results of static energy minimisation and molecular dynamics simulations were used to explore transformations occurring between pyrochlore, defect fluorite and amorphous states. Predictions were made for the volume changes experienced as a consequence of these transformations. It was found that volume changes were lowest for compositions close to the pyrochlore-defect fluorite phase boundary. Finally, pyrochlore to defect fluorite transformation temperatures were predicted for rare-earth zirconate pyrochlores.

Acknowledgements

The copyright of this thesis rests with the author and no quotations from it or information derived from it may be published without the prior written consent of the author.

Table of Contents

Chapter 1

Introduction

In its energy review, published in 2006 [1], the government of the United Kingdom opened the way for a new generation of nuclear fission electricity power stations. At the time of writing, about 20% of Britain's energy consumption is satisfied by nuclear power plants [2, 3], yet Britain's twelve nuclear power stations are nearing the end of their lives, with over half due to be decommissioned by 2011 [4]. Only two are expected to be generating beyond 2020. It is also thought that many coal-fired stations will have to close under new EU regulations on sulphur emissions [5]. Unless Britain starts importing electricity (which is undesirable in terms of security of supply) new generating capacity will have to be built. Given that current estimates put reserves of gas and oil at around forty years [2], nuclear power is a strong candidate for replacing this generating capacity as part of a long term energy strategy.

Through the Kyoto Protocol on greenhouse gas emissions [6], the United Kingdom has made a legally binding commitment to cut greenhouse gas emissions by 12.5% of their 1990 levels no later than 2010. In Europe, Britain is one of two nations (the other being Sweden) that is on course to meet its Kyoto obligations [7], however the government has committed to exceeding this by reducing greenhouse gas emissions by 20% by 2010 [1]. Although time to build will preclude nuclear power generation contributing towards a reduction in CO_2 emissions by 2020, a new fleet of nuclear power stations would help maintain this commitment in the longer term.

Although generating electricity using nuclear fission is desirable in terms of security of supply and low CO_2 emissions, the enduring legacy of nuclear waste represents both technical and environmental issues and is also a barrier to its acceptance by the general public. The responsible management of nuclear waste is therefore of great importance. In an effort to add understanding of materials used for the immobilisation of nuclear waste, the results of simulations performed for glass and ceramic systems used as nuclear wasteforms are presented in chapters 3 and 6 respectively. Furthermore, the structure and interactions occurring at glass-ceramic interfaces are considered in chapter 4 and chapter 5.

1.1 Nuclear Waste Immobilisation

The work contained in this thesis is concerned with glass compositions related to the immobilisation of high level nuclear waste resulting from the reprocessing of nuclear fuel. When fuel is burnt in a nuclear reactor, energy is released by the fission of actinides such as U-235 and Pu-239; this results in the build up of fission products in the fuel. Some of these (e.g. a number of rare earth elements) absorb neutrons, whilst others alter the fuel's structure, reducing the efficiency of the fission process [8]. Eventually, the continued irradiation of a fuel pellet becomes uneconomical and it must be removed from the reactor. After removal however, fuel pellets still contain useful amounts of unfissioned uranium and plutonium. In the closed fuel cycle favoured by France, Japan and Britain the spent fuel is reprocessed to recover this remaining fissionable material [9].

In the United Kingdom, fuel reprocessing proceeds as follows [8]:

- Remove fuel cladding.

- Dissolve fuel in nitric acid.

- Remove insoluble fission products.

- Extract useful fuel elements using solvent extraction.

The waste resulting from this process is a highly acidic radioactive slurry containing fission products (e.g. Rb, Sr, Y, Zr, Nb, Mo, Tc, Ru, Cs), fuel alloying elements (e.g. Fe, Si and Mo), cladding elements (e.g. Al and Mg) and some transuranic elements (e.g. Am, Cm) [10]. This liquid waste is harmful to humans and the biosphere [11]. The responsible disposal of such wastes is an important challenge that needs to be met [10].

Historically, the storage of high level waste in a liquid form has been considered as an acceptable short-term solution [10]. As an example, high level liquid waste was stored in 149 single walled carbon steel vessels at the U.S. Hanford complex [12]. As tank leakage and gas explosion are very real threats, the unstable nature of historical waste facilities has led to a drive towards more stable and easily managed wasteforms with improved longevity [10].

Immobilisation is defined as the conversion of a waste into a wasteform by solidification, embedding or encapsulation (by the IAEA) [11]. The aim of immobilisation is to provide a wasteform that is more stable, can be more easily managed and is suitable for long-term geological disposal [10]. The work in this thesis is related to the structure and properties of glass and ceramic mateerials used as hosts for the immobilisation of high level nuclear wastes.

1.1.1   Vitrification

In the context of this thesis, vitrification describes the process of immobilising waste materials in glass. Figure 1.1, shows a schematic diagram of a vitrification rig similar to that used by the UK and France to immobilise high level wastes arising from reprocessing [8].

A large proportion of high level liquid waste's (HLLW) volume is due to its water content. This is removed by passing the waste through a rotating kiln, known as a calciner, operated at 850°C [8]. As the HLLW flows through the calciner its water content is progressively evaporated to leave a fine powder called the calcine. Caking of the calcine is avoided by the tumbling action induced by the rotation of the calciner.

The calcine is then fused with glass to form a vitrified wasteform. This is achieved by mixing the calcine with glass frit (previously made glass ground into a powder) which is then admitted

to the melter. The calcine-frit mixture is melted using an induction furnace at a temperature of about 1100°C [8]. After about eight hours, the molten glass is drained into stainless steel containers. After solidifying, these containers are moved to interim storage where they are kept for at least 50 years [8, 11].

1.1.2 Ceramic Wasteforms

It has been observed that certain mineral phases containing radioactive elements have been stable for tens to hundreds of millions of years, even when in contact with water. As a result, it has been argued that synthetic analogues of such minerals would make suitable hosts for high level nuclear waste. An example of such a material is pyrochlore. This material will be discussed in chapter 6 in terms of its suitability as a host for nuclear waste. Crystalline materials of this kind offer several potential benefits over vitrified wastes.

Ceramic wasteforms can exhibit higher thermal stability than vitrified wasteforms. This is significant as the radionuclides dispersed in a nuclear waste material, decay and generate heat [11]. Self heating of waste is related to waste loading. The higher the loading the more energy the host matrix must dissipate. Higher thermal stability offers the potential of higher waste loadings, which in turn leads to a reduction in the volume of waste bearing material which needs to be managed [13].

Unlike vitrified waste, where atoms are homogeneously distributed through the glass structure, radionuclides are incorporated into ceramic wasteforms at particular sites in the crystal lattice. This is because the coordination environment of different sites in the crystal structure impose specific size, charge and bonding constraints upon the atoms which they can accomodate [14]. This means the composition of ceramic wasteforms must be tailored to incorporate particular waste elements.
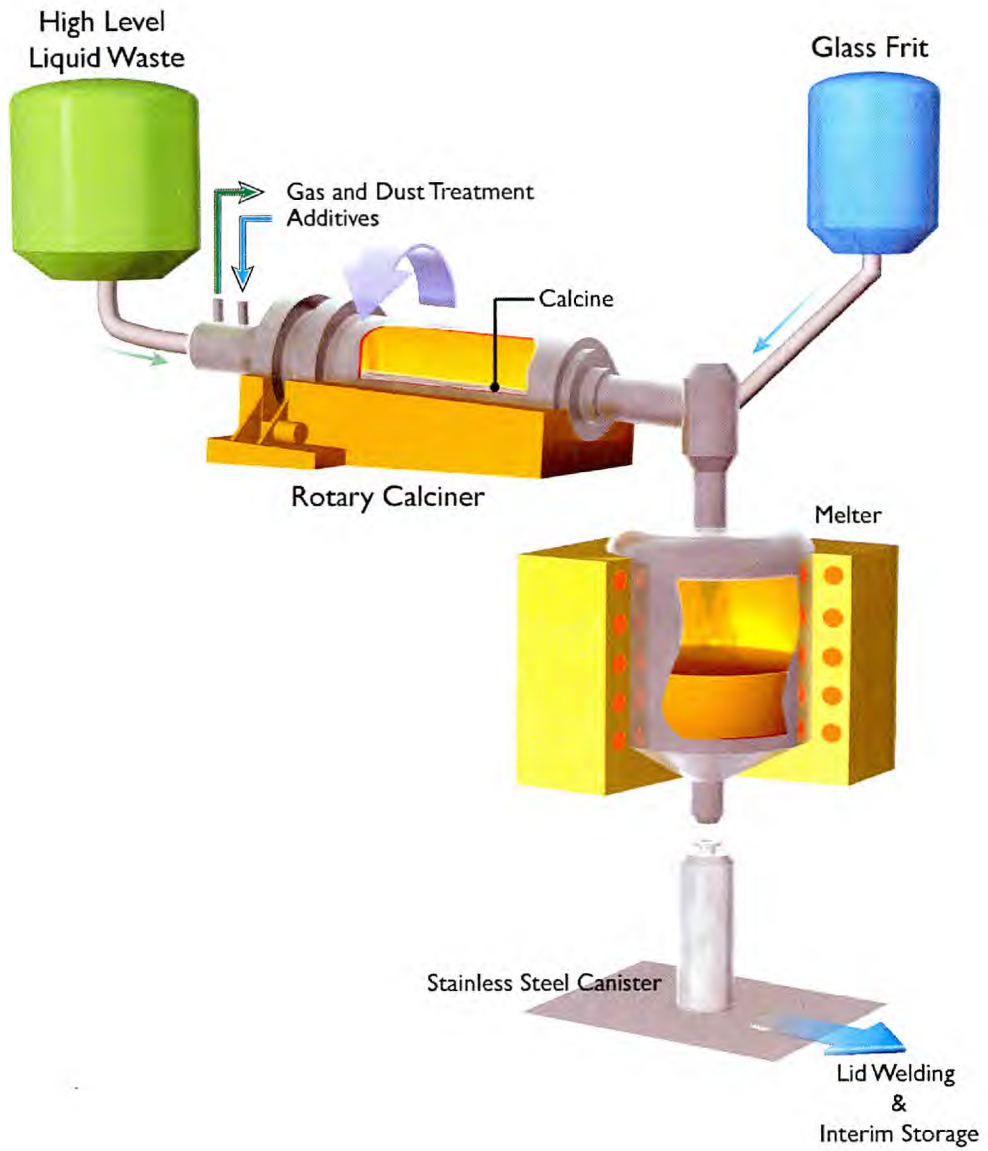
Figure 1.1: Schematic diagram of a typical rig used to immobilise high level nuclear waste.

1.2 The Structure of Glass

Glasses are amorphous solids which do not exhibit long range order. The term glass can be applied to a large range of materials which are X-ray amorphous and have a clearly defined glass transition temperature [15]. This definition is quite broad and can include organic materials such as glycerol [15] and metals in which a glassy state can be induced [16]. The glasses considered by this thesis and those used to make such items as windows, glass bottles, light bulbs and camera lenses can be defined using the more restrictive definition from the American Society for Testing Materials that states: "glass is an inorganic product of fusion which has cooled to a rigid condition without crystallizing" [15].

Typically, glasses are formed by cooling a glass forming composition from the molten state. Many glass forming systems readily form crystalline materials. For instance, SiO_2 has several crystalline polymorphs such as α-quartz, β-quartz and cristobalite [17]. To prevent crystallisation, an amorphous state is induced by rapid cooling from the melt. As heat is removed quickly, there is insufficient time for atoms in the material to undergo the concerted rearrangement required to form a crystalline material, instead a metastable structure is formed which does not exhibit long range order.

The choice of composition for nuclear waste host glasses is a compromise between processability and wasteform durability. Ideally, the glass should have high waste solubility, low processing temperatures, mechanical integrity, low leachability under repository conditions and excellent radiation and thermal stability [10, 11]. Although phosphate and rare earth glasses have been considered as nuclear waste hosts [10] most commercial vitrification plants have employed borosilicate glasses. Before considering borosilicate glass, the structure of silicate and alkali silicate glasses will be described.

1.2.1 Silicate Glass

Although several theories exist to describe the structure of amorphous SiO_2 [18] perhaps the mostly widely accepted is the continuous random network model originally proposed by

Zachariasen [19]. This proposed that silicon atoms in vitreous SiO_2 are invariably coordinated by four oxygen atoms, forming well defined SiO_4 tetrahedral units. These tetrahedra then form a polymerised network in which each tetrahedra shares an oxygen atom with four other SiO_4 units. Oxygen atoms shared by two SiO_4 tetrahedra are known as bridging oxygens. In the glass network it is assumed that there is a random distribution of inter-tetrahedral angles, accounting for the lack of long range order observed in amorphous silica. A representation of a continuous random network structure of an A_2B_3 glass is given in figure 1.2.

1.2.2 Alkali Silicate Glass

In the same paper in which he proposed the continuous random network model [19], Zachariasen defined a set of structural rules for determining which systems can form continuous random network oxide glasses these stated that:

1. No oxygen atom may be linked to more than two cations.

2. Oxygen polyhedra are corner sharing (rather than edge of face sharing).

3. For three dimensional networks, at least three corners of each oxygen polyhedron must be shared.

4. The cation's coordination number must be small, four or less.

These rules have been found to be quite good at predicting glass formation and accurately predict the main glass forming oxides: B_2O_3, SiO_2, GeO_2 and P_2O_5 [16,20]. These oxides are commonly referred to as network formers.

Glasses composed entirely of network formers are rarely used for practical applications. For example B_2O_3 is not water resistant and, although it has good chemical durability, SiO_2 has a very high processing temperature of over 1750°C. The majority of technologically significant glasses contain additional components.
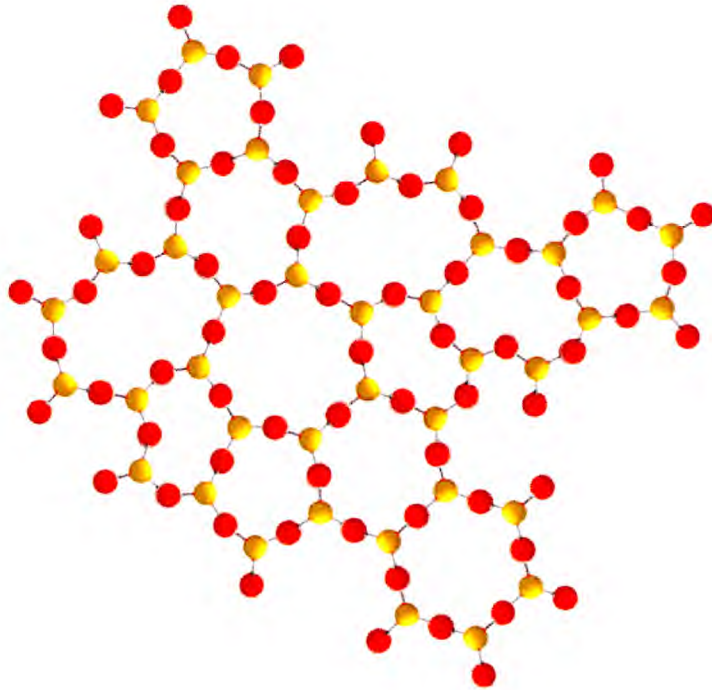
Figure 1.2: Continuous random network of a glass (adapted from [19]).

Alkali oxides such as Li_2O, Na_2O and MgO are often added to SiO_2 as fluxes to lower the melt viscosity and glass transition temperature [15]. This allows alkali silicate glasses to be processed at lower temperatures than SiO_2. Each alkali ion added to the glass leads to the breaking of an Si-O-Si bonds to create a non-bridging oxygen (NBO) which the charge compensating alkali ion is then associated with. Normally oxygen atoms in the silicate network link two silicate tetrahedra, NBOs are only associated with a single tetrahedron. The effect of the alkali additions on the glass structure is therefore to cause depolymerisation of the glass network. The depolymerisation process can be thought of as an acid-base reaction that, for a monovalent alkali oxide (M_2O), proceeds as follows [11]:
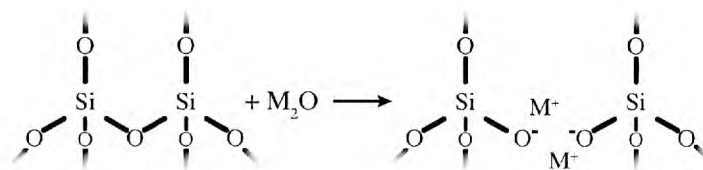
Due to their depolymerising effect, alkali, alkaline earth, transition metal and highly charged ions with a large size, that cannot substitute for network formers, are known as network modifiers [11].

In Zachariasen's continuous random network model [19], the position of network modifiers in the glass network is left unspecified, with modifiers sitting in naturally occurring 'holes' in the glass network close to their charge compensating NBO. Greaves et al. [21, 22] examined the local structure around modifier atoms in various glass compositions using the extended X-ray absorption fine structure (EXAFS) technique. Rather than the homogeneous distribution of modifiers described by Zachariasen [19], they found evidence to suggest that modifier atoms sat in modifier rich ion channels. The theory that nanoscale segregation of oxide glasses occurs, leading to the formation of different regions rich in modifiers and network formers is often referred to as the 'modified random network' (MRN) model. Atomic computer simulations of alkali silicate glasses have also shown evidence to support the MRN model [23, 24]. It has been argued that ion channels of the type predicted by the MRN model would provide rapid migration and percolation channels for the leaching of radionuclides from nuclear waste bearing glasses [25]. The modifier distribution in simulated glasses will be discussed further in chapter 3.

The Mixed Alkali Effect

The addition of a second alkali to an alkali silicate glass leads to a sharp decrease in ionic conductivity [20]. Figure 1.3 shows ionic conductivities for Li-Na, Na-K and K-Li mixed alkali silicate glasses. Conductivity falls, sometimes by orders of magnitude, as the ratio of the two alkali species approaches 50:50. Indeed, the minima in the ionic conductivities for each mixed alkali series, were close to a concentration ratio of 0.5, the point at which there was an equal quantity of each modifier species. The non-linear dependence of glass properties to their mixed alkali concentration ratio is known as the mixed alkali effect [26].

In addition to ionic conductivity, minima are seen in other properties of mixed alkali glasses. Minima have been observed for the following properties: hardness, high-temperature elastic

moduli, electrical conductivity, dielectric constant, dielectric loss and viscosity [27]. By comparison, maxima are observed in the chemical durability and electrical conduction activation energy [27].

It is thought that the mixed alkali effect is related to modifier mobility. Measurements of diffusion coefficients have shown that the mobility of each modifier species is lower in mixed alkali compositions than equivalent single alkali glasses [20]. Reasons for the decreased modifier mobility in mixed alkali glasses are discussed in chapter 3, with relation to modifier distribution in simulated glasses.

1.2.3 Borosilicate Glass

During the vitrification of high level nuclear waste, melting should be carried out between 1100 and 1250°C, as at higher temperatures, excessive volatilisation of both radioactive and non-radioactive waste components occurs [11]. The processing temperature of alkali silicates, although lower than vitreous silica, still tend to be too high for use in the vitrification of high level nuclear waste. To bring down the processing temperature further, glass formers other than silica are added [11]. Borosilicate glasses, as their name suggests, contain both silicon and boron as network formers and represent the first generation wasteform for the immobilisation of high and intermediate level nuclear waste, with plants operating throughout the world [10].

In addition to lowering the processing temperature, the addition of boron (at levels below 15wt%) to silicate glasses has a number positive benefits: thermal expansion coefficient is reduced and chemical durability and resistance to mechanical abrasion are also improved [11].

Silicon in oxide glasses is invariably coordinated by four oxygen atoms. By comparison, boron exhibits a variable coordination state and can exist either as BO_3 triangles or BO_4 tetrahedra. The addition of alkali atoms to vitreous B_2O_3, rather than leading to the formation of NBOs (as described for silicate glasses) instead initially causes the conversion of BO_3 to BO_4 [28–30]. This increases the polymerisation of the boron network and leads to a minimum being observed in the thermal expansion coefficient at around 16 mol.% Na_2O (this is the opposite of what happens when modifiers are added to vitreous silica). This behaviour is normally referred
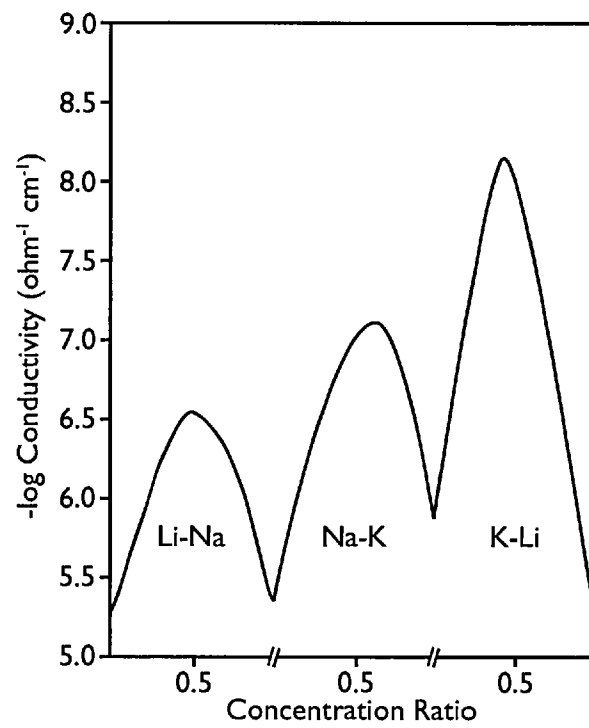
Figure 1.3: Ionic conductivity in mixed alkali silicate glasses [20].

to as the 'boron-anomaly'. The number of fully polymerised BO_4 tetrahedra increases up to a maximum value as a function of alkali concentration, further alkali additions then lead to formation of NBOs in the borate network.

The fraction of three coordinated boron atoms is an important structural parameter in borosilicate glasses. BO_3 is a relatively unstable component in borosilicate glass and is easily leached by acids [11]. In order to minimise the BO_3 population, and therefore improve wasteform durability, nuclear waste glasses are normally based on alkali borosilicate compositions. To further improve durability mixed alkali compositions are chosen. As described above, the presence of more than one modifier species in a glass leads to an overall reduction in modifier mobility and hence the leachability of these species.

The glass compositions chosen for study in this work are based on the mixed alkali borosilicate composition (described further in chapter 2) used by British Nuclear Fuels Limited to immobilise wastes issuing from the reprocessing of magnox waste fuel. Magnox fuel is clad in an aluminium and magnesium alloy and although efforts are made to remove this cladding [8], the resulting waste stream is high in these elements [10,31]. Magnesium is a divalent modifier species whilst alumina is an intermediate oxide.

Intermediates are species which cannot form oxide glasses on their own, but can play a network forming role in the presence of other network formers [16]. Al^{3+} can substitute for Si^{4+}, however due to its lower charge, it relies on the presence of a nearby alkali atom for charge compensation. The effect of this is to cause alkali atoms to move out of their network modifying role, as a result, the number of NBOs in the system decreases on the addition of aluminium, resulting in a more polymerised glass network. In terms of wasteform durability, alkali atoms that charge compensate aluminium are tightly bound to AlO_4 tetrahedra, and are not as readily leached as alkalis that are more weakly bonded to NBOs [11].

1.2.4   A Note on Structural Notation

Experimental techniques such as nuclear magnetic resonance spectroscopy (NMR) allow the local environment of glass constituents to be determined [32]. In particular it is possible to

detect differences in the environment of a network former based on the number of bridging and non-bridging oxygens surrounding it. Results determined in this way are expressed in terms of the number of bridging oxygens a network former has. In chapter 3 comparison will be made between simulation and structural data of this kind. For this reason the notation used to describe such data will now be introduced. The notation used to describe speciation data will be that adopted by Eckert [33] where the number of bridging oxygens is written as the superscript to the network forming species of interest. As an example, a silicon atom with four bridging oxygens is written as:

$$Si^{(4)}$$

Similarly, a borate unit with three bridging oxygens becomes $B^{(3)}$. Likewise, aluminate tetrahedra with four bridging oxygens is described as $Al^{(4)}$ whilst those with three bridging oxygens would be $Al^{(3)}$, This notation is equivalent to Q and N notation sometimes used to describe Si and B speciation.

1.2.5   Glass Ceramic Interfaces

In chapters 4 and 5 results are presented for atomic scale computer simulations of glass-ceramic interfaces. At the atomic scale relatively little is known about the structure of glass at the interface with a ceramic material.

High level nuclear waste contains components, (such as S, Cl and Ru [11]) that are sparsely soluble in borosilicate glass [11, 34]. Precipitation of these phases can occur during vitrification, especially at high waste loadings [34]. Large numbers of crystals, which tend to settle at the bottom of the glass, can interrupt melter operation [34, 35]. In addition, certain crystalline phases are water soluble which tends to decrease wasteform durability. For instance, a water soluble 'yellow phase' (based on an assemblage of alkali sulphates, alkali chromates, alkali molybdates, $CaMoO_4$ and $Ba(Sr)CrO_4$) has been observed in magnox waste glasses [11, 36]. Knowledge of the atomic scale structure of glass-ceramic interfaces could potentially lead to improvements in the composition and processing conditions allowing the presence of undesir-

able crystalline phases in vitrified wastes to be reduced. It is hoped that the work contained in this thesis will contribute to this knowledge.

In certain instances, the presence of a ceramic and glass together in the same material can be desirable. Designed glass-ceramic composite materials have been proposed as hosts for high level nuclear waste [10, 11, 37, 38]. Depending on application, the glass phase can be used either as a binding agent (holding ceramic particles together), or as a matrix, in which ceramic particles are dispersed [11]. Glass-ceramic composite wasteforms offer some benefits. Glass immisicible phases (e.g. sulphates and chlorides) can be contained in the ceramic phase [11]. A glass composite material may also show improved durability in comparison to a monolithic ceramic wasteform, with the glass matrix acting as a further barrier between waste components and the biosphere [37, 38]. The knowledge gained through the use of techniques, such as those described in chapter 3, could help in understanding how waste components partition between the ceramic and glass phase in these materials, and additionally how they would be expected to perform under repository conditions.

1.3   Atomic Scale Glass Simulation Techniques

The lack of periodicity, symmetry and long range order in amorphous materials makes it difficult to determine their structure, at the atomic scale, using experiment [18]. The structure of a defect free crystalline material, can be described by specifying the structure of a single unit cell (defined by a relatively small number of independent parameters). This can be determined from diffraction data obtained from X-ray and neutron sources. By comparison, due to their lack of long-range order, diffraction techniques only yield isotropic structural information related to pair correlations in amorphous materials (this is discussed in more depth in chapter 3). A unique atomic scale definition of a glass cannot be obtained from this pair correlation data [18]. It is for this reason that computer simulation has played such an important role in determining the structure and dynamic processes of glasses. At the time of writing, the two main simulation methodologies applied to the study of glass structures were molecular dynamics and the reverse Monte Carlo technique [39].

The aim of reverse Monte Carlo (RMC) modelling is to produce a model, or a series of models that are consistent with any available experimental data and any applied constraints [40]. In effect, RMC generates a number of candidate structures for a set of experimental data. The structures are generated by randomly displacing atoms (complying with any applied constraints) in the simulation cell. Each atom movement is accepted or rejected based on a probability depending on whether or not it improved the level of agreement between properties of the model system and experimental data [39–41].

During molecular dynamics (described in chapter 2), Newton's law's of motion [42] are solved as a function of time for a simulation cell containing a collection of atoms acting under the influence of forces due to other atoms in the system [43]. Using this method the time evolution of the atoms in the system can be observed as a function of variables such as temperature and pressure. Molecular dynamics simulations of glass normally employ the melt-quench technique (described further in chapter 2), in which a model system is heated to a high temperature, the temperature of the system is then reduced incrementally until an amorphous state is obtained [44].

As mentioned above, the RMC method requires experimental data against which to fit. Due to a lack of suitable experimental data for glass ceramic interfaces, the melt-quench method, which requires only a description of the forces acting between atoms in a system, was chosen for the simulations of glass-ceramic interfaces given in chapters 4 and 5. In addition, Garofalini *et al.* have found some success in using molecular dynamics to simulate glass-ceramic interfaces for battery applications [45,46].

Chapter 2

Method

Atomic scale computer simulations were used to examine glass, glass-ceramic and crystalline systems relevant to nuclear waste immobilisation. In this chapter, the methods used to model these materials are described.

2.1 Glass Simulation

When an assemblage of atoms, with a suitable composition, is cooled quickly from the molten state, a glass can be formed. The glass simulations reported in this thesis were produced using the melt-quench method (first described in section 1.3), in which a good description of the interatomic forces acting in a material were used in conjunction with molecular-dynamics simulations to mimic the thermal processes experienced during a quench and so induce the amorphous state. In simple terms during a melt-quench, the following takes place:

- **Melt:** An atomic system is heated to a high temperature to induce a liquid like state.

- **Quench:** Molten system is rapidly cooled to create an amorphous system.

- **Equilibration and Data Collection:** The system is allowed to equilibrate and statistics are collected from the glass.

2.1.1 Molecular Dynamics

Before moving on to consider the specific details of the melt-quench algorithm it is necessary to understand the principles underlying molecular-dynamics simulations. When given a set of atoms and a description of the forces acting between them (see section 2.1.2), molecular-dynamics allows the time evolution of atom positions to be followed. As such, this technique is well suited to studying the influence of temperature on the time dependent properties of a system, and therefore, is well suited to reproducing the thermal processes involved in glass formation.

At its most basic, during molecular-dynamics the forces between atoms are calculated and the atoms are moved in response to these forces. In the same way that Newton's laws of motion are used to predict the motion of celestial bodies, they can also be used to calculate the motion of atoms acting under the influence of interionic rather than gravitational forces. Newton's second law of motion can be expressed as (assuming that the mass of the object being considered is time invariant):

$$\mathbf{F}_i(t) = m_i \mathbf{a}_i(t) \tag{2.1}$$

where t is time, $\mathbf{F}_i$ is force, m_i is mass and $\mathbf{a}_i$ is the acceleration of an atom i (emboldened text represents a vector quantity). For an ion with a position in cartesian space of $\mathbf{r}_i$ and a potential energy of ϕ, Newton's first law can be rewritten as:

$$-\frac{\partial \phi_i}{\partial \mathbf{r}_i} = m_i \frac{\partial^2 \mathbf{r}_i}{\partial t_i^2} \tag{2.2}$$

The potential energy (ϕ_i) of an ion is dependent on interactions with the other atoms in the system. As a result of the large number of time and position dependent interactions involved, solving equation 2.2 analytically is impractical. Instead, Newton's laws of motion are numerically integrated. Treating time as a discrete quantity, and given knowledge of atom position and momentum at time t, it is possible to determine positions and velocities at some later time, $t + \delta t$. The smaller the timestep δt, the more exact the solution to equation 2.2 becomes. This work, used the velocity Verlet integration method throughout [47]. This is an extension of the original Verlet algorithm [48] which improves efficiency by overcoming the older algorithm's need to store previous simulation frame data in order to calculate velocities. The position and

velocity (**v**) of an atom are calculated as follows:

$$\mathbf{r}(t+\delta t) \;=\; \mathbf{r}(t)+\delta t\mathbf{v}(t)+\frac{1}{2}\delta t^2\mathbf{a}(t) \tag{2.3}$$

$$\mathbf{v}(t+\delta t) \;=\; \mathbf{v}(t) + \frac{1}{2}\delta t[\mathbf{a}(t) + \mathbf{a}(t+\delta t)] \tag{2.4}$$

Therefore, with knowledge of the positions and velocities of atoms at some time t, it is possible to calculate their positions and velocities at some point in the future. This is achieved by repeatedly solving equations 2.3 and 2.4 and incrementing time by δt. The state of the system in the future can be calculated by simply repeating this procedure until the desired time is reached. Although the processing power of computers is always increasing, limits to the size of system accessible by molecular-dynamics still remain. Whether limited by memory or time considerations, the number of atoms in a molecular dynamics system is small in comparison to Avogadro's number. For example, the simulations presented in this thesis contained in the order of 10^3–10^4 atoms, without resorting to large parallel machines, this number of particles is approaching the upper limit of what can be studied in a practical time period with a modern computer. The need to keep δt small to provide reliable solutions to equation 2.2 means that the timescales accessible by molecular dynamics are quite short (in the order of picoseconds).

Comparing the results of a simulation containing several thousand atoms with those obtained from a macroscopic sample poses several challenges. For example, a volume element in a material is constrained by the surrounding bulk. At a surface these constraints break down and sometimes quite extensive atomic relaxation can occur. In macroscopic systems, only a small percentage of the atoms are at the surface and therefore contribute little to bulk properties. This is not the case for the small number of atoms constituting a molecular-dynamics simulation. Here the surface area to volume ratio is considerable and surface effects can hinder attempts to obtain bulk properties from such a system. To counteract this, periodic boundaries are introduced. Illustrated in figure 2.1, periodic boundary conditions give the impression of the simulation cell being embedded in an infinite bulk material. This is achieved by surrounding the primary simulation cell by images of itself; atoms moved in the primary cell are also moved in the image cells. Any atom crossing a periodic boundary is wrapped around to appear at the other side of the cell. For instance, in fractional coordinates, an atom crossing the boundary at $x = 1$ would appear at $x = 0$. As bulk materials were considered by this work, periodic boundary conditions were employed for all molecular-dynamics calculations.

Any atom crossing a periodic boundary wraps around to the other side of the cell.
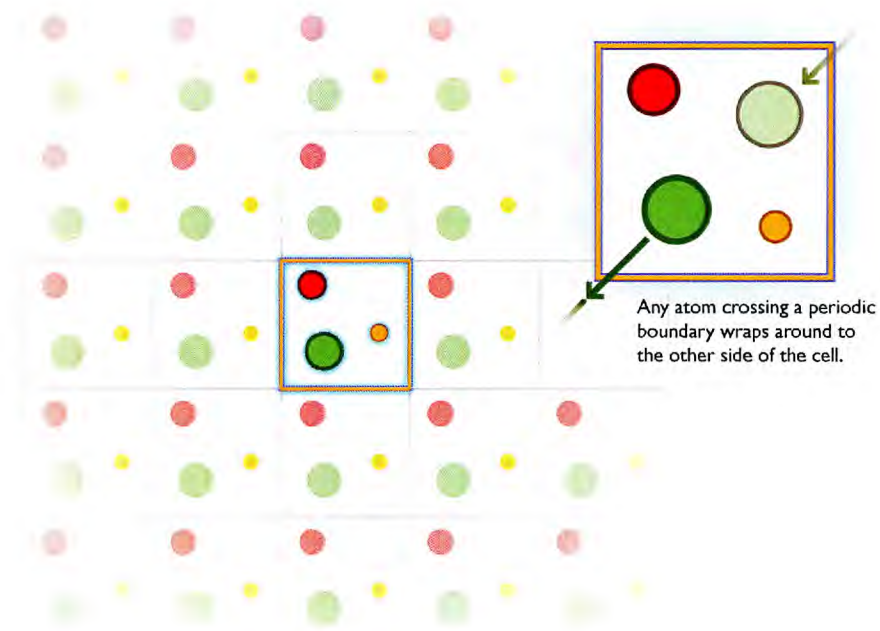
Figure 2.1: Illustration of periodic boundary conditions in two dimensions. The central simulation cell is surrounded by images of itself tesellated in space.

Molecular-dynamics calculates the position and velocity of atoms in a model. A measurable quantity such as temperature is a macroscopic property: somehow the atomic quantities probed by simulation must be reconciled with bulk properties. Statistical mechanics provides the bridge between the atomic scale and macroscopic properties and at its centre is the concept of the thermodynamic ensemble. A thermodynamic ensemble represents all the different ways in which the positions and momenta of atoms in a system can arrange themselves, where each state has one or more extensive quantities in common. Extensive quantities are the independent thermodynamic variables of a system, from which all other quantities can be obtained. For instance, it is implicit in the description of molecular-dynamics given above that, as time develops, the total energy of the system remains constant. In addition the volume and the number of atoms in the system also remain constant. In other words the state of the molecular-dynamics system at each time-step is a member of an ensemble where the number of atoms (N), volume (V) and energy (E) are the extensive variables. This gives rise to what is known as the NVE of micro canonical ensemble.

Bulk properties are extracted from an ensemble by taking an ensemble average. Essentially, the observable value of interest is obtained by taking the average of the observable value over all the states in the ensemble; where the average is weighted in favour of more probable low energy states. For most purposes, it is only possible to sample a finite number of these states. In effect during the equilibration stage of a molecular-dynamics simulation, each timestep represents a member of the ensemble: as the simulation proceeds it provides a way of sampling the more thermodynamically favourable members of phase space. This leads to the Ergodic hypothesis which states that the time average over the states of a single structure is equal to the ensemble average over many structures. It is for this reason that the data presented later were averaged over states obtained from the final 5000fs of the melt-quench procedure.

The aim of the melt-quench procedure is to mimic the thermal processes that give rise to a glass. It is therefore necessary to introduce the concept of temperature to molecular-dynamics. Temperature is an observable property due mainly to the kinetic energies of atoms in the system. Once more, due to the relatively small number of atoms in the system, controlling temperature presents a challenge. Consider a macroscopic sample containing a mole of atoms, when averaged over these many billions of atoms the temperature may appear constant. At the atomic level however, considerable localised fluctuations in the atomic motion take place. A volume element within the material is constantly subjected to these fluctuations in energy and volume. In fact these fluctuations are necessary for the system to explore configurational space and proceed along its thermodynamical trajectory [49]. Basic molecular-dynamics produces states in the *NVE* ensemble, as energy is kept constant, this suppresses fluctuations. Performing dynamics in the canonical, *NVT* ensemble must allow fluctuations whilst making sure that the time averaged temperature remains constant. This is achieved by introducing the concept of a thermostat.

Thermostats couple a notional heat bath of the desired temperature to the molecular dynamics system. Energy can be transferred to and from the atomic system to this bath. High energy fluctuations are permitted by this scheme. For instance if a high energy state was experienced, energy would be transferred from the atoms to the heat bath over a set period of time as the system was gradually brought back into thermodynamic equilibrium. The time period over which this occurs is known as the thermostat's relaxation time. All the molecular-dynamics

runs presented in this thesis were produced in either the canonical (*NVT*) or isobaric-isothermal (*NPT*) ensembles and employed the Nosé-Hoover thermostat (originally proposed by Nosé [50, 51] and developed independently by Hoover [52]). The Nosé-Hoover thermostat extended the basic description of the coupled heat bath by introducing the concept of a thermostat mass. This additional degree of freedom allowed the way in which the atomic system exchanged energy with the bath to be controlled in a more granular fashion than a simple thermostat relaxation time, thus allowing the thermostat to produce true isothermal ensemble members [53].

For calculations in the isobaric-isothermal ensemble, the thermostat was augmented by a barostat. As the name suggests, a barostat allows constant pressure molecular-dynamics. Cell volume was allowed to change in order to give a pressure of 0Pa. A barostat that varied cell volume in an isotropic manner was chosen, in order to maintain the simulation cell's orthogonality. This was considered desirable as it meant that an interface normal to the cell's z-axis could be maintained. This allowed more straightforward analyses and descriptions of the glass-ceramic interface. The barostat used for this purpose was that introduced by Andersen [49].

2.1.2 Describing Interatomic Forces

The quality of the results obtained from molecular dynamics is dependent on the quality of the description of forces operating between atoms in the system under consideration. For this work, a classical Born interpretation of interionic forces was adopted [54]. In this, ions are treated as points acting under the influence of spherical, pair interactions with other atoms in the material. The total energy of the system (U) can be written as the sum of the pairwise contributions to the potential energy, where $\phi_{ij}(r)$ is the potential energy for ions i and j separated by a distance r:

$$U = \sum_i \sum_{i \neq j} \phi_{ij}(r) \qquad (2.5)$$

The bonds in the silicate and borosilicate glass networks have considerable covalent character. In addition, boron can have variable coordination states in these networks. Modelling these phenomena using a classical approach is difficult; therefore, quantum mechanical methods which explicitly consider electronic interactions between atoms may seem preferable for

calculating interatomic forces. Unfortunately they are very computationally demanding, this limits the size of systems that can be studied. Due to their lack of periodicity, glass simulations must be large in order to gain statistically representative glass structures. For this reason and given currently available computational resources, quantum mechanical methods were not used for this work[1].

Pair potentials relate the potential energy of a pair of interacting species to their relative positions and can be decomposed into short, $\phi_{short}(r)$ and long-range $\phi_{long}(r)$, electrostatic contributions:

$$\phi_{ij}(r) = \phi_{long}(r) + \phi_{short}(r) \tag{2.6}$$

The long-range or Coulombic contribution (ϕ_{long}) arises due the electrostatic repulsion/attraction between ions:

$$\phi_{long} = \frac{1}{4\pi\varepsilon_0}\frac{q_i\,q_j}{r_{ij}} \tag{2.7}$$

Where:

ε_0 = Permittivity of free space

r_{ij} = Separation between i and j

q_i, q_j = Charges on ions i and j

The short-range contribution to the pair potential defines the character of the interaction between two ions. As its name suggests, this predominates at small interatomic separations and defines the behaviour of atoms at their equilibrium separations. It is therefore very important, if the results of a molecular dynamics simulation are to be valid, to use a potential form that adequately describes the nuances of the potential surface at these equilibrium separations. The potential used during glass simulations was based on the form proposed by Lennard-Jones [57]:

---

[1]Although not directly applicable to large glass simulations, quantum mechanical methods have been used in the successful derivation of pair potentials which are applicable to MD studies (for examples see [55,56])

$$\phi_{\text{short}} = \frac{\sqrt{A_i A_j}}{r_{ij}^{12}} - \frac{\sqrt{B_i B_j}}{r_{ij}^6} \qquad (2.8)$$

Where:

ϕ_{short} = Short range contribution to potential energy between ions i and j

A, B = Parameters specific to interacting species

The parameters of the short range potential (A and B) are specific to each species. A list of the parameters used for the glass and glass-ceramic simulations is presented in table 2.1. These potentials were based on the consistent valence force field [58–60], with additional values suitable for the simulation of borosilicate glasses being used. The ability of this forcefield to describe glass structures is demonstrated in chapter 3, however it was also necessary for these potentials to describe the ceramic systems involved in interfacial simulations. To this end, static energy minimisation (see section 2.3 for description of technique) was performed for the MgO, CaO, SrO and BaO rocksalt structures, the lattice parameters obtained by this procedure are compared with experimental values in table 2.2. It can be seen that the potentials are in good agreement with experiment. The barium potential reported here was derived for this study.

Once the interactions between pairs of atoms have been adequately parameterised, it is possible to calculate the potential energy of an ion i, based on its position relative to the other atoms in the system, by summing over the pairwise energy contributions with the other atoms:

$$\phi_i = \sum_{i \neq j}^{j} \frac{q_i q_j}{4 \pi \varepsilon_0 r_{ij}} + \frac{A_{ij}}{r_{ij}^{12}} - \frac{B_{ij}}{r_{ij}^6} \qquad (2.9)$$

From the gradient of the potential energy surface, the force (F_i) and hence velocity vector for an ion i can be calculated and the molecular-dynamics time can be incremented:

$$F_i = -\nabla \phi_i \qquad (2.10)$$

		Potential Parameters	
Species	Charge	A $(eV\text{Å}^{12})$	B $(eV\text{Å}^6)$
Al	3+	100.869	0.089
B	3+	0.579	0.001
Ba	2+	232051.153	0.612
Ca	2+	18661.429	66.589
Li	1+	50.055	0.000
Mg	2+	1179.259	103.097
Na	1+	9735.806	103.097
O	2-	42895.736	29.351
Si	4+	368.510	0.000
Sr	2+	47594.021	0.000

Table 2.1: Short range potential parameters for glass and glass-ceramic simulations.

	Lattice Parameter (Å)		
System	Simulated	Experimental	Difference (%)
MgO	4.17	4.19 [61]	-0.48
CaO	4.83	4.81 [62]	0.42
SrO	5.15	5.14 [63]	0.19
BaO	5.54	5.52 [63]	0.30

Table 2.2: Comparison of experimental and simulated lattice parameters for rock-salt structures. Simulated lattice parameters determined using static energy minimisation.

As was discussed earlier in the chapter, periodic boundary conditions were applied to the simulation cell. Although they offer an elegant way of representing a bulk material with a small number of atoms, periodic boundaries introduce some complexity into the calculation of the Coulombic part of the potential energy function.

An atom at the centre of the infinite periodic array described by periodic boundary conditions, not only interacts with its immediate neighbours, but also with all the other atoms in the bulk of the material. For obvious reasons, it is not possible to explicitly calculate equation 2.9 over an unbounded number atoms. Instead the potential is calculated for a finite interaction volume surrounding each atom in simulation cell. Enough atoms must be included within the interaction volume for the potential energy to converge on the infinite sum; this requirement must be balanced against the need to reduce the number of interactions considered in order to promote computational efficiency. Given these conflicting requirements, imagine the spherical interaction volume surrounding an atom at the centre of the system. As the radius (r) of the sphere increases, the number of interacting species inside the sphere's radius is proportional to r^3. From equation 2.7, it can be seen that potential energy only decays as r^{-1} as the sphere expands. As convergence of the Coulomb sum, is also conditional on the order in which the charges are summed [43], its evaluation by conventional means is not practical.

A naïve solution to the problems outlined above might be to simply truncate the Coulomb sum at a certain maximum separation. This is unsuitable as not only would it lead to large errors in the electrostatic energy of the system, truncating the potential would lead to a discontinuity of the first derivative of the energy surface and hence an infinite force at that point. This means such a method is totally unsuitable for use in molecular dynamics simulations. Instead, the long-range interactions for simulations appearing in this work were calculated using an Ewald sum [64]. This method splits the electrostatic sum into real and reciprocal space contributions. The sum is made to converge quickly in real space by applying a shielding function to the point charges [65]. The reciprocal part of the Ewald sum requires that each point charge is 'smeared' to form a charge density expressed by a Gaussian function. This is necessary as an impulse like a point charge would require an infinite series to be represented in reciprocal space. The Gaussian charge distributions are transformed to reciprocal space using a Fourier transform. Due to the periodic boundaries, each atom can be thought not as an isolated point,

but rather an array of repeating points with a frequency related to the lattice vectors of the repeating cell. As such, the transformation into the frequency domain neatly side-steps the slow convergence experienced in real-space. By taking the sum of the real and reciprocal contributions with additional dipole and self-energy correction terms, the Ewald sum allows the long ranged electrostatic energy of the system to be calculated. For implementation details of the Ewald sum algorithm readers are referred to [43].

In summary, short range interactions between ions in simulations of glass and glass-ceramic systems were described using a Lennard-Jones 12-6 potential. As these interactions tend to zero at relatively small separations, the short-range interaction was truncated at separations greater than 9.5Å, to encourage computational efficiency. Electrostatic interactions were calculated using the Ewald sum.

2.1.3 Melt-Quench

The following section gives details of the melt-quench method used to generate glass structures for this work. All glass simulations were performed using Accelrys' Discover code [66]. Figure 2.2 shows the temperature vs. time used during quenches. Each glass composition (see section 2.1.3) was heated to 7000K for 15ps, by performing molecular-dynamics in the NVT ensemble using a time-step of 1fs (1×10^{-15}s). Tests with a longer time-step of 2fs were performed but gave very large fluctuations in the total energy of the system. It is likely that this was because atomic velocities at the high temperatures used during the melting stage of glass formation were sufficient to cause atoms to reach unrealistically small interatomic separations and produce these high energies. As a consequence a 1fs time-step was used for all molecular-dynamics simulations presented in this work. Initial velocities were randomly assigned to atoms using a Boltzmann distribution.

The temperatures used during the first 15ps of the quench were much higher than the melting points of any of the glasses considered here. This was to ensure that a random, liquid like structure was obtained in a relatively short time. For this reason it may be more appropriate to refer to this as a randomisation stage (see figure 2.2).
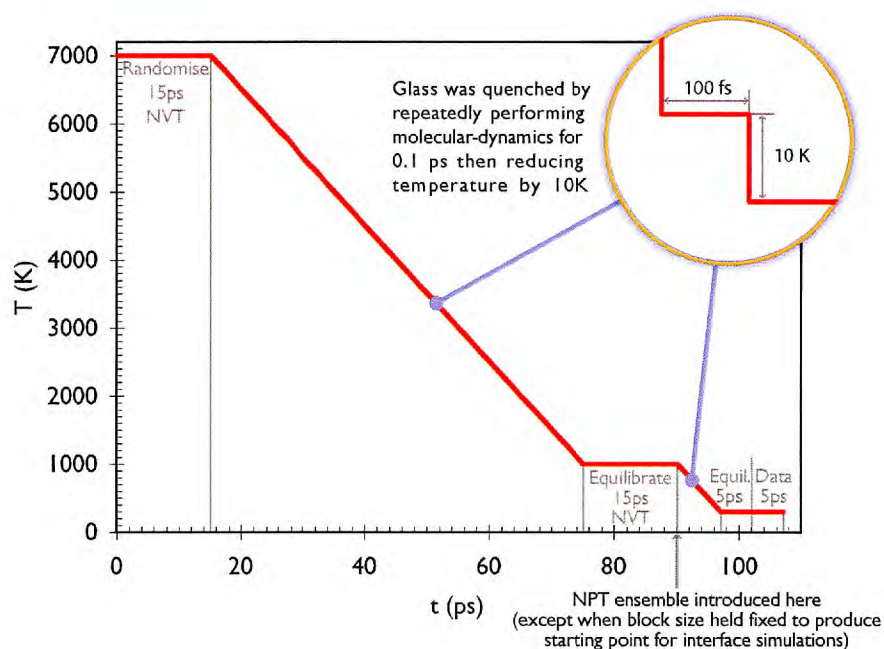
Figure 2.2: Temperature vs. time profile used to create the glass system.

Subsequently, the randomised structure was quenched to 1000K. This was achieved by de-creasing temperature in 10K increments. For each temperature step, 100fs of NVT molecular-dynamics was performed. Temperature was controlled during dynamics runs using the Nosé-Hoover thermostat [2]. At the beginning of each temperature step, atomic velocities were scaled to give the required temperature.

The quench rate for the procedure outlined above was $1 \times 10^{14} \text{Ks}^{-1}$. Although many times quicker than experimental quench rates, it compares favourably with other contemporary sim-ulation studies (e.g. $1 \times 10^{14} \rightarrow 1 \times 10^{15} \text{Ks}^{-1}$ Abbas et al. [67] and $1 \times 10^{13} \text{Ks}^{-1}$ Cormack et al. [68]).

Following the quench to 1000K, another 15ps of NVT dynamics was performed. This equili-bration stage was provided to allow the network and modifier structures to develop. Up until the end of the 1000K equilibration, all dynamics were performed in the NVT ensemble. In the case of glass only simulations the NPT ensemble was introduced at temperatures below

---

[2]Thermostat parameters appropriate to the system's size were chosen automatically by the simulation code

1000K (to reduce unintended residual strain in the glass). Those systems destined to become the starting point for interfacial calculations used the NVT ensemble throughout (in order to provide a glass block with the same x and y dimensions as ceramic system).

From 1000K the glass was quenched to 300K. This was followed by 5ps of room temperature (300K) equilibration. An additional 5ps of NPT dynamics were performed, during which atomic coordinates and velocities were collected at 50fs intervals.

Starting point for glass quenches

The following section gives details of the system-configurations used as the starting point for the melt-quench method. The choices made with respect to system size, composition, simulation cell dimensions and starting configuration are described.

One of the aims of this work was to understand glass ceramic interfaces in the context of vitrified nuclear wasteforms. For this reason, the glass compositions examined were related to the composition used by British Nuclear Fuels Ltd. (BNFL) for vitrification of wastes resulting from reprocessing magnox fuel. The basic glass composition used during the vitrification of magnox waste is given in table 2.4. It is a borosilicate composition which contains approximately equal amounts (in atomic percent) of sodium and lithium as modifiers. Henceforth this glass will be referred to as MW glass.

Magnox waste streams contain many different components. This can be seen in table 2.3 which shows the results of a compositional analysis for a BNFL MW glass containing simulated magnox waste oxides. Magnox fuel assemblies are clad in an alloy of aluminium and magnesium; although efforts are made to remove this cladding during reprocessing, table 2.3 shows that Al and Mg are present in relatively large amounts in the resulting vitrified waste. In an effort to characterise the effect of these additions on interfaces, a magnox waste glass containing Al and Mg was considered. The composition of this MW+Al+Mg glass composition was derived from the compositional analysis given in table 2.3, with fission products and iron contributions removed [31]. This simplified MW+Al+Mg composition, is described in table 2.4.

In order to examine the effect of glass composition on glass ceramic interfaces, three glasses with simpler compositions were also considered. These comprised of a pure silica glass (SiO_2) and sodium silicate (SiO_2+Na) and mixed alkali silicate (SiO_2+Na+Li) glass. In modifier containing glass, the total modifier concentration (in mol %) was chosen to match that of the MW glass. Once more, these compositions are expressed as oxide component concentrations in table 2.4.

The number of atoms in the glass system was chosen such that the interfacial systems were as large as possible without becoming computationally unmanageable. After preliminary tests, a target system size of ~ 3000 atoms for the glass was chosen. The total number of atoms by species are given in table 2.5 for the compositions considered.

Simulation cell dimensions were chosen to give cell volumes consistent with the experimentally determined glass densities shown in table 2.5. Glass blocks from which interfacial systems were generated had the same x and y dimensions as the ceramic block to which they were interfaced. The desired starting density of the glass was then obtained by varying the length of the cell's z dimension to give the required density.

It was shown by Montorsi et al. that starting configuration has little effect on the glass structure resulting from a melt-quench [73]. For this reason initial glass atom positions were assigned at random within the simulation cell. Twenty steps of static energy minimisation were used to remove any 'hot-spots' caused by randomly positioned atoms sitting at small separations, which could have caused unrealistically high velocities during the early stages of randomisation.

2.2 Glass Ceramic Interfaces

Interfaces were constructed between the glass blocks (which were formed in the manner described above) and ceramic supercells. Interfaces were made with the (100) and (110) surfaces of alkali oxides with the rock-salt structure shown in figure 2.3. The ceramic compositions examined were, in order of increasing lattice parameter, MgO, CaO, SrO and BaO. The (110) surface of the rock-salt structure is shown in figure 2.4 in relation to the rock-salt unit cell.

Oxide Component	Nominal-Composition (wt%)	Analysed Composition (wt%)
SiO_2	47.2	47.5
Fe_2O_3	4.82	5.00
MgO	5.29	5.03
Na_2O	8.38	7.82
P_2O_5	0.18	0.08
Cr_2O_3	0.41	0.39
ZrO_2	1.55	1.61
BaO	0.61	0.52
SrO	0.32	0.32
NiO	0.24	0.25
B_2O_3	16.9	16.9
Li_2O	3.76	3.55
RuO_2	0.85	1.13
MoO_2	1.59	1.69
Cs_2O	1.02	1.05
Nd_2O_3	1.45	1.48
Sm_2O_3	0.29	0.29
CeO_2	0.90	0.91
La_2O_3	0.47	0.40
Pr_6O_{11}	0.44	0.43
Y_2O_3	0.19	0.19
Rb_2O	0.12	0.12
TeO_2	0.17	0.13
Totals	99.58	98.96

Table 2.3: Experimentally determined composition for BNFL MW glass containing simulated magnox waste oxides on which MW+Al+Mg composition was based. Reproduced from ref. [31].

	Oxide Component (wt %)					
Glass	SiO_2	B_2O_3	Al_2O_3	Na_2O	Li_2O	MgO
MW Glass	64.7	18.8	–	11.2	5.3	–
	(61.3)	(18.2)		(10.3)	(10.2)	
MW+Al+Mg	54.6	19.6	5.6	9.7	4.4	6.1
	(52.0)	(19.0)	(3.1)	(8.9)	(8.3)	(8.7)
SiO_2	100	–	–	–	–	–
	(100)					
SiO_2 + Na	74.7	–	–	25.3	–	–
	(79.5)			(20.5)		
SiO_2 + Na + Li	83.5	–	–	11.2	5.3	–
	(79.5)			(10.3)	(10.2)	

Table 2.4: Glass compositions (concentrations in brackets are expressed as mol. %.)

		Number of Atoms							
Glass	ρ (gcm^{-3})	Si	B	Al	Mg	Na	Li	O	Total
MW Glass	2.4 [69]	613	364	–	–	206	204	1977	3364
MW+Al+Mg	2.47	551	328	64	89	184	184	1963	3363
SiO_2	2.202 [70]	1000	–	–	–	–	–	2000	3000
SiO_2 + Na	2.38 [71]	795	–	–	–	410	–	1795	3000
SiO_2 + Na + Li	2.35 [72]	795	–	–	–	206	204	1795	3000

Table 2.5: Atom composition for different glasses.

Three different interface creation methods were examined as described below.

2.2.1 Cut and Shut Method for Interface Formation

Named in allusion to the practice of marrying two halves of crash damaged cars together to form one complete car for fraudulent purposes [74], the cut and shut method for interface formation is perhaps the most naïve of those proposed here.

Illustrated in figure 2.5 a ceramic super-cell was generated with the terminating surfaces normal to the z-axis. A glass block generated in accordance with the method from section 2.1.3, was then split in half to create a gap between the upper and lower halves. This was achieved by increasing the glass cell's z-dimension by the desired gap size then translating the top half of atoms (those with z coordinate $\geq$ half of z dimension) by the gap size. The gap height was chosen to be equal to the height of the ceramic block plus two ceramic interlayer spacings. The ceramic super-cell was then inserted at the centre of this gap to produce a ceramic and glass sandwich with a single crystal layer spacing between the glass and the upper and lower surfaces of the ceramic.

Having inserted the ceramic, the glass ceramic system was equilibrated using 15ps of NVT dynamics at 1000K. This was followed by an NPT quench to 300K, 5ps of equilibration and 5ps of data collection at 50fs intervals. These latter stages will be referred to as the equilibration and data collection stages of interface formation.

2.2.2 Gap Close Method for Interface Formation

The gap close method describes a more gradual way to form interfaces. The glass is introduced gradually rather than in the instantaneous way used for the previous cut and shut method. Thus, in the gap close method, the glass and ceramic surfaces are relaxed before being brought together.

The method is summarised in figure 2.6. The glass block was split as before, but before in-
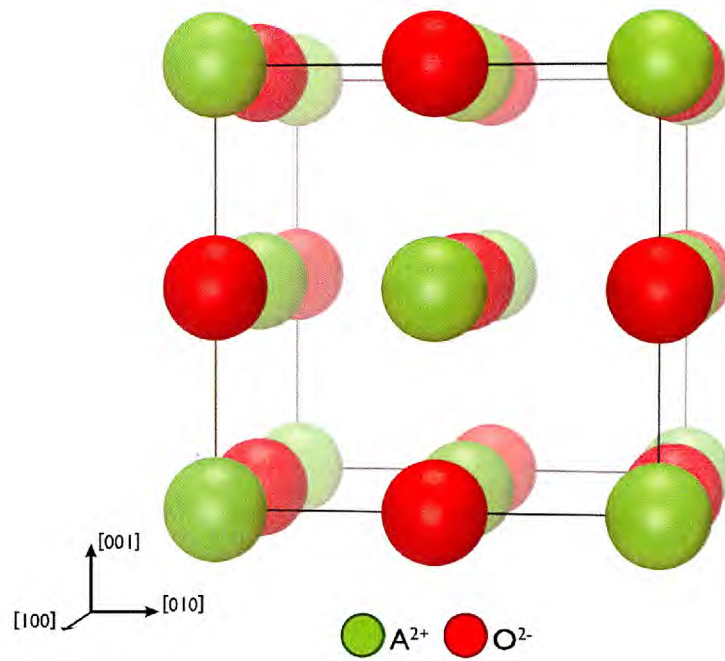
Figure 2.3: Unit cell of the $A^{2+}O^{2-}$ rock-salt structure.
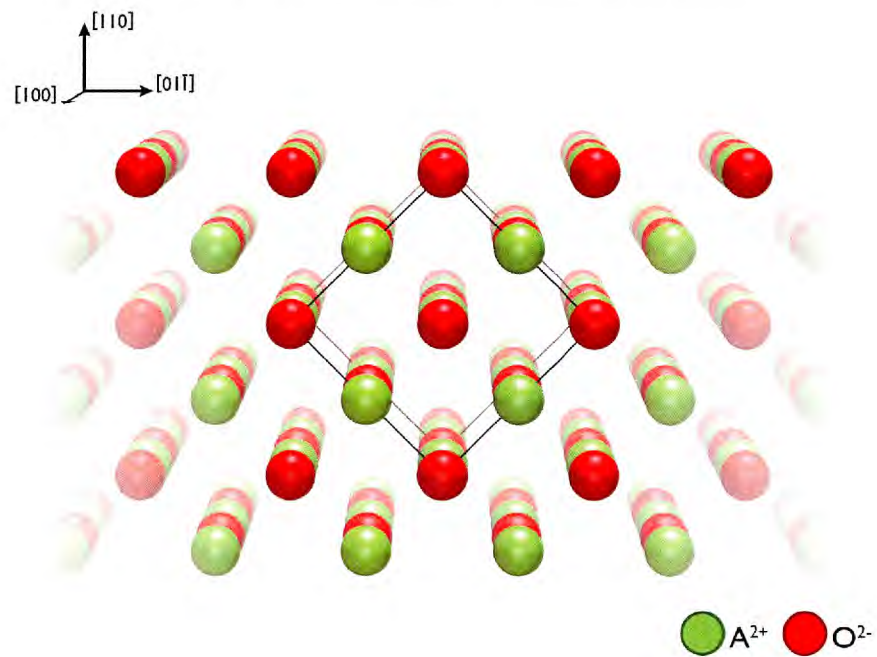
Figure 2.4: The (110) surface of the rock-salt structure. The rocksalt unit cell is highlighted.
Crystallographic directions given relative to rock-salt unit cell (figure 2.3).

a. Form Glass

- Glass block formed via NVT quench.
- Block x and y dimensions match ceramic supercell.
- Height of block chosen to give experimental glass density.

$$\begin{matrix} \text{gap} \\ \text{height} \end{matrix} = 2 \times \begin{matrix} \text{interlayer} \\ \text{spacing} \end{matrix} + \begin{matrix} \text{ceramic} \\ \text{height} \end{matrix}$$

interlayer spacing

b. Cut block and insert ceramic

100 fs

10 K

c. Equilibration & Data Collection
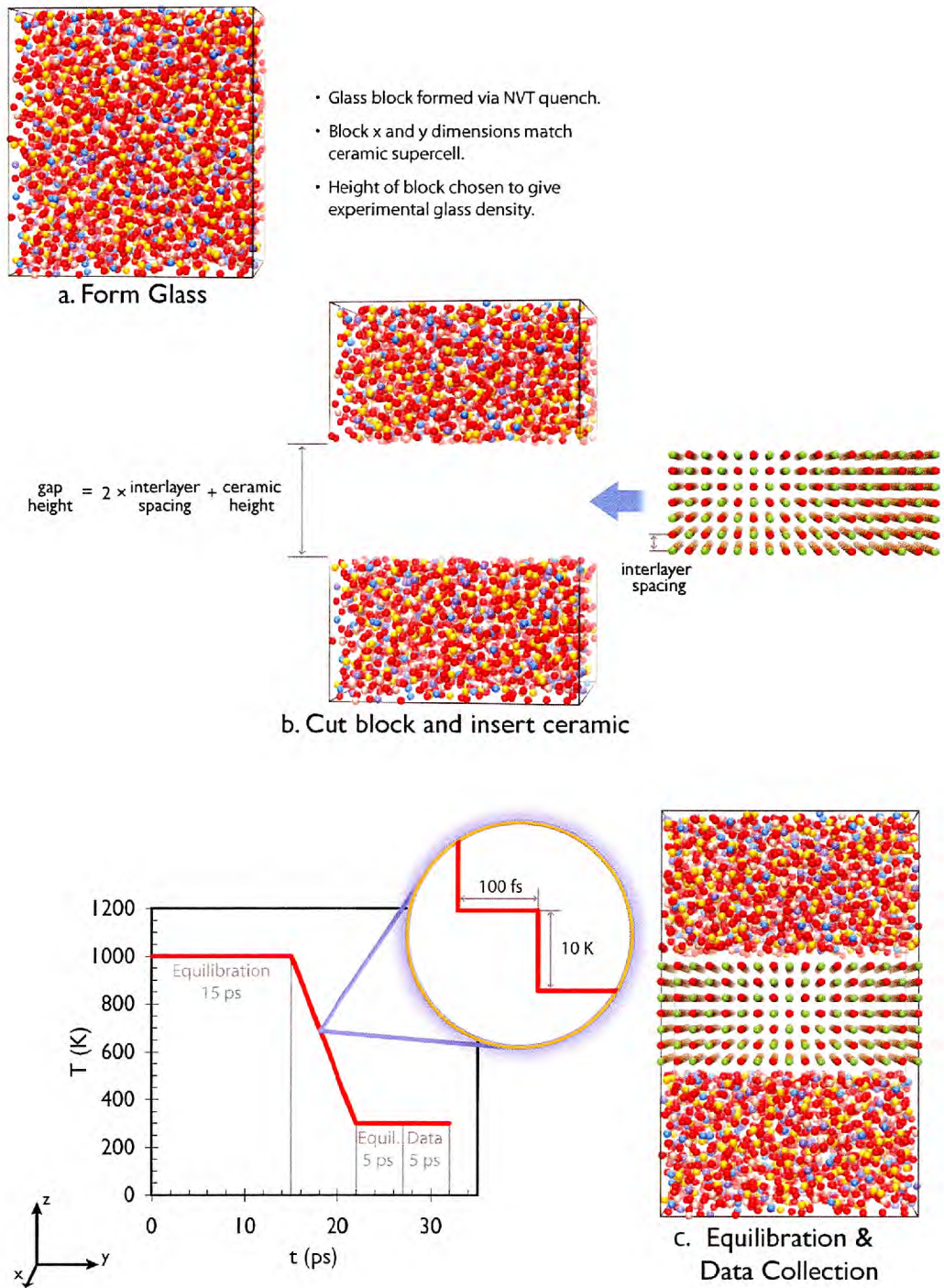
Figure 2.5: Cut and shut method for glass ceramic interface formation.

- Glass block formed in the same way as for other methods.

- Glass split in same way as for the other interface formation methods creating gap adequate in size for ceramic.

- Cut surfaces are equilibrated over 15 ps of molecular-dynamics in the NVT ensemble at 1000 K.

a. Create vacuum surfaces

- Gap increased by 8 Å and ceramic inserted at its centre.

- Top half of glass block moved down in 200 × 0.04 Å steps.

- Ceramic kept in centre of gap by moving downwards in 0.02 Å steps.

- At each step 100 fs of molecular-dynamics performed at 1000 K.

Time

b. Close gap between glass and ceramic

c. Equilibration & Data Collection

Figure 2.6: Gap close method for glass ceramic interface formation.

serting the ceramic, the glass surfaces, exposed during the cut, were equilibrated at 1000K for 15ps. The vacuum surfaces were then introduced gradually to the ceramic by opening the gap by a further 8Å (a distance $\simeq$ 3 MgO (100) layer spacings), inserting the ceramic at the centre of the gap then incrementally closing the gap whilst time was evolved. This was achieved by moving the top half of the glass downwards along the z axis and then reducing the cell's z dimension by the same amount. The gap was closed over 200 steps. At each position 100fs of NVT dynamics was performed. In order to keep the ceramic block close to the centre of the closing gap, the ceramic was translated downwards at half the rate of the top half of the glass. This procedure is described pictorially in figure 2.6b. After the gap was closed the equilibration and data collection stages described previously were performed.

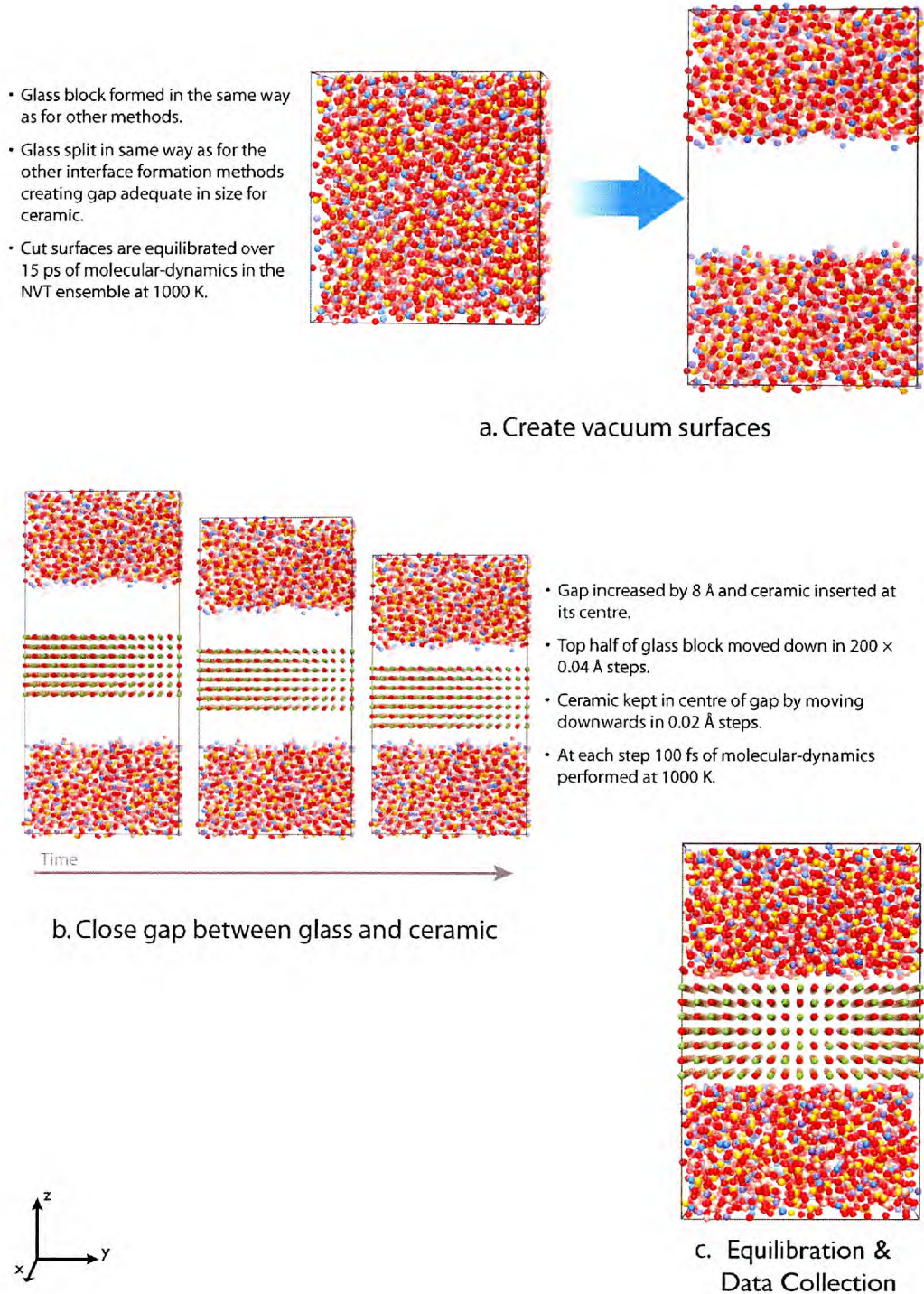In essence, the close gap method is the same as that employed by Garofalini *et al.* to form interfaces between V_2O_5 crystals and lithium silicate glass [45,46,75]. This previous work did not, however, include the gradual introduction of ceramic to glass provided by the incremental gap closing procedure. Instead the relaxed glass surface was placed directly in contact with the ceramic. During the present work it was found that the relaxed glass surfaces did not remain flat but were quite rough. Given the single crystal layer spacing between glass and ceramic, this roughness meant that simply placing the glass in contact with the ceramic resulted in overlap between the glass and ceramic blocks, with glass atoms entering the ceramic and *vice versa*. It is for this reason that the method where the glass was moved towards the ceramic in a gradual fashion was adopted.

Due to a limitation of the Discover code, atomic velocities could not be carried over between gap close steps. Velocities were re-initialised from a Boltzmann distribution each time the cell dimension was changed.

The 8Å increase in gap size was adopted after a larger, 20Å gap had been tried. Over the larger separation, significant glass-ceramic interaction only occurred during the final few angstroms of the gap close. The smaller 8Å gap was used to afford greater temporal resolution to these important later stages.

2.2.3 Quench with Ceramic Method for Interface Formation

Summarised in figure 2.7, the quench with ceramic method avoids the problems associated with surface formation. An initial interface was generated in the same way as the cut and shut method by simply splitting the glass and inserting the ceramic block (see section 2.2.1). Rather than proceeding with the equilibration phase as before, a full melt-quench was performed with the ceramic block *in-situ*. In other words, the glass component of the system is heated to 7000K, randomised and then quenched to 1000K in the same way as the glass block was formed, however due to the presence of the ceramic, the glass structure can form in a modified way to accommodate the ceramic.

As the room temperature structure of the interface was of interest, and to prevent the ceramic block melting or high temperature mixing of the glass and ceramic components: the atoms of the ceramic were held fixed as the system was randomised and quenched to 1000K. Although immobile, interactions between glass and ceramic atoms were still calculated such that the glass could react to the ceramic's presence. The constraint on the ceramic block was released at 1000K during the equilibration and data collection stages of the simulation.

2.2.4 Ceramic Super-Cell and Simulation Cell Dimensions

The dimensions of the (100) super-cells used in this work are given in table 2.6; those for the (110) cells are given in table 2.7. The size of these cells are referred to in terms of 'repeat-units'. The repeat-unit for (100) interfaces was the full rock-salt unit cell shown in figure 2.3. The repeat unit for the (110) interfaces is shown in figure 2.8. In addition, the dimensions of the glass blocks used as the precursors to interface formation are given in table 2.8 for the (100) and (110) glass-ceramic systems examined. Note, interfaces with (110) ceramic surfaces were only constructed for the MW glass composition.

Several considerations were made in choosing the size of the ceramic blocks. Firstly, the size had to be large enough to allow a representative interfacial area to be considered. Secondly, in order to prevent unwanted interactions between the ceramic block and its periodic images along
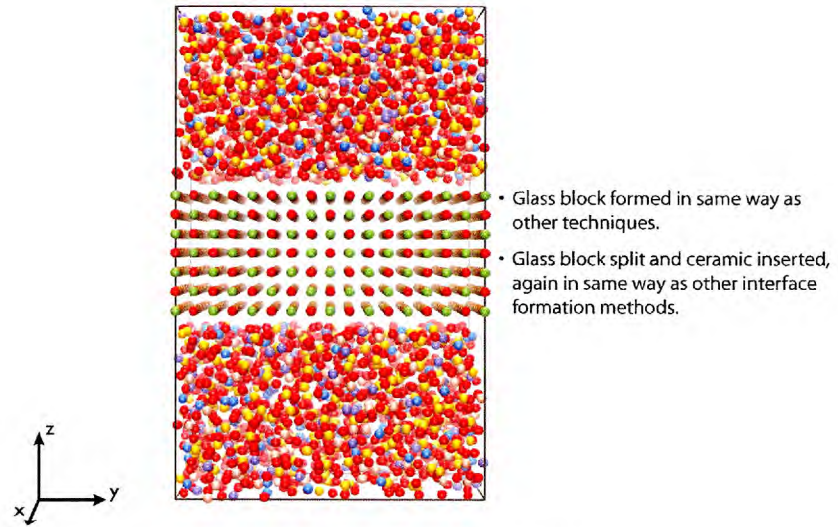
a. Glass block formed and ceramic inserted

- Glass block formed in same way as other techniques.

- Glass block split and ceramic inserted, again in same way as other interface formation methods.

- Glass was formed in presence of ceramic using the same melt-quench recipe used previously for the formation of glass.

- During the randomisation stage of melt-quench, very high temperatures are used. As the state of the interface at technologically relevant temperatures is of interest ceramic atoms were held fixed until quenches reached 1000 K.

- Interactions with fixed atoms were calculated but atoms were not allowed to move.

- Constraints were released during the equilibration and data collection stage of interface formation.

b. Melt-quench performed in presence of ceramic

Figure 2.7: Quench with ceramic method for glass ceramic interface formation.
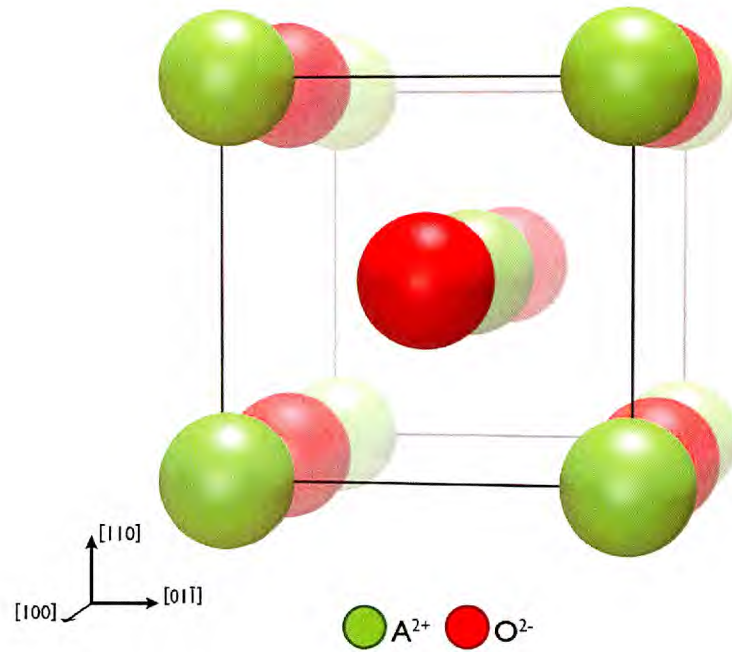
Figure 2.8: Repeat unit for (110) super-cells. Crystallographic directions given relative to rock-salt unit cell (figure 2.3).

	Super Cell Dimensions (x,y,z)	
Ceramic	Repeat Units	Cell Lengths (Å)
BaO	$6 \times 6 \times 2$	$33.238 \times 33.238 \times 11.079$
CaO	$7 \times 7 \times 2$	$33.840 \times 33.840 \times 9.668$
MgO	$8 \times 8 \times 3$	$33.358 \times 33.358 \times 12.509$
SrO	$7 \times 7 \times 2$	$36.066 \times 36.066 \times 10.304$

Table 2.6: Ceramic super-cell dimensions for (100) surface.

	Super Cell Dimensions (x,y,z)	
Ceramic	Repeat Units	Cell Lengths (Å)
BaO	$6 \times 9 \times 2$	$33.238 \times 35.254 \times 7.834$
CaO	$7 \times 10 \times 2$	$33.840 \times 34.183 \times 6.837$
MgO	$8 \times 11 \times 2$	$33.358 \times 32.433 \times 5.897$
SrO	$7 \times 9 \times 2$	$36.066 \times 32.789 \times 7.286$

Table 2.7: Ceramic super-cell dimensions for (110) surface.

Glass	Glass Block Dimensions for Ceramic Super-Cell (Å			
	BaO	CaO	MgO	SrO
MW Glass	$33.238 \times 33.238 \times 36.680$	$33.840 \times 33.840 \times 35.388$	$33.358 \times 33.358 \times 36.418$	$36.066 \times 36.066 \times 31.154$
MW+Al+Mg	$33.238 \times 33.238 \times 36.344$	$33.840 \times 33.840 \times 35.064$	$33.358 \times 33.358 \times 36.084$	$36.066 \times 36.066 \times 30.869$
SiO_2	–	–	$33.358 \times 33.358 \times 41.255$	–
$SiO_2 + Na$	–	–	$33.358 \times 33.358 \times 37.918$	–
$SiO_2 + Na + Li$	–	–	$33.358 \times 33.358 \times 36.322$	–
MW Glass, (110) surface	$33.238 \times 35.254 \times 34.582$	$33.840 \times 34.183 \times 35.032$	$33.358 \times 32.433 \times 37.456$	$36.066 \times 32.789 \times 34.268$

Table 2.8: Glass block dimensions for use with ceramic super-cells. Note, interfaces with (110) surface were only created for MW glass.

the z axis, the height of the glass in the interfacial system was 30Å or more in all simulation cells. This second requirement was introduced to help ensure that the upper and lower surfaces of the ceramic block remained independent i.e. diffusion of atoms towards or away from the one interface with the block would not affect the diffusion processes for the opposite side of the block. The third requirement was that height of the ceramic in the z-direction was sufficient to represent a bulk ceramic.

The first ceramic system considered was the interface of MW glass with MgO (100) system. An $8 \times 8 \times 3$ super-cell was chosen. The x and y dimensions being maximised whilst still maintaining a glass block height $\geq$ 30Å. The (100) super-cell dimensions for BaO, CaO and SrO were chosen to closely match those of the MgO cell. The (110) cell sizes were chosen to closely match the interfacial areas of the (100) cells.

2.3 Static Energy Minimisation

Static energy minimisation describes a class of techniques used for finding local energy minima within an atomic system. In many ways, the equilibration period of a molecular dynamics simulation serves the same purpose as static energy minimisation. As time is evolved, atoms in an MD simulation explore configurational space, in the process it is likely that they will find more favourable low energy states (if given sufficient time). As this process continues, the free energy of the system becomes lower and lower until it reaches a minimum, at which point energy minimisation has been achieved. As the name might suggest, static energy minimisation does not rely on the thermal motion of atoms to sample a system's energy surface.

Equation 2.9 gave an expression for an ion's potential energy (ϕ_i) as a function of its pairwise interaction with the other ions in the system. The total potential energy of the system (U) can be calculated by summing over all pairs of ions:

$$U = \sum_i \sum_{j \neq i} \frac{q_i q_j}{4\pi\varepsilon r_{ij}} + \phi_{short}(r_{ij}) \qquad (2.11)$$

From this it can be seen that the internal energy of the system can be expressed as a function

of atomic position. U is related to the Helmholtz free energy (G) in the following manner:

$$G = U - TS \qquad (2.12)$$

where T is temperature and S is entropy. When T=0K the entropic contribution to free energy becomes zero, at this temperature free energy is equivalent to the internal energy. Minimising the potential energy of the system is therefore equivalent to minimising free energy at a temperature of 0K. As atoms at this temperature are immobile, the classical energy minimisation techniques are often referred to as static.

The energy surface described by equation 2.11 is analogous to a landscape containing hills and valleys. Atoms sitting on the peaks and valley sides of the structure used as the starting point for minimisation, are moved into the valleys during minimisation. Just as a hill walker determines his path from the hill top to valley floor by looking at the direction and magnitude of the slope, the direction and distance an atom is moved during energy minimisation is determined from the gradient of the energy surface. Differentiating U in terms of atomic position at each atomic site, gives a force vector along which the atom should be moved to reduce its energy. This, in conjunction with the second derivative of U is used to determine the distance along this vector an atom should be moved. When the atoms are moved during each iteration, the energy surface changes. Therefore, the minimisation process must proceed iteratively until the force on each atom approaches zero. Convergence is said to have occurred once the change in U between two consecutive minimisation steps falls below a chosen value. This basic energy minimisation algorithm is summarised in the flowchart given in figure 2.9. In addition to allowing atomic coordinates to be minimised, the lattice vectors which define the periodicity of the simulated system can be relaxed to zero strain. As a consequence, static energy minimisation can be used to predict lattice parameters for simulated structures. For instance, static energy minimisation was used to validate the glass potentials by comparing with experimental lattice parameters for MgO, CaO, SrO and BaO structures (see table 2.2). Energy minimisations where lattice vectors were allowed to vary correspond to constant pressure calculations, and those where they were held are known as constant volume calculations.
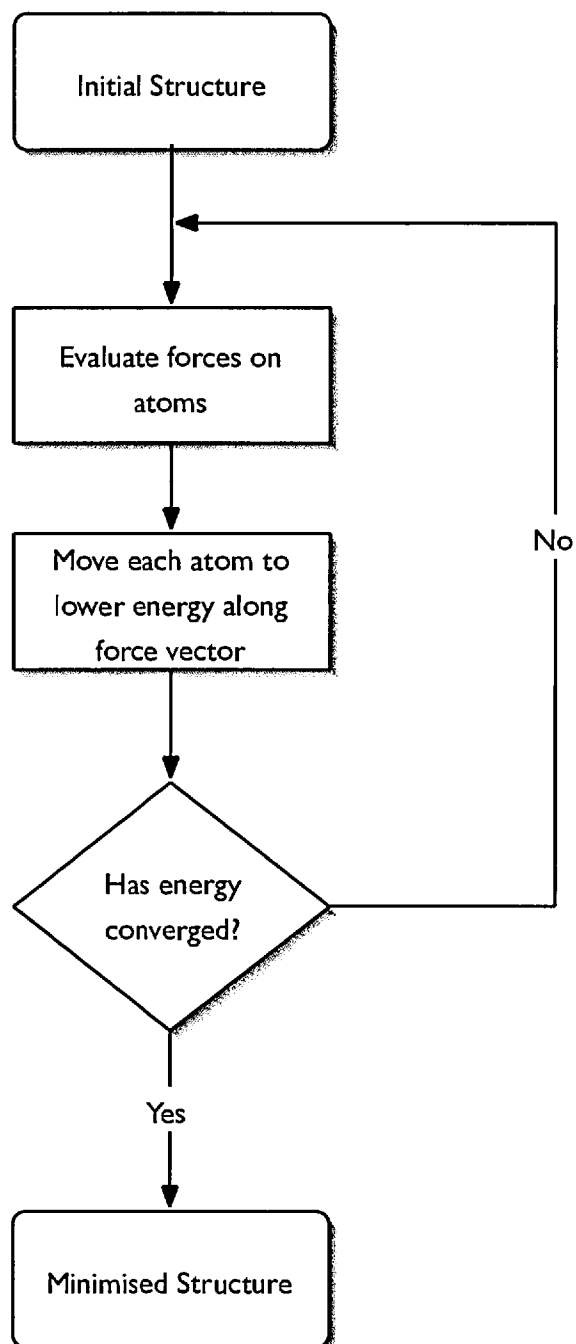
Figure 2.9: The basic energy minimisation algorithm.

2.3.1   The Defective Lattice

Unlike a glass, where no long range order exists, the structure of a perfect crystalline material can be fully described in terms of a set of lattice vectors and a repeating atomic motif. Most crystalline materials are not perfect however, and contain defects. Therefore to understand the properties of real ceramic materials, an understanding of their defect structure is necessary. Chapter 6, relates point defects in pyrochlore oxides to their ability to resist radiation damage and radiation induced volume changes. In the course of this work, super-cell and Mott-Littleton methods were used to describe the defective crystal lattice, these techniques are described below.

Super Cell Methods

Energy minimisation used in conjunction with a defective super cell provides a simple method for studying defect processes. Defects are described explicitly by removing, replacing or inserting atoms at the desired location in the simulation cell. This can then be used as the starting point for lattice relaxation. During minimisation, the lattice can relax in response to the defects it contains. The properties of the defective material can then be extracted from the relaxed structure.

The simulation cell containing the defects is tessellated in space to describe an effectively infinite bulk material. As the number of atoms of the repeat unit is small when compared to Avogadro's number, the effective concentration of defects in the simulated material will be high. This is because the distance between defects in the primary cell and its surrounding images will be limited by the length of the cell's lattice vectors. The small separation can also give rise to large defect-defect interactions. In order to reduce these effects, a large simulation cell is constructed by assembling several unit cells (hence the name super-cell). The additional cells act in effect as a dilutant, reducing defect concentration and increasing inter-defect separations.

In certain cases it is desirable to consider large defect concentrations. In such instances, use of a super-cell allows several defect structures to be considered in the same simulation. For

instance, in chapter 6, super-cells are used to model the structure of disordered fluorite in terms of a defective pyrochlore lattice.

Mott-Littleton

The Mott-Littleton method allows point defects to be studied at the dilute limit, avoiding the potentially unwanted defect-defect interactions associated with super-cell methods. Based on the work of Mott and Littleton [76], in essence it provides a way of coupling a region of defective lattice to a perfect bulk material in order to monitor the response of the lattice to defect. To achieve this the simulation system is decomposed into two regions, a central region containing the defects and an outer region representing the remainder of the lattice (see figure 2.10) [77,78]. Within this two region approach, the total energy of the system (U_{total}) can be written as:

$$U_{\text{total}}(\mathbf{x},\mathbf{y}) = U_{11}(\mathbf{x}) + U_{12}(\mathbf{x},\mathbf{y}) + U_{22}(\mathbf{y}) \tag{2.13}$$

where U_{11} is the potential energy of ions in region I, U_{22} is the energy of the region II and U_{12} is the interaction energy between the two regions. Displacements in region II are represented by $\mathbf{y}$ and the cartesian coordinates of ions in region I by $\mathbf{x}$.

Region I is a sphere which extends from the system's centre outward to a diameter suitable to the system being examined. As the relaxation of the lattice is greatest near the defects, the ions in region I undergo explicit energy minimisation, taking into account the short range and Coulombic interactions with other atoms in region I.

Region II is the outer region and extends from the boundary with region I to infinity. The distance to the defects such that the forces arising from the defects are relatively weak. As a result, the response of the lattice can be calculated using a more approximate continuum approach based on the polarising effects of the defects, rather than the explicit energy minimisation required in region I. The polarisation per unit cell due a defect with charge q can be calculated from [79]:
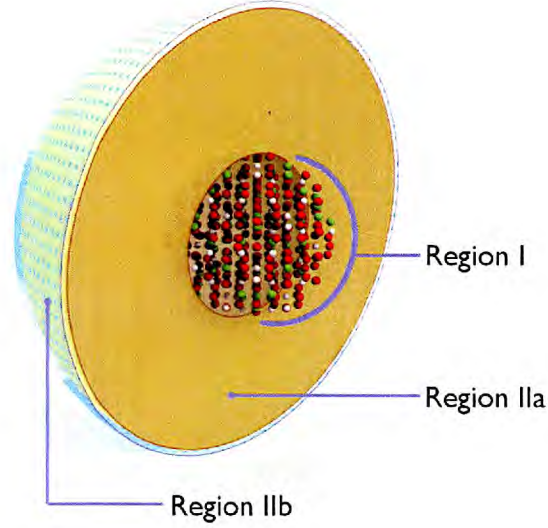
Figure 2.10: Schematic representation of the Mott-Littleton regions.

$$\mu = \frac{Vqr}{r^3}\left(1 - \varepsilon_0^{-1}\right) \tag{2.14}$$

where V is unit cell volume and r is the distance to the defect. For simplicity, equation 2.14 shows the polarisation for materials with isotropic dielectric properties. The polarisation is split into its atomic contributions and the displacements in region II, $\mathbf{y}$, are calculated by dividing each ion's polarisation by the ionic charge [77]. Assuming harmonic behaviour in region II, U_{22} from equation 2.13 can be written as:

$$U_{22} = \frac{1}{2}\mathbf{y}\mathbf{A}\mathbf{y} \tag{2.15}$$

where $\mathbf{A}$ is the hessian or force constant matrix for region II. This poses a problem: region II is infinite in size, therefore $\mathbf{A}$ cannot be evaluated directly. This problem is avoided by expressing U_{22} in terms of a derivative of U_{12}. Using the condition that displacements in region II are the equilibrium values, $\mathbf{y}_e$ then:

$$\left.\frac{\partial U_{\text{total}}(\mathbf{x},\mathbf{y})}{\partial \mathbf{y}}\right|_{\mathbf{y}=\mathbf{y}_e} = \left.\frac{\partial U_{12}(\mathbf{x},\mathbf{y})}{\partial \mathbf{y}}\right|_{\mathbf{y}=\mathbf{y}_e} + \mathbf{A}\mathbf{y} = 0 \tag{2.16}$$

Substituting this into equation 2.15 allows the dependence of U_{22} on $\mathbf{A}$ to be removed, meaning the energy of the defect bearing system becomes:

$$U_{\text{total}}(\mathbf{x}, \mathbf{y}) = U_{11}(\mathbf{x}) + U_{12}(\mathbf{x}, \mathbf{y}) - \frac{1}{2}\left(\frac{\partial U_{12}(\mathbf{x}, \mathbf{y})}{\partial \mathbf{y}}\right)\mathbf{y} \qquad (2.17)$$

In a refinement of the original two region Mott-Littleton method, region II is split further, with the introduction of region IIa which provides a transition between, region I and the continuum region IIb. Within region IIa energy minimisation is performed in one step using the Mott-Littleton approximation, however the interaction with region I is calculated by explicit summation [79]. The sizes of region I and IIa, were determined by performing a series of calculations in which region size was increased incrementally. Defect energy was then plotted against region size and the radius at which energy had converged with respect to region size was used for subsequent calculations. All the Mott-Littleton calculations appearing in chapter 6 were performed using the CASCADE code [80].

Chapter 3

Glass Simulations

The following chapter aims to examine the simulated glass structures produced by the melt-quench method described previously (chapter 2). Prior to a discussion of the features exhibited by glass ceramic interfaces, it will be demonstrated that the simulated glasses are consistent with available experimental data. The glass compositions are considered in order of increasing complexity, starting first with vitreous silica before moving on to the alkali, mixed-alkali and borosilicate compositions.

3.1 Model Comparison with Silicate Glass

The discovery that crystals diffracted X-rays during the early years of the twentieth century by Laue, Friedrich and Knipping has probably extended our knowledge of the structure of crystalline materials more than any other single discovery [81]. The periodicity and symmetry relationships which exist in crystals means that, in most cases, the positions of atoms in the crystal's unit cell can be quite accurately determined. By comparison, the lack of long range order in amorphous materials, means that diffraction data cannot be used to give the full structural characterisation possible with crystals. Although it is not possible to fully characterise the position of the atoms in a glass, diffraction can be used to extract more structural information associated with the relative position of atoms in the system to produce pair correlation

functions. In the following pages, the type of pair correlation functions obtained from the experimental analysis of silica glass are described, these are then compared with data obtained from the simulated systems.

As the name suggests, pair correlation functions describe structural relationships between pairs of atoms in a material. Of these relationships, perhaps the simplest is the radial density function, $\rho(r)$. This describes the average number density of atoms surrounding an atomic site as a function of the distance from that site (r). As MD simulations yield the positions of atoms, $\rho(r)$ can be calculated directly from these results by counting the number of atoms in a series of coordination shells surrounding each site in the system [43].

The procedure used in the direct calculation of $\rho(r)$ from molecular dynamics results is shown in figure 3.1. This shows a central atom surrounded by a random distribution of atoms. The atoms surrounding this site fall into a series of concentric shells with radius increasing by δr between consecutive shells. The number of atoms in each shell are counted to produce a histogram describing the number of atoms surrounding a site as a function of distance from that site, densities are then obtained by dividing the binned values by their respective shell volumes. This calculation is repeated at all other sites in the system to yield $\rho(r)$.

3.1.1 Experimental pair correlation functions

Experimental pair correlation functions cannot be determined in the direct manner described above. Instead, they must be extracted from the interference functions usually obtained from X-ray or neutron diffraction.

When a beam of radiation interacts with a solid, scattering can take place. The portion of the radiation not absorbed by the material can emerge deviated from its original path. The amount of deviation and the intensity of the deviated beam is related to the internal structure of the material it has passed through. When radiation interacts with a single atom, it is scattered in all directions, however in certain directions the scattered radiation constructively interferes and diffraction takes place. If $\mathbf{k_0}$ and $\mathbf{k}$ are the wave vectors for the incident and scattered radiation

As the atomic coordinates are known, pair correlation functions can be calculated directly from the results of a molecular dynamics simulation.

1. Calculate interatomic separations between all atom pairs in the system.

2. Create a histogram by assigning separations to bins of width δr.

3. Normalize histogram frequencies by dividing through by the number of atoms in the system.

4. Represent pair correlations as radial density function $\rho(r)$ by dividing by bin volume:

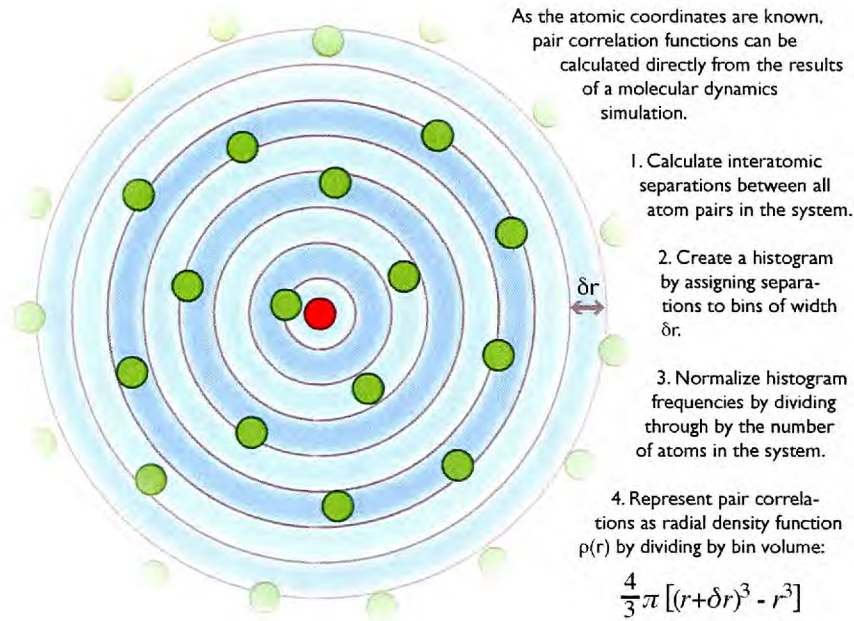$$\frac{4}{3}\pi \left[(r+\delta r)^3 - r^3\right]$$

Figure 3.1: As atomic coordinates are known, pair correlation functions can be calculated directly from simulation results as shown here.

then the scattering vector, $\mathbf{Q}$, can be defined as [18]:

$$\mathbf{Q} = \mathbf{k} - \mathbf{k_0}$$

This relationship is illustrated in figure 3.2a. The magnitude of the scattering vector is dependent on the radiation's wavelength (λ) and scattering angle (2θ):

$$Q = \frac{4\pi \sin\theta}{\lambda} \tag{3.1}$$

The superposition of waves scattered coherently from different atoms leads to interference, whether this is constructive or destructive depends on the phase difference between the scattered waves. Constructive interference is favoured by a phase difference of 2π which is equivalent to a path difference of λ (or integer multiples thereof). Figure 3.2b shows how Q is related to interatomic separation (r_{ij}) as a function of the path difference. This means that interatomic separations can be measured and as a result pair correlation functions can be obtained, experimentally, by measuring the intensity of the radiation scattered by a sample for a series of Q values. The interference function, $I(Q)$, is described by the Debye relationship:
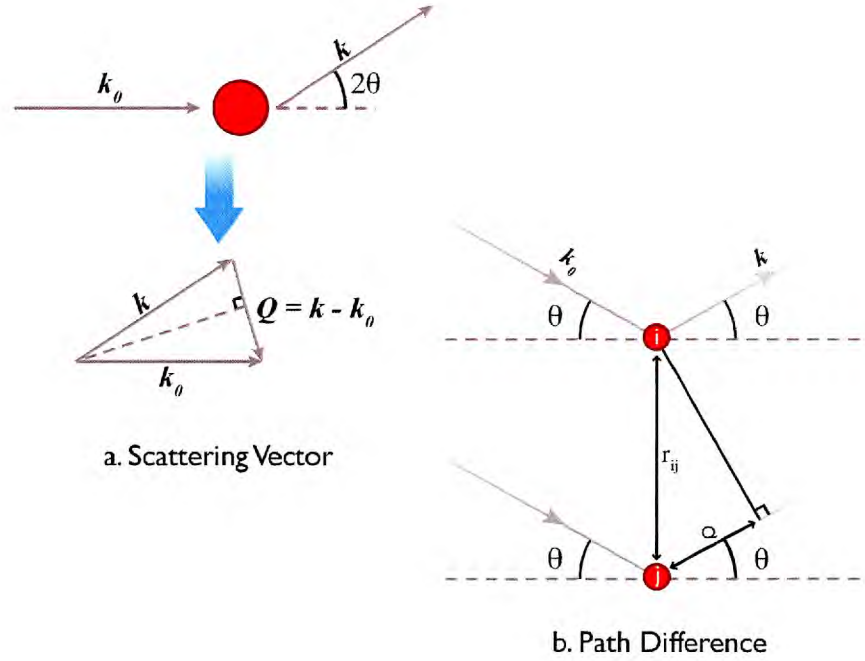
a. Scattering Vector

b. Path Difference

Figure 3.2: Geometric relationship between scattering vector and interatomic separation.

$$I(Q) = \sum_i \overline{b_i^2} + \sum_{i \neq j} \sum \overline{b_i} \, \overline{b_j} \frac{\sin r_{ij} Q}{r_{ij} Q} \tag{3.2}$$

where $\overline{b}$ represents the average neutron scattering length (for neutron diffraction), and is a measure of the scattering efficiency for an atomic species. The Debye equation, as expressed above involves a double summation over the interatomic separation vectors, as these are unknown it is rephrased as the integral over the component correlation functions, $\rho_{ij}(r)$:

$$I(Q) = \sum_i \overline{b_i^2} + \sum_i \sum_j \overline{b_i} \, \overline{b_j} \int_0^\infty 4\pi r \rho_{ij}(r) \frac{\sin Qr}{Q} dr \tag{3.3}$$

The component correlation functions are the deconvolution of $\rho(r)$ into component pair contributions, in the case of SiO_2 there are three component pairs: Si–O, Si–Si and O–O.

In the experimental literature, the interference function is normally published in a modified form which does not include the self scattering term ($\sum_i \overline{b_i^2}$) or contributions due to the average

density, ρ^0 (which is not recorded by the diffraction experiment) hence the reciprocal space interference function, $Qi(Q)$ is expressed as:

$$Qi(Q) = \sum_i \sum_j \overline{b_i}\, \overline{b_j} \int_0^\infty 4\pi r \left[\rho_{ij}(r) - \rho^0\right] \sin Qr\, dr \qquad (3.4)$$

Although equation 3.4 is written in terms of component correlation functions, experimentally it is very difficult to extract the individual effects of the Si–O, Si–Si and O–O contributions as there is considerable overlap between their individual contributions. It does, however, show how reciprocal space interference functions are related to the real space correlation functions, and for this reason provides the framework for the comparison of experimental and simulated results which follows.

3.1.2 Comparing the Results of Simulation and Experiment

For a comparison of pair correlation functions to be valid, it is necessary that both sets of data have been treated in the same way. Experimentally determined correlation functions are affected by the resolution of the diffractometer used and the different scattering lengths of the elements in the sample. Correlation functions obtained from molecular dynamics results must also include these effects for a comparison with experimental data to be valid.

The range of Q values which diffraction experiments can explore has a finite upper bound. As real space pair correlation functions are obtained from $Qi(Q)$ by a sine fourier transform, the maximum experimental scattering vector Q_{max} determines the resolution of the pair correlation function in real space. The higher Q_{max} the greater the real space resolution. Truncating the interference function at Q_{max} causes broadening of the peaks in the real space correlation functions. If any sort of valid comparison is to be made between simulation and experiment, the effect of this truncation has to be reflected in the simulated results [18,82].

Abruptly cutting off the interference function at Q_{max}, creates a step function, which leads to the formation of spurious satellite ripples around the peaks of any resulting real space correlation function. To reduce this effect, a windowing function $M(Q)$ is introduced that gradually

attenuates the interference function to zero at Q_{max}:

$$4\pi r \left[\rho(r) - \rho^0 \right] = \frac{2}{\pi} \int_0^\infty Qi(Q)M(Q)\sin rQ \, dQ \qquad (3.5)$$

The neutron diffraction data used here for comparison was taken from Grimley, Wright and Sinclair [83]. The windowing function adopted by their work and so too in the comparison that follows was provided by Lorch [84, 85] and is illustrated in figure 3.3

The resolution of the real space correlation function is related to Q_{max} by the component peak function, $P_{ij}(r)$, which is proportional to the fourier transform of the Lorch function:

$$P_{ij}(r) = \frac{\overline{b_i}\,\overline{b_j}}{\pi} \int_0^\infty \frac{\sin(\pi/Q_{max})}{\pi/Q_{max}} \cos rQ \, dQ \qquad (3.6)$$

The radial density function, $\rho(r)$ was obtained directly from the coordinates obtained during the final stages of the melt-quench procedure using the method described in figure 3.1. To avoid unwanted broadening from the binning procedure used in creating a histogram a small bin width (δr) compared with the width of the component peak function at half its maximum height $\delta r_{1/2}$, was used. In line with Wright's recommendation that δr should be $\leq 0.1\delta r_{1/2}$ a value of 0.01Å was used [82]. The effects of thermal broadening were included in the simulated correlation function by taking the average of the interatomic separations obtained over the final 5ps of the data collection stage of the simulation at 300K.

The simulated total correlation functions, $t_{ij}(r)$, were calculated from the $\rho(r)$ density functions as follows:

$$t_{ij}(r) = 4\pi r \left[\rho(r) - \rho^0 \right] \qquad (3.7)$$

The peak functions relevant to the current comparison are plotted in figure 3.4 these were calculated using a Q_{max} value of 45.2Å (the same value quoted for the experimental data) and the neutron scattering lengths given in table 3.1. These were combined with the simulated component total correlation functions by fourier convolution. The component correlation broadened functions were then added together to produce the total correlation function $T(r)$ which was plotted in figure 3.5 together with the experimental data from reference [83].
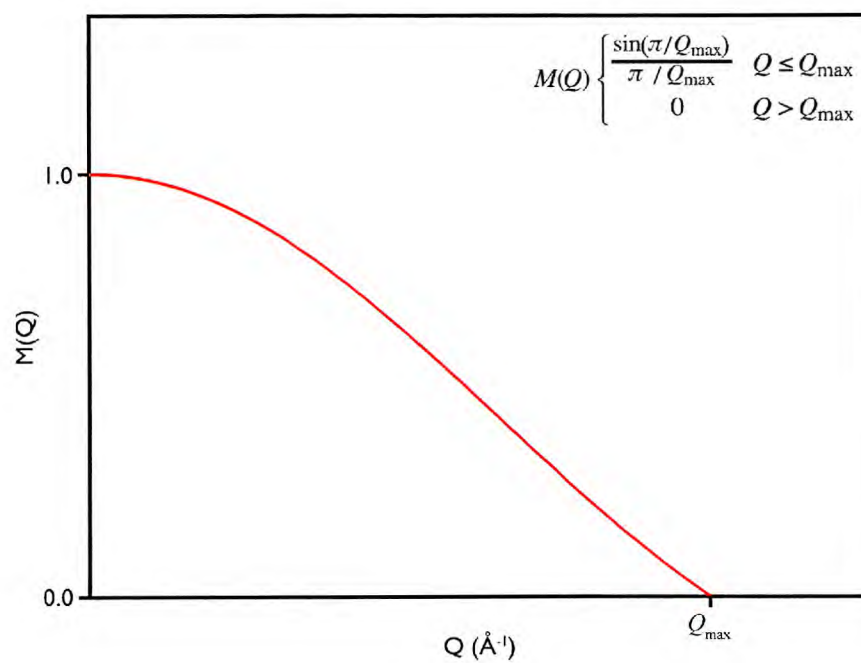
$$M(Q) \begin{cases} \dfrac{\sin(\pi/Q_{\max})}{\pi \, / \, Q_{\max}} & Q \le Q_{\max} \\ 0 & Q > Q_{\max} \end{cases}$$

Figure 3.3: The Lorch function used to gradually truncate the interference function.

Element	Average Neutron Scattering Length (fm)
Oxygen	5.803
Silicon	4.1491

Table 3.1: Neutron scattering lengths (taken from [86]).
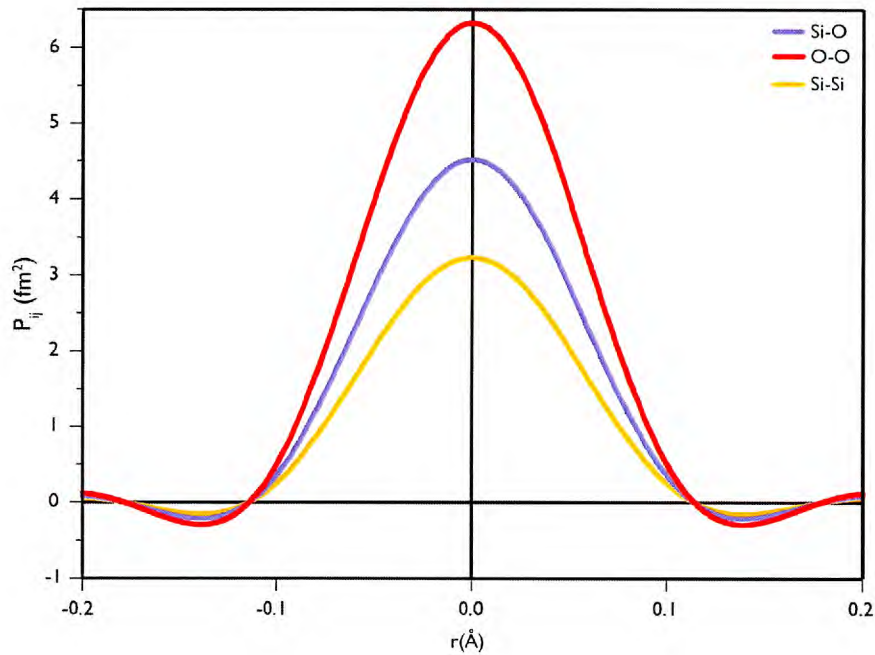
Figure 3.4: Component peak functions used in comparison of simulated and experimental SiO_2 pair correlation functions.

The agreement between experimental and simulated results are in good general agreement. Wright proposed a standard reliability index (R_x) to measure the goodness of fit between experimental and simulated correlation functions which is defined as follows:

$$R_x = \sqrt{\sum_i \left[T_{\text{expt}}(r_i) - T_{\text{sim}}(r_i) \right]} \qquad (3.8)$$

where the subscripts expt and sim indicate experimental and simulated values respectively. The value of R_x for the SiO_2 simulation presented here was 8.3% which compares well with other simulations of this type (for comparison, a value of 8% was quoted by Cormack and Park [87]).

The position and height of the first peak, representing the Si–O separations is in very good agreement with the neutron diffraction results. The position of the second peak is also in very good agreement, being lower than experiment by only 0.02Å. The main contribution to this peak comes from O–O pairs; it is slightly broader than the experimental peak indicating that
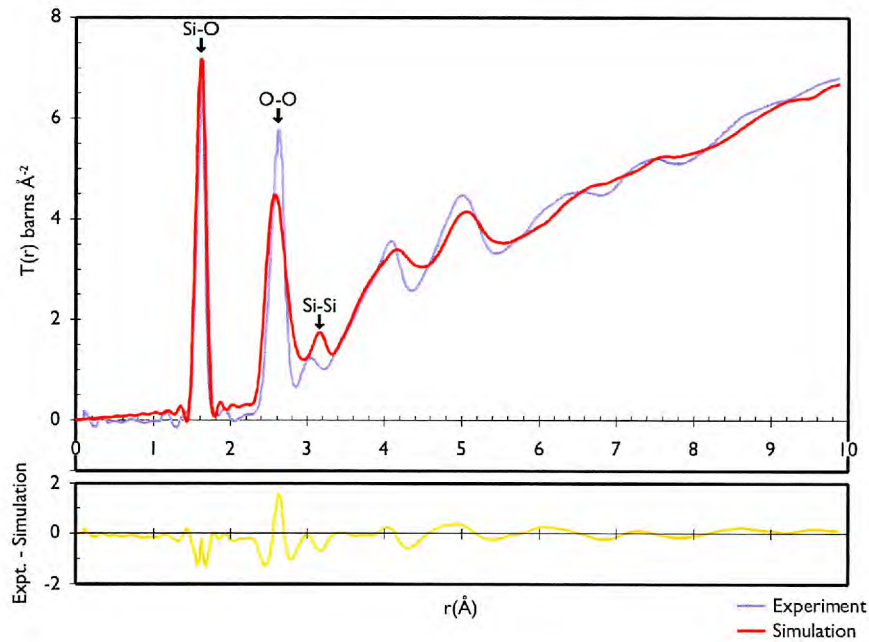
Figure 3.5: Comparison of experimental and simulated total correlation functions for vitreous silica (experimental neutron diffraction data by Grimley *et al.* [83]).

a slightly wider range of O–O separations were found in the simulated glass than might be expected.

Since the first two peaks in figure 3.5 are due to Si–O and O–O pairs, they describe atomic separations in the SiO_4 tetrahedra of a glass. The good level of agreement between the experimental and calculated correlation functions, indicates that these building blocks are well described in the model system.

The third peak in figure 3.5 (between 2.8 and 3.4Å) can be attributed to Si–Si interactions and describes the intermediate range order of the glass. In vitreous silica, tetrahedra are joined by bridging oxygens, this first Si–Si peak therefore shows how the tetrahedra are arranged relative to one another. In this regard there was some disagreement between the model and experiment: the model Si–Si peak position was some 0.3Å higher than expected, indicating that the packing of the tetrahedra was less efficient in the model than in the real glass. Although the model density of 2.17 g cm^{-3} was lower than the experimental value of 2.20 g cm^{-3} (from [70]), it

is not thought that this small difference ($\sim 1.4\%$) was sufficient to account for the shift in the Si–Si peak. As a result this may indicate that the simulated glass had a larger Si–O–Si bond angle than would expected experimentally (the bond angle distribution is discussed below).

3.1.3 O-Si-O Bond Angle Distribution

Silicate glasses are built from SiO_4 tetrahedra it is important therefore that any simulated glass correctly describes the shape of these basic building blocks. From the peak positions in the total correlation function (figure 3.5) it has been shown that the Si–O bond length in the simulated glass match experiment well. It is important however to correctly replicate the distribution of tetrahedral O–Si–O bond angles (the O–Si–O angle is defined in figure 3.6).

Experimental bond angle distributions are obtained from the shape and position of the Si–O peak in the radial distribution function, by assuming regular undistorted tetrahedra. Poulsen has reported a Gaussian distribution centred about $109.3°$ with a root mean squared deviation of $4.2°$ [88]. This has been plotted with the distribution obtained from the simulated silica glass in figure 3.7. In comparison, the simulated distribution was wider than experiment, with a peak width (full width at half maximum) of $17.1°$ compared to $9.9°$. The position of the peaks, however, were broadly the same: the experimental peak sat at $109.3°$, whilst the model gave a modal bond angle of $106.0°$.

The results of this comparison show that the simulated glass had a larger range of tetrahedral angles than experiment. In reality, the directed nature of the Si–O covalent bonds means that SiO_4 forms very regular tetrahedra with only small deviation due to thermal vibrations. The less regular tetrahedra found in the model glass (suggested by the broad angular distribution) were probably a consequence of the two body potential form used; as the forcefield did not impose an explicit penalty for departures from the equilibrium bond angle a broad distribution resulted. It must be emphasised, especially in light of the good agreement with the first peak of the pair-correlation, and the good agreement in modal bond angle, that most of the tetrahedra in the model system showed only small differences from the ideal.
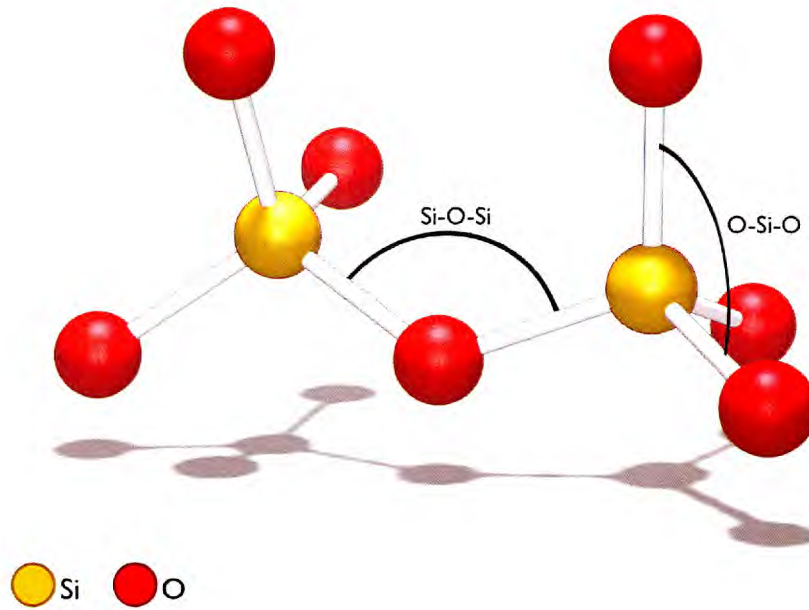
Figure 3.6: The O-Si-O bond angle describes the shape of SiO_4 tetrahedra, the Si-O-Si bond angle shows how tetrahedra relate to each other.
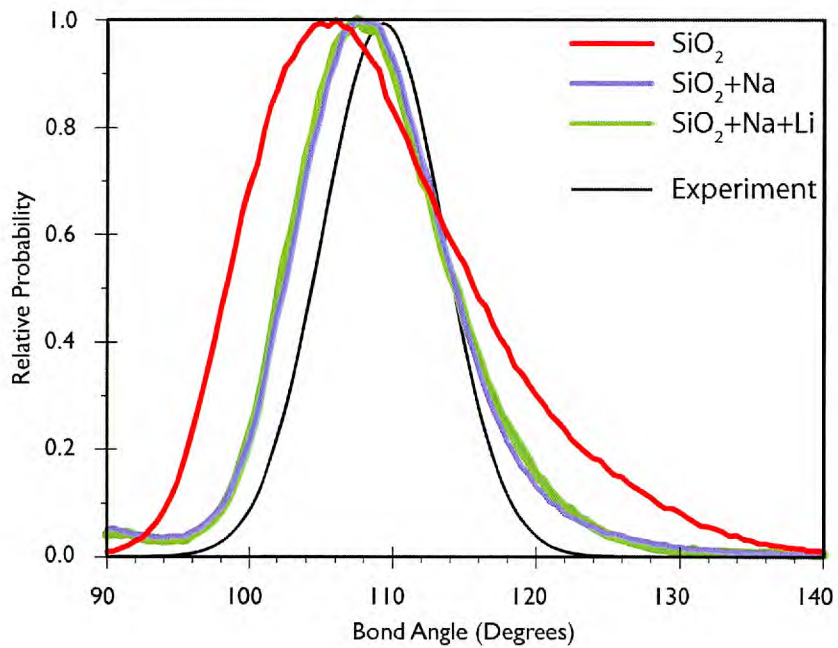

Figure 3.7: O-Si-O bond angle distribution, experimental distribution from [88].

3.1.4 Si-O-Si Bond Angle Distribution

The O-Si-O bond angle describes the structure of the silicate tetrahedron, the Si-O-Si bond angle describes how neighbouring tetrahedra arrange themselves in relation to each other (see figure 3.6 for an example). The Si-O-Si bond angle distribution is important to any description of the secondary and long range structure of glass. It is unfortunate, therefore, that a canonical description of this distribution cannot be constructed purely from experimental pair correlation functions. The one dimensional nature of such data means that Si-O-Si distributions are obtained indirectly, by first fitting a structural model to the experimental correlation function, then measuring angles from this model.

An example of a very early model, was that adopted by Mozzi and Warren [89]. This made simple assumptions based on a fixed Si-O bond length and an even distribution of torsion angles. Trial fits to experimental data gave a distribution with a modal bond angle of $\sim 144°$ and a full width at half maximum (FWHM) peak width of $\sim 35°$ [89]. With a peak skewed towards smaller bond angles.

Yuan and Cormack [90] published a review of angular distributions for SiO_2 which highlighted the differences present in distributions obtained from different experimental data using various structural models. They considered experimental data obtained from neutron/X-ray diffraction and nuclear magnetic resonance spectroscopy (NMR). Those results obtained from X-ray and neutron diffraction showed very similar modal bond angles of 147°. More variation was seen in the widths of the bond angle distributions since they varied from 20° to 30°. Interestingly, the NMR technique consistently yielded distributions which were both narrower and had higher modal bond angles than distributions from diffraction data.

The variation in the Si-O-Si angles predicted by these distributions can be seen in table 3.2. Much of the difference arises from the structural models used to interpret the experimental data. For instance, the results of Mozzi and Warren [89] and also Poulsen [88] were interpreted using the simple structural model described above; even though the modern high energy X-ray source used by Poulsen had a better resolution both sets of results gave very similar distributions. As before, their model employed simple geometrical constraints to form a set of analytical

expressions through which pair distribution data could be interpreted. An alternative to this kind of approach is to generate an explicit atomic scale representation of the glass, in which atom positions are fully described (much like the results of an MD simulation). This can then be refined to provide a good match to the experimental data; bond angles can then be calculated directly from the structural model. Such an approach was taken by Gladden [91] and Neuefeind et al. [92], in which initially random structures were refined to give excellent agreement with experiment using a Monte-Carlo method. They predicted distributions with modal bond angles of 146° and 147° and widths of 21° and 35° respectively. An interesting extension to this technique was used by Tucker et al. in which a glass was initially generated using molecular-dynamics then refined to match experiment again using a Monte-Carlo method, this gave a width of 20° and a peak position of 153° [93].

The discussion above, has hopefully highlighted some of the vagaries involved in a comparison with experimental Si-O-Si bond angle distributions. The Si-O-Si distribution obtained from the simulations performed for this work is shown in figure 3.8 and a modal bond angle of 154° was obtained with a peak width of 36°. As before, the peak position showed good agreement with the distributions given in table 3.2. In particular agreement was good with the distribution obtained using reverse Monte-Carlo data by Tucker from the NMR data due to Mauri [94]. Again, the distribution was much wider than those obtained from experiment which, as suggested for the O-Si-O angles, was probably a consequence of the lack of explicit bond bending terms in the forcefield. The result is, however, comparable to other two-bodied potential sets. As an example, the well regarded partial charge model of van Beest, Kramer and Santen (sometimes known as the BKS potentials) [56, 95] gave a very similar bond angle distribution to that seen here, with a modal angle of 152° and peak width of 36° [90].

In this section, it has been shown that there was good general agreement between experimental pair correlation functions and the O–Si–O and Si–O–Si bond angle distributions for silica glass. This suggests that the simulation method employed gives a reliable description of the silicate network which can be applied to the study of glass-ceramic interfaces.

Year	Reference	Modal Angle (°)	Width FWHM (°)	Notes
1969	Mozzi & Warren [89]	144	35	XRD results interpreted using simple model based on bond lengths and equal distribution of torsional angles.
1992	Gladden [91]	146	21	Neutron diffraction results interpreted using reverse Monte-Carlo refinement of a space filling sphere model.
1995	Poulsen, Neuefeind et. al. [88]	147	35	High energy XRD interpreted using similar model to Mozzi & Warren.
1996	Neuefeind & Liss [92]	147	17	High energy XRD and neutron diffraction interpreted by a Monte-Carlo model in which -Si-O-Si-O... chains were built.
2000	Mauri et. al. [94]	151	17.5	NMR data interpreted using bond angle calculations made using density functional theory for crystalline quartz polymorphs.
2003	Yuan & Cormack [90]	147	23–30	Molecular dynamics and reasoned argument from literature.
2005	Tucker et. al. [93]	152.6	20.45	Molecular dynamics results refined by reverse Monte-Carlo against neutron diffraction data from [83].

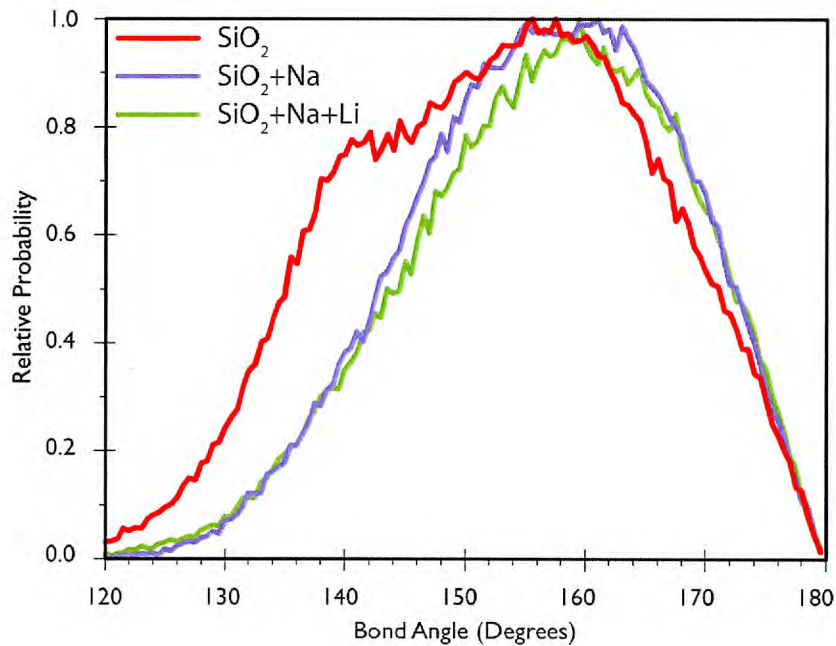Table 3.2: Si-O-Si bond angle distributions obtained by different authors using different methods.

Figure 3.8: Si-O-Si bond angle distribution.

3.2 Sodium Silicate and Sodium Lithium Silicate Glass

It was seen in the previous section that simulations of vitreous silica showed, with a few caveats, good agreement with available experimental data, here, the alkali containing compositions are now considered.

Silicate compositions containing alkali species represent a technologically more significant class of materials than pure silicate glass. The alkali atoms act as network modifiers to depolymerise the silicate network and as a result lower the melting point and processing temperature of the material. For obvious reasons this helps reduce the cost of manufacture. In terms of the vitrification of nuclear waste, the less obvious benefit is that lower processing temperature reduces the chances of losing volatile fission products during processing [11]. Again this has positive implications for reducing the cost and complexity of any vitrification plant and associated gas treatment equipment. It is clear that any glass model must correctly describe alkali ion behaviour.

When an alkali ion is introduced into the silicate network it becomes associated with an oxygen ion and through a localised charge compensation reaction a non-bridging oxygen (NBO) is formed. Given that glass compositions are normally expressed in terms of oxide concentrations the effect of each M_2O unit (where M is a monovalent cation) on the network can be expressed as follows:

$$2Si^{(4)} + M_2O \rightarrow 2Si^{(3)}$$

where $Si^{(n)}$ is an Si atom connected to n bridging oxygens. In other words, each M_2O unit converts a bridging oxygen (BO) into two non-bridging oxygens (NBOs). In this way, the connectivity of the glass is reduced.

3.2.1   Bond Angles in SiO_2+Na

Figures 3.7 and 3.8 show the O-Si-O and Si-O-Si angle distributions for the simulated SiO_2+Na glass. In comparison to the alkali free, SiO_2 glass, the tetrahedral, O–Si–O angle, moved from $106°$ for SiO_2 to $108°$ SiO_2+Na, which is much closer to the 'ideal' value of $109.3°$. The width of the distribution, $12°$, was also much closer to the experimentally expected $9.9°$.

It could be argued that the changes seen in the inter-tetrahedral Si-O-Si bond angle distribution were the result of the network moving to a state of lower internal strain. It is tempting to think that a less interconnected network has more conformational freedom, and as a result would show a narrower Si-O-Si distribution, since the added freedom to explore conformational space allows more of the network to approach equilibrium bond angles. This conjecture is supported by experimental data. For instance, Henderson's EXAFS study showed Si-Si separation decrease with increasing Na_2O concentration, this was interpreted in terms of a decrease in Si–O–Si angles [96]. Such a conclusion has also been supported by neutron diffraction experiments refined using the Monte-Carlo method [97].

The simulation results for SiO_2+Na glass showed the expected narrowing of the bond angle distribution, with a width of $29.5°$ compared to a value of $36.0°$ for the pure silica glass. The

modal bond angle did not move to a lower value, in fact there was a slight increase to 157°. The fact that the simulated SiO_2+Na glass did not show the peak moving to lower angles was not unexpected. Yuan and Cormack [90] noticed that the two bodied BKS potentials also failed to reproduce the shift, whereas a force field that included bond bending terms did.

Before moving on to consider the MW glass, it is interesting to compare the bond angle distributions in the SiO_2+Na and SiO_2+Na+Li glasses. In general these were very similar. This suggests, that from the network's point of view, overall alkali concentration was more important to the structure, than the glass being a single or mixed alkali composition.

3.3 Magnox Waste Glass

As a borosilicate composition, MW glass contains both silicon and boron as network formers. As has already been demonstrated in this chapter (see section 3.1) the melt-quench method and forcefield employed, generates reliable descriptions of silicate and alkali silicate glass networks. Unlike the silicate network, in which silicon sits in regular tetrahedra, boron will form both BO_3 triangles and BO_4 tetrahedra depending on its environment. In the following section, the structure of the simulated MW glass was compared with the available experimental data to show that the simulation method was suitable for generating amorphous borosilicate structures.

Using the notation introduced in section 1.2.4, table 3.3 shows the speciation of the simulated MW-glass in terms of the number of bridging oxygens connected to the network formers for the MW and MW+Al+Mg glasses. Considering just the MW glass for a moment, it can be seen that for the silicate network 80% of the tetrahedra were fully polymerised whilst the remainder was accounted for by silicate units with a single non-bridging oxygen, $Si^{(3)}$. A small amount of $Si^{(2)}$ was present in the system. Structural models and experimental data indicate that this species is only present when very high alkali concentrations are present [98]. Therefore, this, and the over coordinated $Si^{(5)}$ species should be considered as defect species. Thankfully their population was low which is a good sign that the model was viable.

Unlike the silicate network, where alkali atoms act as network modifiers and lead to the creation

of non-bridging oxygens, in the compositional range considered here, alkali atoms associated with the borate network are thought to bring about the conversion of trigonal BO_3 to tetrahedral BO_4 [98–100]. To avoid confusion, it must be made clear that in the context of the current analyses $B^{(3)}$ refers to trigonal boron with three bridging oxygens rather than a more highly coordinated boron atom with a non-bridging oxygen. Consulting with table 3.3 it can be seen that in the MW glass, most boron existed as $B^{(4)}$, although almost a quarter of boron atoms were $B^{(3)}$. The $B^{(2)}$ population, whilst not insignificant, was still low at $\sim 4\%$, again this must be considered as an artefact of the simulation method.

So, how well do these results compare with experiment? The ^{11}B NMR study of Roderick et al. [69] showed that for a glass with the MW composition, the boron speciation was as follows: $B^{(4)} = 69\%$ and consequently $B^{(3)}=31\%$. The model system's $B^{(4)}$ population was 71.9% and therefore showed an excellent level of agreement with experiment falling well within the quoted error of $\pm 5\%$. The $B^{(3)}$ value was somewhat lower in the simulated glass, however if the contribution due to $B^{(2)}$ was included then the value increased to 28.1% and once more fell within the experimental error.

The speciation of the silicate network was compared with experiment in a similar fashion. The NMR/Raman results of Bunker et al. [101] suggest the following speciation for a $20Na_2O\cdot 20B_2O_3\cdot 60SiO_2$ glass: $Si^{(4)}$ 75% and 25% $Si^{(3)}$. Again this tallies well with the structural results presented in table 3.3. It should be noted that this comparison was made with a single alkali composition whereas the MW glass contains both Na and Li. As will be discussed later (see section 3.4), the main effect of having mixed rather than a single alkali species is one of alkali redistribution rather than altering bridging oxygen speciation. As was seen for the silicate glasses discussed earlier, the speciation of the network does not change significantly on going from a single to a mixed alkali composition. This comparison therefore seems quite reasonable.

The MW+Al+Mg glass shows a species distribution similar to that of the MW glass for the silicate and borate networks. The MW+Al+Mg glass shows an increase in the population of $Si^{(3)}$ units, with a concomitant decrease in the number of $Si^{(4)}$ units when compared to the MW composition. This is interesting as adding aluminium to borosilicate glasses is normally associated with increased network polymerisation (see section 1.2.3), however the MW+Al+Mg

glass described here shows decreased polymerisation; indicating that the addition of the divalent Mg ions to the system seem to have counteracted the polymerising effect of the aluminium. The speciation of aluminium was predominantly $Al^{(4)}$, in addition there was also a significant population of $Al^{(2)}$ and $Al^{(3)}$. It was expected that most aluminate units would occur as $Al^{(4)}$: it is thought that the high number of $Al^{(3)}$ and $Al^{(2)}$ was due to statistical noise brought about by the small number (64 atoms) of Al in the MW+Al+Mg system.

3.4 Alkali Distribution

As will be shown in following chapters (chapters 4 and 5) the spatial distribution of alkali species in the glass adjacent to a ceramic interface is significantly different to that in the bulk of the glass. To fully appreciate this change, it is necessary to understand the distribution of the alkali species in a glass that does not contain a ceramic interface.

In the following section, the Voronoi tessellation is used to describe the volume occupied by each alkali ion. This allows the structure and clustering behaviour of alkali ions in the simulated glasses to be described.

3.4.1 Voronoi Tessellation

The Voronoi tessellation is a particularly useful geometric construct, lying at the heart of computational geometry [102]. For a set of sites distributed in space, the Voronoi tessellation partitions space into a set of domains. The volume enclosed by such a domain represents the region of space in which points are closer to the generating site than any other [102]. Figure 3.9 shows the Voronoi tessellation for a set of randomly distributed sites, from this, some of the Voronoi tessellation's interesting properties can be observed:

- Edges in the Voronoi diagram are equidistant between two sites.

- Edges are perpendicular bisectors of the lines connecting two sites.

Species	MW Glass (%)	MW+Al+Mg Glass (%)
$Si^{(2)}$	1.4 (0.1)	3.8 (0.1)
$Si^{(3)}$	18.2 (0.5)	26.5 (0.8)
$Si^{(4)}$	80.1 (0.8)	69.1 (0.7)
$Si^{(5)}$	0.3 (0.2)	0.6 (0.2)
$B^{(1)}$	–	0.9 (0.1)
$B^{(2)}$	4.2 (0.4)	6.8 (0.2)
$B^{(3)}$	23.9 (0.9)	27.4 (1.1)
$B^{(4)}$	71.9 (1.1)	64.9 (1.2)
$Al^{(1)}$	–	1 (0.3)
$Al^{(2)}$	–	4.9 (0.1)
$Al^{(3)}$	–	22.0 (1.9)
$Al^{(4)}$	–	71.7 (3.6)
$Al^{(5)}$	–	0.4 (0.1)

Table 3.3: Bridging oxygen speciation for network formers in simulated MW and MW+Al+Mg glasses (values are expressed as percentages of each network former's total population, values for standard deviation over the range of MD frames sampled are given in parentheses).

- Sites which share edges are nearest neighbours.

These interesting properties have made it useful in many fields from city planning (e.g. where best to site hospitals and mobile phone masts to cover the largest population), to route finding applications [103]. An example of its use in materials science and metallurgy can be found in the work of Wigner & Seitz who used the Voronoi construct to study conduction in metals [104]. It has also been used to define the volume occupied by each atom in molecular dynamics glass simulations by Delaye and Ghaleb [105, 106].

In the present work, the nearest neighbour property of the Voronoi diagram was used to define coordination polyhedra around alkali atoms in the simulated glasses. From these it was possible to show spatial relationships between alkali atoms and highlight any alkali clusters/channels. The Voronoi tessellations presented here were generated from atomic positions using the *qhull* computer package [107].

3.4.2 Voronoi Tessellations of Simulated Glasses

Figure 3.10, shows the Voronoi domains for a molecular dynamics frame from the data collection stage of the SiO_2+Na melt-quench simulation. Although quite impressive in appearance this figure is not very enlightening. Only Voronoi domains at the edge of the simulation box can be seen, and the relationship alkali atoms have with the network is lost. In an effort to overcome these obvious shortcomings, figures 3.11,3.13, 3.15 and 3.17 were devised. For each alkali containing glass, these show a representative cross section through the Voronoi cells associated with the alkali species. These have been given in the context of the network by showing a slice, with a thickness of $\sim 3\text{Å}$, through the system centred about the Voronoi cross section. As this kind of representation can only ever show a small portion of the system, they are supported by statistics obtained from the Voronoi diagram. Histograms showing the distribution of alkali cell volumes are given in figures 3.12,3.14, 3.16 and 3.18. To shed some light on how the alkali atoms organise themselves in relation to each other, tables 3.4, 3.5, 3.6 and 3.7 are given. These show the proportion of alkali cells that:
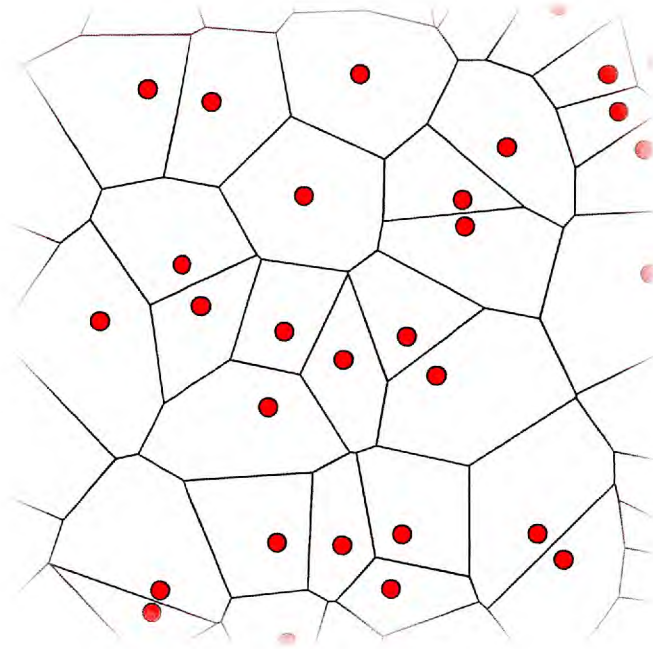
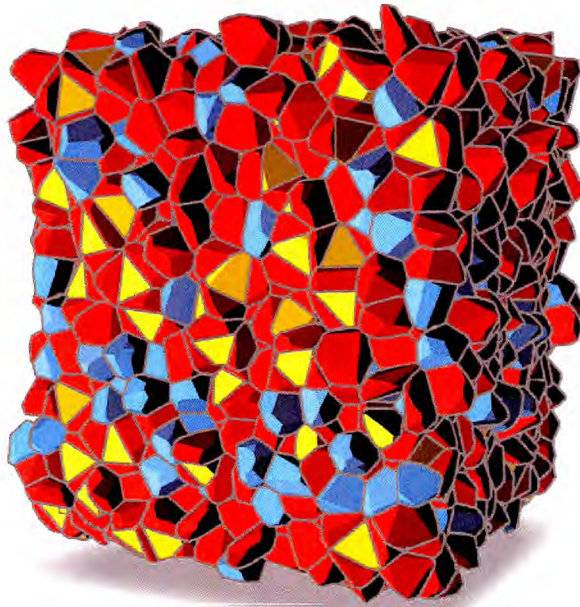Figure 3.9: Voronoi diagram for a random set of points.

Figure 3.10: In 3D, Voronoi cells can be obtained from a Delaunay tetrahedralisation, shown here are the Voronoi domains for the SiO_2+Na glass.

- Share faces with no other alkali atoms.

- Share faces with another alkali of the same kind.

- Share faces with two different kinds of alkali species.

- In the case of the MW+Al+Mg glass share faces with three different kinds of alkali atoms.

The average volume for each of these alkali environments have also been reported.

Alkali Distribution in SiO_2+Na

The cross section taken through the SiO_2+Na glass, (figure 3.11), indicates that considerable alkali aggregation has taken place; almost all alkali cells share at least one face with another alkali cell. In several cases, these extended alkali structures form into quite extensive networks. In this glass, the morphology of these networks was perhaps best described as string like, with little branching taking place.

These observation that alkali atoms seemed to aggregate, was reiterated by the alkali environment statistics given in table 3.4. These showed that over 97% of the Na cells shared a face with other sodium cells.

Alkali Distribution in SiO_2+Na+Li

The introduction of the second alkali species represented by the SiO_2+Na+Li composition poses new questions. For instance, does the presence of Li significantly alter the Na environ-

Modifier Site	Neighbouring Modifiers	%	Avg. Volume of Environment ($Å^3$)
Na	Na	97.4 (0.4)	19.9
Na	None	2.6 (0.4)	21.6

Table 3.4: Table showing incidence of alkali-alkali environments in SiO_2+Na (values in parentheses indicate standard deviation for each observation).
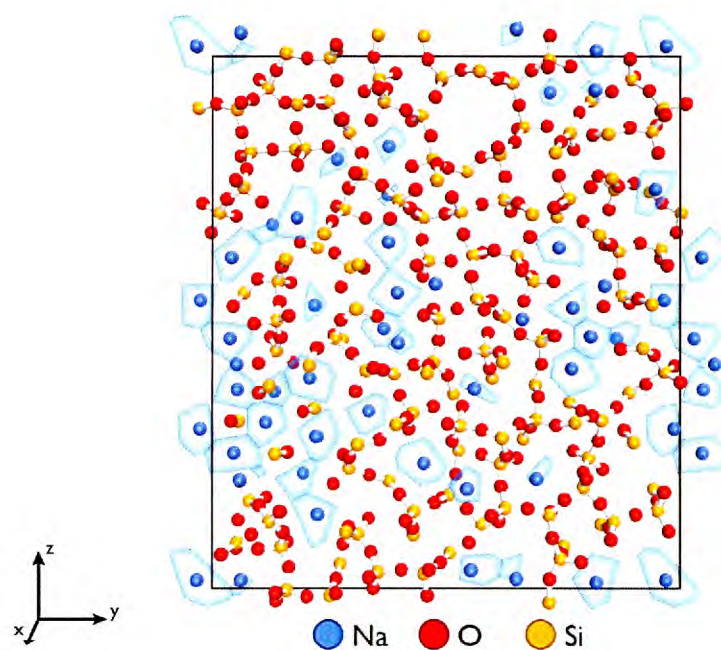
Figure 3.11: Slice through SiO_2+Na glass, showing cross-section through Voronoi cells for alkali species (YZ plane).

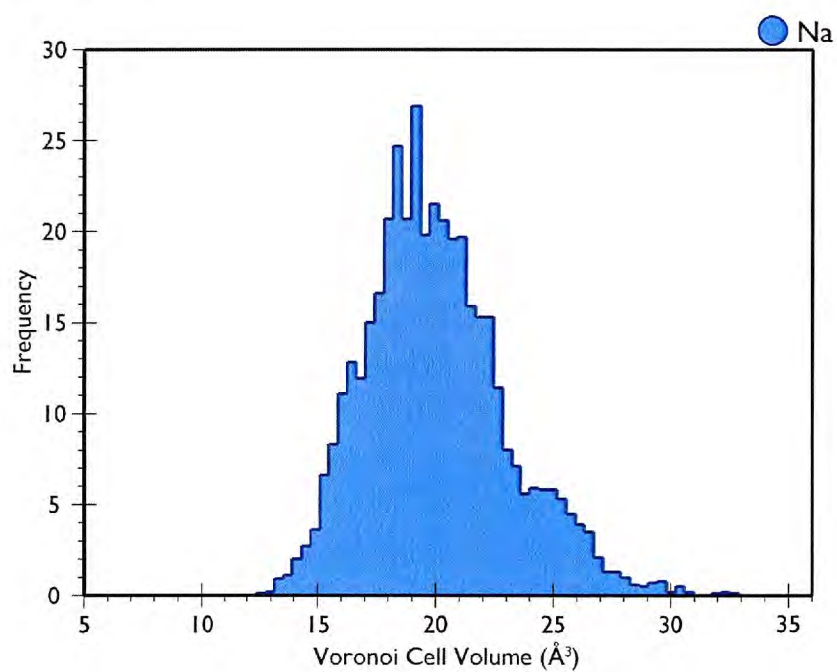Figure 3.12: Histogram of Voronoi cell volumes for alkali species in SiO_2+Na glass.

ment? Does the sort of clustering described in SiO_2+Na still occur when two alkali species coexist? If so do Na and Li mix or form segregated regions rich in each species? Each of these will be discussed below, in turn.

As would be expected, the Voronoi cells belonging to Li ions were generally smaller than those belonging to Na, as shown by cell volume histograms in figure 3.14. Gaussian peak fits to these distributions showed that the most likely volume was $19.6Å^3$ for Na and $15.2Å^3$ for Li. In addition, the Na peak position in this glass was not significantly different to the value seen in SiO_2+Na of ($19.4Å^3$) (see figure 3.12). At least in terms of the volume therefore, adding a second alkali species to the glass did not significantly change the Na environment.

Turning now to consider the clustering behaviour of the two alkali species, the section of glass in figure 3.13 does show evidence of clustering. For a better idea of the degree of this clustering and the mixing of different species it is necessary to turn to the alkali environment statistics of table 3.5. Once more, only a small number of alkali atoms (1.2% for Na and 2.2% for Li) sat in isolated sites. Again this suggests that alkali aggregation was favoured in this glass.

In terms of alkali mixing, the majority of Na and Li sites were bordered by both Li and Na neighbours: this environment for 71% of Li and 73% of Na atoms. Additionally, substantial numbers of Li and Na atoms were bordered by a single different species. These coordination statistics indicate that Li and Na do not segregate into single alkali regions. Rather they suggest that mixed alkali clusters are favoured.

Alkali Distribution in MW Glass

The presence of the borate network in the MW glass significantly changed the distribution and intermixing of the sodium and lithium alkali atoms. The clustering seen in the Voronoi cross section in figure 3.15 was quite different in character to that found in the silicate glasses. The string like clusters found in the SiO_2+Na and SiO_2+Na+Li compositions, were not in evidence here. Instead long thin clusters gave way to pairs of connected cells as shown in figure 3.15. These qualitative observations were borne out by the coordination statistics for this glass (table 3.6). When compared to SiO_2+Na+Li the number of sodium atoms sitting
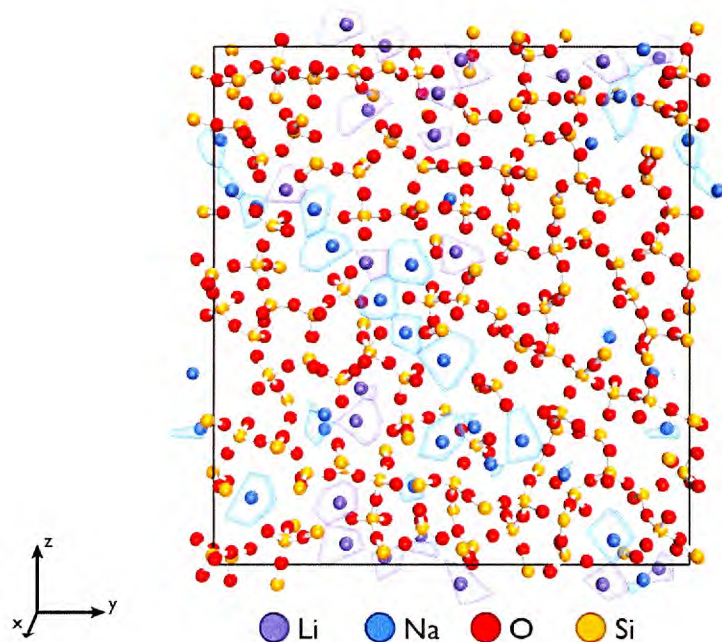
Figure 3.13: Slice through SiO_2+Na+Li glass, showing cross-section through Voronoi cells for alkali species (YZ plane).

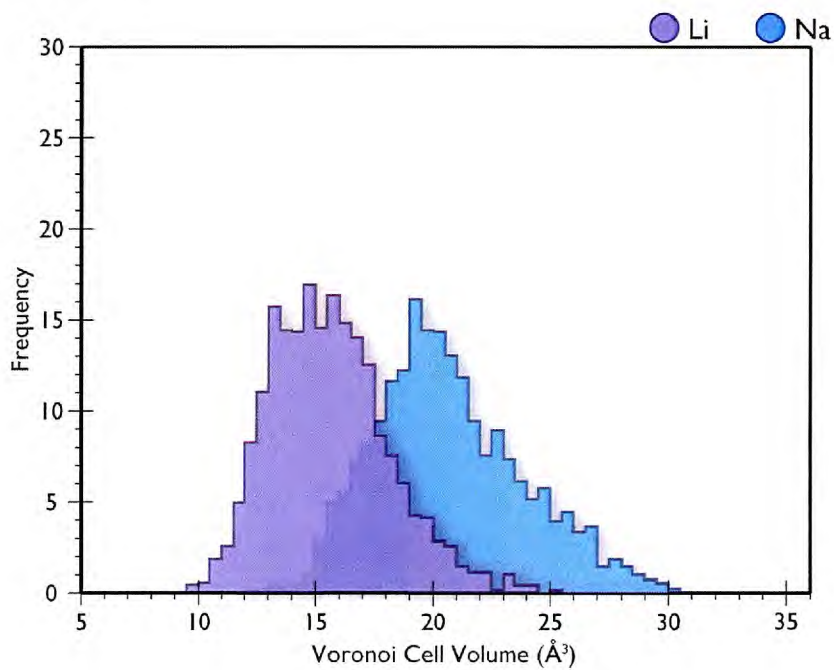Figure 3.14: Histogram of Voronoi cell volumes for alkali species in SiO_2-Na+Li glass.

Modifier Site	Neighbouring Modifiers	%	Avg. Volume of Environment (Å^3)
Li	Li,Na	70.8 (1.3)	15.4
	Li	14.2 (0.8)	16.0
	Na	13.7 (0.9)	16.1
	None	1.2 (0.6)	14.5
Na	Li, Na	73.3 (1.3)	20.4
	Li	14.2 (0.9)	21.6
	Na	11.3 (0.8)	21.2
	None	2.2 (0.3)	21.4

Table 3.5: Table showing incidence of alkali-alkali environments in $SiO_2+Na+Li$ (values in parentheses indicate standard deviation for each observation).

outside clusters nearly doubled for Na (3.9%) whilst the number increased by around six times to 7.4% for Li.

Although still the single most prevalent environment, the number of alkali atoms sitting in mixed alkali sites bordered by both Na and Li saw a dramatic reduction. Again, comparing with $SiO_2+Na+Li$, this number fell from 71% to 41% for Li and from 73% to 56% for Na.

The volume of almost all the alkali environments was smaller in MW glass. This was particularly apparent when the Li volume distributions in figure 3.16 are compared with the distributions seen in $SiO_2+Na+Li$. In MW glass, the Li peak position moved from 15.2Å^3 to 14.0Å^3.

Alkali Distribution in MW+Al+Mg Glass

The alkali distribution seen in the MW+Al+Mg composition was again quite different to the MW glass. In figure 3.17 it can be seen that relatively small additions of aluminium and magnesium led to the reappearance of contiguous areas of Na. These co-existed with the isolated and cell pairs seen for the MW glass. Once more heterogeneous alkali coordination environments were favoured by Na and Li, although the concentration of atoms in these sites was reduced. It is likely that this reduction was due to the introduction of Mg: the overall concentration of
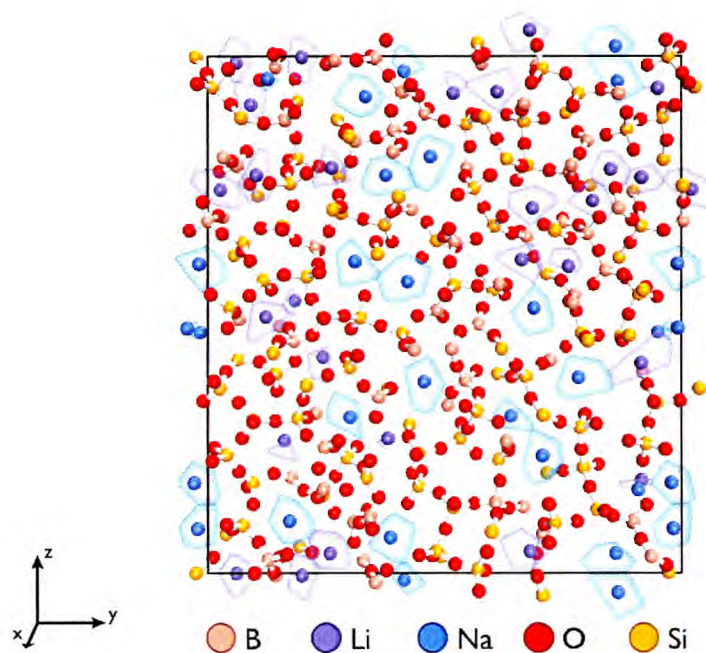
Figure 3.15: Slice through MW glass, showing cross-section through Voronoi cells for alkali species (YZ plane).

Modifier Site	Neighbouring Modifiers	%	Avg. Volume of Environment (Å^3)
Li	Li, Na	41.2 (1.2)	14.4
	Na	28.6 (0.8)	15.0
	Li	20.9 (1.0)	14.2
	None	7.4 (0.9)	14.7
Na	Li, Na	55.5 (1.3)	19.8
	Na	24.1 (1.4)	19.6
	Li	16.4 (1.1)	19.8
	None	3.9 (0.7)	19.5

Table 3.6: Table showing incidence of alkali-alkali environments in MW glass (values in parentheses indicate standard deviation for each observation).
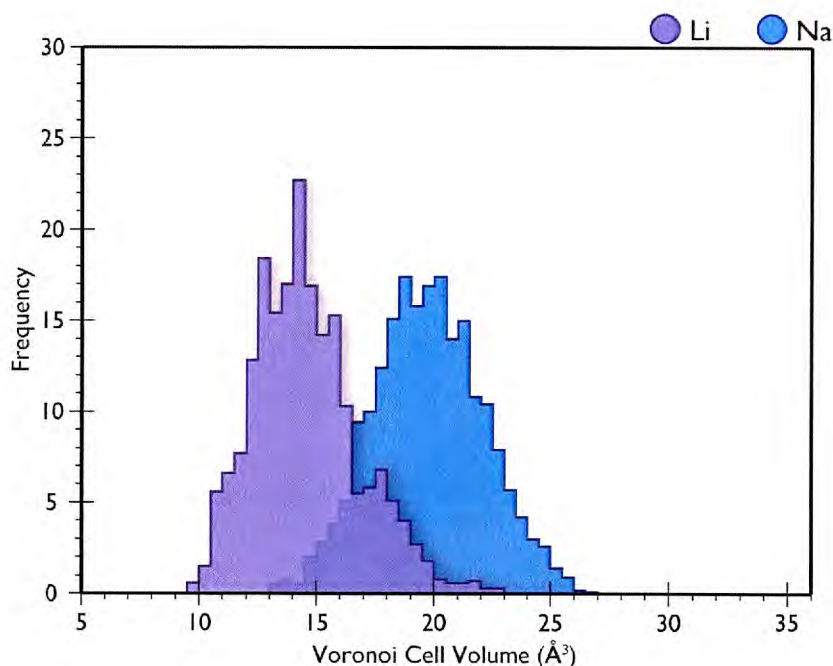
Figure 3.16: Histogram of Voronoi cell volumes for alkali species in MW glass.

alkali sites with two different kinds of alkali neighbours was comparable between the MW and MW+Al+Mg glasses. Magnesium showed a very slight preference for sitting in clusters with Li, Mg and Na.

Peak fits to the volume distributions, shown in figure 3.18, gave peak positions of 12.0, 13.2 and 18.6Å^3 for Mg, Li and Na respectively. Once more the Na and Li peaks moved to lower values. Although there was a consistent decrease in the volume of the alkali environments from SiO_2+Na through to MW+Al+Mg, it is interesting to notice that the relative positions of the Na and Li peaks in SiO_2+Na+Li, MW and MW+Al+Mg compositions stay quite constant. This can be seen when the distances between the Na and Li peaks are compared. These were were 5.7, 5.4, 5.4Å^3 for the SiO_2+Na+Li, MW and MW+Al+Mg glasses respectively. This indicates that the reduction in volume between glass compositions was shared equally between the different alkali species. It must be emphasised that Voronoi volumes were obtained from systems which had been equilibrated using constant pressure molecular dynamics calculations, meaning relaxation of the simulation's box had been allowed during glass formation.
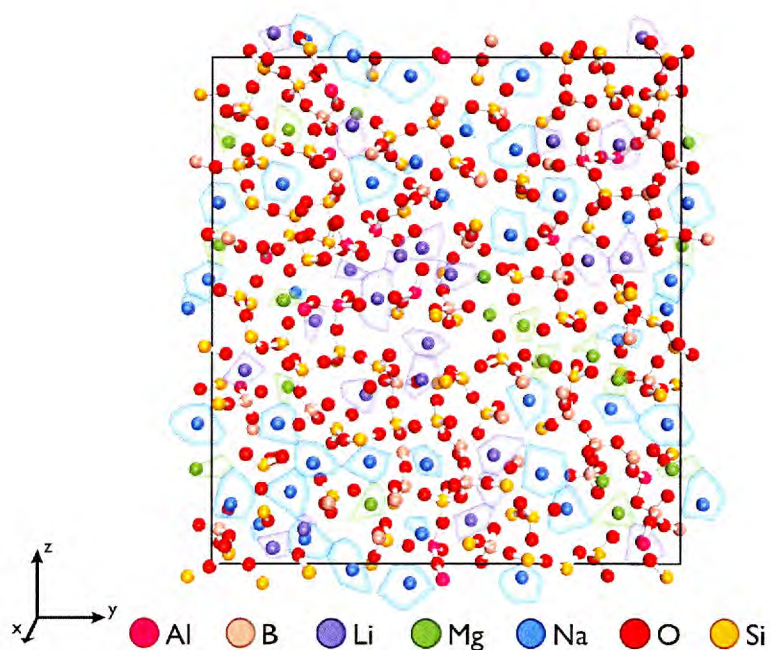
Figure 3.17: Slice through MW+Al+Mg glass, showing cross section through Voronoi cells for alkali species (YZ plane).
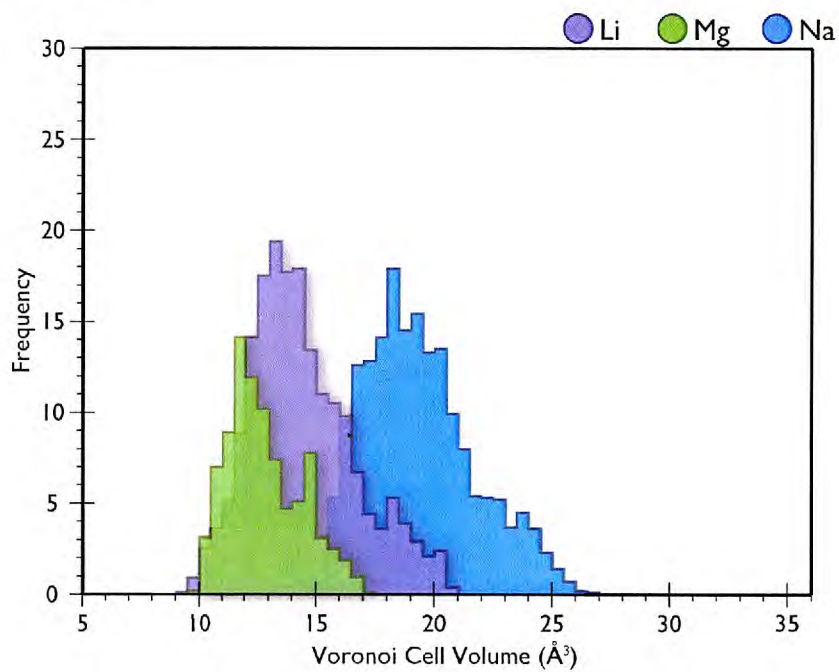

Figure 3.18: Histogram of Voronoi cell volumes for alkali species in MW+Al+Mg glass.

Modifier Site	Neighbouring Modifiers	%	Avg. Volume of Environment (Å^3)
Li	Li, Na	26.6 (1.1)	14.9
	Na	18.8 (0.8)	14.4
	Li	17.0 (0.7)	13.9
	Li, Mg, Na	11.6 (1.2)	14.4
	Mg, Na	8.7 (0.7)	13.9
	Li, Mg	8.0 (1.0)	14.0
	None	6.3 (0.8)	13.8
	Mg	2.9 (0.7)	15.5
Mg	Li, Mg, Na	9.1 (1.5)	12.7
	Li, Na	8.5 (1.5)	12.7
	Na	8.5 (1.0)	13.0
	Mg, Na	6.5 (1.3)	13.3
	Mg	5.1 (0.7)	12.0
	Li	4.7 (0.8)	12.7
	None	3.1 (1.1)	13.3
	Li, Mg	2.9 (0.9)	12.2
Na	Li, Na	29.3 (0.9)	19.6
	Li, Mg, Na	15.7 (1.1)	18.9
	Na	15.0 (1.0)	18.9
	Mg, Na	14.5 (1.3)	19.4
	Li	8.9 (0.6)	20.4
	Li, Mg	8.0 (0.6)	18.3
	None	5.4 (0.5)	18.5
	Mg	3.1 (0.5)	20.0

Table 3.7: Table showing incidence of alkali-alkali environments in MW+Al+Mg glass (values in parentheses indicate standard deviation for each observation).

3.4.3   Alkali Aggregation and Mixing

Both the Voronoi coordination data and cross sectional images, presented in the previous section, showed evidence for alkali aggregation. In Zachariasen's original random network theory [19] it was assumed that alkali atoms would be uniformly distributed through the glass and as a result would not tend to cluster until high alkali concentrations were reached. More recently, Greaves [22] proposed the modified random network theory in which using EXAFS (extended X-ray absorption fine structure) results he argued that alkali ions would cluster to form alkali rich ion channels. The aggregation of alkali species shown by the results given here is consistent with the modified random network theory.

The coordination data also showed that, in mixed alkali compositions, atoms often sat in heterogeneous coordination environments suggesting that there was considerable intermixing of Li and Na atoms within alkali clusters.

3.5   Implications for Alkali Mobility Processes

In this work, the effects of radiation damage on glass have not be considered explicitly. From the alkali structures discussed above, however, it may be possible to suggest which glass composition would be expected to show the best radiation tolerance.

In repository conditions self-irradiation of nuclear waste bearing glass occurs mainly in the form of α-decay of actinides and β-decay of fission products. During the first 500 years of storage, β-decay predominates, with α-decay being more important on longer time scales [108].

Studies of β-irradiation on sodium aluminoborosilicate nuclear waste glasses have shown evidence for irradiation induced alkali segregation. Boizot et al., whilst using Raman spectroscopy, observed an increase in the $Si^{(3)}:Si^{(2)}$ ratio and a conversion of tetrahedral BO_4 to trigonal BO_3 under β-irradiation [109]. The change from $Si^{(2)}$ to $Si^{(3)}$ indicates increased polymerisation of the silicate network (i.e. a decrease in the number of NBOs) and was interpreted in terms of a movement of Na out of the network into Na rich areas. Furthermore,

tetrahedral borate is stabilised by nearby alkali cations, therefore a decrease in BO_4 population also points towards a movement of Na away from the glass network. The natural conclusion to draw from this was that irradiation induced Na segregation had taken place. Interestingly, no change in aluminium environment was reported [110].

The mixed alkali effect describes the profoundly non-linear variation in glass properties as a function of the relative fraction of different alkali species in the system. Properties, such as electrical conductivity, related to the movement of the mobile alkali species can be several orders of magnitude lower in a mixed alkali glass, than in similar glasses containing only a single alkali species (see section 1.2.2). NMR examinations of various mixed alkali alumi-noborosilicate glasses, by Ollier *et al.* have revealed that the degree of network polymerisation and borate conversion experienced under irradiation could be linked to the mixed alkali effect [111]. Mixed alkali glasses containing sodium and potassium were compared with sodium and lithium compositions. Of these, the mixed alkali effect is more pronounced in the Na:Li series of glasses, and it was found that the Na:Li ratio also had a far more pronounced effect on alkali segregation than the Na:K ratio. No polymerisation increase was observed in 50:50 Na:Li compositions, this is interesting because this composition also shows the lowest electrical conductivity in the Na-Li series (it also corresponds with the MW based compositions studied here) [110].

Conductivity is linked with the ability of conducting species to migrate, low electrical conductivity and decreased polymerisation are suggestive of low alkali ion migration in this glass. In addition, the conversion of BO_4 to BO_3 under irradiation was also linked to the ability of the charge balancing cation to migrate. The conversion of BO_4 to BO_3 increased as cation radius decreased, in the series K→Na→Li [111]. This suggests that in order to reduce β-irradiation induced structural changes, alkali migration must also be reduced. Radiation tolerance might therefore also be expected to be better in those glasses in which limited alkali migration takes place.

Durability is an important material selection criterion for choosing glass compositions suitable for use as nuclear wasteforms [11]. The rate of dissolution of an alkali containing glass is initially determined by the rate of alkali diffusion in the glass [20]. Reducing the rate of alkali

diffusion in a glass would therefore be expected to decrease its rate of dissolution by water thus increasing its durability. Experimentally there is good evidence to suggest that this is the case, many of the effects of glass composition on chemical durability can be understood in terms of changes in glass diffusion coefficients [20]. An understanding of the alkali migration pathways in simulated glasses, could therefore provide insight into which glass compositions would be expected to show resistance to dissolution by water and thus provide durable wasteforms.

3.5.1   Proposed Mechanisms for Alkali Migration

Various molecular dynamics studies have been used to study alkali ion migration in glass systems [68, 112–114]. These showed that, for the most mobile atoms in the system, alkali migration occurs in a series of concerted hops between homogeneous sites. Of the proposed mechanisms, that given in reference [112], for Na migration in a sodium silicate glass, is perhaps most specific in its detail and is repeated here.

Concerted Hop Mechanism

In the concerted hop mechanism each hop process involves the cooperative motion of two Na atoms. Shown in schematic form in figure 3.19, the migrating atom momentarily moves into a transitional site, then a fraction later a second Na atom moves into the site left vacant by the first Na atom. The first Na atom then moves out of the transitional site to its destination.

This mechanism has been likened to vacancy migration in crystalline materials because as the ion hops forward along its channel, the empty site previously occupied by a sodium ion moves in the opposite direction [68]. It has been suggested that Na migration adopts this concerted motion as it allows the migrating ion's environment to change gradually. On moving into the transitional state, the sodium ion maintains coordination with some of the oxygen atoms that surrounded it at its initial site. It then breaks the links with its initial site by hopping into a site recently vacated by another Na atom.

This need to maintain a similar coordination environment during alkali migration was explored

by Habasaki *et al.* [113] in an effort to explain aspects of the mixed alkali effect such as the drop in ionic conductivity. In a simulated Li-K mixed alkali glass they substituted Li for K at several sites in the system. The energy associated with this substitution was then calculated using static energy minimisation in conjunction with classical pair potentials. Notionally this is similar to calculating the energy of a substitutional defect in a crystal. As a result they found that Li sitting in a K environment increased the energy of the system by 200 kJmol^{-1}. Therefore a hop by an alkali atom into a site previously occupied by another type of alkali species can be thought of as unfavourable. This finding was supported by the observations, made from the results of molecular dynamics simulations, that migration trajectories for Li and K never crossed and instead proceeded in separate Li and K channels.

3.5.2 Migration Path Prediction from Alkali Cluster Morphology

As described above, alkali atoms migrate in a series of hops between similar nearest neighbour sites. Ion migration would therefore be expected to occur readily in glasses with extensive, interconnected alkali clusters (as this would provide more pathways through the glass along which migration could take place). In the following section 'hop' networks were generated for each glass from their Voronoi tessellations. This allowed the size and interconnectivity of clusters in these glasses to be analysed. From the structure of these clusters it was possible to infer the compositions in which migration would be most prevalent.

Hop networks were generated from each glass' Voronoi tessellation by creating connections between each alkali and its nearest alkali neighbours (i.e. those alkali atoms which share a face with each site's Voronoi cell). This resulted in networks where each node represented an alkali site and the edges showed potential paths for hops between sites. Due to the energy penalty associated with hops between heterogeneous sites (see section 3.5.1), edges were only between nodes with the same species, this resulted in distinct sub-networks for each alkali type in the glass as shown in figure 3.20. In addition, combined networks were generated, where hops between heterogeneous sites were allowed (e.g. figure 3.20c). The aim of these combined alkali graphs was to see to what extent the alkali intermixing described in section 3.4.2 might block ion migration.
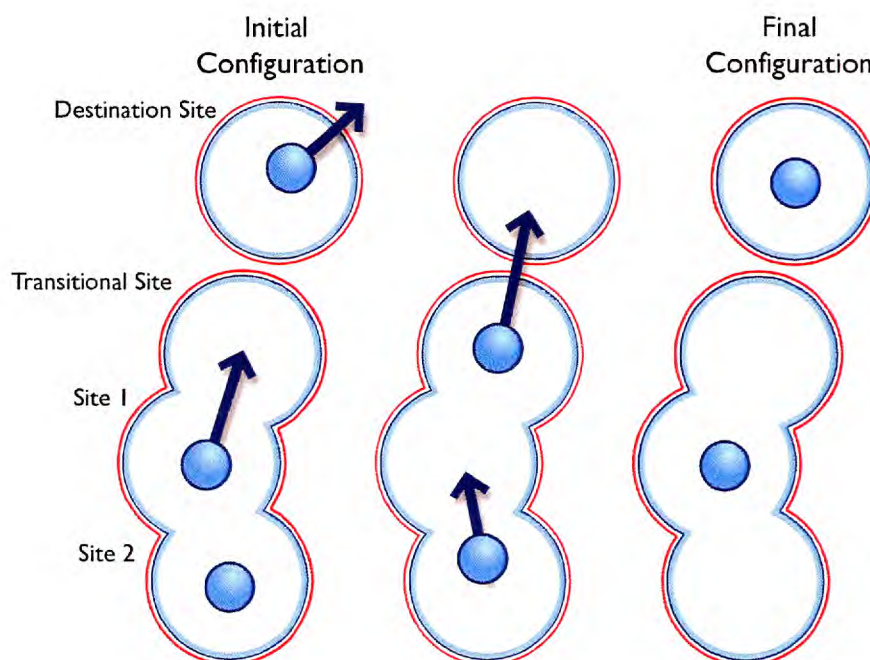
Figure 3.19: Alkali migration occurs by a concerted hopping mechanism (after [112]).

Spanning Clusters

As periodic boundaries were employed during simulations, any cluster that extended from one face of the simulation cell to the other is effectively infinite in size. In terms of mass transport, the presence of these spanning clusters in a system is important. For instance, in percolation theory[1], their existence can be used to define when a material has exceeded its percolation threshold. Above this threshold, mass transport through random media shows an abrupt increase. In a glass, the existence of these clusters might also be expected to encourage rapid alkali ion migration.

Each alkali containing glass was examined for spanning clusters by searching the alkali network for any path that led from alkali sites coincident with the simulation cell's (100) face

---

[1]Percolation theory was originally concerned with the movement of fluids through porous media. It was found that movement through such random media could be likened to electricity moving through a random network of resistors. When the connectivity of these networks exceeded a critical value its resistance fell dramatically. Similarly mass transport through a random system shows an abrupt change at a threshold value known as the percolation threshold [16].

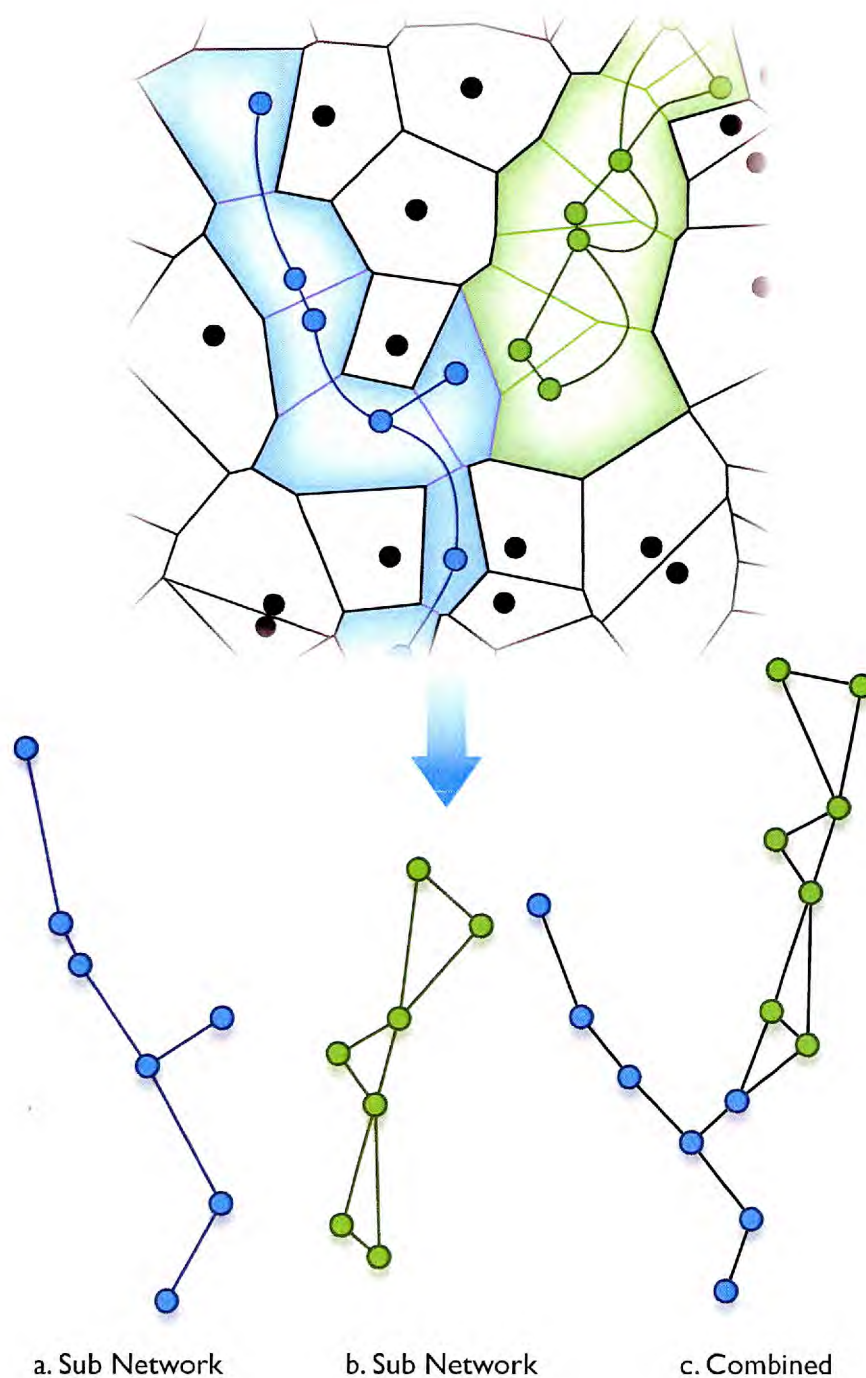a. Sub Network   b. Sub Network   c. Combined

Figure 3.20: Hop networks were obtained from Voronoi tessellation. Edges were formed between face sharing sites of the same kind. For each glass, individual networks were formed for each alkali species (a & b) and also a global alkali network showing what could happen if hops were allowed between dissimilar alkali sites (c).

across the cell to those touching the simulation cell's $(\bar{1}00)$ face, on the opposite side of the cell. This procedure was then repeated for the planes normal to the cell's [010] and [001] axes. Ten different frames from the data collection stage of the simulations were tested in this manner for each glass.

Spanning clusters were only found in the SiO_2+Na glass. In all ten of the frames examined spanning paths were found along all three of the x, y and z axes. The remaining glass compositions did not show this behaviour, showing that of the compositions considered only the SiO_2+Na glass was above the percolation threshold.

Alkali Cluster Topology

Visualisations of alkali cluster topology were made for each glass. Figures 3.21, 3.22 and 3.23 show the topology of the individual alkali networks in SiO_2+Na+Li, MW and MW+Al+Mg glasses. These aim to show the connections between each alkali site and its neighbours. It must be emphasised that these figures show topology and do not portray accurate atomic positions and separations (in the same way that distances on the London Underground map are not representative of the real distances between stations). These figures were created using the NetworkX and graphviz software packages [115, 116].

Many of the observations made earlier for the Voronoi cross sections are reiterated by these diagrams. In particular, the differences between the SiO_2+Na+Li and MW glass compositions are perhaps most significant. SiO_2+Na+Li exhibited large Na clusters containing loops and branches. The Na clusters in MW glass however, were far simpler showing less branching, fewer loops and appeared more string-like than clumped. Interestingly, some branching and looping reappeared for the Na clusters in MW+Al+Mg diagram.

As each glass contained approximately the same number of alkali atoms[2], the number of clusters in each glass can be used as a rough measure of how interconnected they were. A large number of clusters indicating that atoms sat in many, smaller clusters, whilst fewer clusters suggest more interconnection between the sites.

---

[2]SiO_2+Na, SiO_2+Na+Li and MW compositions all contained 410 alkali atoms whilst MW+Al+Mg had 457

Table 3.8 shows the average number of clusters in each glass, averaged over ten MD frames. Particularly striking was the increase in the number of Na clusters from SiO_2+Na to the mixed alkali SiO_2+Na+Li, going from 6 to 29. Even though the number of Li atoms in SiO_2+Na+Li was almost the same, the number of Li clusters was larger at 45. The large number of clusters in the individual networks was not mirrored in the combined network, which only had one more cluster than the single alkali glass, thus confirming the earlier finding that there was profound mixing of the two alkali species. As migratory hops are thought to only happen between like sites, this mixing of the two species would block continuous motion through the alkali network.

Longest Path Lengths

In the graphs of alkali topology, certain paths were shown in red. These indicate the longest paths in each alkali sub-network. The length of these paths gives an impression of the maximum number of migratory hops a alkali atom could achieve in these glasses (without requiring network rearrangement). In the current context, a longest path was defined as: the path passing through the largest number of vertices when paths that detour backtrack or loop were excluded. In graph theory, this metric is defined as a network's diameter [117]. In certain cases, more than one path was found that contained the same maximum number of hops; in these instances, the length of the path was calculated in angstroms by summing the individual atomic separations traversed by the path, the longer path measured in this way was then given.

The results of the longest path analyses are shown in figure 3.24. As expected the SiO_2+Na

Glass	Number of Clusters			
	Na	Li	Mg	Combined
SiO_2+Na	6	-	-	6
SiO_2+Na+Li	29	45	-	7
MW	39	34	-	12
MW+Al+Mg	35	31	16	9

Table 3.8: Number of clusters in simulated glasses by alkali species. Only clusters containing two or more atoms were included.
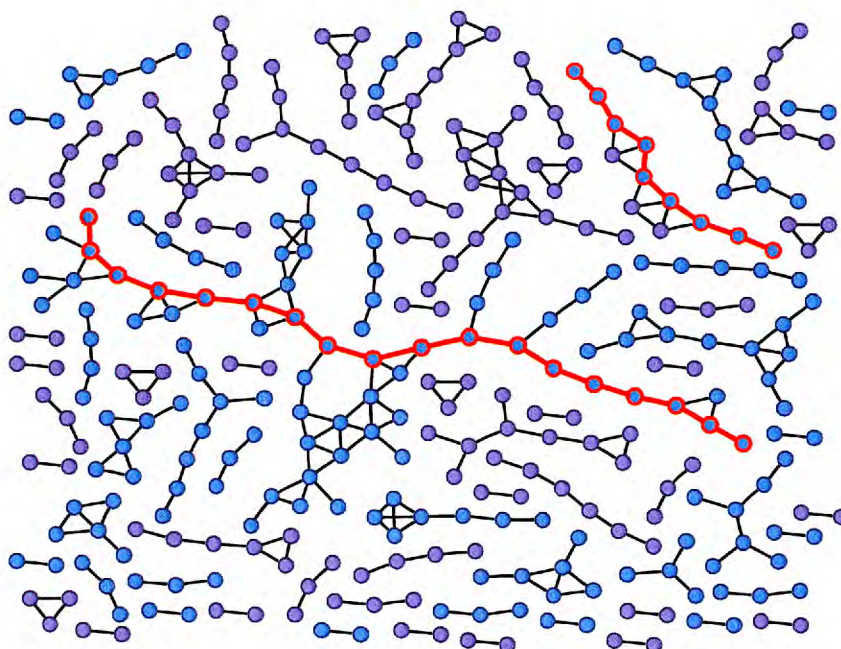
Figure 3.21: Graph showing topography of SiO_2+Na+Li alkali network, longest paths, containing most inter-site hops, are highlighted in red for each alkali species (Li- ⬤ ,Na- ⬤).

glass showed the longest path length (for an individual network). For all the mixed alkali compositions the sodium path length, when measured in site to site hops, was longer than the lithium path length. In the SiO_2+Na+Li glass the longest Na path was more than twice that of the longest Li path. This is interesting as both Na and Li occur in similar numbers within this glass so may be expected to show similar path lengths. The alkali environment statistics of section 3.4.2 showed that both alkali species had the same proportion of atoms sitting in mixed alkali sites, which would also lead to the belief that they should have similar longest path lengths. That they do not perhaps suggests that the topography of the Li network has more branches than the more string-like Na network, making the longest path shorter. This difference is greatly reduced in the MW composition, mainly due to a large reduction in the Na chain length. This finding is consistent with the qualitative observation, made from the Voronoi cross section, that there were fewer long chains and many more Na atoms sitting in pairs. Combined with the earlier alkali environment statistics it seems likely that many of the Na atoms sit in pairs at the expense of long chains in the borosilicate glass. The MW+Al+Mg results are also consistent with the observation that the presence of Al and Mg in the glass led
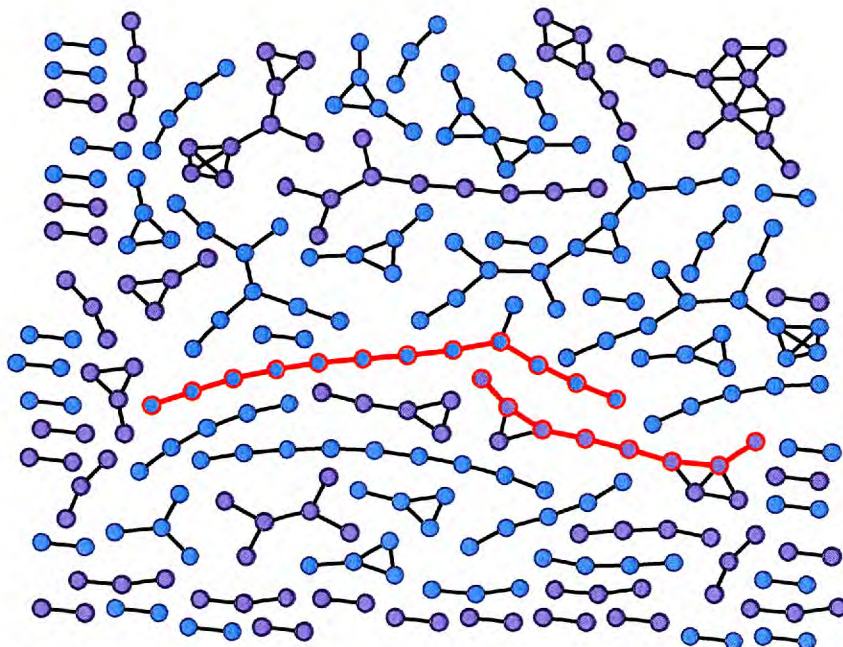
Figure 3.22: Graph showing topography of MW glass alkali network, longest paths, containing most inter-site hops, are highlighted in red for each alkali species (Li-⬤,Na-⬤).

to longer ion channels than in MW glass.

Clearly the individual alkali networks showed significant changes in longest path length between compositions. It is therefore surprising that the longest paths for the combined network were so similar. Especially striking is the similarity between the SiO_2+Na, SiO_2+Na+Li and MW glasses with lengths of 29, 31 and 32 hops respectively. This may suggest that the distribution and connectivity of alkali sites in these glasses were very similar with differences between the mixing behaviour of the different alkali species accounting for changes in the maximum hop-lengths of the individual Na and Li networks.

3.5.3   Conclusions

As SiO_2+Na had the fewest clusters and the longest maximum path length, it can be concluded that, of the compositions considered, the Na clusters in this glass were the largest and most in-
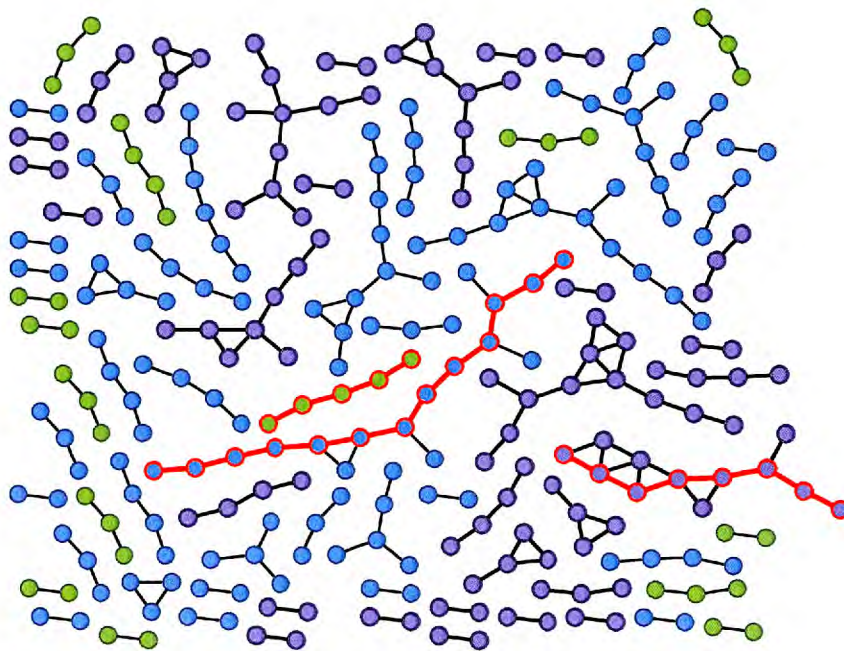
Figure 3.23: Graph showing topography of MW+Al+Mg glass alkali network, longest paths, containing most inter-site hops, are highlighted in red for each alkali species (Li- ⬤ ,Mg- ⬤ ,Na- ⬤).
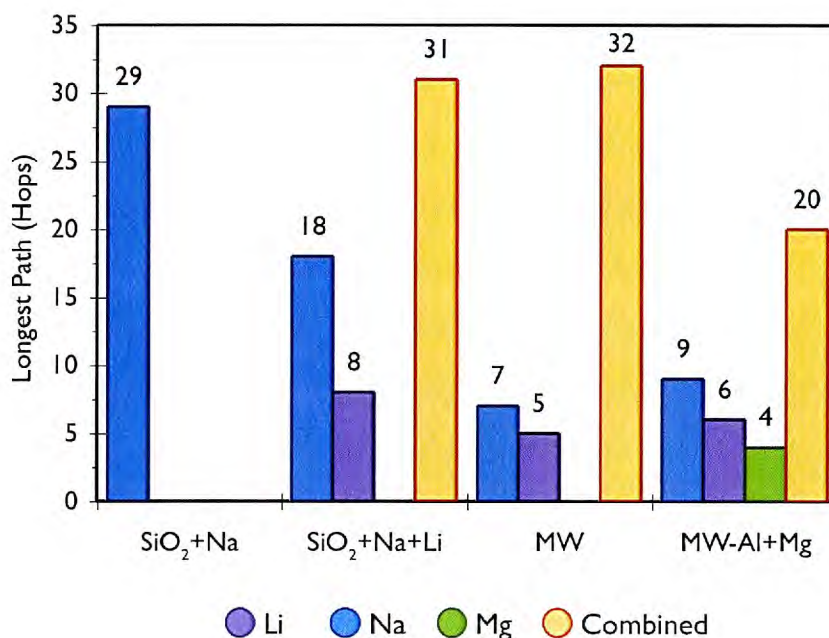
Figure 3.24: Longest paths measured in hops.

terconnected. Conversely, the borosilicate glasses, MW and MW+Al+Mg, had short maximum path lengths accompanied by a large number of small clusters.

The interconnection of atoms in the clusters in SiO_2+Na (and the existence of spanning clusters), would allow Na atoms to hop through the glass structure along several largely independent pathways, without requiring rearrangement of the silicate network. It is thought this would favour rapid ion migration. By comparison, the large number of smaller clusters found in MW and MW+Al+Mg would probably hinder the hopping processes associated with ion migration.

In section 3.4 it was found that there was considerable intermixing of Na and Li in the mixed alkali glasses considered. This intermixing seems to have had a dramatic effect on the structure of the alkali clusters in these glasses. In comparison to the single alkali glass (SiO_2+Na), the mixed alkali glasses (SiO_2+Na+Li, MW and MW+Al+Mg) contained a lot of small clusters. However, if the Na and Li hop networks were combined, the number of clusters and maximum path length statistics became comparable to SiO_2+Na. This suggests that Li atoms sitting in Na clusters (or the other way around), disrupts the pathways available for fast ion migration.

With fast migration favoured by hops between homogeneous sites, the presence of, for example a Na site within a mainly Li cluster could block migration. This would be particularly true if the cluster morphology prevented alternative paths being found around the blocking atom. The topology of the clusters in the simulated SiO_2+Na+Li, MW and MW+Al+Mg glasses was perhaps best described as string like, with clusters having few side branches or loops. The tendency for alkali atoms in these glasses to sit in coordination environments with heterogeneous alkali neighbours suggests that the ability for alkali atoms to perform migratory hops would be supressed in these glasses. As alkali diffusion can be linked to the early stages of glass dissolution by water, the MW and MW+Al+Mg glasses would be expected to show better durability than the SiO_2+Na and SiO_2+Na+Li glasses.

Chapter 4

Glass Ceramic Interfaces

In the following chapter, the results of computer simulations on glass-ceramic interfaces are presented and the presence of the interface and their effect on the structure of the glass and ceramic components of the system are discussed.

4.1   Comparison of Interface Formation Techniques

In chapter 2, three different methods were described for creating glass-ceramic interfaces. The main features of each technique were as follows:

- **Cut and shut:** A glass block was split to create a gap into which a ceramic supercell was placed. The system was then equilibrated at 1500K and quenched to 300K.

- **Gap close:** Glass block was split in two, the halves were then separated to create a gap 8Å larger than needed by the ceramic supercell. This gap was then closed, gradually bringing the glass into contact with the ceramic supercell. Equilibration and data-collection was then performed in the same way as the other methods.

- **Quench with ceramic:** A glass-ceramic system was created in the same way as the cut and shut method. Rather than equilibrating at 1500K however, the ceramic atoms were

held fixed and the melt-quench procedure originally used to create the glass block was performed. The constraint on the ceramic atoms was released at 1500K and equilibration and data-collection performed.

In an effort to see which of these three simulation methods yields the most reasonable glass-ceramic interfaces, interfacial simulations were performed between the (100) surface of MgO and SiO_2, SiO_2+Na, SiO_2+Na+Li and MW glasses using each interface formation method.

Atomic scale visualisation of the resulting interfaces revealed systems which all had similar attributes: little or no intermixing of the glass and ceramic had occurred. The structure of the ceramic was largely unperturbed and the (100) surface at the interface had remained flat and in approximately the same position as when the simulation started. In all three methods, the glass component was amorphous and displayed evidence of the movement of modifiers to the interface.

4.1.1   Definition of Interfacial Energy

To allow further comparison of the different interface generation methods, the interface formation energy for each simulated system was calculated. Here, interfacial energy was defined as: the energy difference between the interfacial glass-ceramic system and the glass and ceramic components considered independently.

The interfacial energy, when defined in this way, is a measure of how stable the combined glass and ceramic components are in comparison to when separate. Bearing this in mind, the interfacial energy ($E_{\text{interface}}$) can be expressed as:

$$E_{\text{interface}} = \frac{E_{\text{glass,ceram}} - (E_{\text{glass}} + E_{\text{ceram}})}{A} \qquad (4.1)$$

where:

$E_{\text{glass,ceram}}$ = Energy of system containing glass ceramic interface.

E_{glass} = Energy of glass block with free surfaces.

E_{ceram} = Energy of ceramic block with free surfaces.

A = Interfacial area in glass-ceramic system.

An interfacial energy obtained in this way for a system is dependent on how the initial glass and ceramic components are configured. For this reason, the interfacial energy was further defined as the energy difference between separate glass and ceramic blocks, each with two free surfaces (equilibrated *in vacuo*) and the final energy of the interfacial system.

In section 2.2 the method by which the glass-ceramic systems were created was described. Put simply, a glass block was split in half to create a gap along the cell's z-axis into which a ceramic block was inserted. A very similar procedure was used to create glass and ceramic blocks with free surfaces from which E_{glass} and E_{ceram} were calculated. In the case of the glass component, two free surfaces were created by splitting the glass block in half to create a 50 Å gap. Similarly each ceramic block was placed at the centre of a simulation cell 50 Å larger than the block along the z-axis. The same glass and ceramic blocks used at the start of the interface generation also provided the starting point for the calculation of E_{glass} and E_{ceram}. The cut surfaces were equilibrated with the vacuum by performing 7000fs of NPT molecular dynamics at 300K. Average values for E_{glass} and E_{ceram} were calculated from the average obtained over a further 5000fs of NPT molecular dynamics.

4.1.2   Interfacial Energies Compared

Interfacial energies were calculated for each interface formation technique, these are given in table 4.1. Lower (i.e. more negative) energies indicate more stable interfacial systems. In all the cases considered, the quench with ceramic method gives the lowest energies. This is followed, in turn by the gap-close and cut and shut methods.

During the relatively short time accessed by molecular dynamics, little rearrangement of the highly polymerised glass networks would be expected to occur. This might help to explain why the quench with ceramic method gives lower energies than either of the other interface

	$E_{\text{interface}}$ (Jm^{-2})		
System	Cut & Shut	Gap Close	Quench with Ceramic
SiO_2–MgO	-1.39	-2.59	-3.25
SiO_2+Na–MgO	-1.57	-2.48	-3.37
SiO_2+Na+Li–MgO	-1.27	-2.12	-3.15
MW–MgO	-0.52	-2.04	-2.85

Table 4.1: Comparison of interfacial energies for different interface generation methods. Energies are for (100) ceramic surfaces.

formation methods.

The glass transition temperature (T_g) of the simulated glasses was estimated. This was achieved by plotting each glass' potential energy as a function temperature and finding the temperature at which the gradient of the data changed. These estimates are given in table 4.2. Both cut & shut and gap-close techniques were equilibrated at relatively high temperatures (the high temperature stage of their equilibration was performed at 1000K). This temperature is below the glass transition temperature of the simulated glasses, which means that for these techniques, it would have been difficult for rearrangement of the silicate/borate networks to occur. By comparison, during the quench with ceramic method it is thought that the glass component of the system has more time to relax in response to the ceramic before its structure becomes frozen at T_g.

The close-gap energies were lower than the equivalent cut & shut values. It is thought that this can be attributed to the free surfaces that existed during the early stages of the close-gap method. The gradual introduction of the glass' surface to the ceramic would have allowed some time for surface relaxation to occur in response to the ceramic's potential. This relaxation of the borate and silicate networks could have allowed the close-gap method to achieve lower energies than the cut & shut systems (where the added conformational freedom associated with the free surface did not exist).

As a result of the high quench rates associated with MD generated glass structures, the T_g values of the simulated glasses are high. In a real glass T_g would be lower, therefore the structures

Glass	T_g (K)
SiO_2	3800
MW	3680
SiO_2+Na+Li	3650

Table 4.2: Estimated glass transition temperatures for simulated glasses.

generated by the quench with ceramic method were probably more like experimentally generated glass-ceramic systems than those from the other methods. The low energies obtained using the quench with ceramic method suggest that this method produces the best equilibrated and therefore most reasonable interfacial structures. For this reason, the glass-ceramic results presented from this point onward were obtained from simulations performed using the quench with ceramic method.

4.2   The Effect of Glass Composition on Interfacial Energy

Interfacial energies were calculated for the interface between the (100) surface of MgO and each of the glass compositions considered. This gives an indication of the relative stabilities of the interfaces made with each glass. Figure 4.1 shows the results of this comparison.

It is interesting that SiO_2 doesn't have the highest energy. The lack of modifier atoms means that SiO_2 is the most polymerised glass. The less constrained network brought about by modifiers might be expected to allow the glass to relax more effectively, producing a less strained and lower energy structure at the glass-ceramic interface. The SiO_2+Na+Li and MW glasses however, both have higher energies than SiO_2. This is unexpected.

In effect, the interfacial energy represents the energy change in going from a system with free surfaces to one without. The unexpectedly low SiO_2 energy may show that the energy associated with SiO_2's free surface was very high, leading to a large and negative change in interfacial energy on interface formation. In comparison the SiO_2+Na+Li and MW glasses may form relatively stable free surfaces. If so, from an energetic point of view, these glasses might see less benefit from interface formation than SiO_2. This seems quite likely as, of those glasses
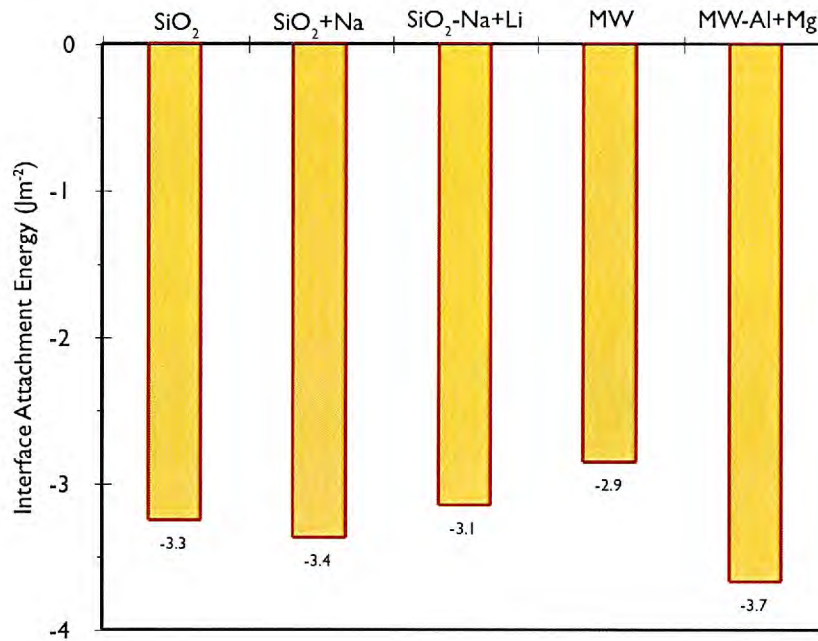
Figure 4.1: Comparison of interfacial energies for interfaces between the 100 surface of MgO and the five glass compositions considered.

considered, SiO_2 shows the least interfacially induced network relaxation (this is discussed further in section 5.3.2).

The difference in energy between the MW and MW+Al+Mg compositions is also striking. The addition of a small number of Mg and Al atoms to the MW composition brought about a significant change in interfacial energy: the MW glass has the highest energy whilst MW+Al+Mg has the lowest. Unlike the SiO_2 energy discussed in the previous paragraph, it seems unlikely that the large energy difference between MW and MW+Al+Mg was caused by MW+Al+Mg having an unusually large surface energy. Instead it seems likely that the energy of the MW+Al+Mg system was lower due to the presence of Mg and Al. In effect, Mg and Al helped stabilise the interface of MgO-(100) with MW+Al+Mg.

4.3   Interfacial Energy as Function of Ceramic Substrate

The interfacial systems examined by this work contained ceramic materials with the rocksalt structure. One reason that MgO, CaO, SrO and BaO, were chosen for study was because many of their properties are linearly dependent on cation radius. For example, figures 4.2, 4.3 and 4.4, show experimentally determined lattice parameter, bulk-modulus and lattice energy have been plotted against cation radius for these materials (cation radii are VI coordinate ionic radii from Shannon [118]). As a consequence it may be expected that the interfacial energies for MgO, CaO, SrO and BaO with a particular glass, may also show a linear dependence on cation radius. To explore this possibility, interfacial energies were calculated from the results of the interfacial simulations.

Simulations were performed for interfaces between the MW and MW+Al+Mg glasses and the (100) surfaces of all four ceramic compositions. In addition, for the MW glass, interfaces were generated with the (110) terminating surface of each ceramic. Interfacial energies for the MW glass, (100) and (110) results are plotted against cation radius in figure 4.5. Similarly, the interfacial energies obtained for MW+Al+Mg glass are plotted in figure 4.6.
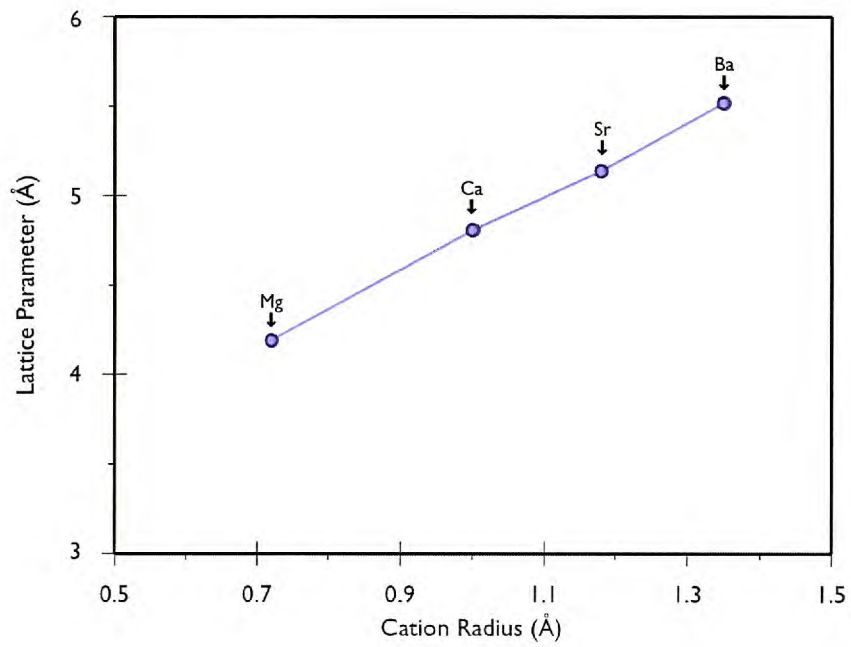
Figure 4.2: The lattice parameters of the rocksalt structures considered showed a linear dependence to their cation radius (data taken from references given in table 2.2).
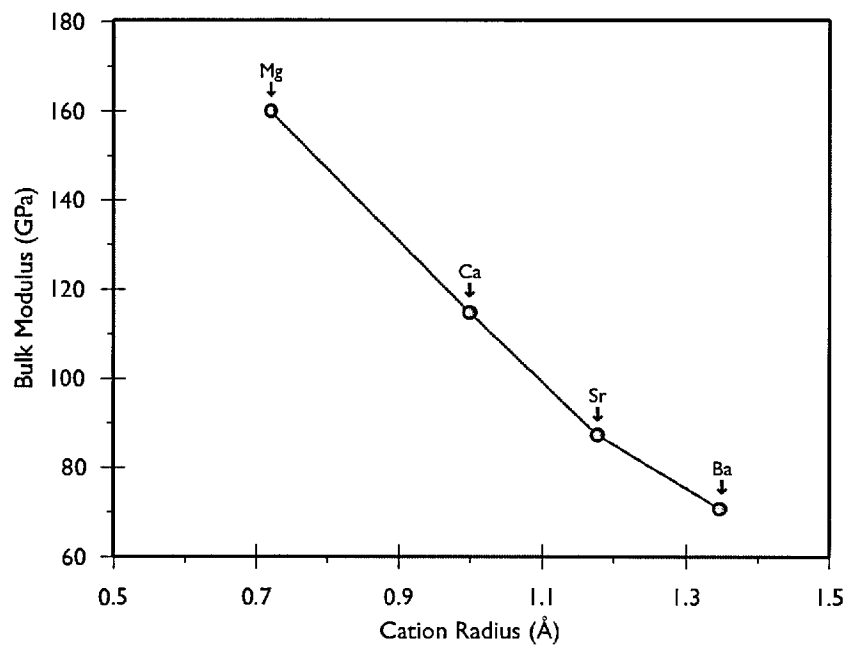
Figure 4.3: Bulk modulus varies linearly with cation radius for the $A^{2+}O$ crystal structures studied (values taken from [119]).
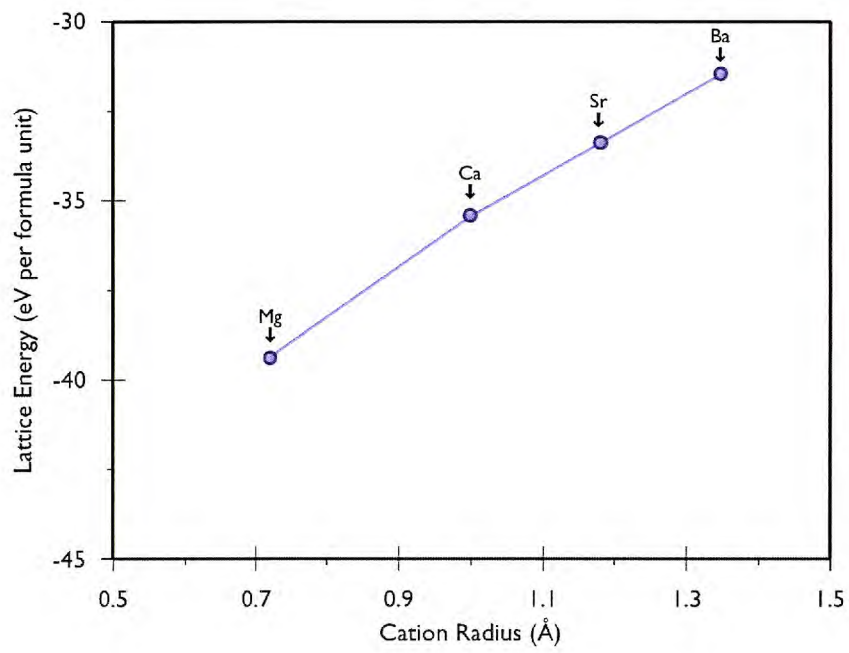
Figure 4.4: Graph showing linear dependence of lattice energy on cation radius for the $A^{2+}O$ structures considered (data taken from [120]).

4.3.1   Comparison of (100) and (110) Interfacial Energies

Figure 4.5 shows that, for all the ceramic compositions, the (110) surface exhibits substantially lower interfacial energies than the (100) surface.

The energy associated with the (100) surface of the rocksalt structure has previously been shown to be lower than that for the (110) surface [121]. The interfacial energies given in figure 4.5 suggest that the higher energy (110) surface was stabilised to a greater degree by interface formation than the already relatively stable (100) surface. This may indicate that, for a specific glass composition, ceramic surface energy could be used as an indicator of interfacial energy. This is likely to be an overly simplistic view; a systematic study of interfaces containing different combinations of glass and ceramic would need to be performed to confirm any correlation between interfacial and surface energies.

In general, the interfacial energies for both terminating surfaces showed a linear dependence on ceramic cation radius. The (110) energies for MgO, CaO and SrO, increase linearly from -5.14 for MgO to -3.9 Jm^{-2} for SrO. Over the same range, the (100) interfaces show a similar but smaller increase. The upward trend in energy with increasing cation radius does not continue beyond SrO; BaO had a lower energy than SrO for both the (100) and (110) cases. Indeed, for the (100) surface the interface with BaO gave an energy lower than that seen for MgO. This is an interesting effect, as it suggests a change in interface behaviour between SrO and BaO.

4.3.2   Comparison of MW and MW+Al+Mg Glasses

When attachment energies were compared, as a function of glass composition in section 4.2, it was found that the MW+Al+Mg glass had a significantly lower energy than the MW glass even though both glasses have very similar compositions. This comparison was extended to the CaO, SrO, and BaO ceramic compositions.

The trend shown by the MW+Al+Mg energies (shown in figure 4.6) is the same shape as that exhibited for the MW glass/(100) interfaces. That is to say, a small increase in energy between MgO and CaO, followed by a larger increase on going to SrO, again followed by a drop
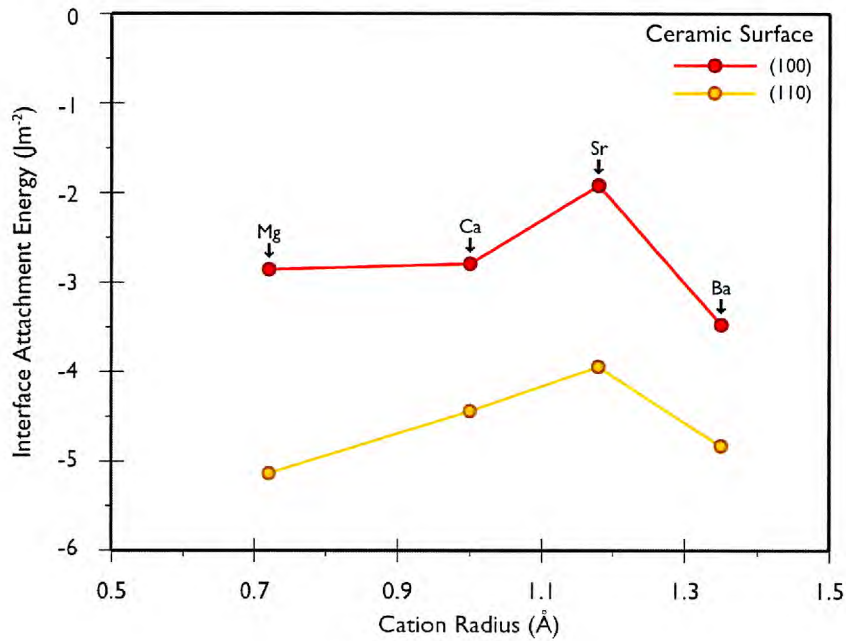
Figure 4.5: Interfacial energies for MW glass systems plotted against ceramic cation radius.

in energy on going to BaO. Comparison of the MW and MW+Al+Mg energies in table 4.3 demonstrates that the Al and Mg additions to the MW glass brought about a decrease in interfacial energy. In general, the MW+Al+Mg values are about 0.5 Jm^{-2} lower than the equivalent MW energy. This once more suggests that Mg and Al stablilise the glass ceramic interfaces and would therefore be expected to also improve the ability of the glass to wet the ceramic's surface.

Ceramic System	Interfacial Energy (Jm^{-2})		
	MW (100)	MW+Al+Mg (100)	Difference
MgO	-2.85	-3.67	-0.82
CaO	-2.79	-3.29	-0.50
SrO	-1.92	-2.39	-0.47
BaO	-3.48	-3.98	-0.50

Table 4.3: Comparison of (100) surface interfacial energies for MW and MW+Al+Mg glasses.
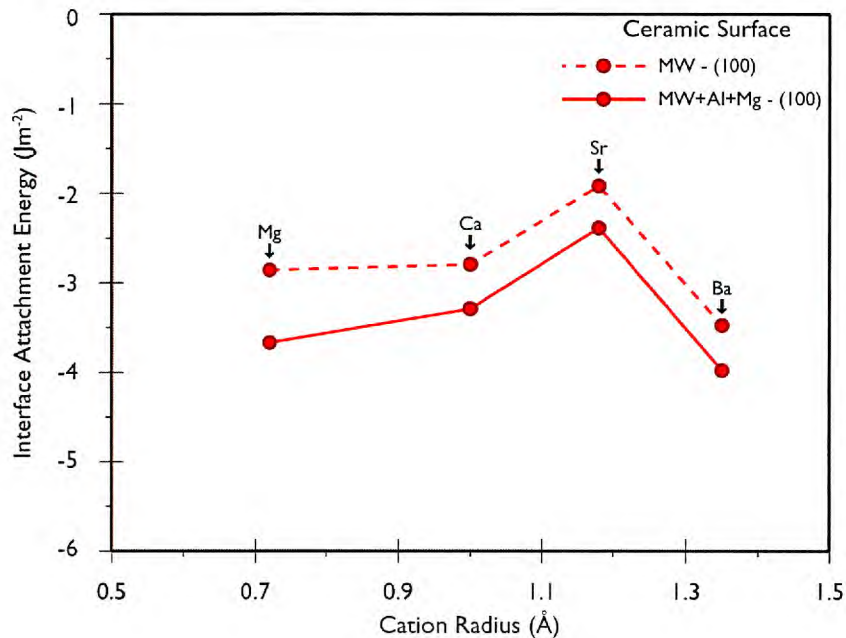
Figure 4.6: Interface interfacial energies for MW+Al+Mg glass systems plotted against ceramic cation radius (MW glass data included for purposes of comparison).

4.3.3 BaO

The plots of interfacial energy against cation radius described above, suggest that interface energy is proportional to ceramic cation radius. However, in all cases, the energy of interfaces with BaO did not follow this trend: BaO data points are consistently lower in energy than would be predicted using a linear model.

The low BaO interfacial energies might suggest a problem with the potential model employed. This possibility was considered, however, the barium pair potentials are consistent with those used to describe other ceramic interactions. The pairwise interactions between the ceramic cations and oxygen are plotted in figure 4.7 from the potential parameters given in table 2.1. A visual examination of the potential energy curves show a systematic progression in both the depth and position of the potential energy minima, consistent with the change in cation radius. Static energy minimisation was used in conjunction with these pair potentials in order to allow a comparison of the experimental and simulated lattice parameters to be made (shown in fig-

ure 4.8). Once more, the potential model replicates the experimental values well. The internal energy of the crystal (lattice energy), was also calculated and is compared with experiment in figure 4.9. The lattice energies produced by the potential model are consistently lower than experiment. Although this is a failing of the potential set, the general trend matches the experimental values which supports the view that the low BaO interface energies were caused by a change in interfacial behaviour for BaO, rather than an artefact of the potential model.

4.4 Interfacially Induced Changes to Ceramic

The following section considers the structural changes experienced by MgO, CaO, SrO and BaO resulting from the presence of the glass ceramic interface.

4.4.1 Changes at (100) Interfaces

Figure 4.10 shows the top three layers of MgO, CaO, SrO and BaO from MW glass (100) interfaces in the absence of the glass. The MD frames from which these images were generated are representative of the equilibration and data collection stage of the simulations and show the state of the ceramic at a temperature of 300K. The left hand column of the diagram shows views along the ceramic's [100] direction whilst the right of the diagram shows plan views of the same structure. To allow direct comparison of the different systems, all images are drawn to the same scale.

Between MgO and BaO, the plan views of the (100) surfaces show that the surface remained very regular. The regular, undistorted grid of the (100) surface in figure 4.10 shows that glass induced surface relaxation was small in the plane of the surface.

The side-on views of the ceramic blocks show that in certain cases, ions sat proud of the ceramic surface. The number of ions above the surface plane increased in order of increasing ceramic cation radius from MgO to BaO.

The MgO surface was almost completely flat. The surface of CaO was also flat however several
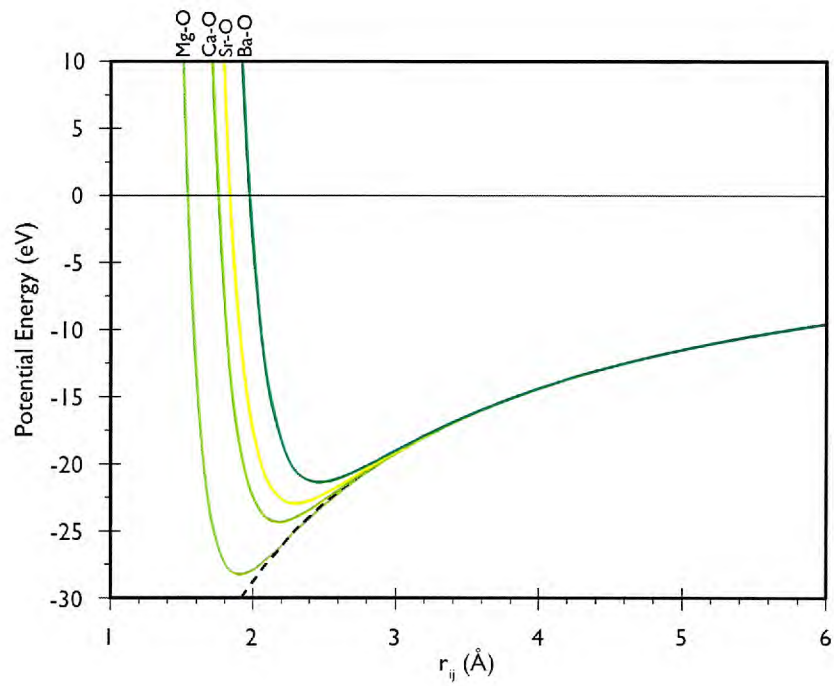
Figure 4.7: Plot of potential energy vs. separation for pairwise interactions between O^{2-} and 2+ ceramic cation species (the Coulombic contribution to the energy is shown as a dashed line).
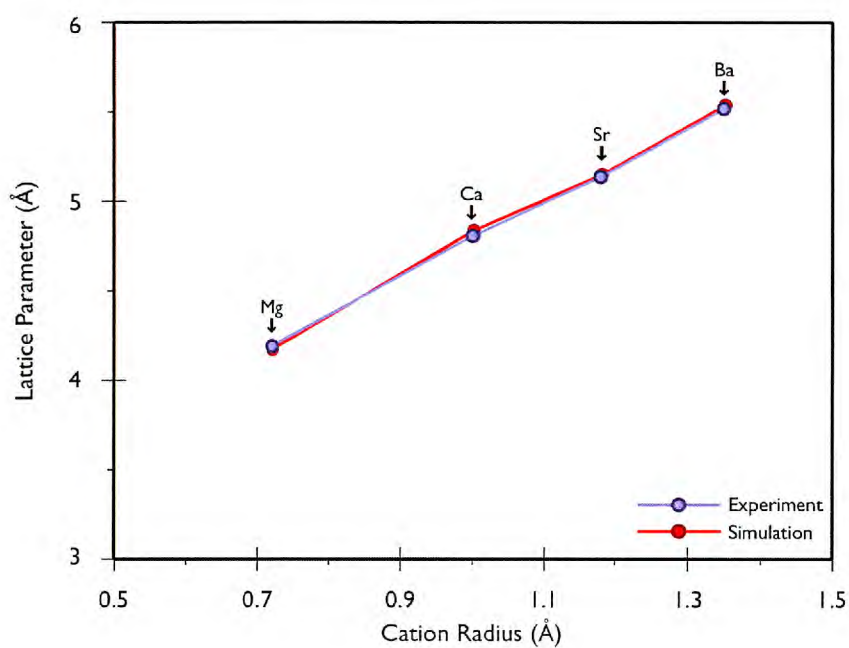
Figure 4.8: Comparison of simulated and experimental lattice parameters for the rock-salt structures considered plotted against A^{2+} cation radius (see references in table 2.2 for source of experimental data).
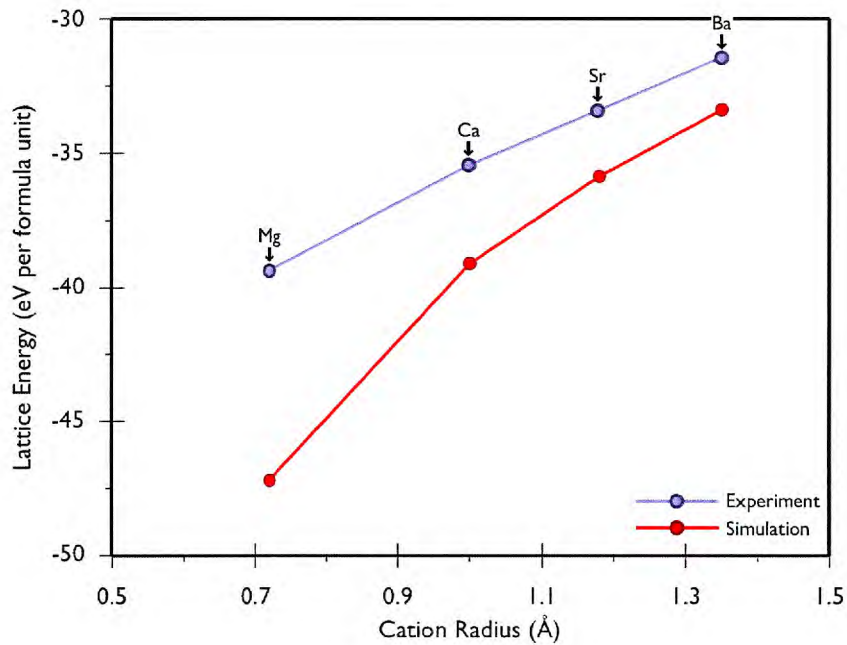
Figure 4.9: Comparison of simulated and experimental lattice energies plotted against cation radius for rock-salt structures considered (experimental data from [120]).

anions sat proud of the surface. The trend continued with SrO with entire rows of atoms bowing upwards. Even more surface distortion was presented by the BaO surface. At this surface, anions bonded to the glass were pulled out of the surface to form surface vacancies; the anion sitting directly above the vacancy but separate to the surface. Valentin *et al.* [122] used density functional theory calculations to show that the oxygen vacancy defect formation energy for {100} surfaces of rocksalt decreased in the MgO, CaO, SrO and BaO series (with values of 9.26, 9.24, 8.62 and 7.67 eV respectively). This is consistent with the behaviour witnessed at the glass ceramic interfaces where oxygen atoms were seen sitting above the surface in BaO and SrO but not in MgO or CaO.

4.4.2 Changes at (110) Interfaces

A view of the MgO-(110) surface is shown in plan view (i.e. viewed down the z-axis) in figure 4.12a. When the ceramic block is considered as a series of layers, for (100) each atom at
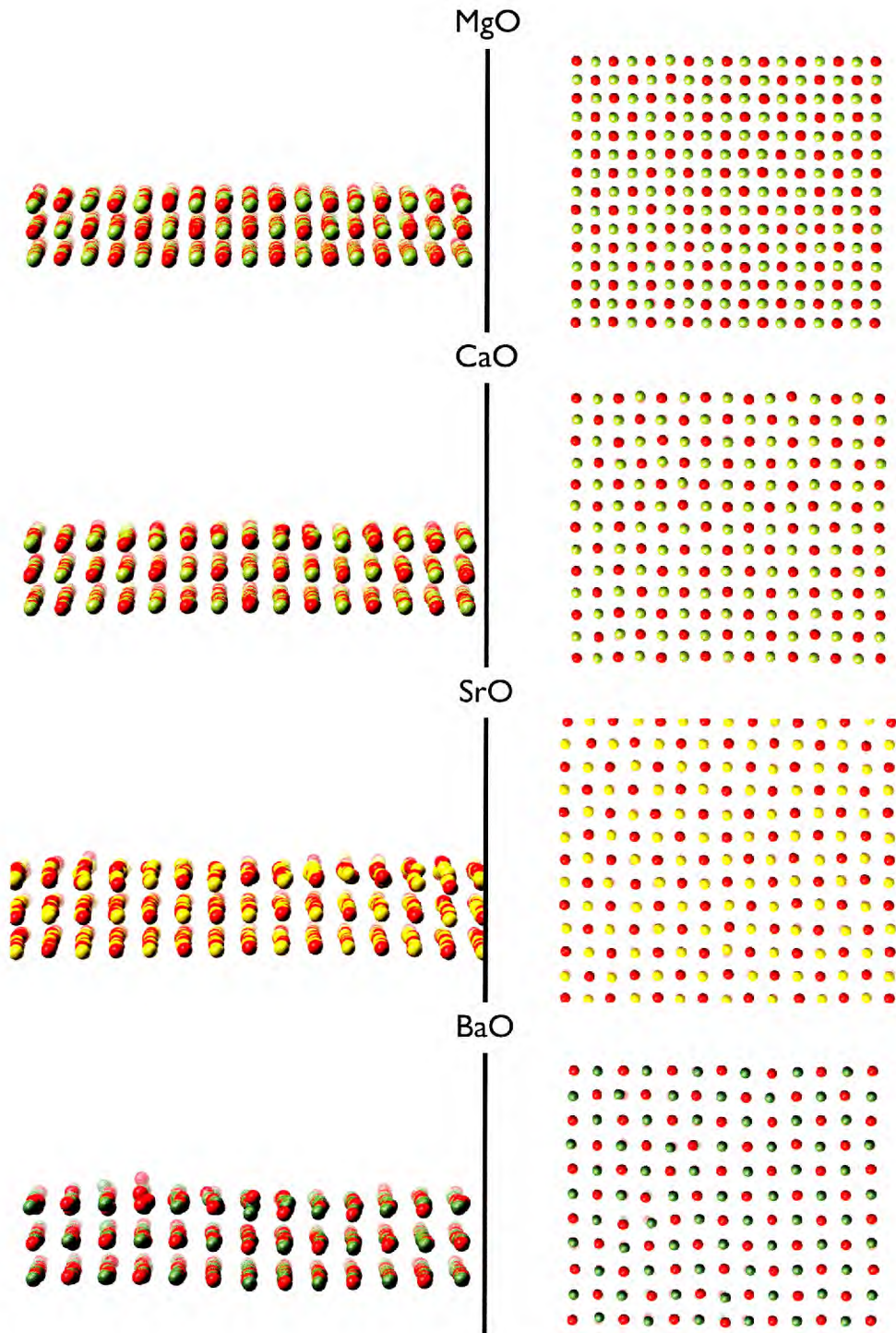
MgO

CaO

SrO

BaO

Figure 4.10: Representative images of top three layers (100) ceramic blocks taken from equilibration and data collection stage of melt-quench. Left: view down [100]. Right: view down [001]. In both cases [010] runs left to right across page.
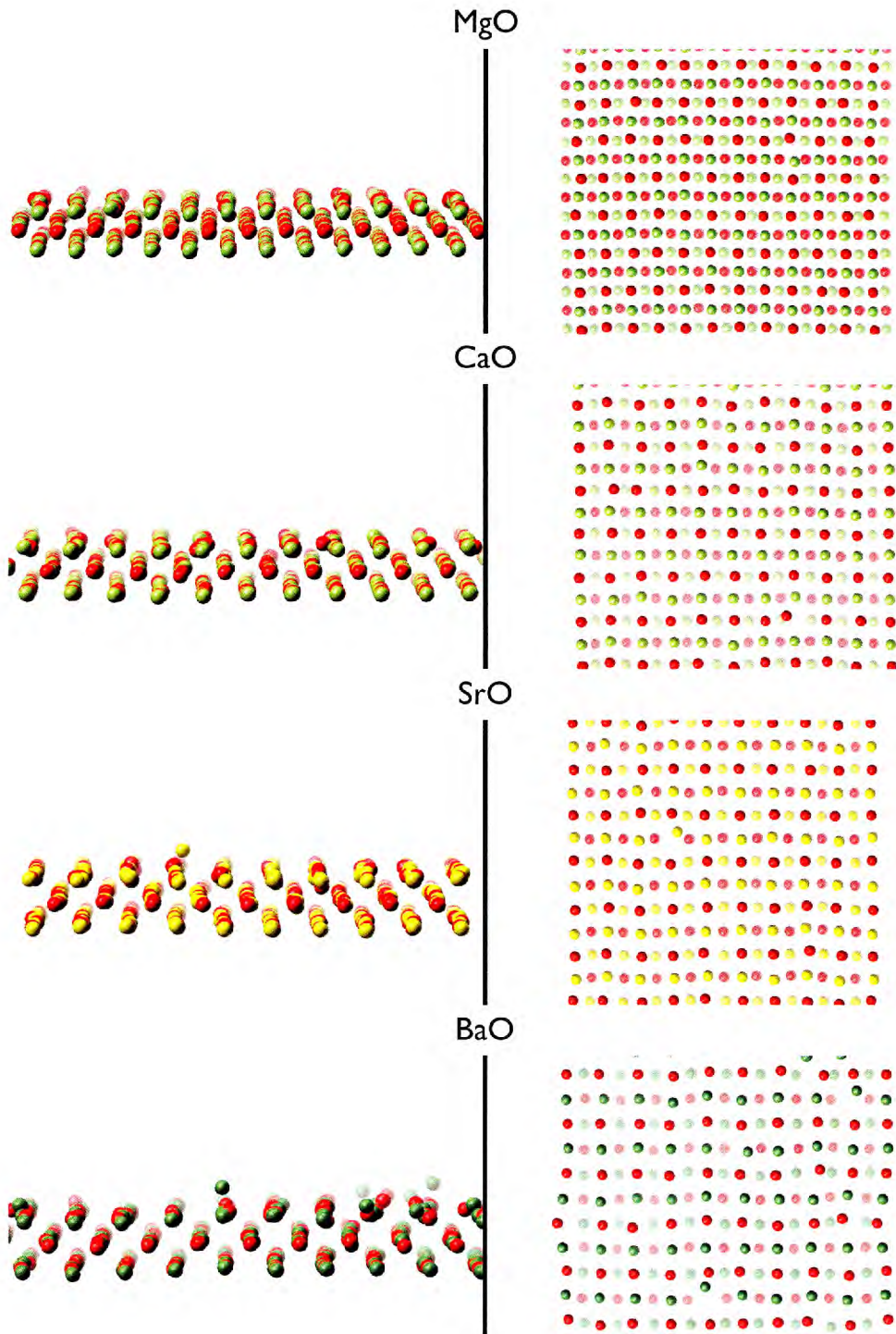
Figure 4.11: Representative images of top three layers of (110) ceramic blocks taken from equilibration and data collection stage of melt-quench. Left: view down [100]. Right: view down [001] with [100]. In both cases [010] runs left to right across page.

the ceramic surface sits directly above an atom in the layer below. By comparison, atoms in the top layer of the (110) surface sit above atoms two layers below, whilst the rows of atoms in the second layer of atoms are offset relative to the surface layer along the $[01\bar{1}]$ direction. When viewed along the $[100]$ direction (figure 4.12b) this gives the surface the appearance of ridges and furrows running along $[100]$. Rows containing either Mg or O at $90°$ to the $[100]$ direction run across the furrows and ridges (i.e. from top to bottom in figure 4.12a).

Figure 4.11 shows visualisations of the top layers of ceramic blocks taken from (110) interface simulations. In comparison to the (100) surface, the plan views of the surface seem to show more glass induced modification of the ceramic surface plane occurred with the (110) surface.

In MgO, relaxation was limited to the contraction of O–O distances between surface ridges (this can be explained in terms of borate tetrahedra sharing an edge with surface anions, see section 4.4.3 below). Whilst in CaO ions were displaced from their sites by the glass. In the (100) cases, ions leaving the surface were displaced directly upwards out of the ceramic's surface. Here, ions were displaced so that they no longer sat above their original site, presumably due to the less dense packing of the surface along $[0\bar{1}1]$. Again, the number of displaced atoms increased with ceramic cation radius on moving from SrO to BaO.

At the (100) surface, certain atoms left the surface to form vacancies. These were found to be anions. By comparison, the side views of the (110) surfaces, showed that for this surface, cation vacancies were also formed. As interactions between the ceramic and glass were calculated using the same set of potentials and the same simulation method for both surfaces, this would suggest that the configuration of the (110) surface allowed the glass to bond more strongly to ceramic cations than at the (100) surface. Movement of the glass relative to the ceramic and the strong bond between them could then account for cations being pulled out of the surface.

Surface disruption was particularly evident at the (110) surface of BaO. In figure 4.11 a highly perturbed area is visible at the right of the surface images. In this region, several Ba^{2+} ions appear to have broken free of the surface. Although clearly still a ceramic, the large perturbation may be showing the early stages of BaO dissolution by the glass. During interface formation, atoms in the ceramic block were held fixed until the temperature fell below 1500K.
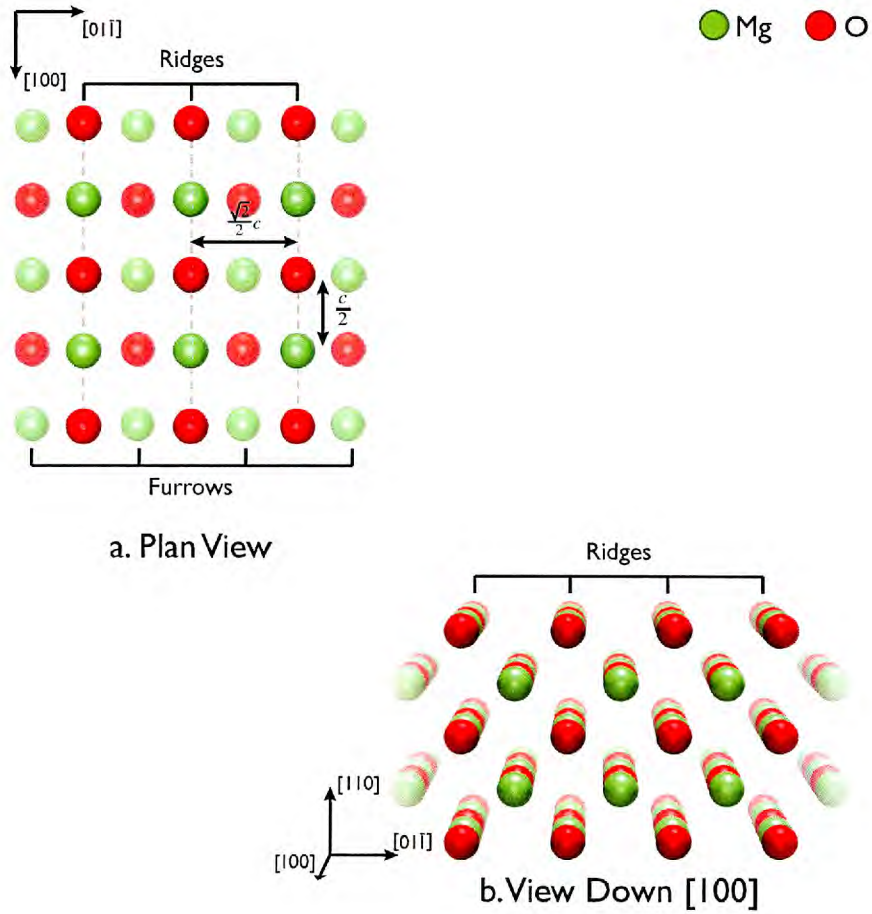
Figure 4.12: a. Plan view of the MgO-(110) surface, b. view along the [100] direction showing the distinctive ridge and furrow configuration of the (110) surface (directions in diagram are given relative to the MgO unit cell).

This temperature was well below the melting point of all the ceramic compositions considered (as shown in table 4.4), meaning that the mixing of ceramic and glass cannot be explained by ceramic melting.

Barium can act as a network modifier in glasses and as discussed in chapter 3, network modifiers can migrate relatively quickly through the glass structure. Once free from the ceramic surface therefore, barium atoms from the ceramic might be expected to migrate away from the ceramic surface. This ability for the ceramic to effectively dissolve in the glass may also account for BaO's low interfacial energies.

In conclusion, at both surfaces, the ability of the glass to perturb the ceramic surface increased with ceramic cation radius. The (110) surface was more susceptible to perturbation than the (100) surface.

4.4.3 Furrow Bridging

A significant number of the borate polyhedra in the glass adjacent to the ceramic interface were found to include anions from the ceramic surface. At the MW glass, MgO-(100) interface, the ceramic surface never contributed more than one anion to a borate unit. By comparison a large proportion of the borate polyhedra at the MW glass, MgO-(110) interface contained two surface anions. Analysis revealed that, of the ten borate units that contained ceramic anions, seven were tetrahedra (the remaining three were BO_3 units) and of these, 53% contained two anions which sat in the ceramic surface.

Composition	Melting Point (K)
MgO	3098
CaO	2886
SrO	2804
BaO	2246

Table 4.4: Melting points for ceramic compositions (taken from [123]).

[1̄10]
[01̄1]
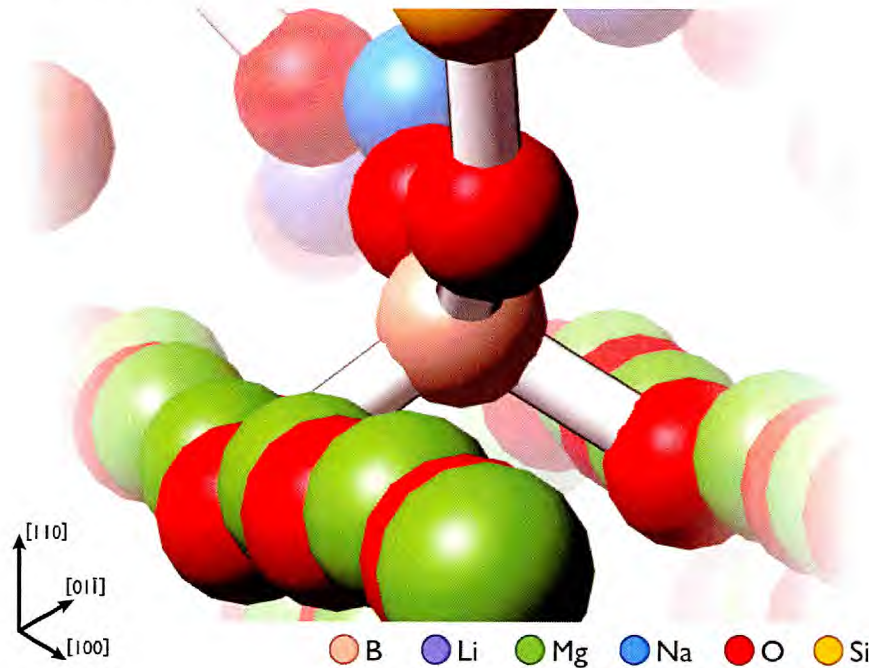[100]

○ B   ○ Li   ○ Mg   ○ Na   ● O   ○ Si

Figure 4.13: A borate unit spanning a furrow in at the MW glass MgO-(110) interface.

Further examination of the borate units which contained two ceramic anions showed that they took on a distinct configuration at the surface. An example of this is shown in figure 4.13 where a BO_4 unit shares two vertices with the ceramic. When viewed along the ridges and furrows of the (110) surface (i.e. from left to right in the plan view given in figure 4.12) the boron atom sits directly above a surface furrow and forms bonds to oxygen atoms in the ridges on either side; effectively, leading to a borate unit being formed with one edge forming a bridge across the furrow.

The average B–O bond length was found to be 1.49Å in the MW glass, MgO-(110) system. Based on this length, a regular borate tetrahedron would be expected to have an edge length of 2.43Å. For a tetrahedron to form an edge with the ceramic, a surface anion separation close to this value would be required. The average inter-ridge spacing at the MW glass MgO-(110) surface was found to be 2.96Å. The average separation between the ceramic anions which formed the edge of borate tetrahedra was to 2.48Å. This shows that surface relaxation occurred allowing the inter-ridge spacing to become compatible with the borate tetrahedral edge length.

Furrow bridging by boron was only observed at the MW glass MgO-(110) interface. It is thought that CaO, SrO and BaO's increased lattice parameters meant that the inter-ridge spacing became too large for bridging to occur at interfaces with these ceramics.

4.5 Alkali Distribution at Interfaces

The spatial distribution of alkali species, both parallel and perpendicular to the interfaces was examined. It was found that the presence of the ceramic phase had a definite and profound effect on the alkali distribution at the interfaces considered. In the following section, these changes are discussed.

4.5.1 Alkali Enhancement at Interface

In every system which contained alkali atoms, it was found that the concentration of at least one alkali species increased towards the glass-ceramic interface. Figure 4.14 shows a representative frame taken from the data-collection stage of the SiO_2+Na glass and MgO-(100) ceramic interface simulation. To allow the distribution of Na atoms to be seen more easily, the Si and O atoms have been removed from the right of this figure. This shows that the concentration of sodium atoms was considerably enhanced, leading to the formation of a 'sodium blanket' at the interface. To a varying degree, this sort of interface induced enhancement was seen in all the modifier containing systems examined.

Density Fluctuations

In an effort to quantify the magnitude of the alkali enhancement described above, the density of alkali atoms was calculated as a function of distance from each interface. These density distributions were obtained in the following manner. The simulation cell was decomposed into a series 0.19 Å histogram bins along the z-axis, perpendicular to the interface. The z-coordinate of an atom was thus a measure of the perpendicular distance to the glass-ceramic interface. The
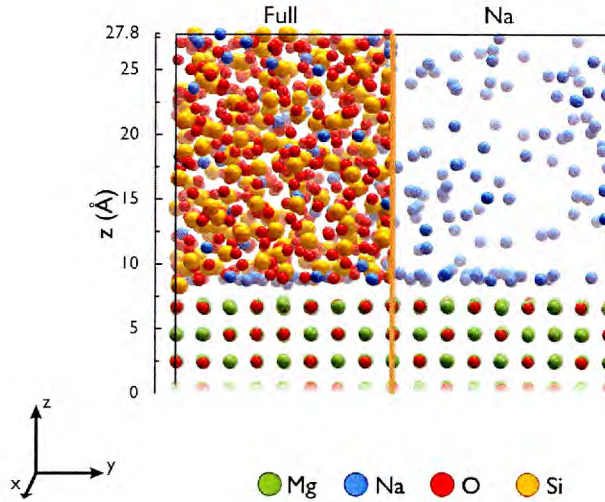
Figure 4.14: The interface between SiO_2+Na and MgO-(100) showing the distribution of modifier atoms in the system.

total number of each species in each slice was calculated and divided by the slice volume to give the localised number density for that species. This procedure was repeated for all the data collection frames of the simulation to produce a time averaged concentration profile.

Glasses are often considered to be compositionally homogeneous, however, at the nanometre length scale considered in atomic scale computer simulation, sometimes quite substantial fluctuations in density and composition have been reported [124, 125]. Fluctuations are initially frozen in at the glass transition temperature and reflect the degree of heterogeneity present in the super-cooled liquid from which the glass was formed. As a result, glasses with high fictive temperatures, such as those created by the high quench rates typical of molecular simulation, would be expected to show a higher degree of density fluctuation than more slowly cooled glasses. In order to prevent the noise associated with these fluctuations from masking any significant trends in concentration, each density distribution was the average of four separate distributions, derived as follows. First, the sandwich like configuration of the glass ceramic simulations meant that each system effectively contained two interfaces (one at the top and one at the bottom surface of the ceramic block). This symmetry allowed two density distributions to be obtained from each simulation. Second, another two distributions were obtained by per-

forming another simulation for each glass-ceramic system. To ensure that this second run was not the same as the first, initial velocities were assigned using a different random seed and the glass block was split at a different point.

During molecular dynamics there is nothing to prevent movement in space, of the system as a whole. Although each half of the two simulated interfaces obtained from molecular dynamics effectively described the same system, there was no guarantee that the interface would occur at the same position along the z-axis in both. Before combining the four halves to create the density distribution, it was necessary to compensate for any system drift. This was achieved by expressing the z-coordinate of each atom relative to a common reference point. As the centre of each ceramic block was relatively unperturbed by the presence of the interface, the average z-coordinate of the middle layer of atoms in each interfacial system was used for this purpose. Having expressed the z-coordinate relative to the middle layer, the concentration profile was obtained by taking the average of the four distributions.

4.5.2 Alkali Density Plots

A full set of alkali density distributions were plotted and can be found in the pages that follow (table 4.5 is provided to make navigating these figures easier). These concentration profiles are shown in context with a visualisation of the interfacial system they represent[1]. To allow straightforward comparisons to be made between the density of different alkali species and different glass compositions, alkali densities were expressed as a percentage of the homogeneous number density for that species in the equivalent bulk glass. For example, an Na density of 200% at an interface with MW glass represents a region containing twice as many Na atoms as would be expected in a homogeneous bulk MW glass.

The height of the first peak in each alkali density distribution was measured to allow comparison of the modifier concentration increases seen at each interface. These values appear in table 4.6, values marked by N/A mean that no distinct initial peak was observed.

Several general observations can be made from the modifier density plots. The largest increase

---

[1]Visualisations were made using a combination of VMD [126] and Raster3D [127–129].

Glass	Ceramic	Figure
SiO_2+Na	MgO-(100)	4.15, p.121
SiO_2+Na+Li	MgO-(100)	4.16, p.122
MW	MgO-(100)	4.17, p.123
	CaO-(100)	4.18, p.124
	SrO-(100)	4.19, p.125
	BaO-(100)	4.20, p.126
MW	MgO-(110)	4.21, p.127
	CaO-(110)	4.22, p.128
	SrO-(110)	4.23, p.129
	BaO-(110)	4.24, p.130
MW+Al+Mg	MgO-(100)	4.25, p.131
	CaO-(100)	4.26, p.132
	SrO-(100)	4.27, p.133
	BaO-(100)	4.28, p.134

Table 4.5: Concentration profile table of figures.

in alkali concentration was found in the SiO_2+Na+Li glass (figure 4.16). Here the concentration of Li at the interface with MgO-(100) was almost ten times that found in the bulk SiO_2+Na+Li glass.

In general, the Li concentration was enhanced to a greater degree than the Na concentration for mixed alkali glass interfaces. The only exception was for the MW MgO-(100) interface (figure 4.17) where the Na concentration was 588% and Li was 569%, however this increase is essentially the same.

Although some form of alkali increase was observed at every interface considered, in some mixed alkali glasses this increase was not observed for all the alkali species. For example, no distinct Na peak is observed at the interface between MW glass and the (100) surface of BaO (figure 4.21). Instead, the Na concentration increased gradually with distance from the interface (by comparison the Li peak had a height of 265% at the same interface). Similarly, the initial peak of the Na distribution in the MW+Al+Mg SrO-(100) system (figure 4.27) was

no larger than the fluctuations seen further from the interface.

Enhancement as a Function of Ceramic Composition

For the MW and MW+Al+Mg glasses, interfaces were generated for the MgO, CaO, SrO and BaO ceramics. In the case of MW glass both (100) and (110) terminating surfaces were considered. When placed in order of increasing lattice parameter, in general, the level of modifier enhancement at the glass-ceramic interfaces decreased.

Comparing the interfacial peak heights for each ceramic composition showed that, with the exception of Li at the interface with MgO (figure 4.21), the concentration of alkali atoms at the (110) interfaces were lower than at comparable (100) interfaces. The largest difference is seen at the CaO interface: the relative concentration of Li atoms at the (100) interface with MW glass (figure 4.18) was 738%, at the (110) interface, however (figure 4.22), the Li concentration is less than half at 316%.

		Height of Initial Peak (%)		
Glass	Ceramic Surface	Li	Na	Mg
MW	MgO-(100)	569	588	-
	CaO-(100)	738	454	-
	SrO-(100)	563	221	-
	BaO-(100)	738	199	-
MW	MgO-(110)	856	515	-
	CaO-(110)	316	205	-
	SrO-(110)	305	170	-
	BaO-(110)	265	N/A	-
MW+Al+Mg	MgO-(100)	468	468	935
	CaO-(100)	474	383	592
	SrO-(100)	534	N/A	297
	BaO-(100)	578	N/A	378
SiO_2+Na	MgO-(100)	-	654	-
SiO_2+Na+Li	MgO-(100)	990	767	-

Table 4.6: Height of initial peaks in alkali density distributions.
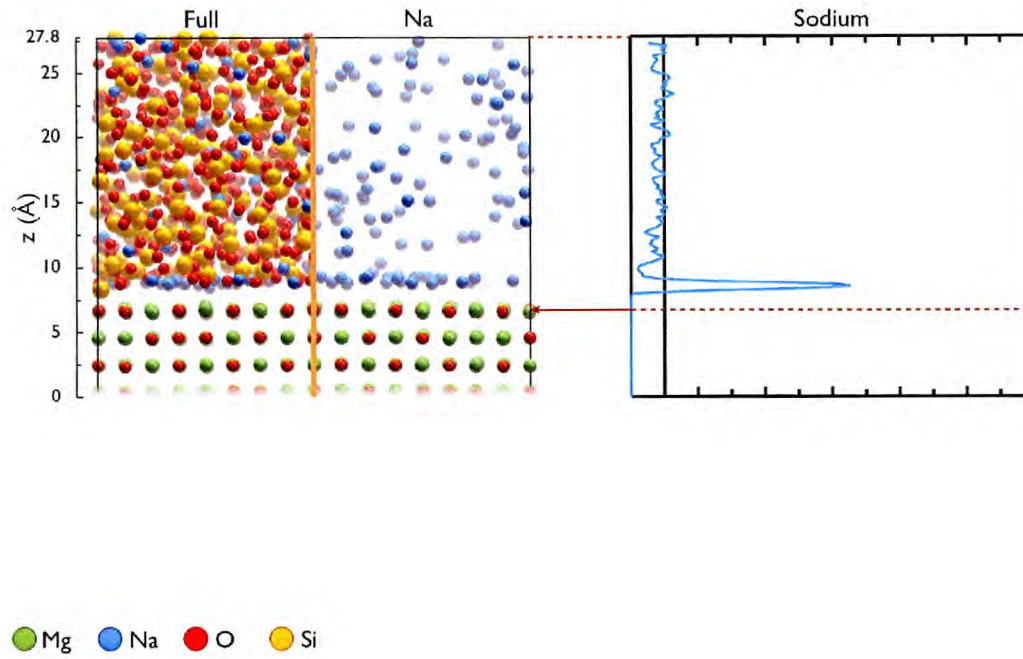
Figure 4.15: Alkali Concentration Profile: SiO_2+Na MgO-(100).
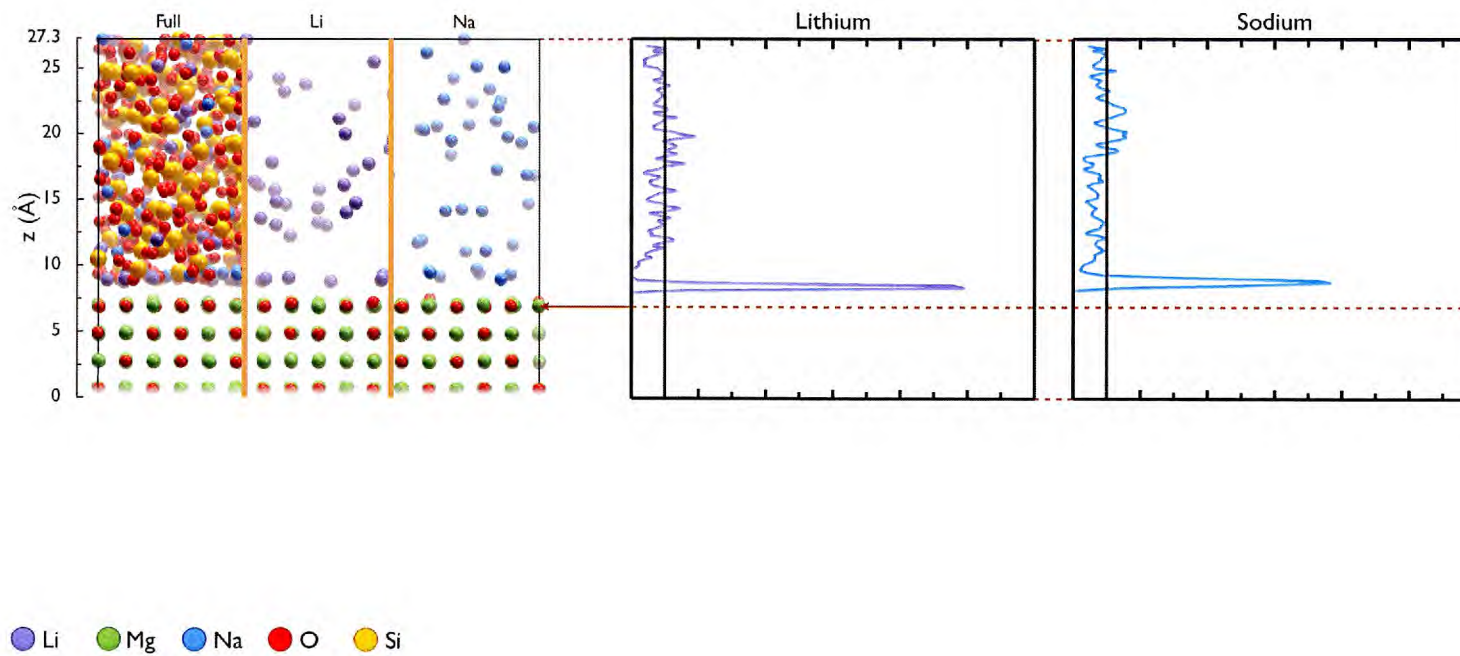
Figure 4.16: Alkali Concentration Profile: SiO_2+Na+Li MgO-(100).
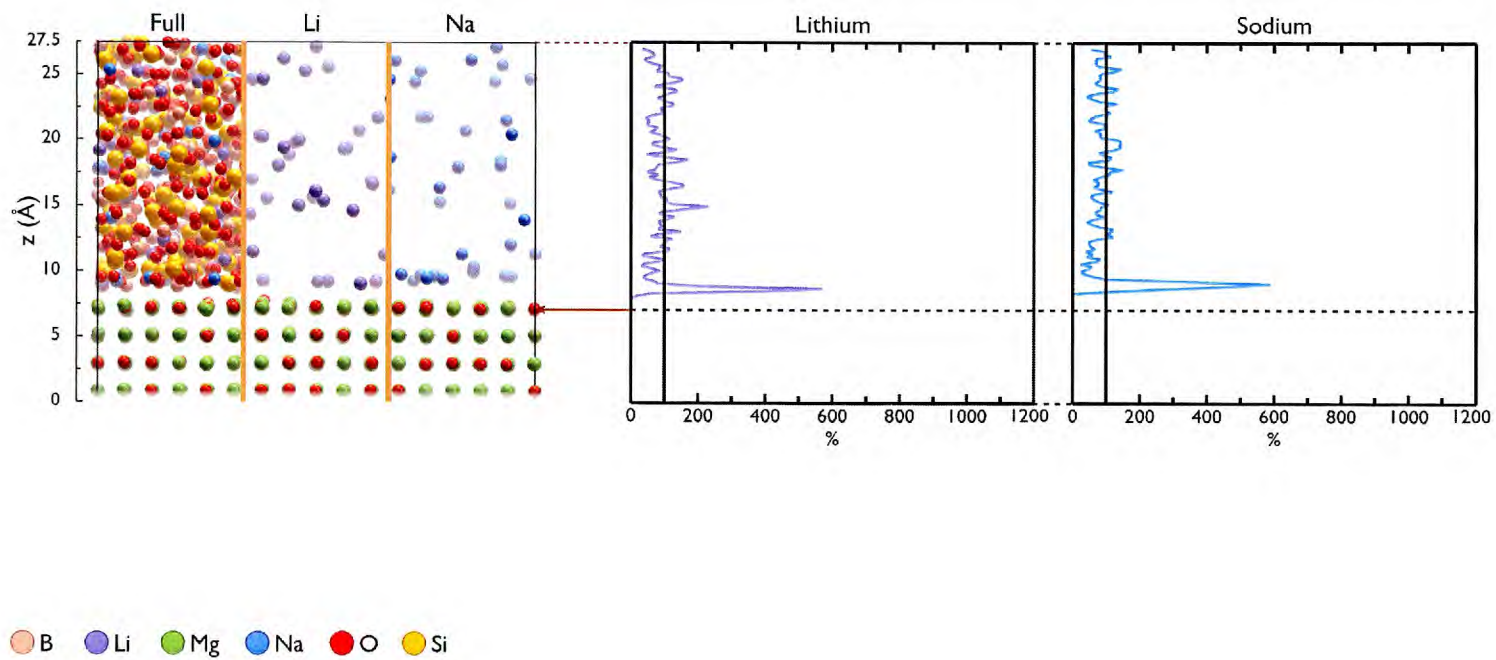
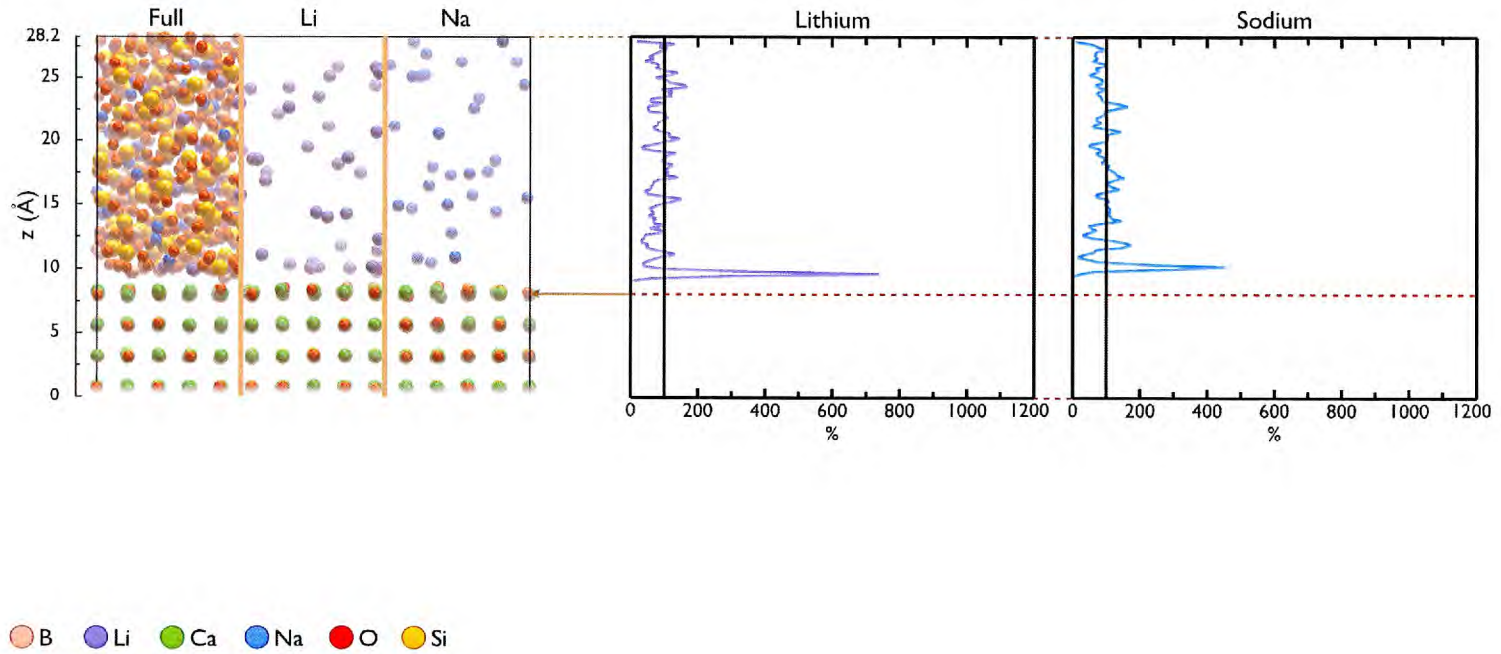Figure 4.17: Alkali Concentration Profile: MW MgO-(100).

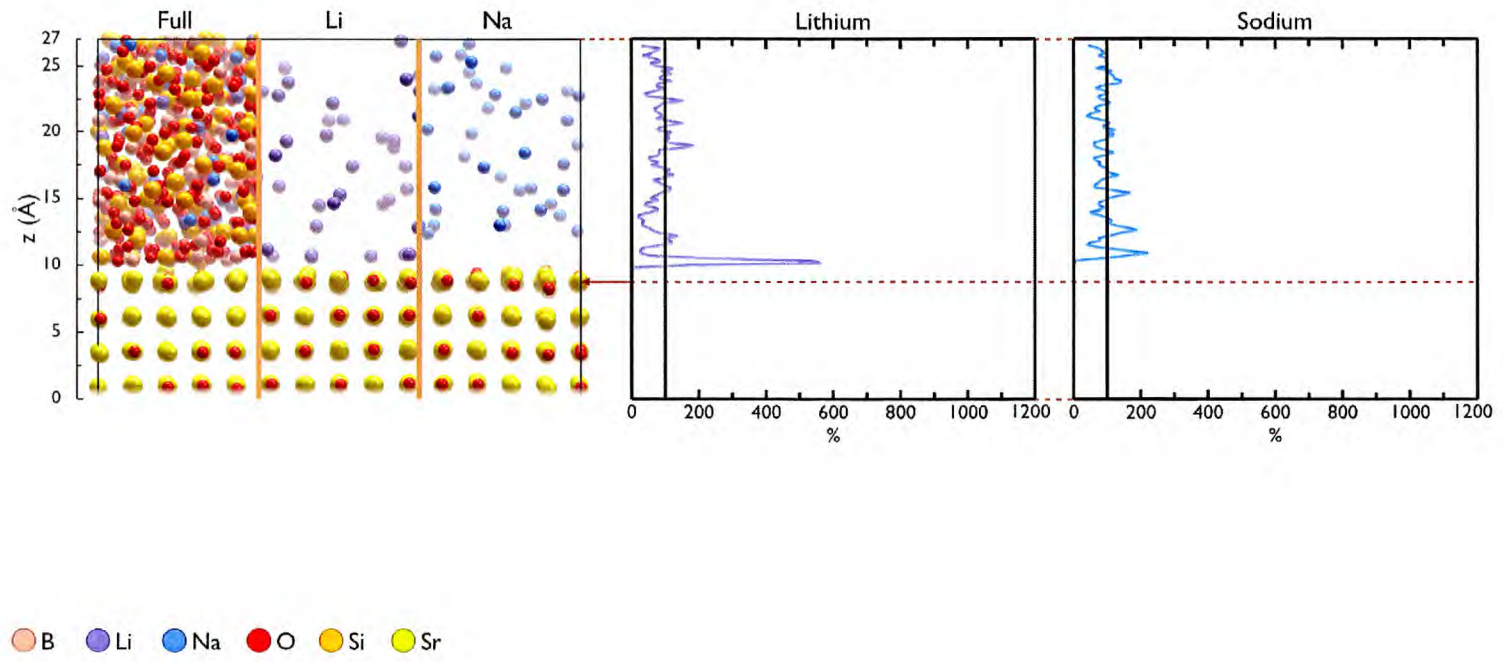Figure 4.18: Alkali Concentration Profile: MW glass CaO-(100).

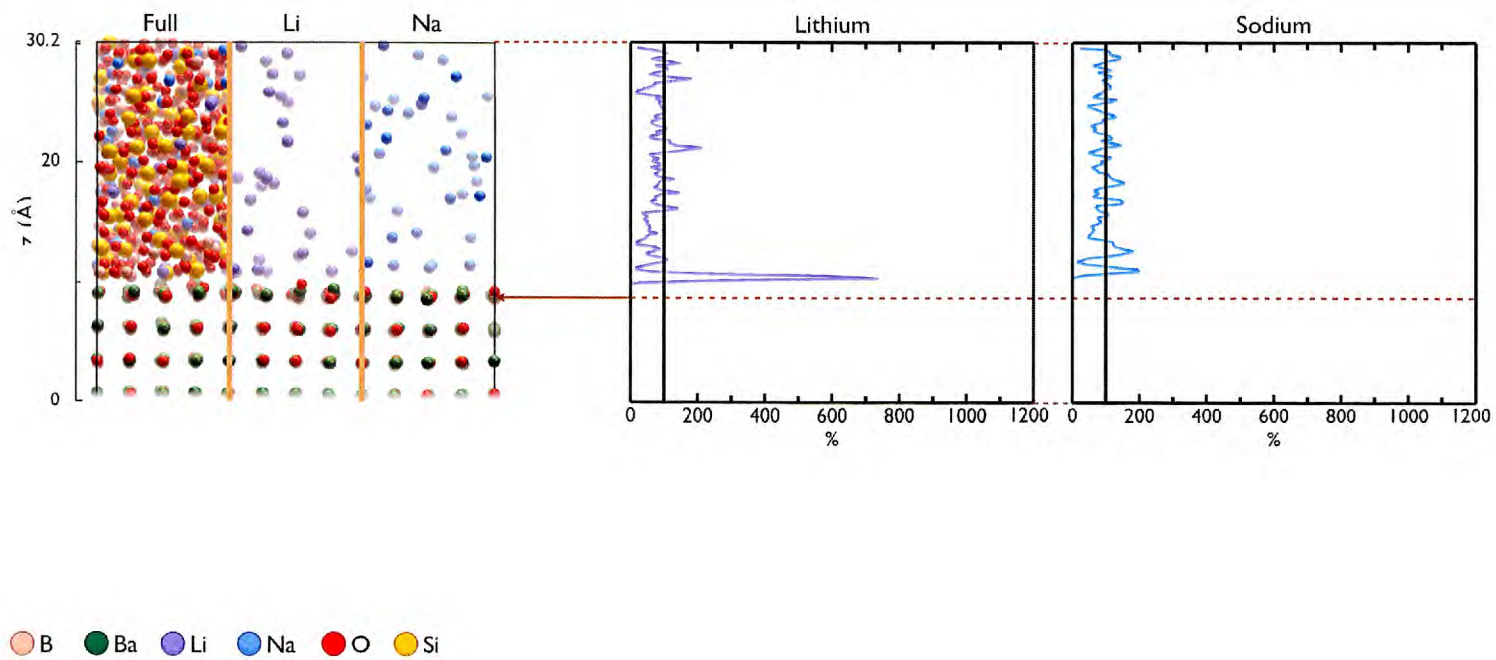Figure 4.19: Alkali Concentration Profile: MW glass SrO-(100).

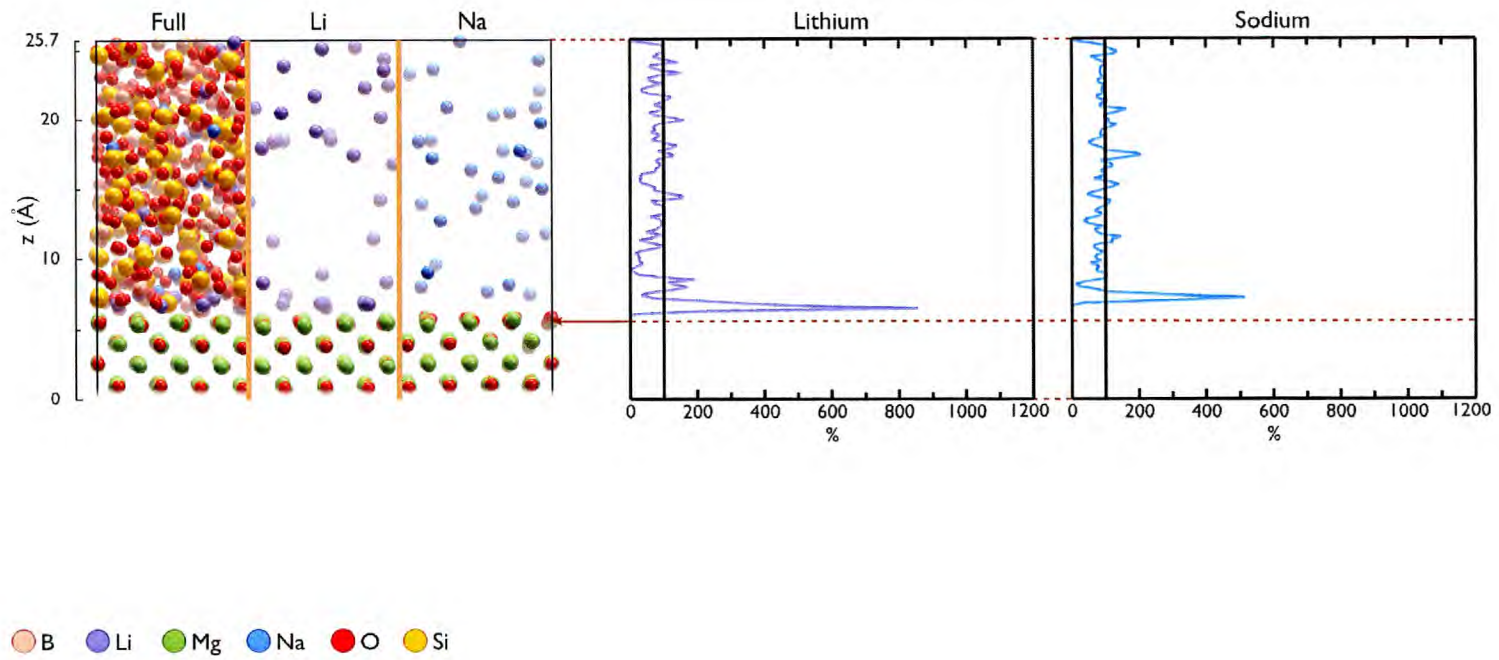Figure 4.20: Alkali Concentration Profile: MW glass BaO-(100).

Figure 4.21: Alkali Concentration Profile: MW glass MgO-(110).
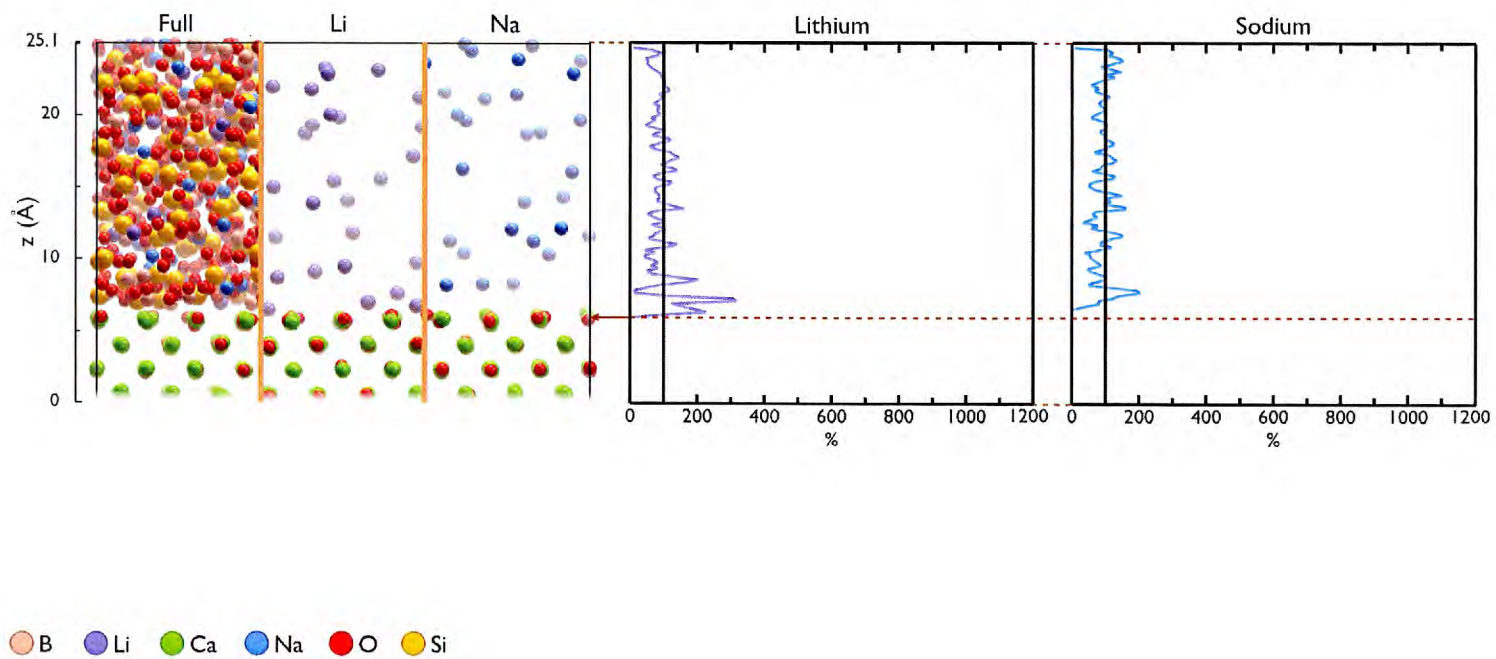
B   Li   Ca   Na   O   Si

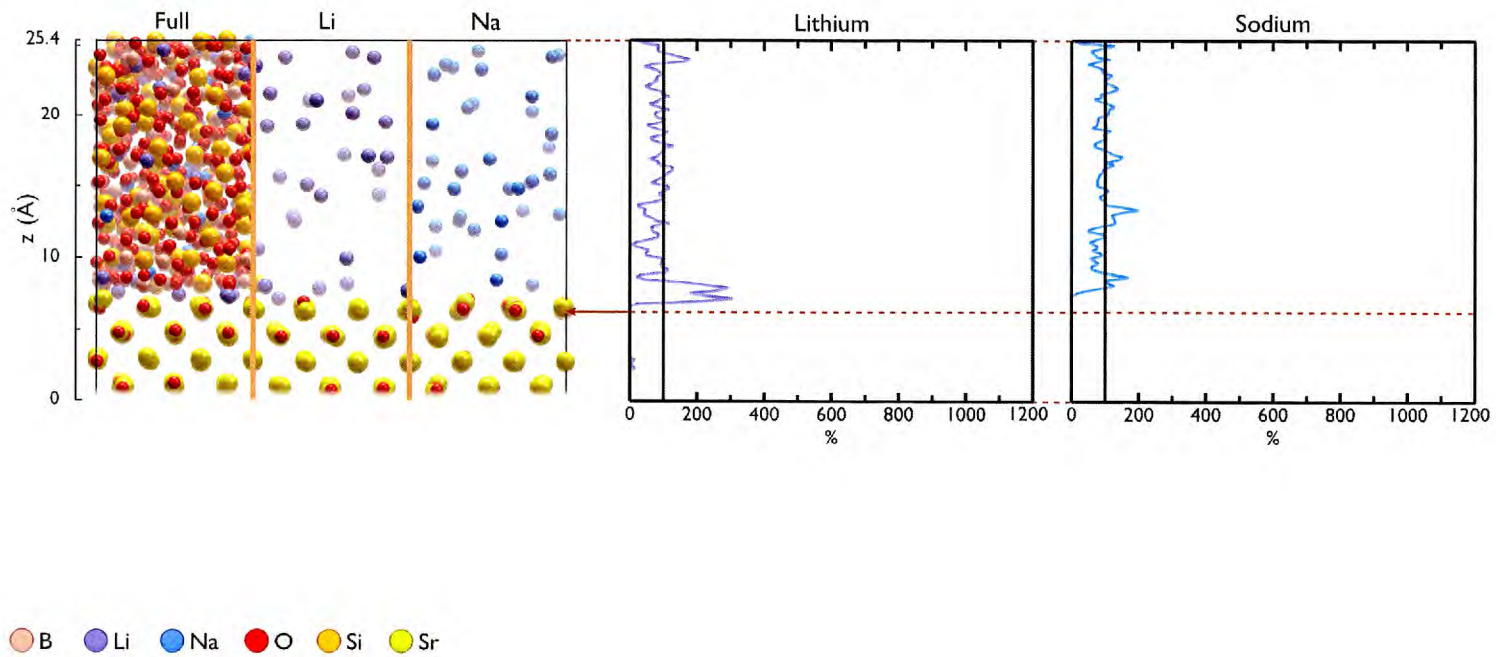Figure 4.22: Alkali Concentration Profile: MW glass CaO-(110).

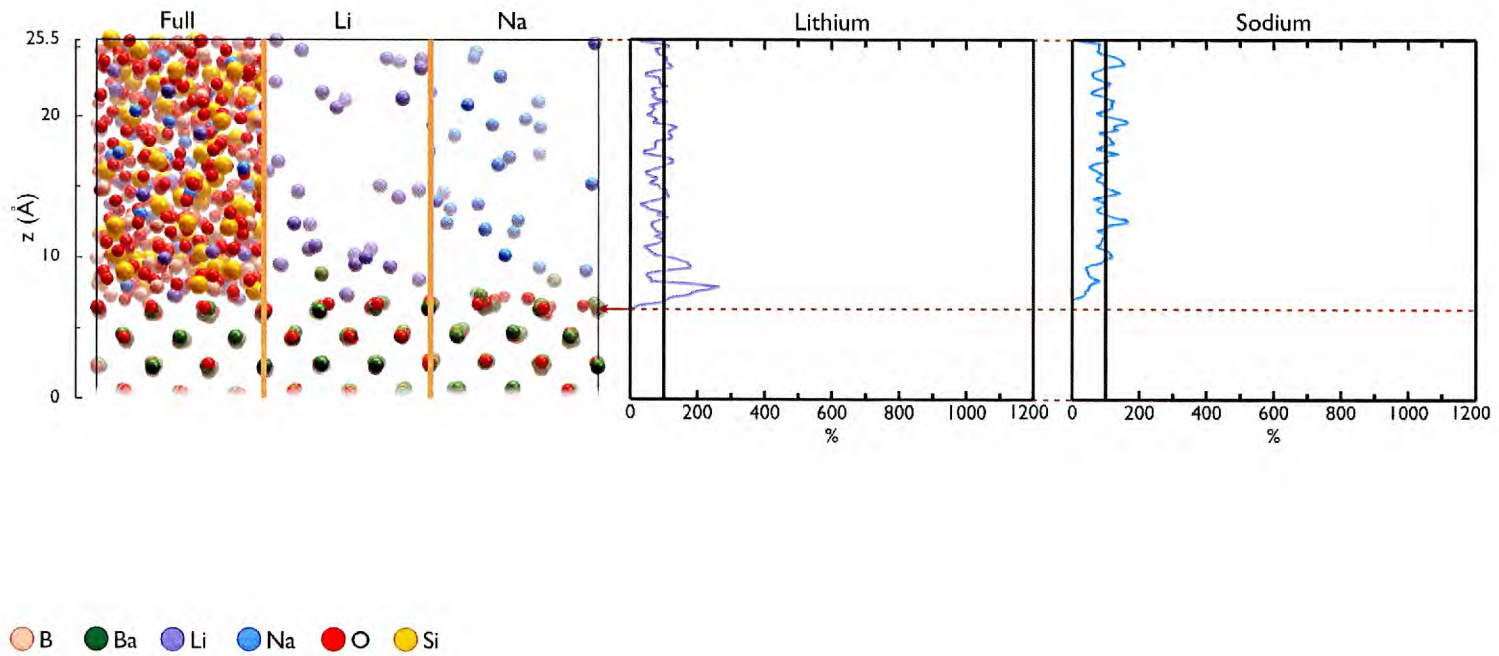Figure 4.23: Alkali Concentration Profile: MW glass SrO-(110).

Figure 4.24: Alkali Concentration Profile: MW glass BaO-(110).
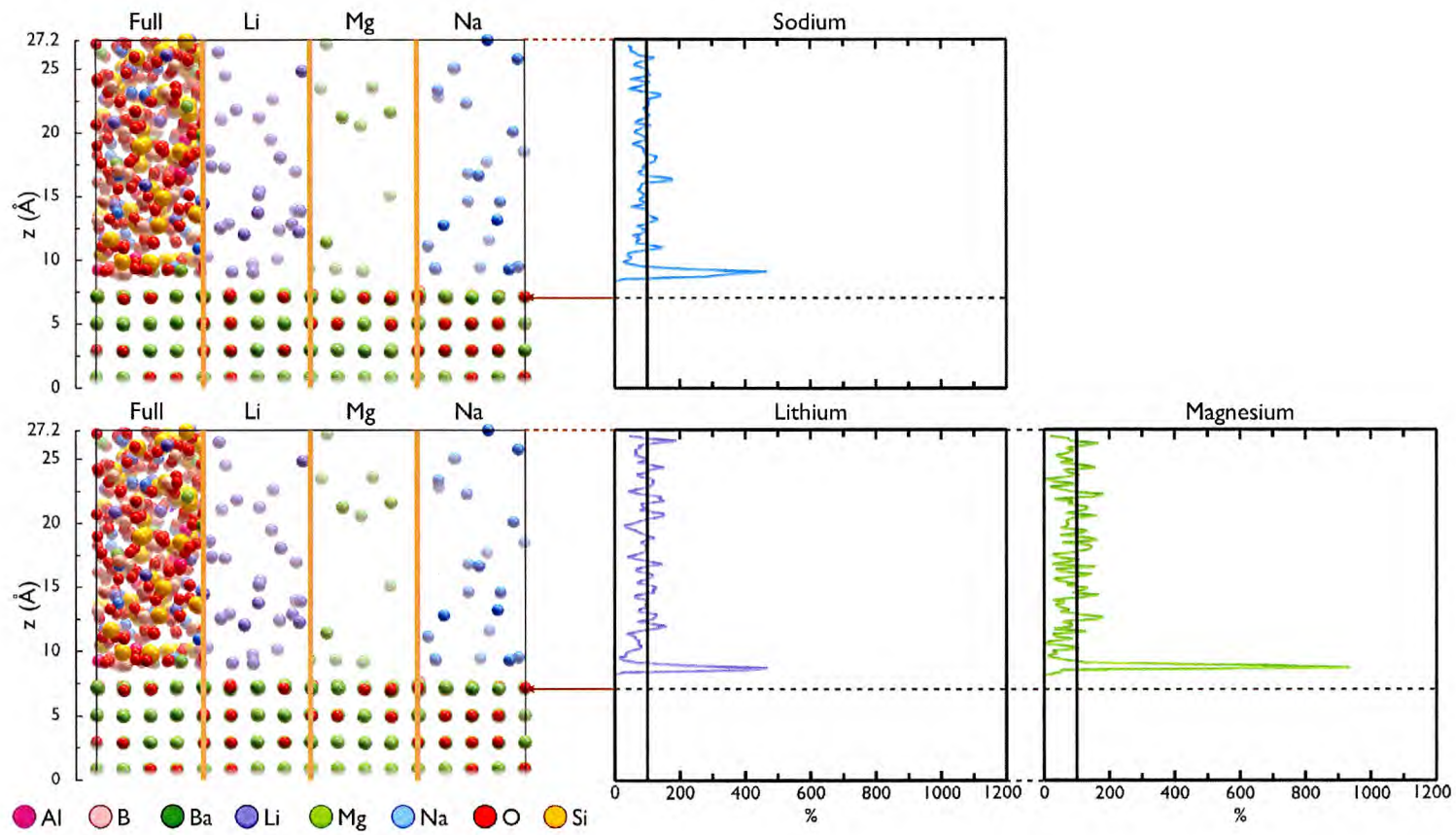
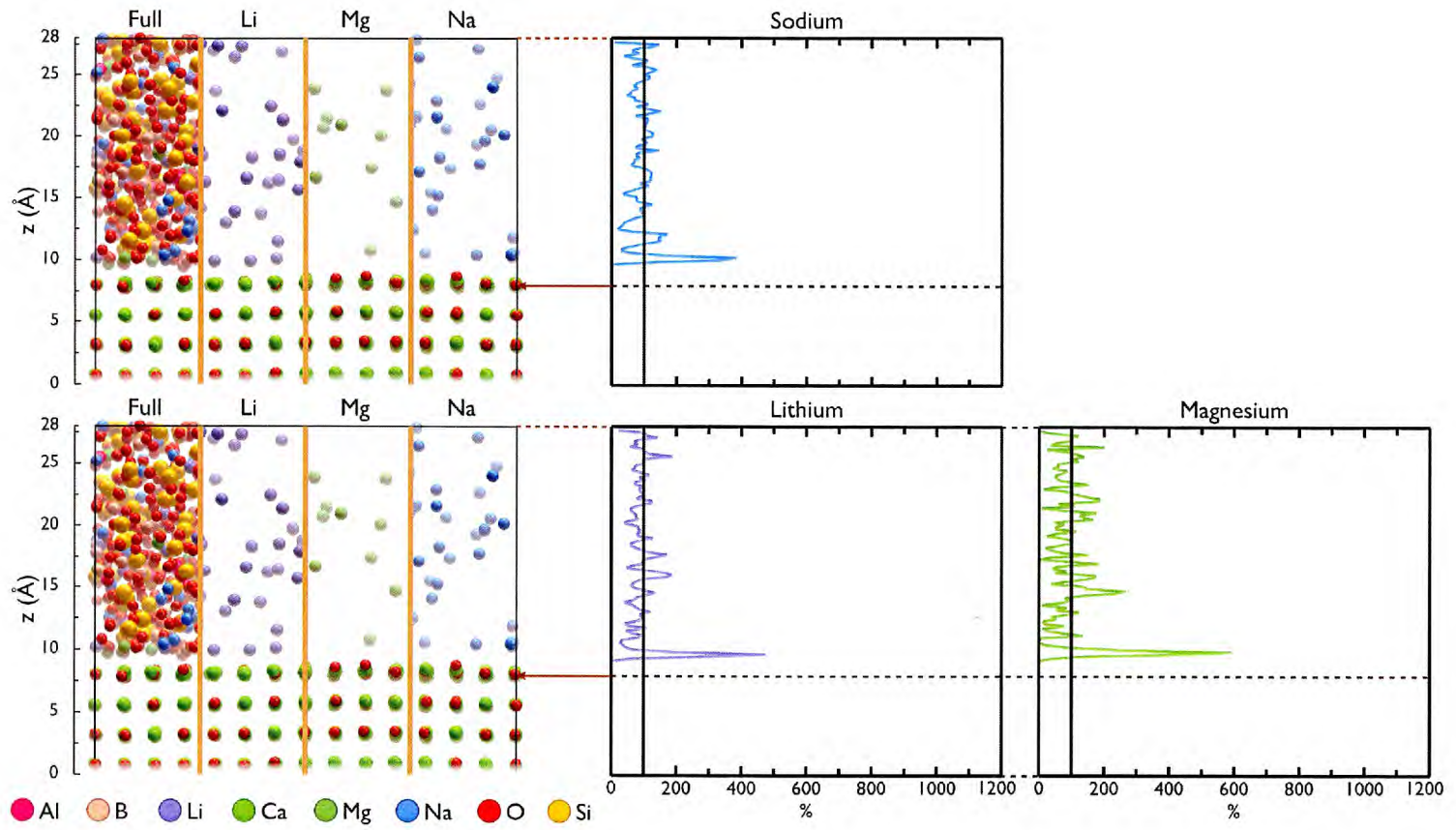Figure 4.25: Alkali Concentration Profile: MW+Al+Mg glass MgO-(100).

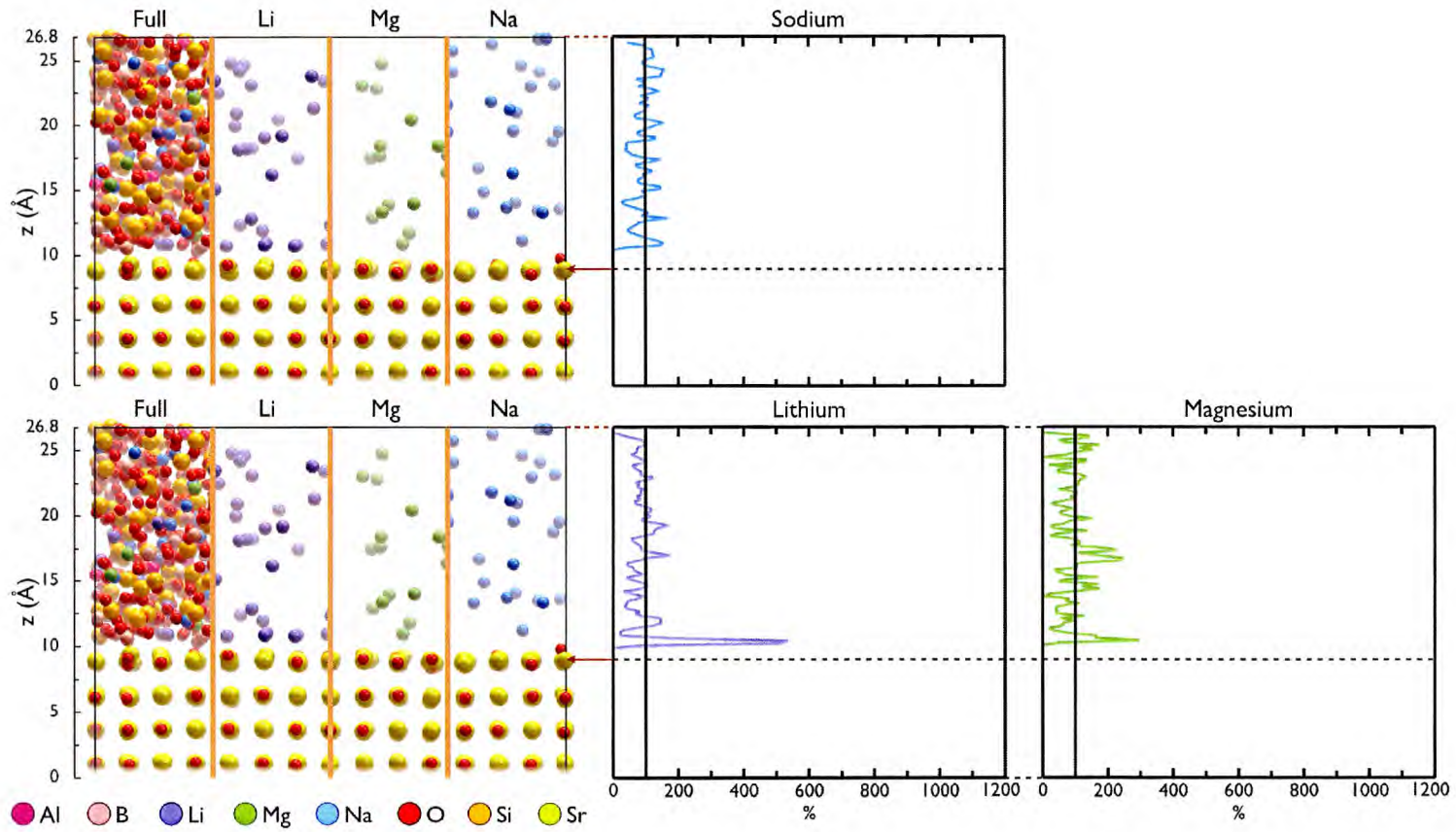Figure 4.26: Alkali Concentration Profile: MW+Al+Mg glass CaO-(100).

Figure 4.27: Alkali Concentration Profile: MW+Al+Mg glass SrO-(100).
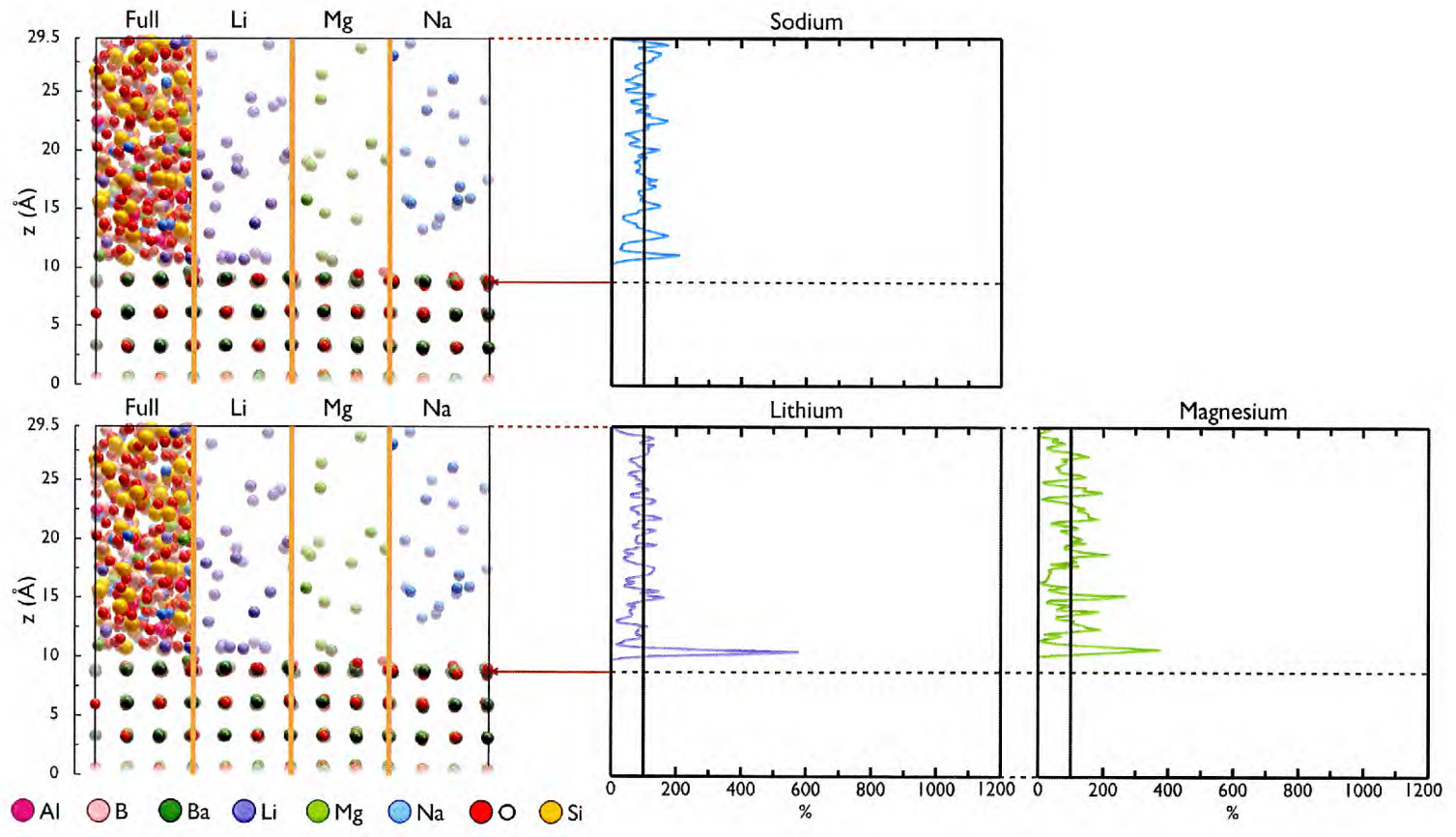
Figure 4.28: Alkali Concentration Profile: MW+Al+Mg glass BaO-(100).

4.5.3   Position of Alkali Ions at Interface

The density distributions given above have shown the distribution of alkali atoms as a function of their distance from the interface. Their positions relative to different crystallographic sites in the ceramic surface are now considered. For each interface, surface concentration maps were generated which highlight the correspondence between particular crystallographic sites in the surface of the ceramic block and different species in the glass. Before going on to discuss the results obtained from these diagrams the details of their construction are described.

Construction of Surface Density Maps

On the whole, the top layer of the ceramic blocks in the interfacial systems remained flat and maintained periodicity (see section 4.4). This meant that the cation sites in the top layer of each ceramic block could be considered as crystallographically equivalent. This convenient property allows alkali atom positions to be expressed relative to the position of cation sites in the ceramic surface.

In each map, black represents areas of high concentration whereas low concentrations are shown as white. For example, if a surface concentration map shows a black spot above the ceramic's anion site for sodium atoms, this would indicate that sodium atoms were associated with ceramic anions. In effect the maps give a plan view of the most probable sites for the alkali atoms adjacent to the ceramic surface.

The position of each glass atom was calculated relative to each cation in the top layer of the ceramic block. Surface concentrations were then calculated using a two dimensional binning procedure. Using a grid with a $0.1 \times 0.1 \text{Å}$ resolution, the number of atoms sitting over each grid cell was calculated. A greyscale plot was then made to show the density calculated for each cell. The data was normalised, so that the areas with the highest concentration appeared black in the final diagram. Positions were expressed relative to the surface repeat unit, meaning that not only were the results obtained by averaging over the simulations equilibration period, but also by averaging over the entire area of the ceramic block's upper and lower surfaces. In

each case, the maps shown below were obtained from a 5Å slice of glass immediately above the top layer of each interfacial system's ceramic block.

Surface Density Maps for (100) Interfaces

Maps for the interfaces between MW glass and the (100) surface of MgO, CaO, SrO and BaO are given in figures 4.29, 4.30, 4.31 and 4.32 respectively.

All the maps show the same basic alkali distribution. In all cases, including maps for the SiO_2+Na, SiO_2+Na+Li and MW+Al+Mg glasses, the regions of high alkali concentration correspond with the position of oxygen atoms in the ceramic's surface; as expected, the positively charged alkali ions are localised above the ceramic's negatively charged anions.

Each atom in the bulk of the rocksalt structure is coordinated by six other atoms. An atom sitting at the (100) surface is only coordinated by five atoms, as there is no layer of atoms above it, there is a potential cation site to be occupied. In effect each atom in the ceramic's surface is under-coordinated. The strong association between alkali atoms and ceramic anions demonstrated by the surface concentration maps suggests that alkali atoms at the glass-ceramic interface helped satisfy the coordination sphere of the atoms in the ceramic surface. By sitting close to the negatively charged anions, this would also help the alkali atoms to reduce the electrostatic contribution to their potential energy.

Figure 4.29: Density plot of alkali species above interface of MW-glass with (100) surface of MgO (view down z-axis).

Figure 4.30: Density plot of alkali species above interface of MW-glass with (100) surface of CaO (view down *z*-axis).
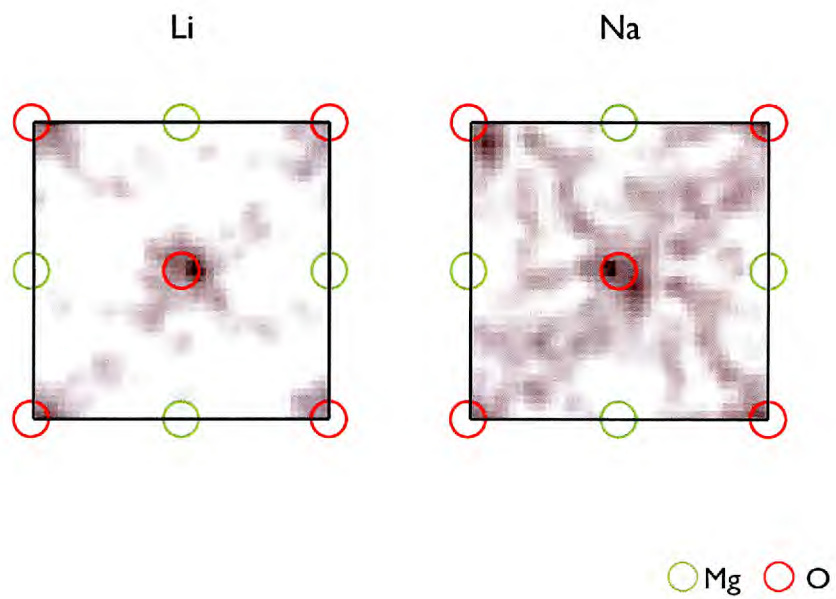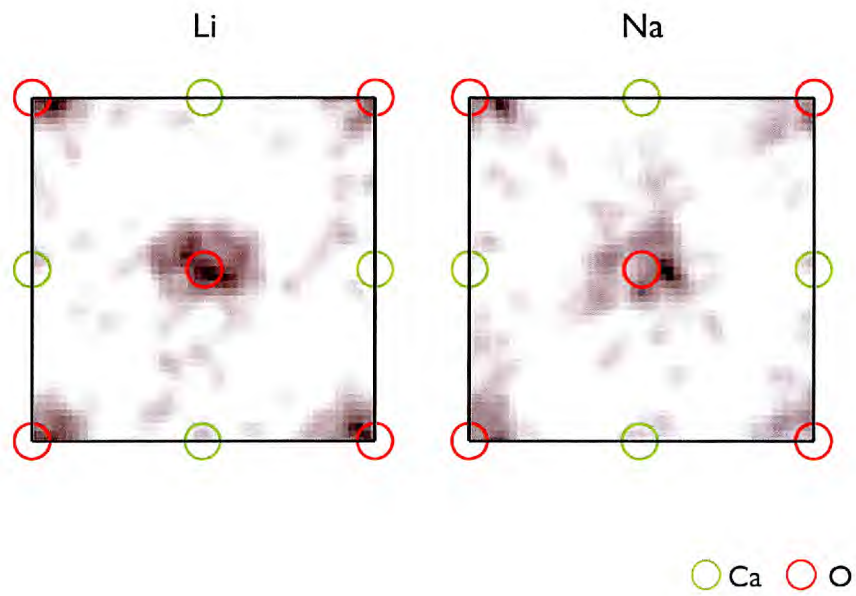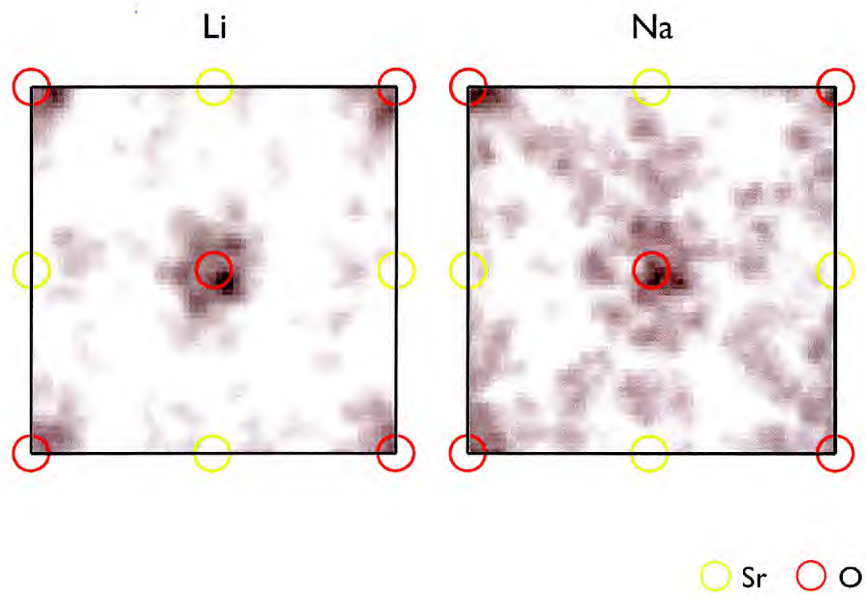
Figure 4.31: Density plot of alkali species above interface of MW-glass with (100) surface of SrO (view down z-axis).
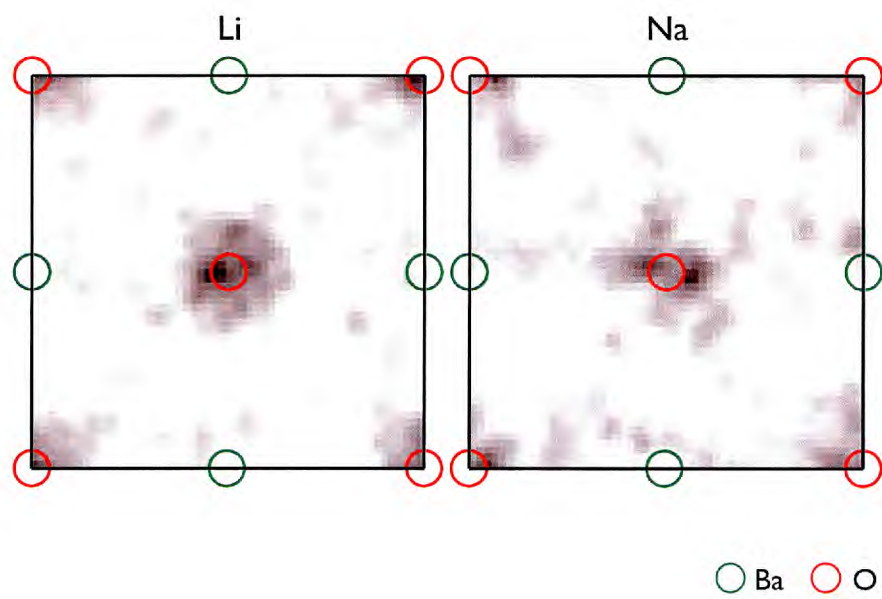
Figure 4.32: Density plot of alkali species above interface of MW-glass with (100) surface of BaO (view down *z*-axis).

Surface Density Maps for (110) Interfaces

Surface density maps were also prepared for the alkali atoms at the (110) interfaces considered. Maps for interfaces made with the MW glass are shown in figures 4.33, 4.34, 4.35 and 4.36, for the MgO, CaO, SrO and BaO ceramics.

At the (100) interfaces, alkali atoms sat directly above anion sites in the ceramic surface. This was not the case for the (110) interfaces considered. Examination of the surface concentration maps for the MW glass, MgO-(110) interface (figure 4.33) shows dark spots, equidistant between two anions in the ceramic's top layer and directly above cations in the second layer of the ceramic. Using the terminology introduced earlier (in section 4.4.3) this position can be described as lying directly above furrows in the ceramic surface. Both Li and Na maps showed regions of high concentration in this region. The surface maps for the (110) interfaces for CaO, SrO and BaO, showed distributions similar to that of the MgO interface.

The surface concentration maps for the alkali species at the MW glass, MgO-(110) ceramic interface is particular striking (see figure 4.33). In comparison to the maps for equivalent (110) interfaces between MW glass and CaO, SrO and BaO, the regions of high alkali density are more tightly localised over the cation site from the second layer of the ceramic block. The positions occupied by the alkali atoms above this surface, therefore correspond to what would be ceramic cation sites, if another layer was added to the ceramic block. This indicates that, at the MW glass, MgO-(110) ceramic interface, the glass adjacent to the interface may have been structurally similar to a layer in the rocksalt structure.

Figure 4.33: Density plot of alkali species above interface of MW-glass with (110) surface of MgO, dashed circles show position of atoms in second layer of ceramic block (view down *z*-axis).

Figure 4.34: Density plot of alkali species above interface of MW-glass with (110) surface of CaO, dashed circles show position of atoms in second layer of ceramic block (view down *z*-axis).

Figure 4.35: Density plot of alkali species above interface of MW-glass with (110) surface of SrO, dashed circles show position of atoms in second layer of ceramic block (view down *z*-axis).
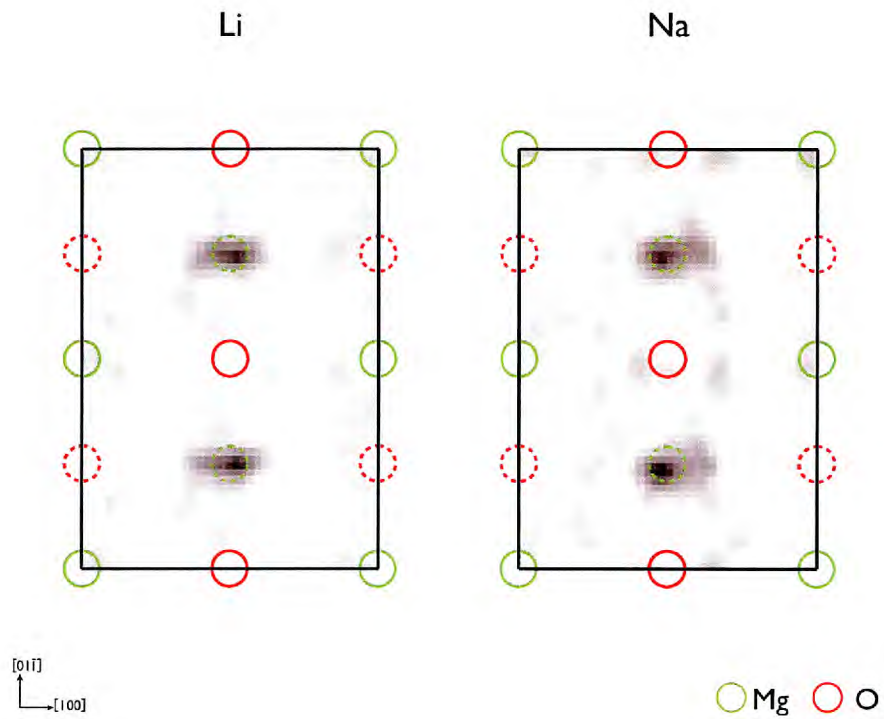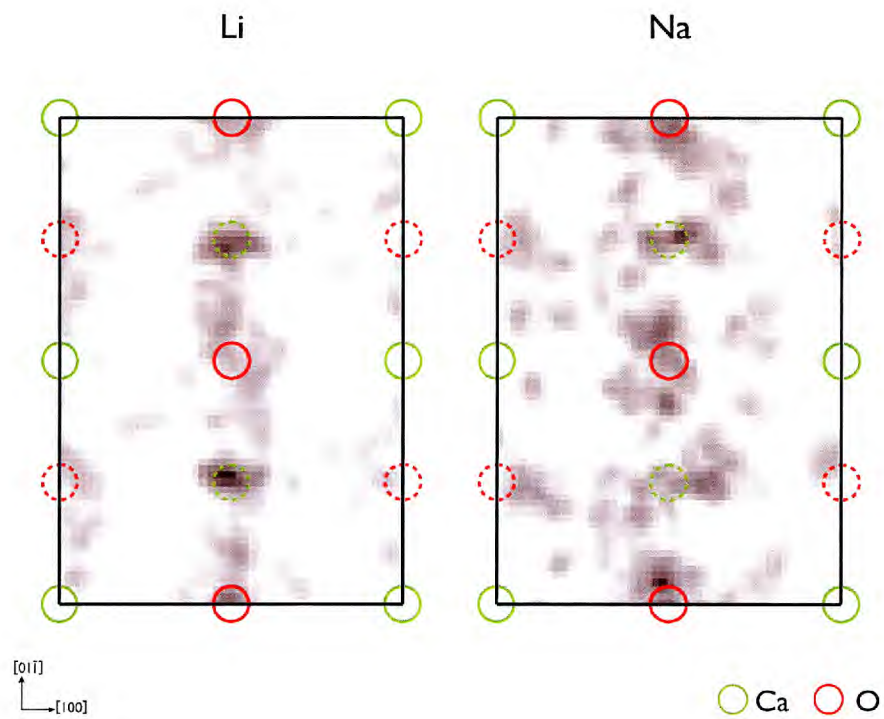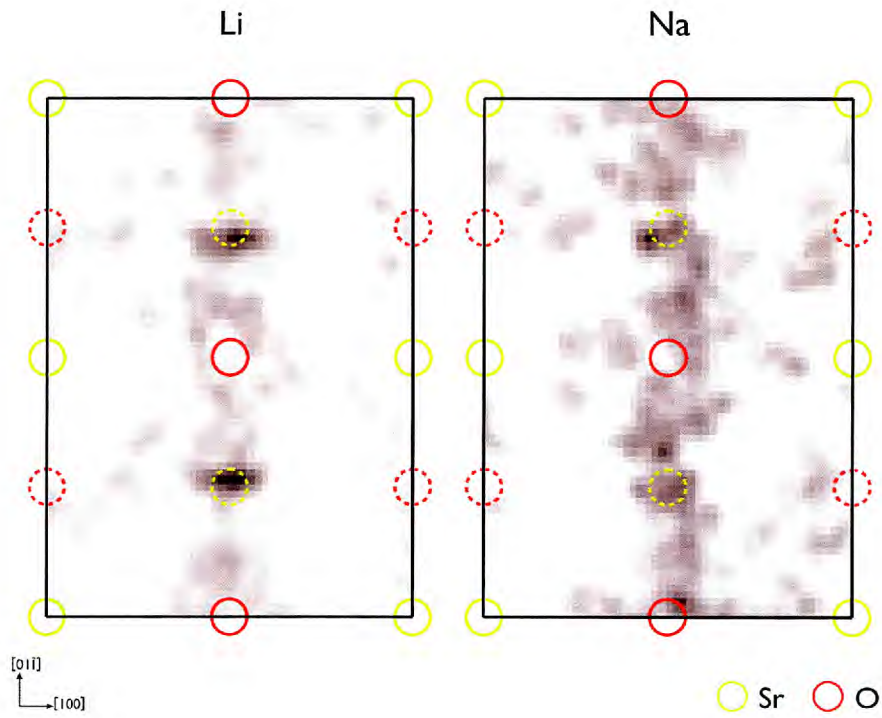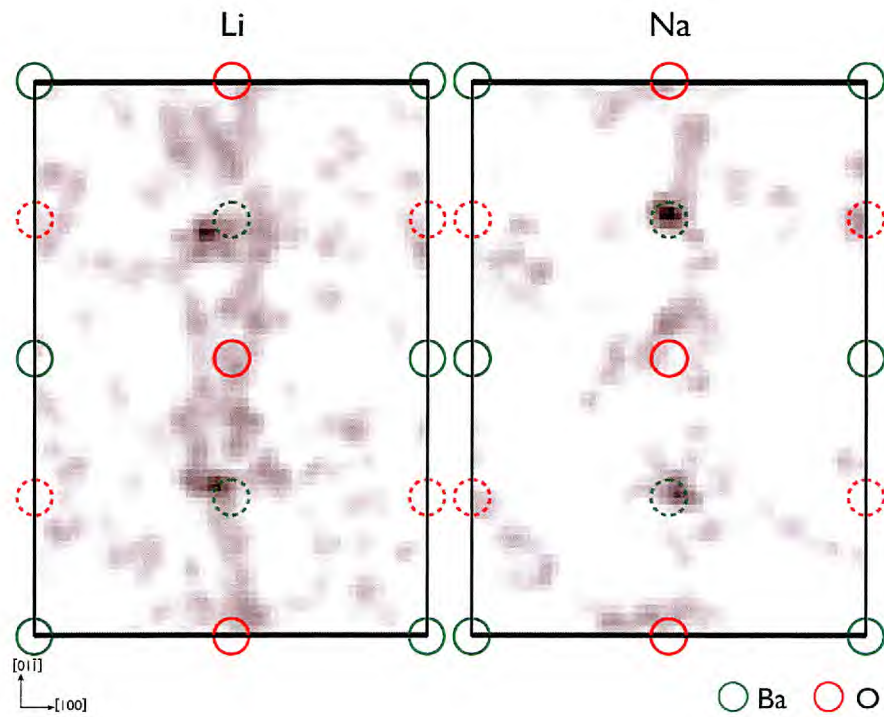
Figure 4.36: Density plot of alkali species above interface of MW-glass with (110) surface of BaO, dashed circles show position of atoms in second layer of ceramic block (view down z-axis).

4.5.4 Discussion of Changes to Alkali Distribution

The results presented above showed that the alkali concentration in these glasses increased towards the ceramic surface. At interfaces with (100) ceramic surfaces, alkali atoms sat in sites directly above oxygen atoms in the surface. By comparison most alkali atoms at the (110) interfaces sat between surface anions (sometimes close to positions that would have accommodated cations if the ceramic had continued). In the following section, possible reasons for the behaviour of alkali atoms at glass-ceramic interfaces are discussed.

Comparison with Free Surfaces

The alkali distribution at the surface of a glass, equilibrated with a vacuum, bears certain similarities to that observed for glass-ceramic interfaces during the current work.

Abbas *et al.* [67] performed molecular dynamics simulations to determine the concentration of alkali atoms as a function of distance from the vacuum surfaces of a mixed alkali aluminoborosilicate nuclear waste glass. The method they used generated surfaces which were similar to freshly fractured glass surfaces (i.e. interactions with the environment such as hydroxylation had not yet taken place). The results of their study showed an increased concentration of alkali atoms (Ca^{2+} and Na^+) at the surface of the glass.

At a glass fracture surface, oxygen atoms that would normally bridge two structural units might only be connected to a single silicon or boron atom. In addition network forming silicon and boron atoms may be under-coordinated. Abbas *et al.* [67] explained the movement of modifier atoms to the glass surface as follows: modifiers moved out of their role stabilising NBOs and went to stabilise under-coordinated oxygen atoms at the glass' surface. This was found to have the additional effect of forming an alkali depleted zone to a depth of 4Å beneath the surface.

It seems likely that alkali atoms must move towards glass-ceramic interfaces for the same sort of reasons that they move towards free surfaces. In effect, a glass-interface with a ceramic represents a discontinuity in the glass network (and indeed the bulk structure of the ceramic phase) in the same way that a surface does. The response of the ceramic and glass near an

interface can therefore be considered as an attempt by both components to mitigate the effects of the interface. Alkali atoms at the interface could act to charge compensate anions in both the glass and ceramic phase adjacent to the interface. In so doing they could also allow the coordination environment of atoms in the ceramic surface to mimic that found in the ceramic's bulk.

Effects of Ceramic Surface on Interface Alkali Concentration

In general, alkali concentration at the interface was found to decrease as ceramic cation radius increased. Alkali concentration was also lower at (110) interfaces with MW glass than the (100) surfaces. It is likely that the concentration differences between the various ceramic surfaces can be related to the density of sites in the ceramic surface.

The lattice parameters for MgO, CaO, SrO and BaO were found to be 4.17, 4.83, 5.15 and 5.54 Å from static energy minimisation calculations. As these compositions all share the same structure, the density of atoms (per unit area) at their (100) surfaces is: $\frac{4}{c^2}$. The increase in lattice parameter (c) from MgO to BaO means that the number of anion sites in the ceramic surface, with which alkali atoms in the glass can interact decreases. This means that fewer alkali atoms were required to charge compensate sites in the ceramic surface.

A similar explanation might account for the difference in alkali concentration between (100) and (110) interfaces. The number of sites, per unit area, in the top layer of the the (110) ceramic blocks can be expressed as: $\frac{4}{\sqrt{2}c^2}$. There are $\sqrt{2}$ times more atomic sites at the (100) surface than the (110) surface. For the reasons described above, this could help account for the lower alkali concentration at (110) interfaces.

Given that the (100) surface contained $\sqrt{2}$ times more sites than (110) over the same area, it might be expected that the concentration of alkali atoms at (100) interfaces would also be $\sqrt{2}$ times higher than those at the equivalent (110) interface. This was not the case. With the exception of the MW glass MgO interfaces, the ratio was found to be somewhat higher (for instance a value of around 2.3 was found for the MW CaO interfaces). A possible reason for this difference could be due to the position of alkali atoms at the (110) interface, where, rather

than being associated with a single ceramic site, they tended to sit above a furrow between two anions. This might account for why alkali concentration was lower than expected at the (110) surface. In addition, it is likely that the ability of alkali ions to reach sites in the ceramic surface is affected by the response of the glass network to the ceramic interface.

Peak Positions

The order in which alkali concentration peaks occurred at the interface was found to be consistent for all the interfaces considered. In systems with glasses containing Li and Na, the lithium peak was always closer to the interface than the sodium peak. In MW+Al+Mg glasses (which had Na, Li and Mg as modifiers) the order was Li, Mg then Na (as shown for the interface of MW+Al+Mg and CaO-(100) in figure 4.37). This ordering seems to scale with the size of the different alkali species. The Shannon [118] VI coordinate radii for Li, Mg and Na are 0.72, 0.76 and 1.02 Å respectively. These show that, when moving away from the interface, the peaks occurred in order of increasing alkali radius.

The ability of smaller ions to sit closer to the interface may suggest a reason for the concentration difference between Na and Li at the interfaces considered. In general, Li concentration was higher than Na (with the exception of the MW glass MgO-(100) interface). The number of ceramic anion sites with which alkali atoms could associate, was limited. Competition for this limited number of sites could help account for the lower Na concentration at the interface. The smaller Li ions could get closer to the interface, meaning that the available ceramic sites were preferentially occupied by Li at the expense of Na. Saturation of the surface by Li could account for the lack of distinct peaks in the Na distributions of SrO and BaO at interfaces with the MW glass.

Alkali Depletion

In previous work [67] it was observed that alkali atoms moved into charge compensating roles at the free surface of a glass. This led to the formation of an alkali depleted zone just below the surface. A similar effect was observed here for the glass ceramic interfaces.
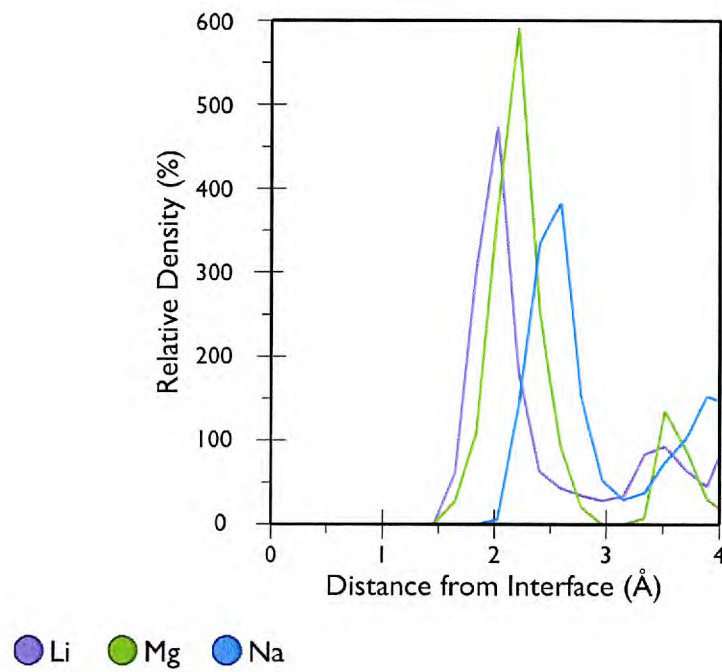
Figure 4.37: Region close to the interface of MW+Al+Mg glass and CaO-(100). This shows that peaks occurred in modifier size order when moving away from interface.
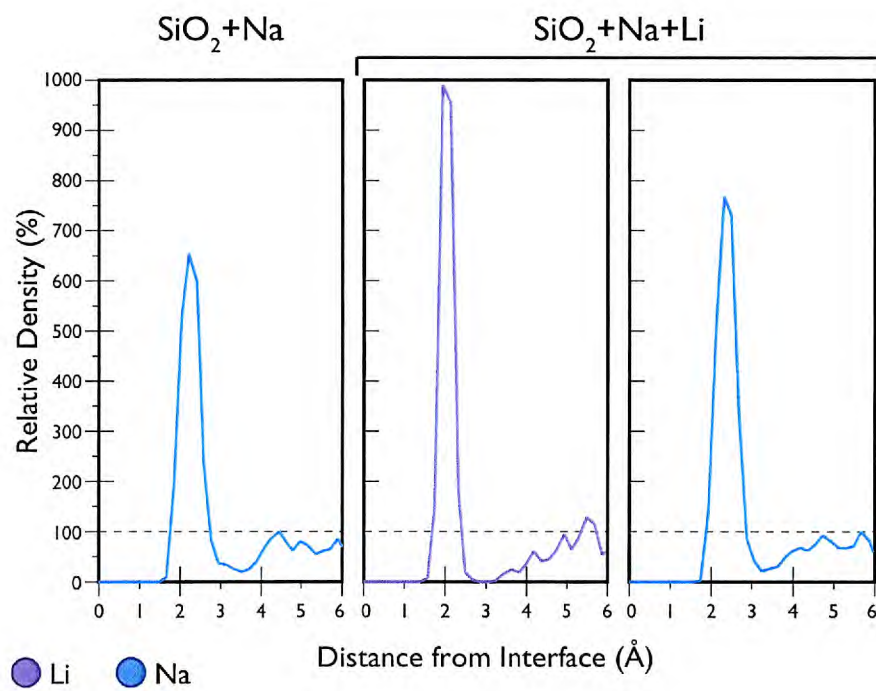
Figure 4.38: Alkali distribution close to the interfaces of SiO_2+Na and SiO_2+Na+Li with MgO-(100). Behind the initial peak a region of low alkali concentration existed.

Alkali depletion was most noticeable at the interfaces between the silicate, SiO_2+Na and SiO_2+Na+Li glasses and the MgO-(100) ceramic. The concentration profiles for these interfaces are given in figure 4.38. In both cases, the Na concentration dropped to below 50% of its level in the bulk glass in a region extending for distances between 2.8 and 4Å from the interface. The depleted region for Li in SiO_2+Na+Li was even more apparent: no Li atoms were found in a region $\sim$ 1Å in breadth, $\sim$ 3Å from the interface. Although not as pronounced as that seen in the silicate glass compositions, depletion of alkali concentration was also observed at the interfaces made with the MW and MW+Al+Mg glasses.

Peak Splitting at (110) Interfaces

Figure 4.39 shows the initial peaks of the Li concentration profiles for interfaces of MgO, CaO and SrO with MW glass. In the case of MgO, the first peak was monolithic, those of CaO and SrO however were double peaks.

The first lithium peak in the MgO-(110) concentration profile sat 1.4 Å away from the interface. The layer spacing of the MgO-(110) block, calculated from a lattice parameter of 4.17 Å would be expected to be 1.5 Å (as layer spacing = $\frac{1}{2\sqrt{2}}c$). In addition, the surface concentration map (figure 4.33) showed that Li atoms sat above cation sites in the second layer of the ceramic block. This is interesting as, if the ceramic structure had continued its cations would have sat at approximately the same position as those occupied by modifier atoms near the interface. In effect, a partially occupied layer of the MgO cation sublattice was formed in the glass.

By comparison, layer spacings of 1.71 and 1.82Å would be expected for the CaO and SrO (110) surfaces. The first of the two Li peaks was only 0.6 Å from the CaO interface and 1.3 Å from the SrO interface. Rather than sitting further from the interface as might be predicted from the increased lattice parameter the Li modifiers sat closer.

Visualisation of each interface revealed that Li atoms sitting above the furrows in the CaO and SrO surfaces were almost level with the plane of the interface, whilst those in the MgO system were well clear of the ceramic's surface. It seems likely that this change in behaviour was due to the increase in inter-ridge spacing between the CaO and MgO structures. It seems that the
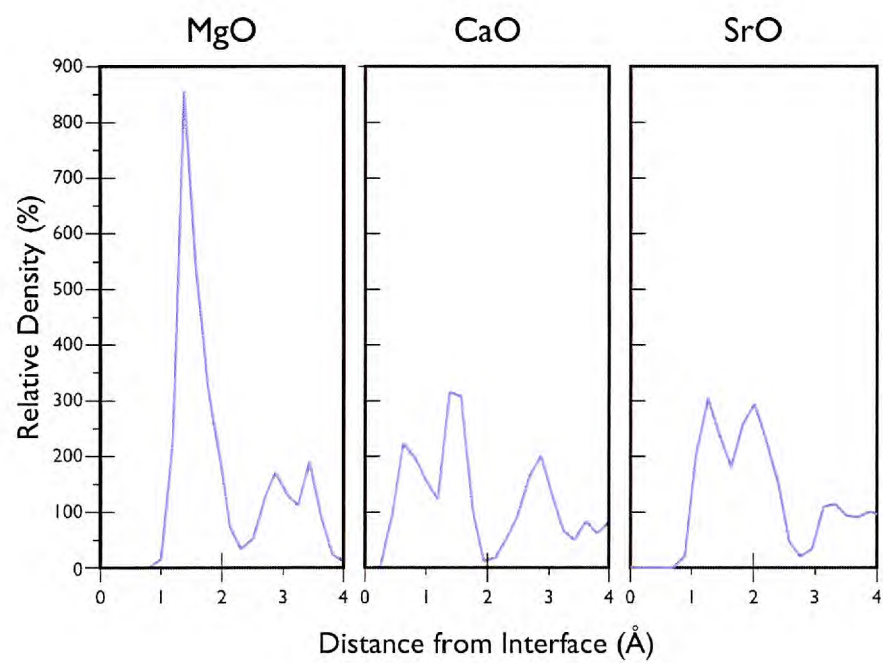
Figure 4.39: The Li peaks nearest to the interface for (110) interfaces with MW glass. The peaks for CaO and SrO showed splitting, this may indicate that Li atoms occupied two distinct environments at these interfaces.

lattice parameter of MgO was too small to provide furrows wide enough to accommodate the Li ions and the its electrostatic field (see section 5.3.1) was sufficient to maintain the observed separation between the modifiers and the ceramic surface. The furrow width in CaO, however, was sufficiently wide to accommodate the Li ion allowing the alkali ions to sit closer to the interface.

Concluding Remarks

The creation of an alkali rich layer in the glass near to a glass ceramic interface poses some interesting questions. This layer has the appearance of a partially occupied ceramic cation sublattice layer (as shown by the alkali concentration maps in section 4.5.3). By using the ceramic as a template, the alkali ions became partially ordered and in this way, some of the crystal's periodic nature was imparted to the glass. Although not considered here, this could have implications for devitrification in nuclear wasteforms. It is possible that alkali atoms deeper in the glass could template off the alkali atoms close to the interface, in this way, the ordering imposed by the interface could be propogated through the glass structure encouraging crystallisation. It is possible that an ordered layer would provide pathways for cation migration and reduce wasteform durability.

Chapter 5

Interfacially Induced Changes to Glass Network

In the previous chapter, the distribution of alkali ions at glass-rocksalt interfaces were described. Here, interfacially induced changes to the structure of the glass network adjacent to ceramic interfaces are described.

5.1 Network Former Density Profiles

Density profiles showing the density of network forming species at glass ceramic interfaces were created in the same way as described in section 4.5.2. Again, these are presented with a visualisation of the interfacial system that they represent. To allow particular concentration profiles to be located more easily, table 5.1 is provided.

Glass	Ceramic	Figure
SiO_2	MgO-(100)	5.1, p.156
SiO_2+Na	MgO-(100)	5.2, p.157
SiO_2+Na+Li	MgO-(100)	5.3, p.158
MW	MgO-(100)	5.4, p.159
	CaO-(100)	5.5, p.160
	SrO-(100)	5.6, p.161
	BaO-(100)	5.7, p.162
MW	MgO-(110)	5.8, p.163
	CaO-(110)	5.9, p.164
	SrO-(110)	5.10, p.165
	BaO-(110)	5.11, p.166
MW+Al+Mg	MgO-(100)	5.12, p.167
	CaO-(100)	5.13, p.168
	SrO-(100)	5.14, p.169
	BaO-(100)	5.15, p.170

Table 5.1: Network former density profiles, table of figures.
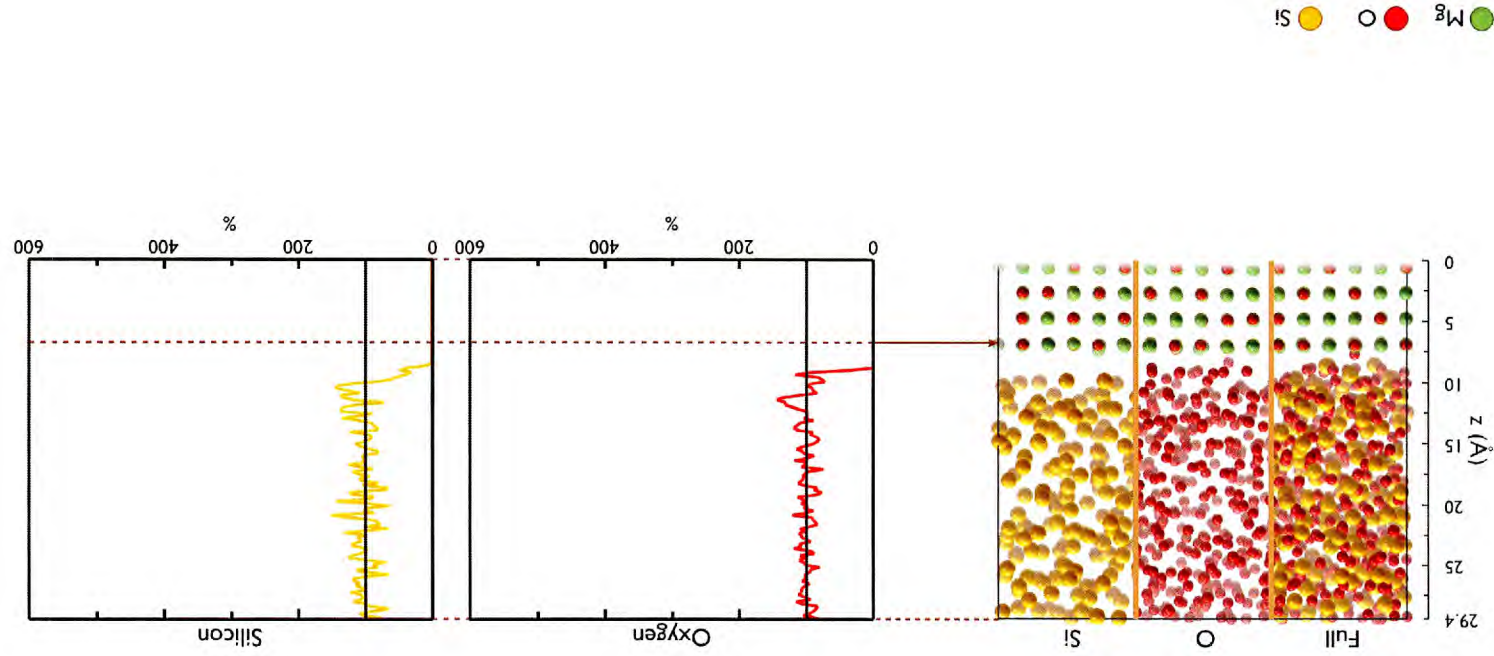
Figure 5.1: Network Former Concentration Profile: SiO_2 MgO-(100).
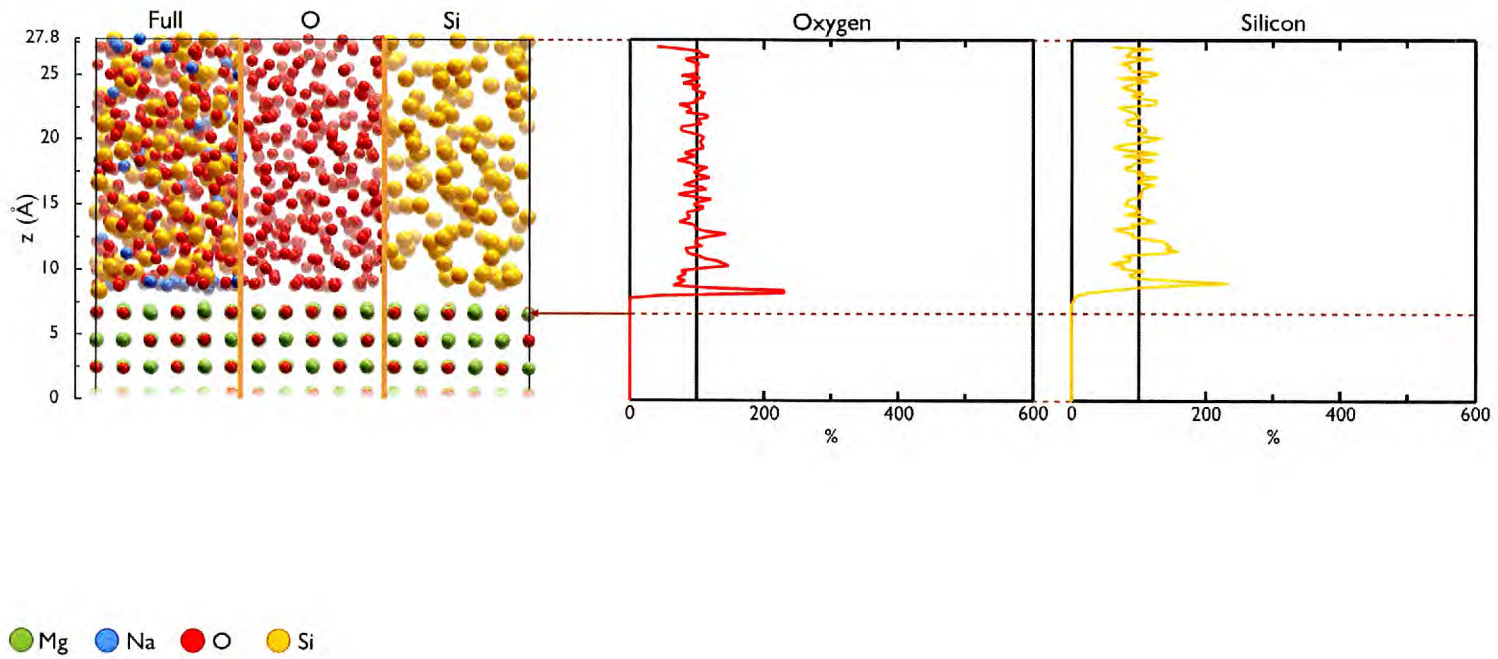
Figure 5.2: Network Former Concentration Profile: SiO_2+Na MgO-(100).
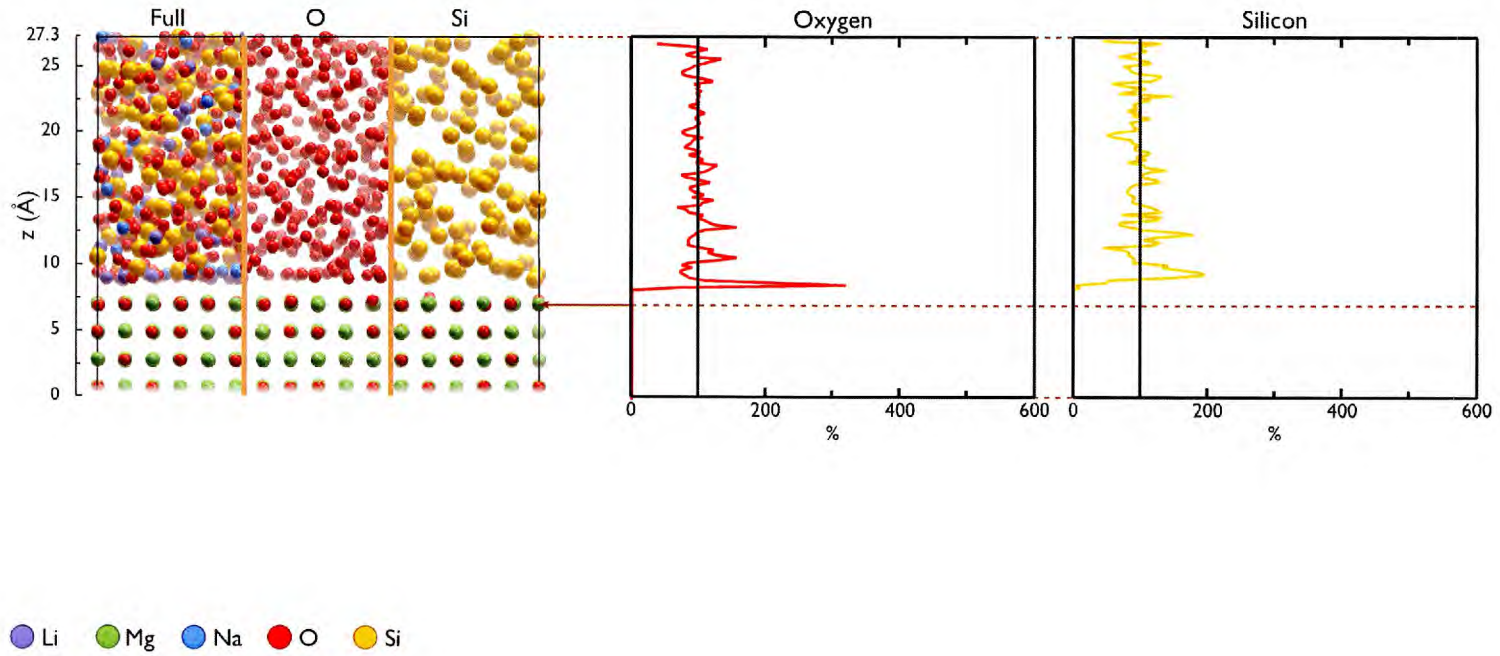
Figure 5.3: Network Former Concentration Profile: SiO_2+Na+Li MgO-(100).
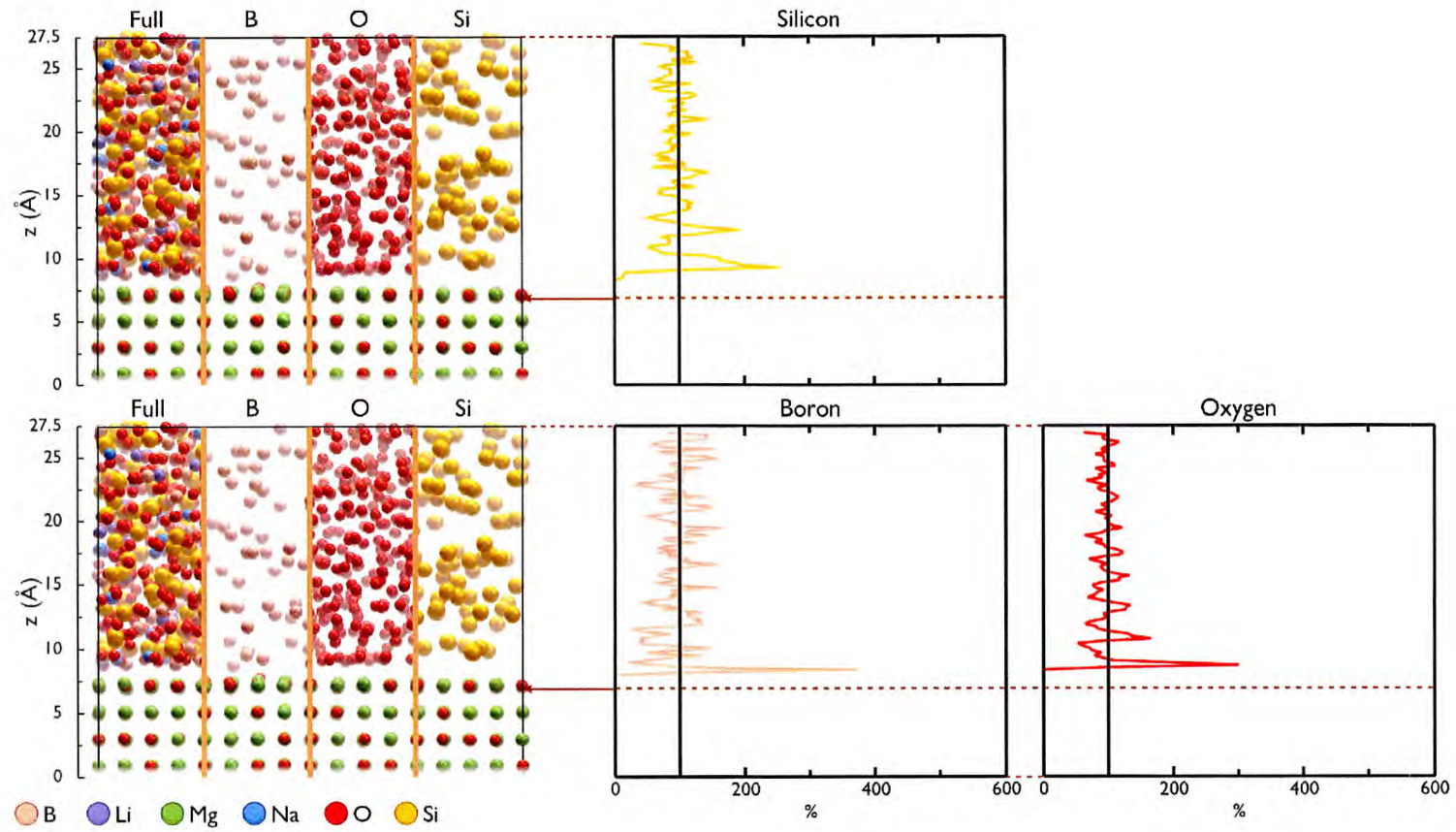
Figure 5.4: Network Former Concentration Profile: MW glass MgO-(100).
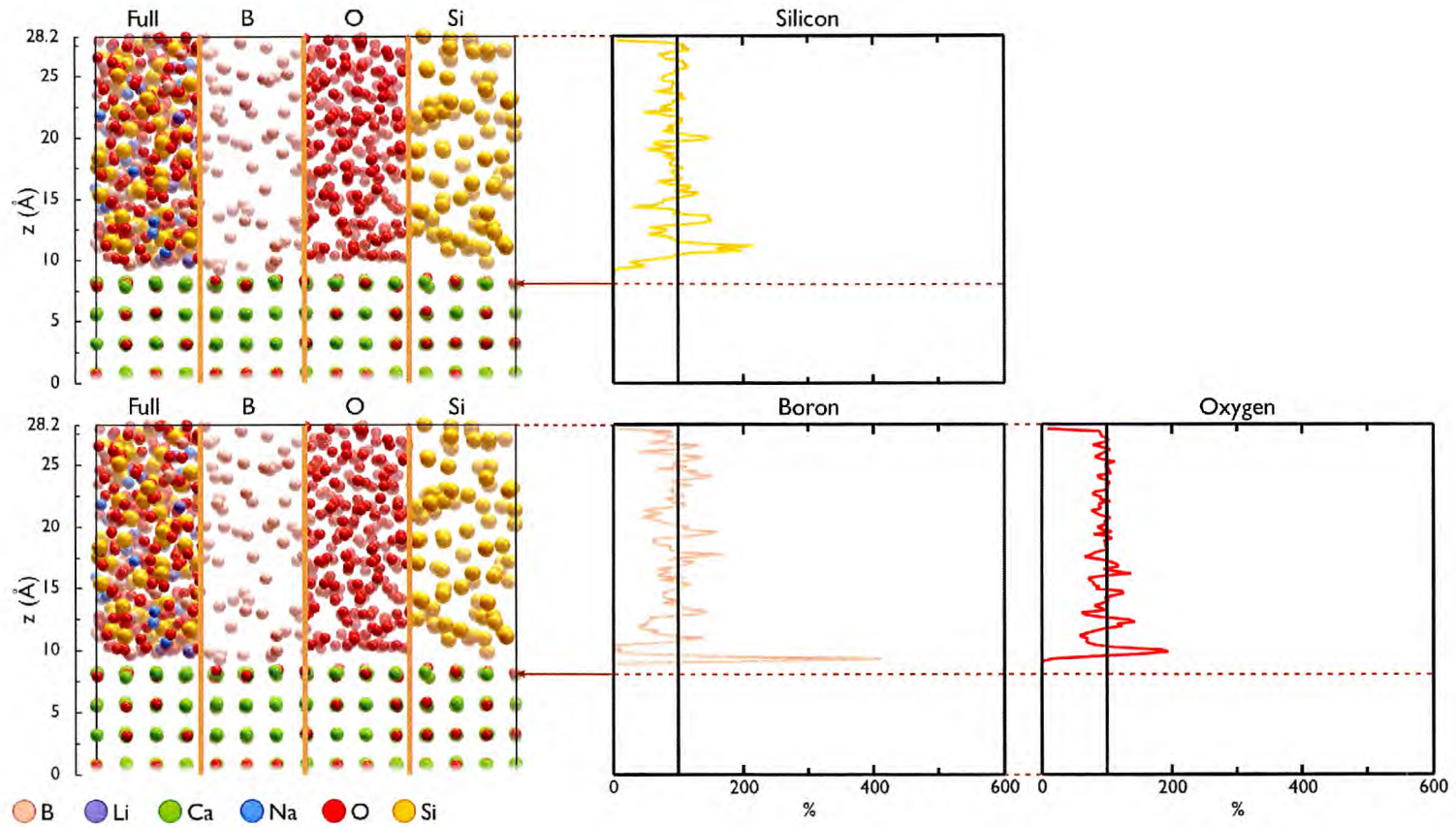
Figure 5.5: Network Former Concentration Profile: MW glass CaO-(100).
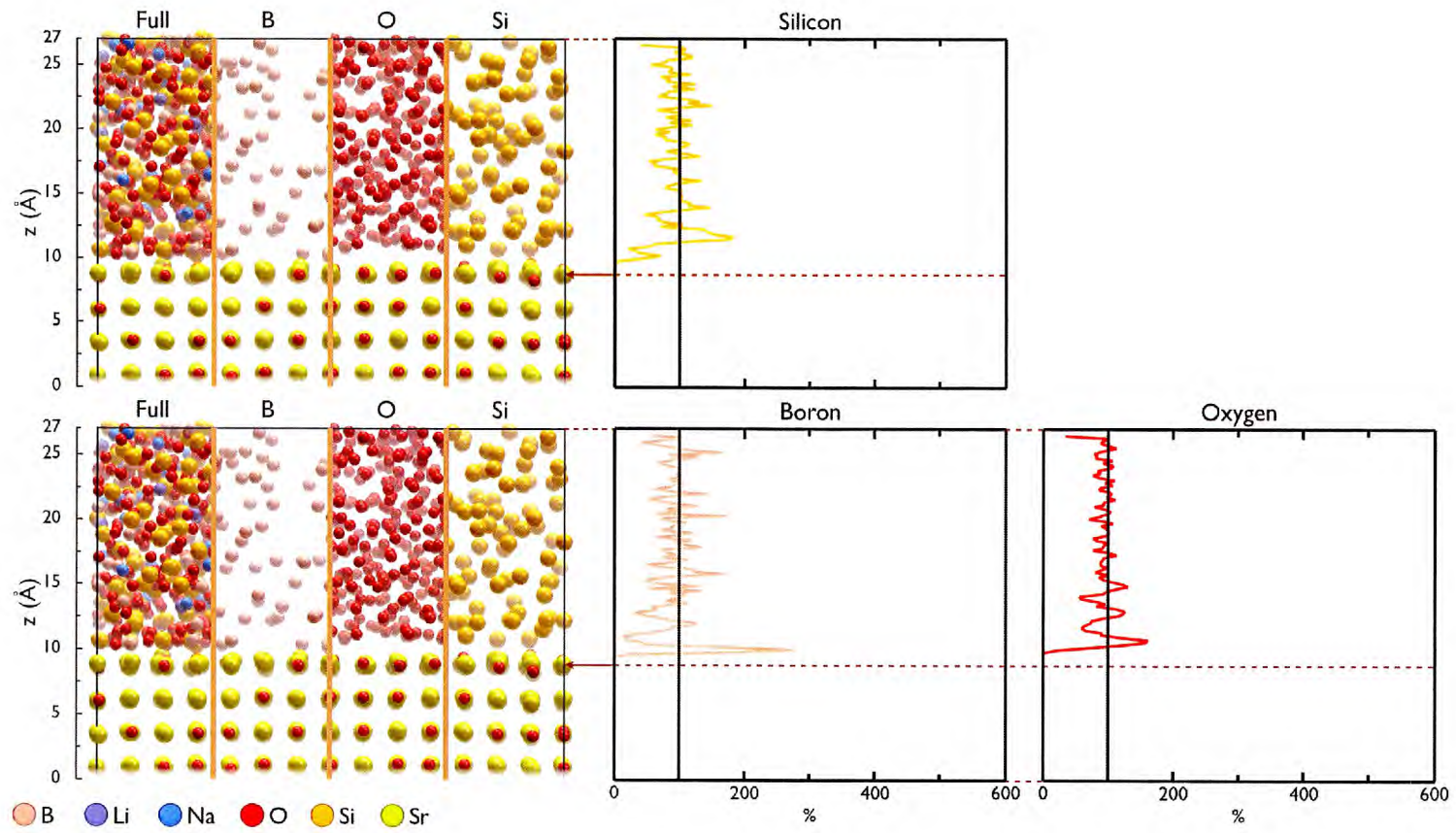
Figure 5.6: Network Former Concentration Profile: MW glass SrO-(100).
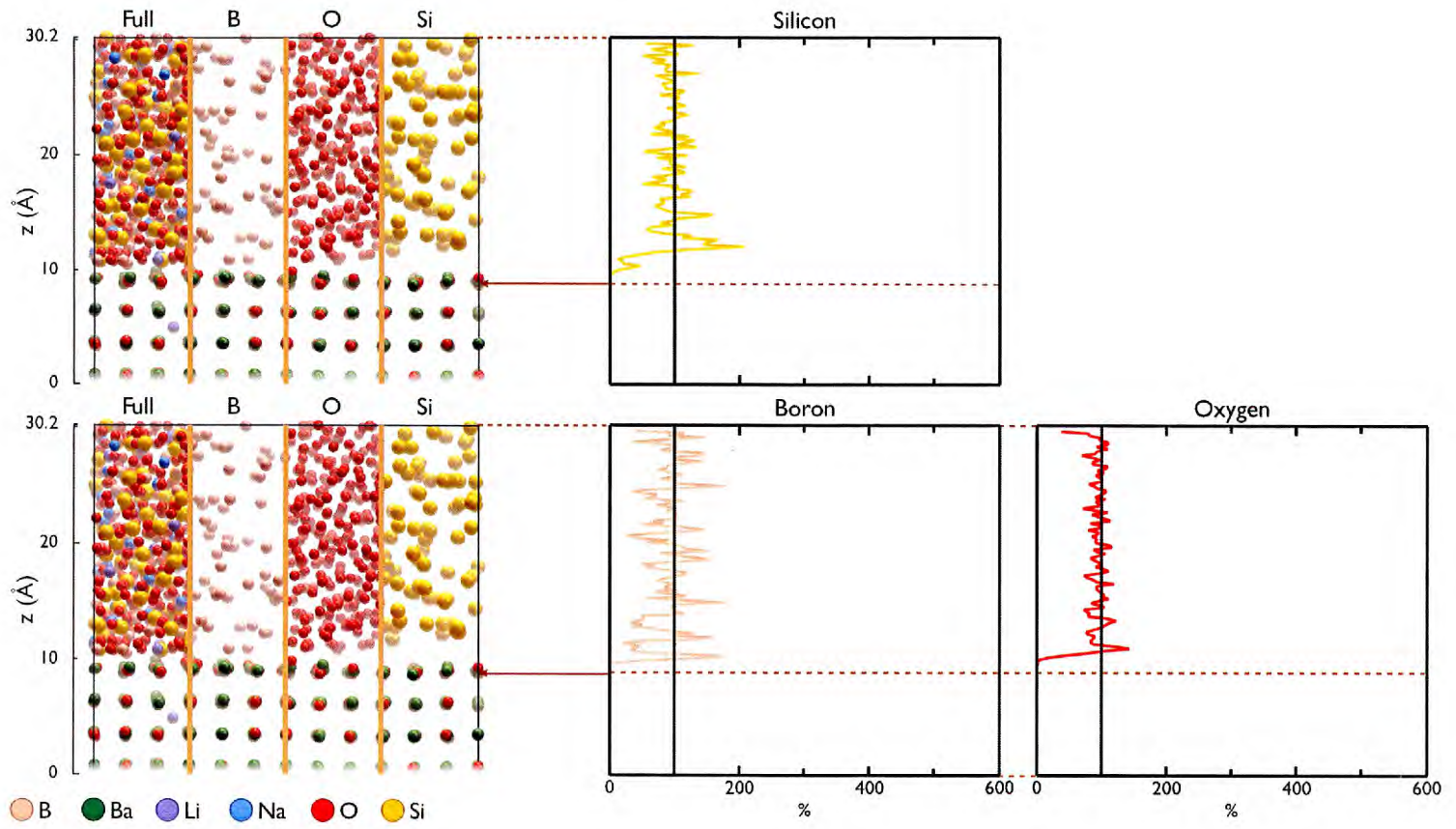
Figure 5.7: Network Former Concentration Profile: MW glass BaO-(100).
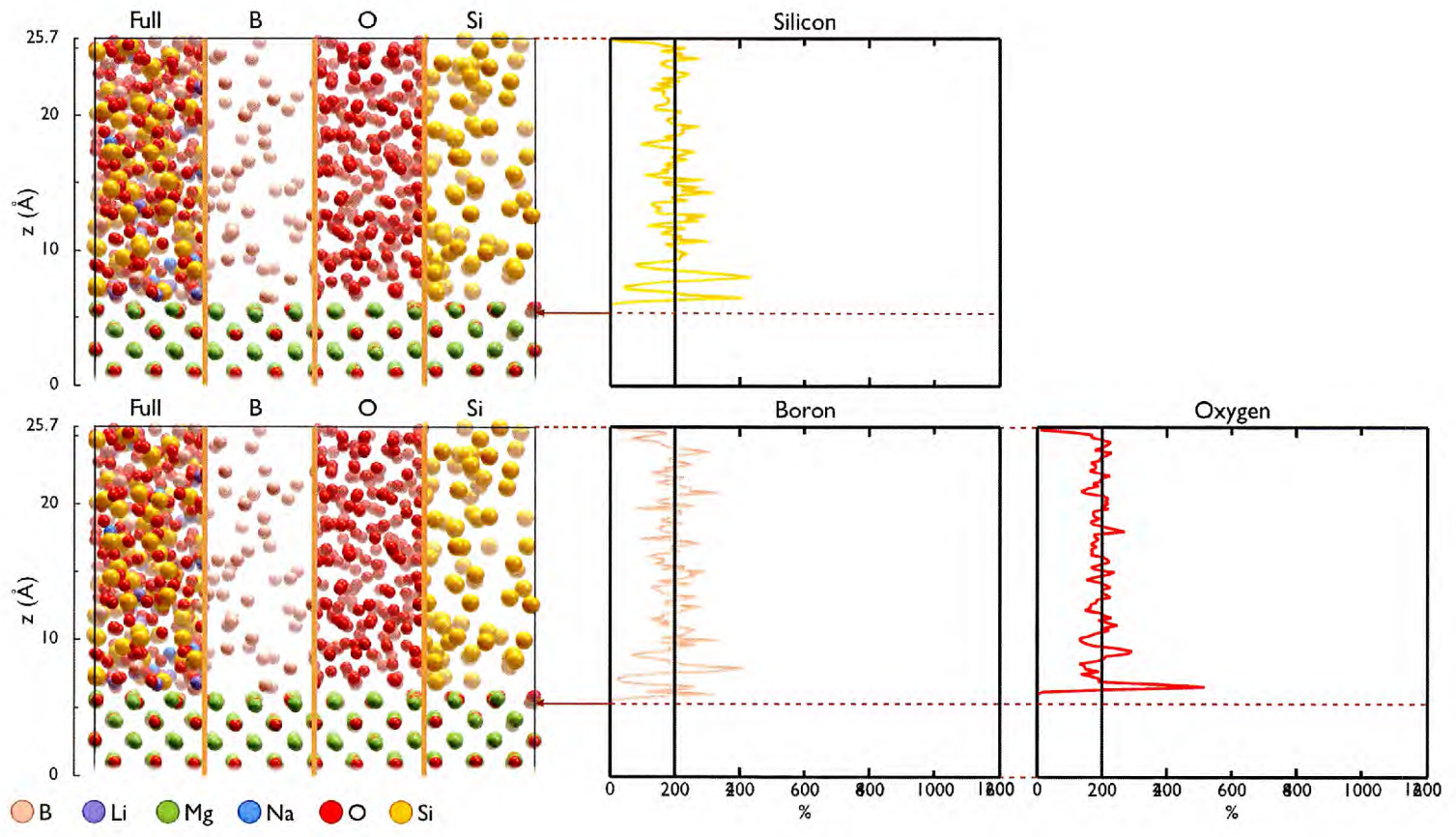
Figure 5.8: Network Former Concentration Profile: MW glass MgO-(110).
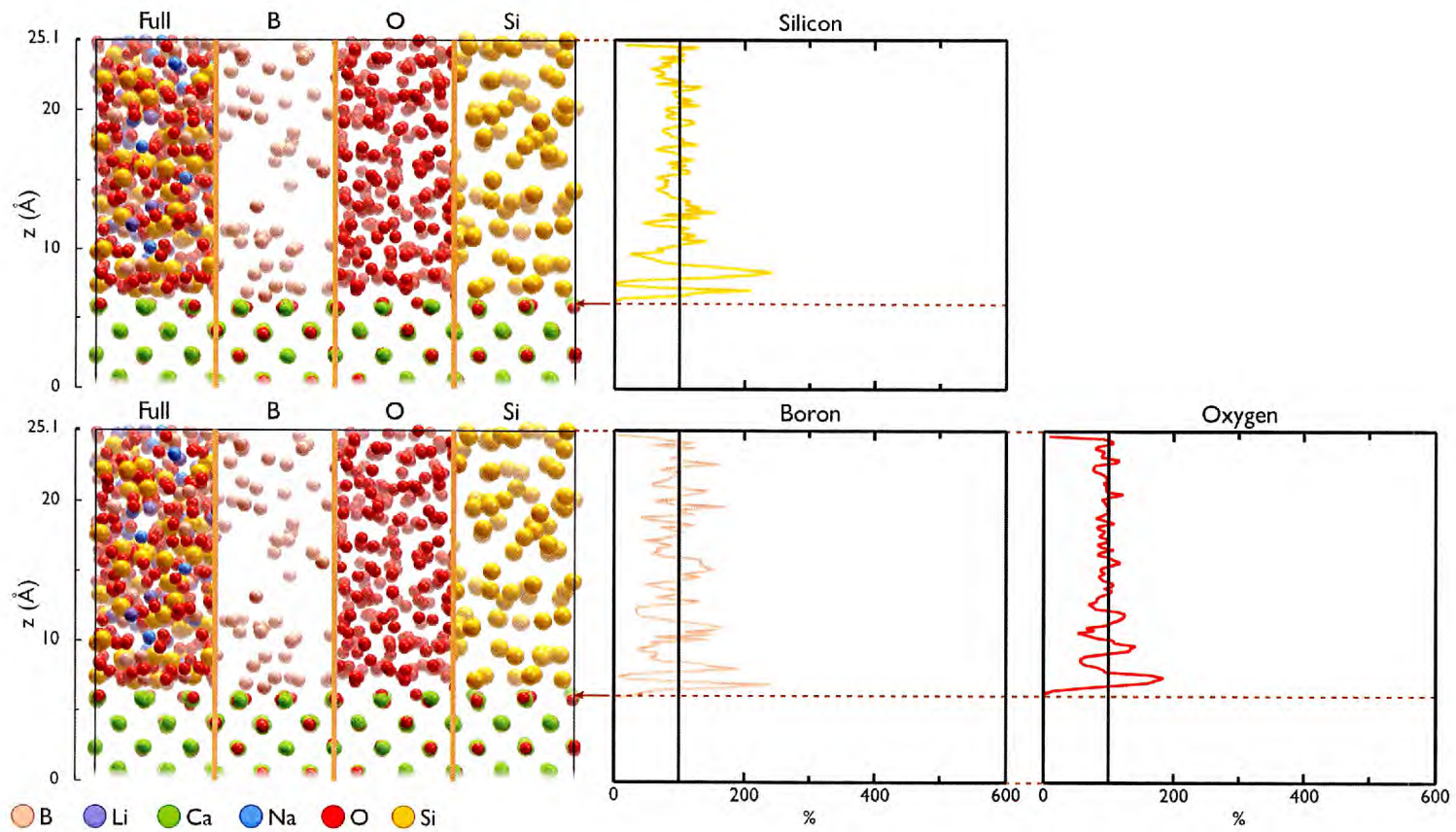
Figure 5.9: Network Former Concentration Profile: MW glass CaO-(110).
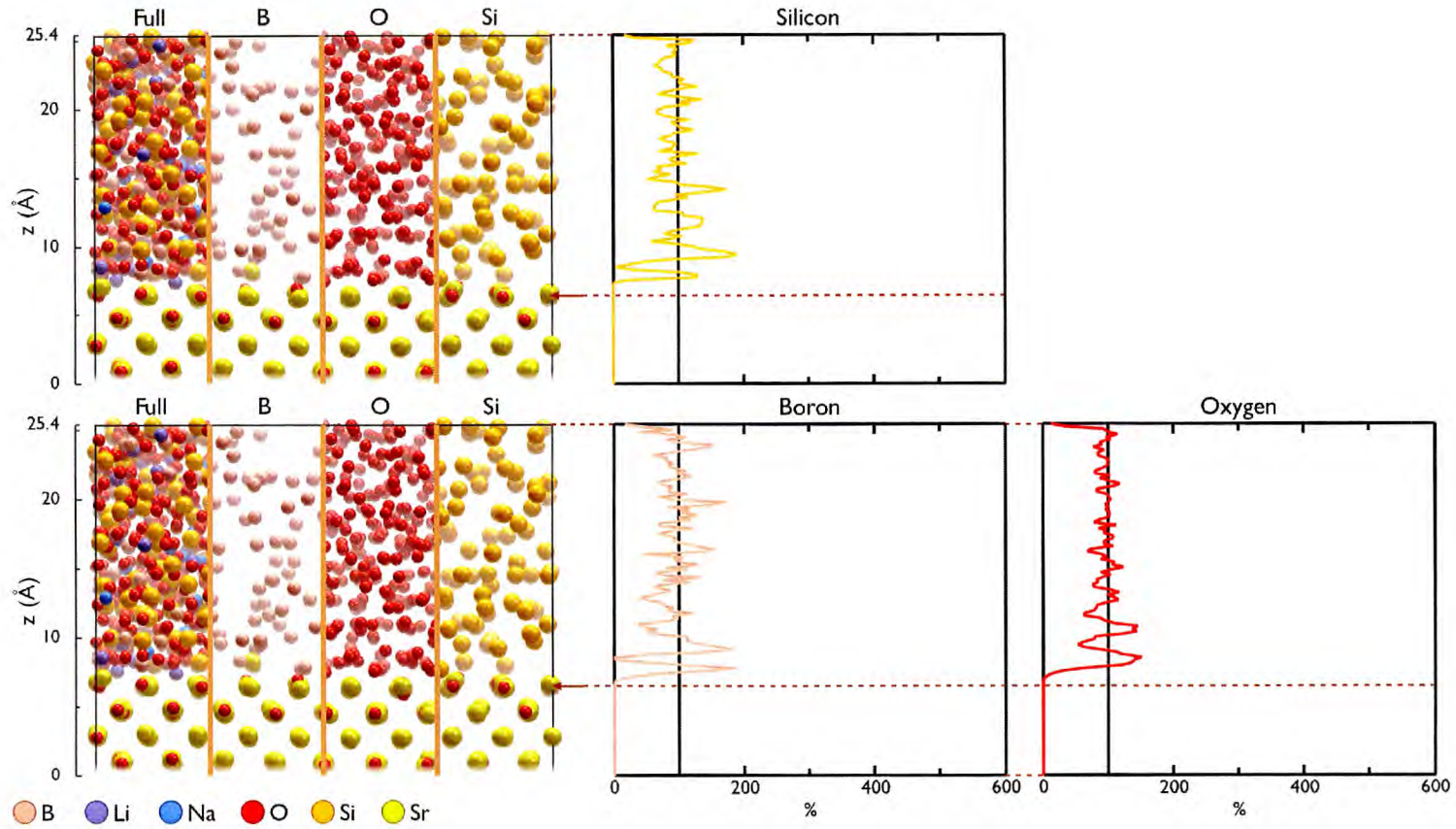
Figure 5.10: Network Former Concentration Profile: MW glass SrO-(110).
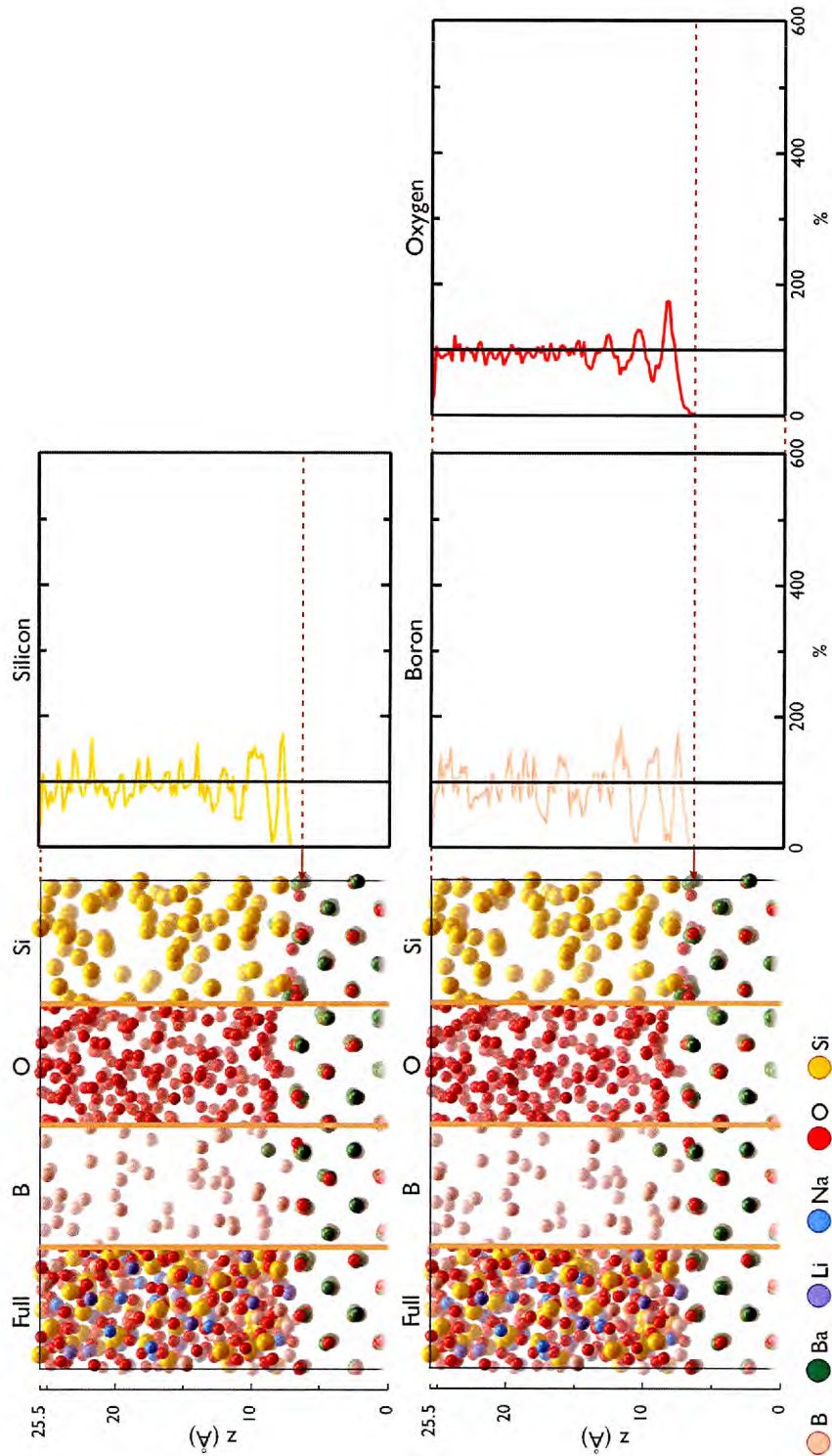
Figure 5.11: Network Former Concentration Profile: MW glass BaO-(110).
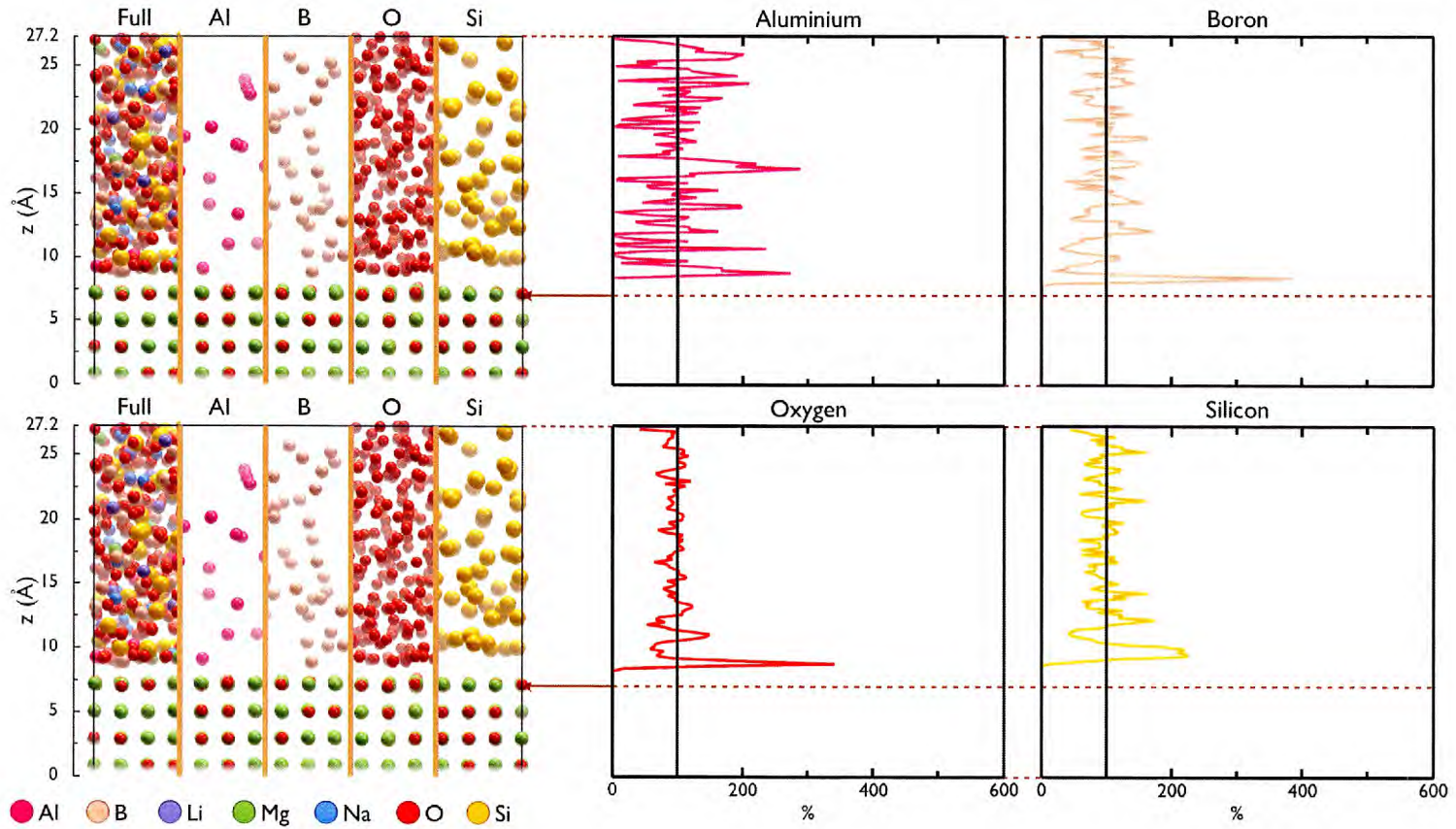
Figure 5.12: Network Former Concentration Profile: MW+Al+Mg glass MgO-(100).
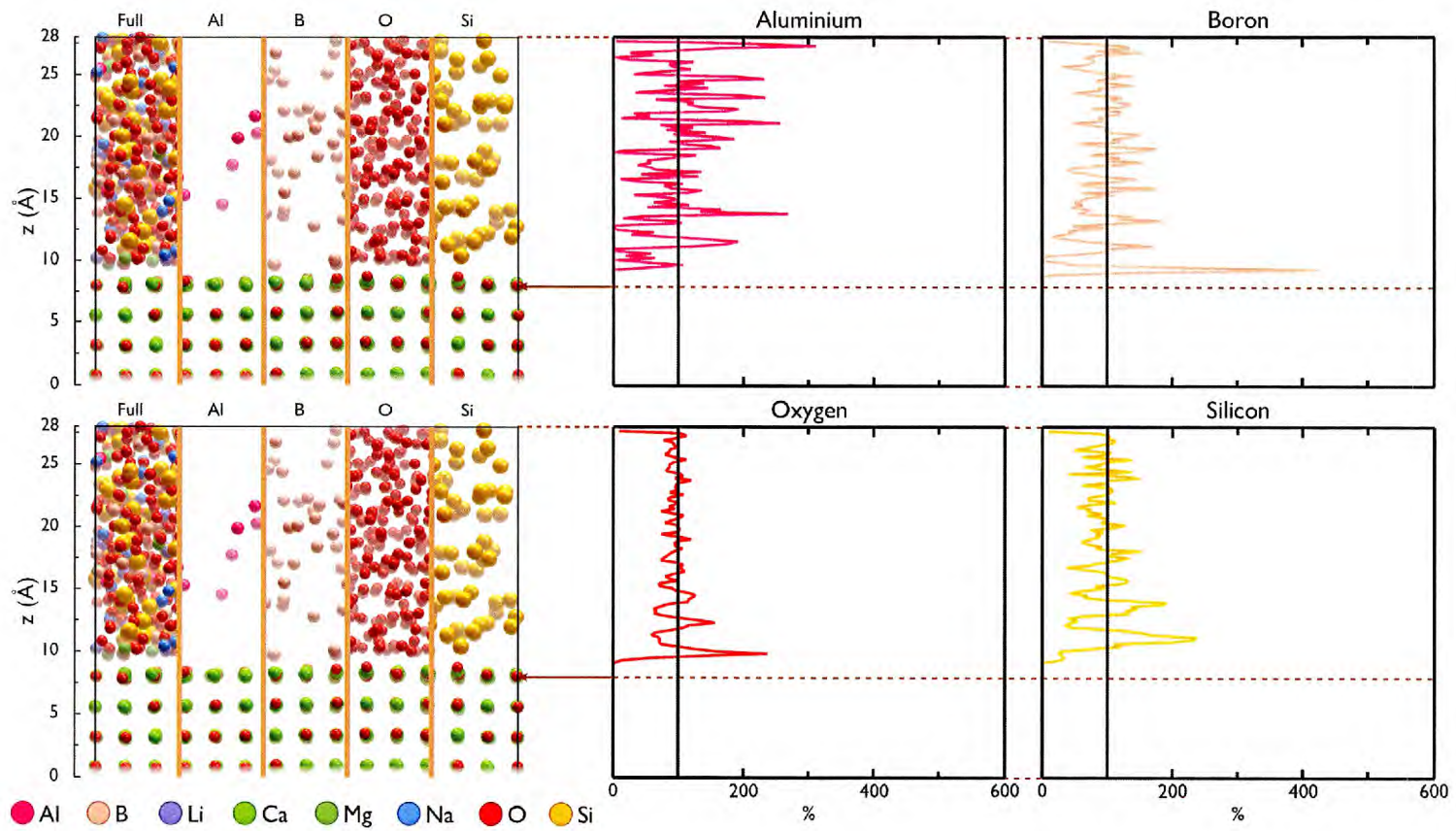
Figure 5.13: Network Former Concentration Profile: MW+Al+Mg glass CaO-(100).
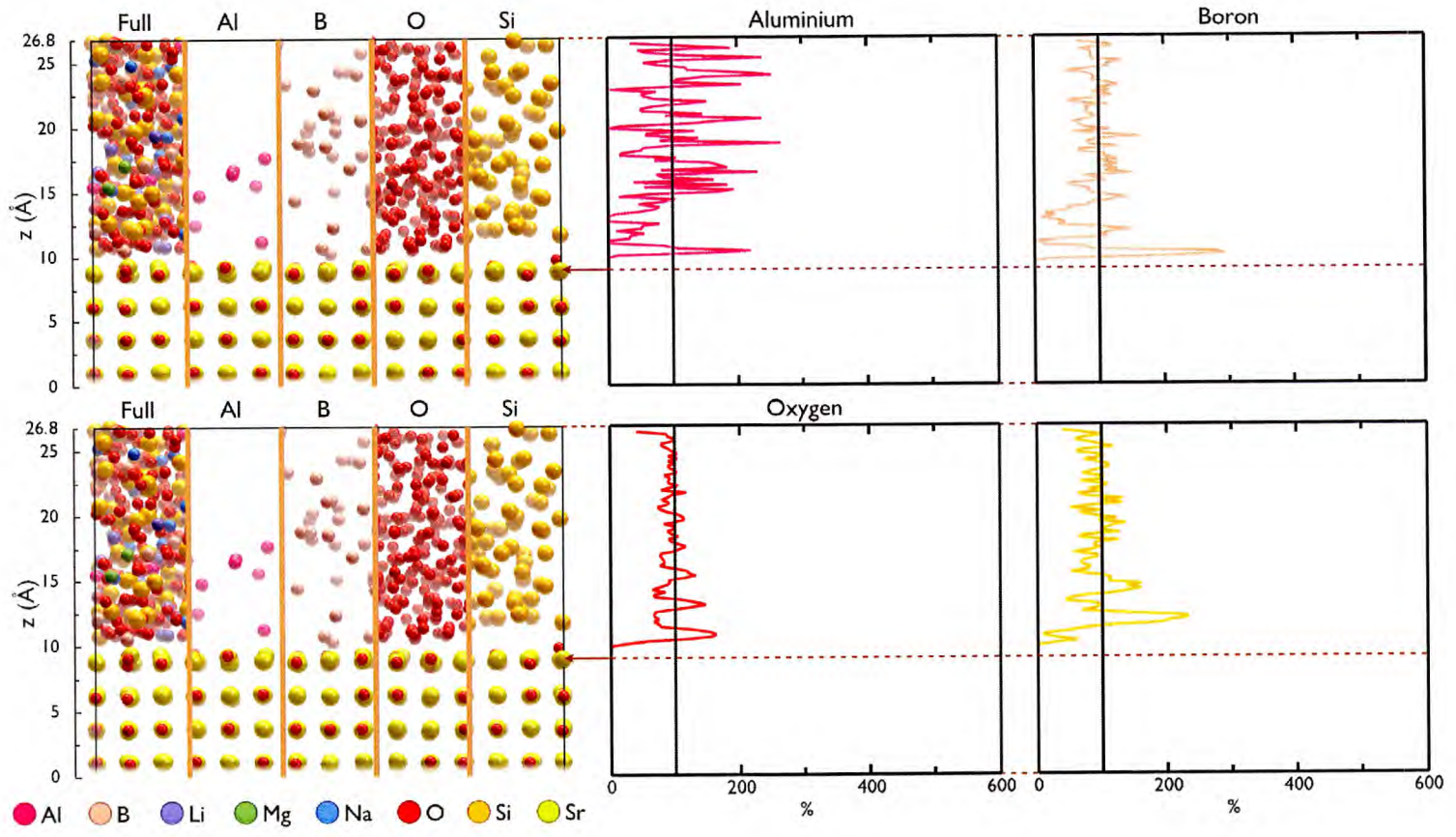
Figure 5.14: Network Former Concentration Profile: MW+Al+Mg glass SrO-(100).
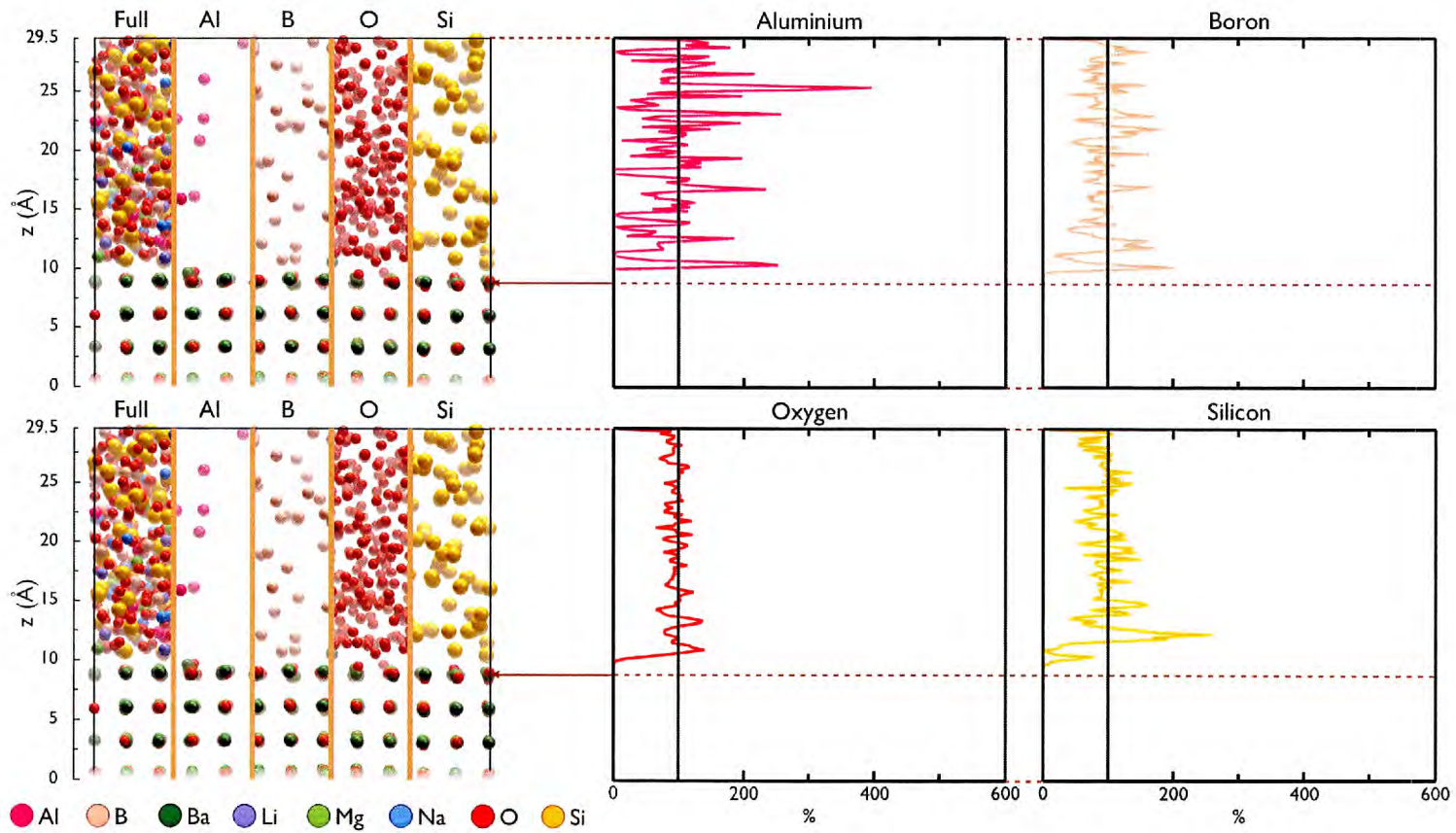
Figure 5.15: Network Former Concentration Profile: MW+Al+Mg glass BaO-(100).

5.1.1 General Observations

In the previous chapter (section 4.5.1), enhancement of modifier species in the glass close to interfaces with the (100) and (110) surfaces was described. In certain cases, modifier concentrations close to the interface were up to ten times higher than in the bulk glass. The density profiles given in figures 5.1 to 5.15 show that concentration increases also occurred for network formers close to most of the glass ceramic interfaces considered.

Unfortunately, the small number of aluminium atoms in the MW+Al+Mg glass meant it was difficult to get reliable statistics for Al and resulted in the noisy density profiles seen above. As a result it was not possible to determine with sufficient certainty if Al enhancement occurred at the MW+Al+Mg glass-ceramic interfaces.

Table 5.2 lists the heights of the first major peak of the network former density profiles, to provide a quantitative measure of the level of network former enhancement at each interface. At the (100) interfaces, Si concentrations ranged between 181% for the MW glass SrO-(100) interface (figure 5.6) , to 258% for the MW+Al+Mg BaO-(100) interface (figure 5.15). Increases in oxygen density close to the interface were also seen; the largest oxygen concentration was 340% at the interface between MW+Al+Mg glass and MgO-(100) (see figure 5.12).

The concentration of boron also saw significant enhancement at the (100) interfaces. In particular, the largest boron peaks were seen at the interfaces between the MW and MW+Al+Mg glasses with CaO-(100) which had relative densities of 412% and 420% (see figures 5.5 and 5.13).

Of the (100) interfaces considered, only the interface between MgO and SiO_2 (figure 5.1) showed no enhancement of network forming species close to the interface. Possible reasons for the behaviour of this system are discussed in section 5.3.2.

The peak heights in table 5.2 show that there was a general trend for oxygen peak height to decrease as ceramic cation radius increased. For example, the oxygen peak height more than halved between MgO and BaO for both the MW and MW+Al+Mg series of interfaces. This trend, was not however seen for Si and B.

		Height of Initial Peak (%)		
Glass	Ceramic Surface	Si	O	B
MW	MgO-(100)	254	299	374
	CaO-(100)	215	193	412
	SrO-(100)	181	161	275
	BaO-(100)	206	143	175
MW+Al+Mg	MgO-(100)	225	340	385
	CaO-(100)	237	236	420
	SrO-(100)	231	162	292
	BaO-(100)	258	139	200
SiO_2+Na	MgO-(100)	234	230	-
SiO_2+Na+Li	MgO-(100)	196	318	-

Table 5.2: Height of first major peak in network former density profiles.

Peak Order

Figure 5.16 shows a region of the density profiles for the network forming species at the MW glass CaO-(100) interface, where the profiles have been plotted on the same axes so that the relative order of the boron, silicon and oxygen peaks at this interface can be seen (the same profiles are plotted separately in figure 5.5). This interface has been chosen as its density plots are representative of those found at most of the (100) interfaces.

Moving from the interface into the glass, the peaks occur in the following order: boron, oxygen and silicon. Interestingly, the position of the second boron peak corresponds with the first Si peak. When modifier species are included, the order of peaks moving away from the interface was (for reference, ionic radii from [118] are given in brackets): B (0.27Å), Li (0.76Å), O (1.4Å), Na (1.02Å) and Si (0.4Å). This peak order was seen at all the MW and MW+Al+Mg glass (100) interfaces considered. This order was also maintained at the SiO_2+Na and SiO_2+Na+Li interfaces, albeit without boron and in the case of the SiO_2+Na interface, without Li.
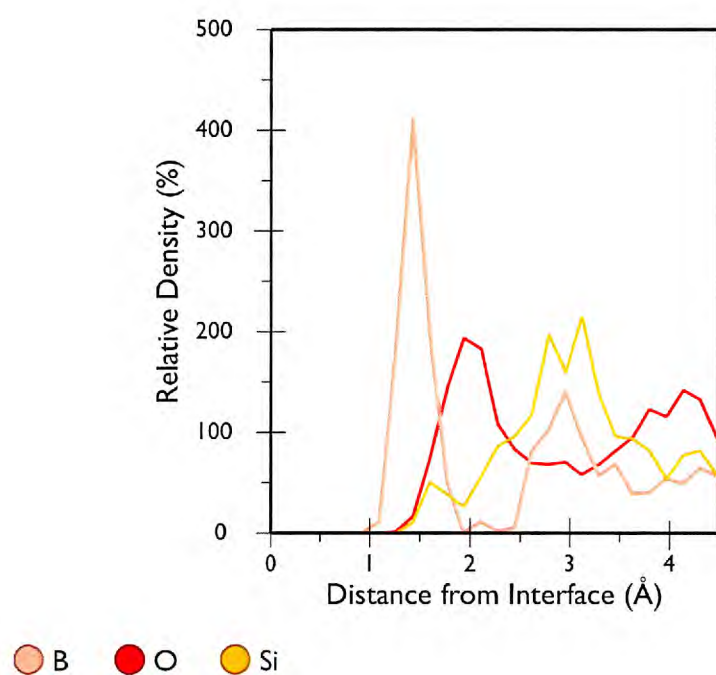
Figure 5.16: Detail of the density profiles for network formers at MW glass CaO-(100) interface.

Direct Bonding of Si and B to Ceramic

Just as in the simulated bulk glass, the boron and silicon atoms at the glass-ceramic interfaces sat in borate (BO_3 and BO_4) and silicate (SiO_4) polyhedra. These could interact with the ceramic surface in a number of ways: one, two or even three oxygen atoms in a silicate/borate polyhedron could become associated with the ceramic surface. Alternatively, a polyhedron's silicon or boron atom could bind directly to anions in the ceramic's surface. By this method, silicon and boron atoms could become coordinated by anions in the ceramic's surface, so that the ceramic surface contributed anions to silicate and borate units at the interface, leading to a boron/silicon polyhedron sharing an edge or vertex with the ceramic.

At the (100) interfaces, the main boron peak sat closer to the interface than the first oxygen peak. This suggests that the borate units represented by this peak contained anions from the ceramic. This view was confirmed by visualisation of the interface which showed borate units (mainly tetrahedra) in which one vertex was an anion in the ceramic surface.

By comparison, the first major silicon peak sat further from the interface than the first oxygen peak. This shows that the silicon atoms were separated from the ceramic surface by a layer of oxygen atoms. This suggested that, most silicate units close to the interface did not contain anions from the ceramic's surface. As a result, the response of these silicate units to the ceramic surface seems mainly be due to the interaction of their oxygen atoms with the ceramic surface.

Although the main silicon peak in the (100) systems was separated from the interface by the oxygen peak, a small Si peak was predicted at the interfaces between MW glass and CaO-(100), SrO-(100) and BaO-(100); these are highlighted in figure 5.17. Computer visualisation of the region represented by these sub-peaks, showed that they were due to silicon atoms in tetrahedra which shared an oxygen vertex with the ceramic surface (i.e. silicon atoms bound to surface anion sites). As the low peak height indicates, the population of these vertex sharing silicon tetrahedra was relatively low. For instance, the largest sub-peak in figure 5.17 was seen at the MW glass SrO-(100) interface and represented a population of 15 silicate units distributed over both the upper and lower surfaces of the ceramic block.
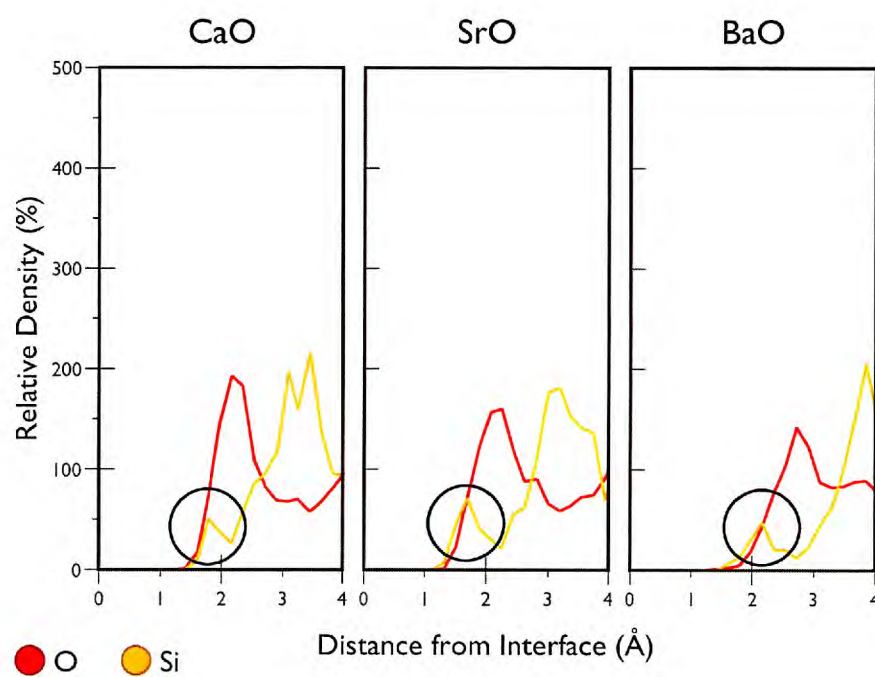
Figure 5.17: Region between interface and first major peak of Si density distributions for MW glass (100) interfaces. The small peaks close to interface due to direct bonding of Si to ceramic are highlighted.

Comparison of (100) and (110) Interfaces

At the (100) interfaces, although most of the borate units close to the interface shared an anion with the ceramic surface, silicon tetrahedra did not. Instead the first peak of (100) silicon density profiles sat further from the interface than the first oxygen peak. The distribution of network formers at (110) glass-ceramic interfaces showed significant differences to those of the (100) interfaces.

The density profiles for network formers at the MW glass CaO-(110) interface are plotted on the same axes in figure 5.18. This not only allows a comparison with the equivalent (100) plot given in figure 5.9, but also allows the relative position of the B, O and Si peaks at this interface to be seen.

A major difference between the density profiles for (100) and (110) is in the position of the first silicon peak: at the (100) interfaces this sat further from the interface than the oxygen peak. By comparison, the first silicon peak at (110) interfaces sat nearer to the interface than the oxygen peak indicating that a significant number of silicon atoms bonded to ceramic anions at the (110) surface. To confirm this interpretation, the number of silicon atoms bonded to ceramic anions for the (100) and (110) interfaces of MW glass and CaO were counted. For every one hundred ceramic anion sites in the ceramic surface only 5 directly bonded silicon atoms were found for (100) whilst the number was 21 at (110) interfaces; in other words, more than four times the number of silicon atoms bonded to ceramic anions at the (110) interface than did at the (100) CaO interface with MW glass. A similar difference was found between the (110) and (100) MW glass interfaces for MgO, SrO and BaO.

5.2 Periodicity

The density profiles for the network formers (section 5.1) showed evidence of regular density oscillations close to the interface. Unlike the random fluctuations which would be observed in a bulk glass, the oscillations in the boron, oxygen and silicon profiles have the appearance of damped sine waves with well defined, and constant frequencies. Oscillations were seen in all
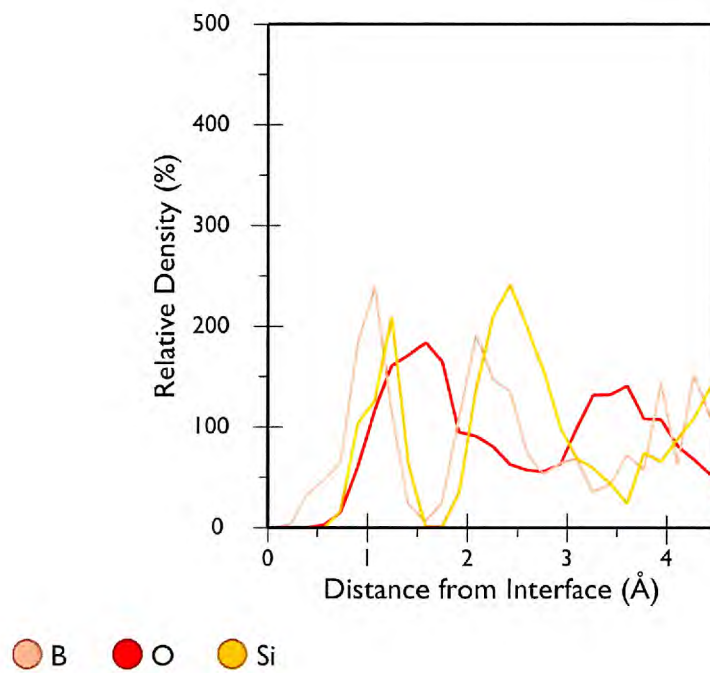
Figure 5.18: Density profile for network formers close to interface of MW glass with CaO-(110) ceramic (these density profiles are plotted separately in figure 5.5).

systems except the SiO_2 MgO-(100) system.

A typical example of the density oscillations observed at (100) interfaces can be seen in figure 5.19 which shows the densities of B, O and Si close to the MW glass CaO-(100) interface. Within 8Å of the interface, regular density oscillations can be seen for all three network forming species. In particular, the oxygen profile appears sinusoidal with an amplitude that decays with distance from the interface. In addition, peaks in the Si and B profiles correspond to troughs in the O density, suggesting that their densities were mutually related. Although the discussion which follows will focus on the MW glass interfaces, density oscillations were not restricted to the MW glass interfaces: with the exception of the pure silicate glass, oscillations were seen at interfaces with all other glasse (i.e. SiO_2+Na, SiO_2+Na+Li and MW+Al+Mg).

The presence of regularly spaced peaks in the density profile of network formers close to glass-ceramic interfaces is potentially very significant. Each peak in the density profile can be thought of as a densified layer of atoms parallel to the interface. The presence of regularly spaced layers of atoms, as signified by the regular peak spacing seen in the network former density profiles, indicates that, the presence of the ceramic led to partial ordering of the glass close to the interface. This view is further supported by the correlation between the silicon/boron profiles and their respective oxygen profiles: the position of silicon and boron density peaks corresponded to troughs in the oxygen distribution. This suggested alternating oxygen and silicon/boron layers exist parallel to the interface.

In the random network of the bulk glass, the orientation of borate and silicate polyhedra are essentially random. The effects of this on the density profiles for a bulk glass can be seen in figure 5.20, which shows profiles for a section of the bulk MW glass. In this figure, the position and separation of peaks is essentially random. Additionally, there was no correlation between the individual O, Si and B curves, with no systematic correspondence between boron/silicon peaks and oxygen troughs being evident.

The regularly spaced and alternating oxygen and boron/silicon layers parallel to glass ceramic interfaces can be interpreted in terms of alignment of the borate and silicate polyhedra relative to the interface. In section 5.1.1, increased oxygen densities and hence oxygen rich layers
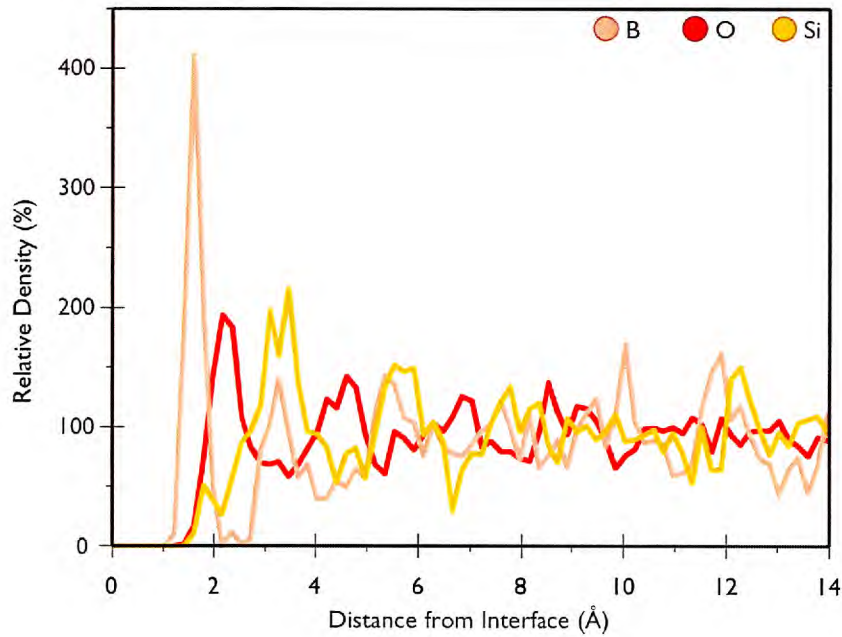
Figure 5.19: Density profile for network formers at the interface of MW glass and (100) surface of CaO.

were observed close to most glass ceramic interfaces considered. As oxygen atoms in the glass network were bound to boron and silicon atoms, the formation of such layers would have required the alignment of borate and silicate polyhedra close to the interface. Silicate and borate units could align themselves to contribute, one, two or three oxygen atoms to an oxygen layer (as demonstrated by figure 5.21).

The orientations shown in figure 5.21 may also help explain why alternating oxygen and silicon/boron layers were observed. In figure 5.21a, a tetrahedron is shown with its lowest anion sitting in the plane at the bottom of the diagram; the bond between this anion and the cation at the tetrahedron's centre is shown pointing along the plane's normal. In this configuration, the tetrahedron can be thought of as containing three layers normal to the z axis: the lowest anion, the cation at the centre of the tetrahedron and the three anions forming the upper tetrahedral facet. In a similar manner, tetrahedra with an edge (figure 5.21b) or face (figure 5.21c) constrained to a particular plane, contain three layers. The density distributions for a layer of tetrahedra, with alignments similar to those given in figure 5.21, would give an O layer, fol-

lowed by an Si layer and then another O layer. In other words a distribution similar to the alternating O-Si-O pattern seen in the interfacial density distributions.

5.2.1 The Effect of Ceramic Composition on Density Oscillations

The period of oscillation for the oxygen density profile at each interface was examined. This was performed to see if the period of density oscillations in the glass close to the interface was affected by glass composition or the interface's ceramic surface.

Figure 5.23 shows the oxygen profiles for the MW glass (100) and (110) interface for the MgO to BaO series of ceramics. In order to measure the oxygen peak spacing, a function describing a damped sine wave was fitted to the density profiles:

$$\rho(r) = A \cdot \exp[-b(r-s)] \cdot \cos\left[\frac{2\pi}{\lambda}(r-s)\right] + d \tag{5.1}$$

where r is the distance to the interface, A and b determine the rate amplitude decay, s describes the position of the first peak, λ is the period of oscillation (in Å) and d is the intercept with the density axis.

This function was fit to each oxygen profile by a least squares method [130, 131] as implemented by the gnuplot computer package [132]. The results of these fits for the MW glass interfaces are overlaid onto the plots in figure 5.23. The fit parameters (A, b, d, s) for each interface are given in table 5.3. In addition, peak separations were measured directly from the oxygen curves, the results, obtained by taking an average of the separations between the first three peaks are also given in table 5.3.

The period of oscillation (λ) was plotted against ceramic cation radius in figure 5.24. As the cation radius increased, a small decrease in peak spacing was seen for both the (100) and (110) surfaces. The measurements made by curve fitting and direct measurement from the plots gave slightly different results, however, the same trend of decreasing oscillation period with increasing ceramic cation radius, was observed using both methods.
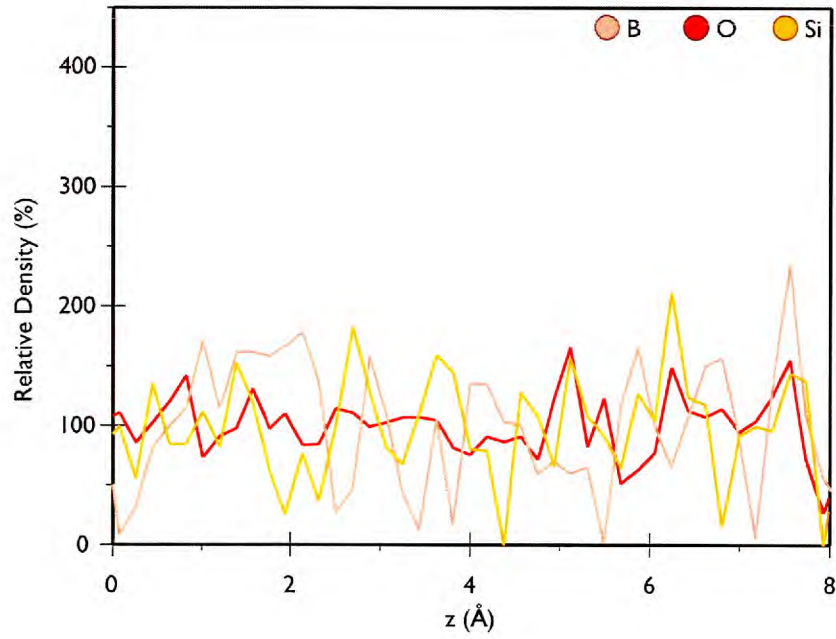
Figure 5.20: Network former density profiles taken along z-axis of MW glass. From this it can be seen that, in the bulk glass, density peaks were randomly distributed and the B, O and Si curves appeared uncorrelated.
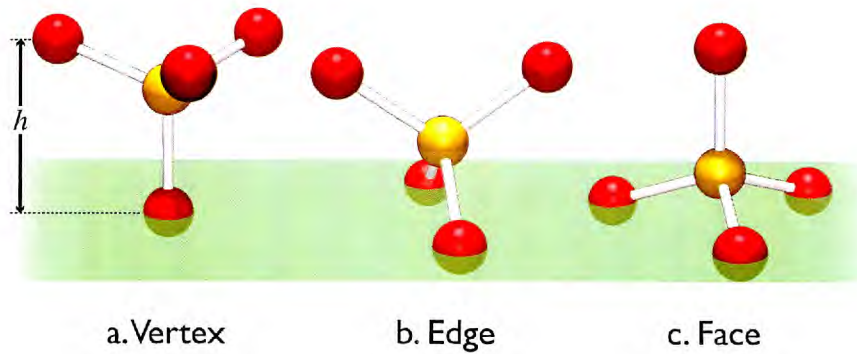
Figure 5.21: Silicate tetrahedra could contribute a. a single vertex, b. two anions or c. three anions to an oxygen layer close to the interface.

System	Fit Parameters					Direct Measurement
	A	b	s (Å)	d (%)	λ (Å)	λ (Å)
MW-MgO-(100)	87.84	0.363	2.394	98.56	2.189	2.273
MW-CaO-(100)	74.47	0.363	2.315	94.52	2.159	2.263
MW-SrO-(100)	61.28	0.350	2.271	92.40	2.107	2.230
MW-BaO-(100)	33.97	0.641	2.904	93.15	2.006	2.140
MW Al+Mg-MgO-(100)	129.87	0.605	2.246	97.43	2.121	2.177
MW Al+Mg-CaO-(100)	74.10	0.267	2.301	95.62	2.257	2.308
MW Al+Mg-SrO-(100)	58.19	0.224	2.441	94.83	2.280	2.189
MW Al+Mg-BaO-(100)	25.49	0.075	2.579	96.80	2.185	2.406
SiO$_2$+Na-MgO-(100)	79.56	0.492	2.227	96.90	2.172	2.213
SiO$_2$+Na+Li-MgO-(100)	78.62	0.731	2.323	99.04	2.030	2.160
MW-MgO-(110)	160.52	0.478	1.691	94.85	2.307	2.308
MW-CaO-(110)	74.88	0.258	1.693	96.98	2.208	2.229
MW-SrO-(110)	57.21	0.221	2.498	95.61	2.191	2.199
MW-BaO-(110)	60.71	0.251	2.257	94.26	2.190	2.138

Table 5.3: Parameters for equation 5.1 fitted to interfacial oxygen density profiles and peak spacing measurements made by a direct method.
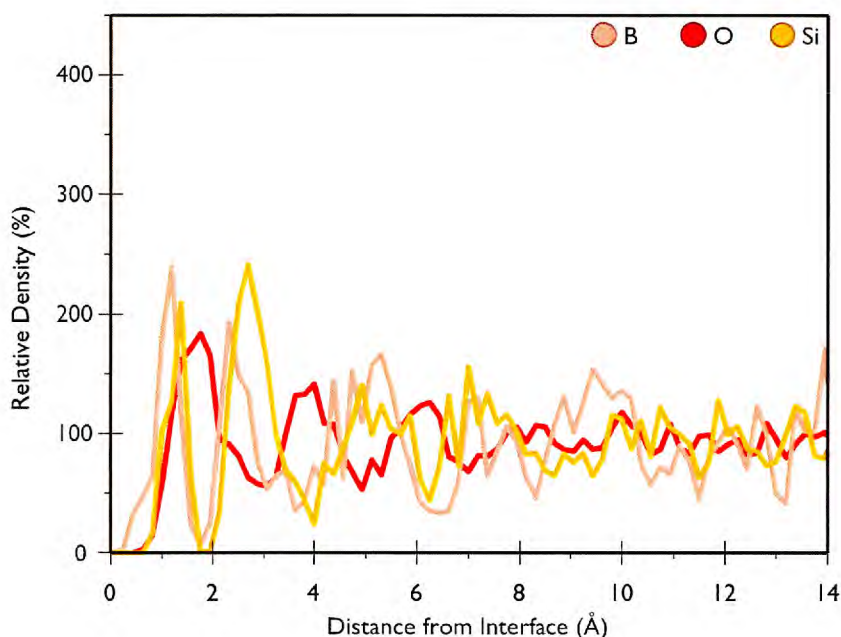
Figure 5.22: Density profile for network formers at interface between MW-glass and (110) surface of CaO.

The density profiles from which figure 5.24 was derived were generated using a binning method by counting the number of atoms in a series of 0.1875 Å slices parallel to the interface. The width of each bin meant that there was an uncertainty in the position of density profile peaks of ± 0.094 leading to an uncertainty in the peak spacing (λ) value of ± 0.1875Å.

The peak separation in the oxygen density profiles for the MW glass interfaces decreased by a small amount over the MgO to BaO range. For the (100) interfaces, the change was 0.18Å and only 0.11Å for the (110) systems. For both families of interface, the change in peak separation observed between MgO and BaO was within the error given above. The magnitude of the change in peak spacing was also small in comparison to the change in lattice parameter, which on going from MgO to BaO increases by over 30%.

The small changes in peak-spacing seem to indicate that oxygen peak spacing in the glass near the interface, was effectively independent of ceramic composition and the ceramic's terminating surface. This suggests that, although the ceramic seems to have induced layering in the
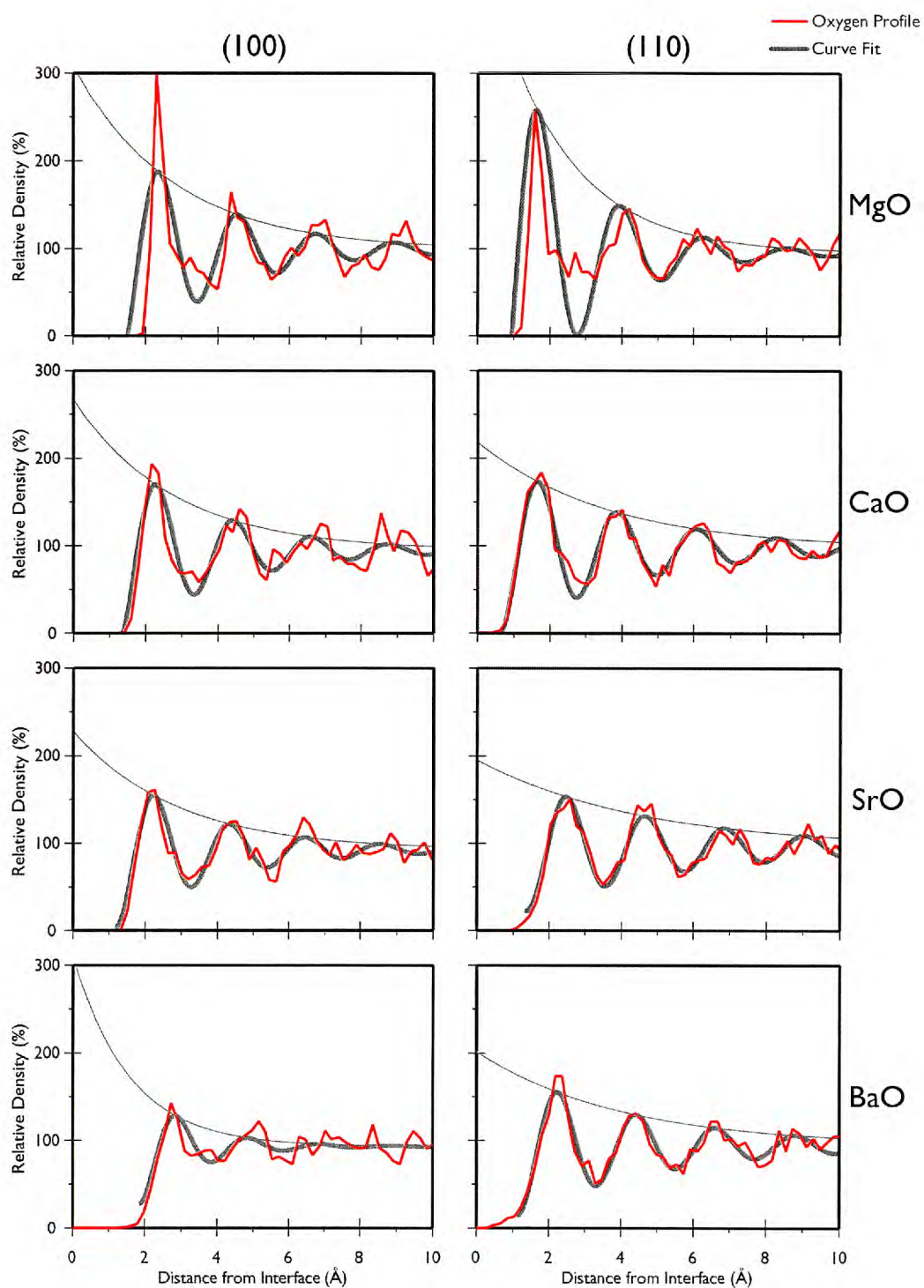
Figure 5.23: Oxygen density profiles and least squares fits for MW-glass interfaces.
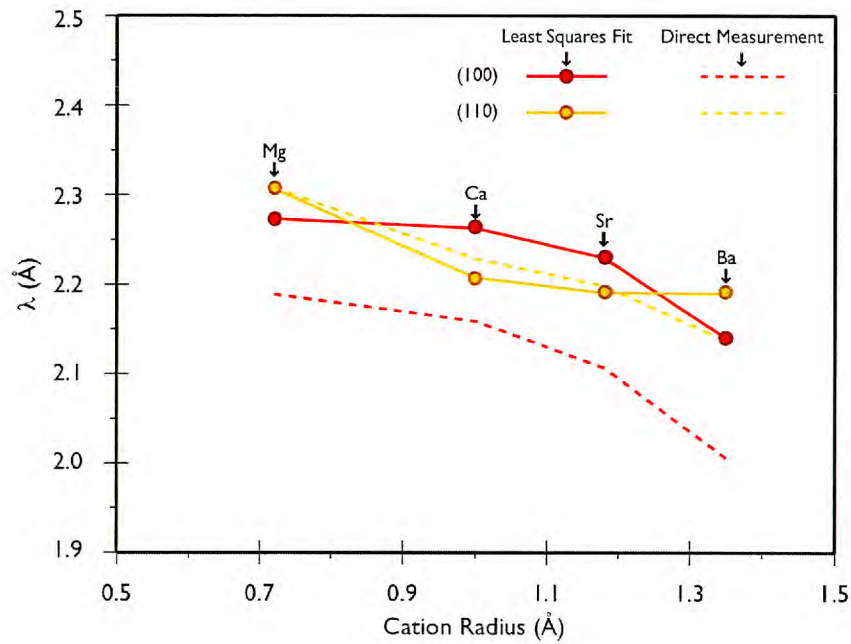
Figure 5.24: Peak spacing vs. ceramic cation radius for interfaces with MW glass.

glass, the spacing of these layers was governed by the glass network. It is also interesting to note that layer spacing was similar between the silicate (SiO_2+Na, $SiO_2+Na+Li$) and the borosilicate (MW and MW+Al+Mg) glasses. As the silicate glasses did not contain boron and yet had very similar peak spacings, this may indicate that in borosilicate interfacial systems, the layer spacing was determined by the silicate portion of the glass network.

It is interesting to note, that the oxygen peak separations were similar to the height of a silicon tetrahedron. Based on an Si-O bond length of 1.6Å, the height of an SiO_4 unit (labelled h in figure 5.21), is 2.1 Å. This may suggest that the vertex and face constrained tetrahedral alignments illustrated in figures 5.21a and 5.21c were favoured over the edge constrained configuration of figure 5.21b.

5.2.2 Alignment of Borate and Silicate Units Relative to Surface

The partial layering of the glass close to the interface (evidenced by periodic oscillations in the glass' density profiles) indicated that oxygen atoms in the silicate and borate units close to the interface were associated with the ceramic's surface and as a result formed a densified oxygen layer just above the interface. Surface concentration maps were generated (as described in section 4.5.3) to see with which sites in the ceramic's surface these oxygen atoms were associated.

(100) Surfaces

Figure 5.25 shows the concentration maps for oxygen at the MW glass (100) interfaces. Each map represents the first oxygen peak of their respective density profiles (i.e. between the plane of the interface and 2.7, 2.9, 2.7 and 3.13 Å away from the interface for MgO, CaO, SrO and BaO interfaces respectively). These maps revealed that an interesting structural change occurred between MgO and CaO.

The MgO map (figure 5.25) shows a distinctive diamond pattern, indicating that the oxygen atoms nearest the interface were mainly associated with surface cations, with a smaller population sitting along the $< 110 >$ surface vectors running between surface cation sites. By comparison, the maps for CaO, SrO and BaO, show a quite different oxygen distribution. Rather than a diamond, the distribution for these systems was a box pattern. In addition, the areas of high oxygen concentration at these interfaces sat above surface interstitial sites rather than cation sites.

At all the MW glass (100) interfaces, the side length of the box or diamond described by the regions of high concentration in the surface maps was close to the edge length of a silicon tetrahedron (2.6Å). To highlight this, a square of side length 2.6 Å was overlaid (in orange) onto the concentration maps in figure 5.25. This correlation between the tetrahedral edge length and the concentration maps is interesting as it may suggest that tetrahedra at the interface oriented themselves along the edges of the box/diamond distributions found in the surface

maps. Computer visualisation of the simulation results was used to test this theory.

Figure 5.26, shows a small portion of the glass above the MW glass MgO-(100) interface. The position and orientation of the silicate tetrahedron shown in this figure was typical of that of many of the silicate and borate tetrahedra found at this interface. The silicon atom at its centre sat over an anion in the ceramic surface, whilst two of the three oxygen atoms in its base sat over ceramic cation sites, this resulted in the third basal anion sitting over an interstitial site in the ceramic's surface. This arrangement, where the base of a tetrahedron is associated with the ceramic and one of its edges runs along a $< 110 >$ direction parallel to the surface, accounts for the main features of the MgO-(100) surface map in figure 5.25.

The nearest neighbour Mg–Mg distance along $< 110 >$ was 2.9 Å at the MgO surface. This value is close to the tetrahedral edge lengths of boron and silicon (2.4 and 2.6Å respectively) though already larger. This helps explain why a diamond pattern was seen in the surface map in figure 5.25. By aligning an edge along $< 110 >$ the borate and silicate units were able to lower their energy through the association of two of their oxygen atoms with cations in the ceramic. At the same time, the silicon/boron atoms at the tetrahedron's centre were able to sit over a ceramic anion site, further lowering the energy of the system. By comparison, the Ca–Ca distance along $< 110 >$ is 3.4 Å: substantially larger than the tetrahedral edge length.

Figure 5.27 shows a region of the MW glass CaO-(100) interface. The four membered ring shown in this figure was typical of the structures found close to the (100) interfaces of MW glass and CaO, SrO and BaO. As was seen for the MgO-(100) interface, the silicon atoms in each tetrahedron sat over anions in the ceramic surface. Unlike the MgO interface, however, the oxygen atoms in the tetrahedra did not sit over ceramic cations, instead sitting over surface interstices. The lattice parameter of the CaO surface is larger than that of MgO, as a result the nearest neighbour Ca–Ca distance is larger than the silicate and borate tetrahedral edge lengths. Without significant relaxation of the surface (which did not take place as shown in section 4.4) it would be unlikely that the silicate and borate tetrahedra could align themselves to bring more than one of their oxygen atoms over a ceramic cation (i.e. the configuration illustrated in figure 5.21a). The nearest neighbour separation between interstitial sites on the CaO surface was 2.4 Å, a value compatible with borate and tetrahedral edge lengths. Through

Figure 5.25: Oxygen Surface concentration maps for MW glass (100) interfaces. An orange box, with side length equal to that of an SiO_4 tetrahedron has been overlaid on the plot.

association of their oxygen atoms with ceramic interstitial sites, the silicate and borate units allowed more of their anions to sit closer to the interface (lowering the energy of the system), whilst still allowing boron and silicon atoms to sit over ceramic anions.

In conclusion, at (100) interfaces it seems that, certain alignments were favoured by borate and silicate units close to the glass-ceramic interface. At the MgO-(100) interface, the nearest neighbour Mg–Mg distance was compatible with borate and silicate tetrahedral edge lengths. This meant that tetrahedra tended to align one of their edges along the ceramic's $< 110 >$ directions. The increases in lattice parameters of CaO, SrO and BaO led to the alignment of tetrahedral edges along $< 100 >$ being favoured at these interfaces.

(110) Interfaces

As was discussed earlier (see section 5.1.1), many of the silicate and borate units close to (110) interfaces were bonded directly to the ceramic surface (i.e. they incorporated oxygen atoms from the ceramic). With the exception of the MW glass MgO-(110) interface, where furrow bridging took place (see section 4.4.3), the directly bonded silicate and borate units tended to only share a single vertex with the ceramic. Visualisation of the interface revealed that these vertex sharing poyhedra favoured the configuration shown in figure 5.21, with one oxygen in the ceramic surface and the remaining three sitting in the oxygen rich layer parallel to the interface.

Figure 5.28, shows surface concentration maps for oxygen at MW glass (110) interfaces with MgO, CaO, SrO and BaO. As was seen for the (100) interfaces, the CaO, SrO and BaO maps appeared quite similar with dark bands (representing areas of high oxygen concentration) running perpendicularly to the ridges and furrows of the (110) surface. By comparison, the map for the MgO interface shows dark spots sitting over anion sites from the second layer of the ceramic block.

The MgO map can be explained in terms of furrow bridging by borate and silicate units. Figure 5.29 shows scale drawings of silicate and borate tetrahedra in furrow bridging configuration, these have been superimposed onto the MW glass MgO-(110) oxygen surface concentration
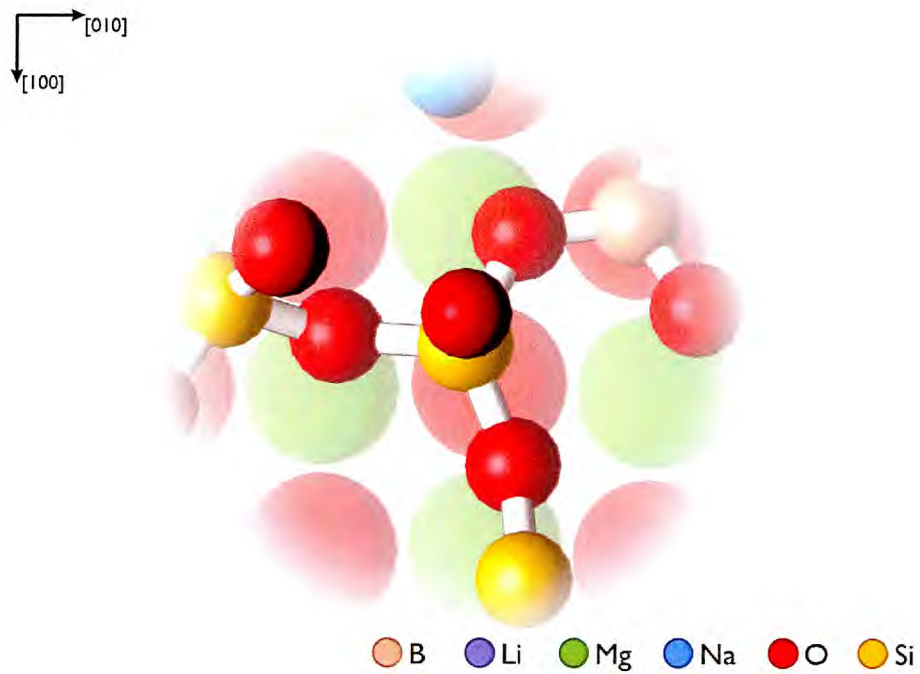
Figure 5.26: The smaller ceramic cation separation in the MW glass MgO-(100) system meant that silicon tetrahedra were aligned such that the silicon atom sat above a ceramic anion and one of the tetrahedral edges became associated with a pair of surface cations. To allow their easy identification, atoms belonging to the ceramic have been enlarged.
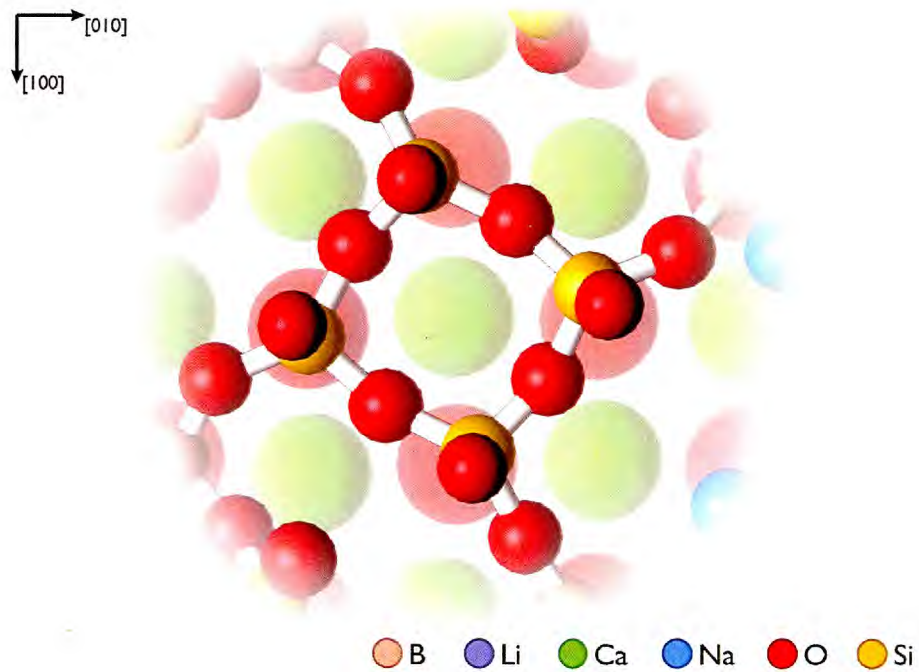
Figure 5.27: Plan view of portion of MW glass CaO-(100) interface, showing that silicon tetrahedra aligned their basal oxygens to sit over surface interstices. To allow their easy identification, atoms belonging to the ceramic have been enlarged.
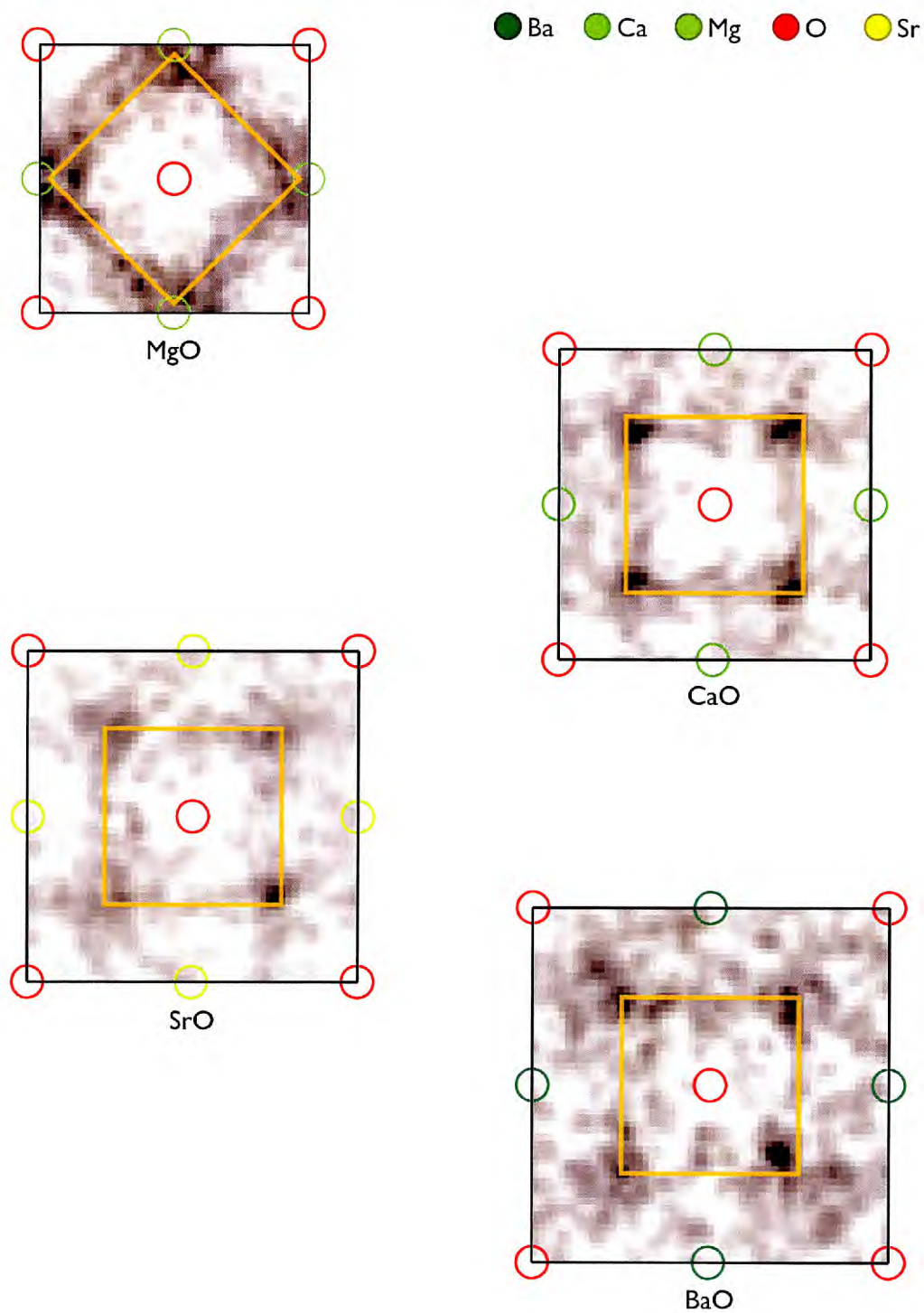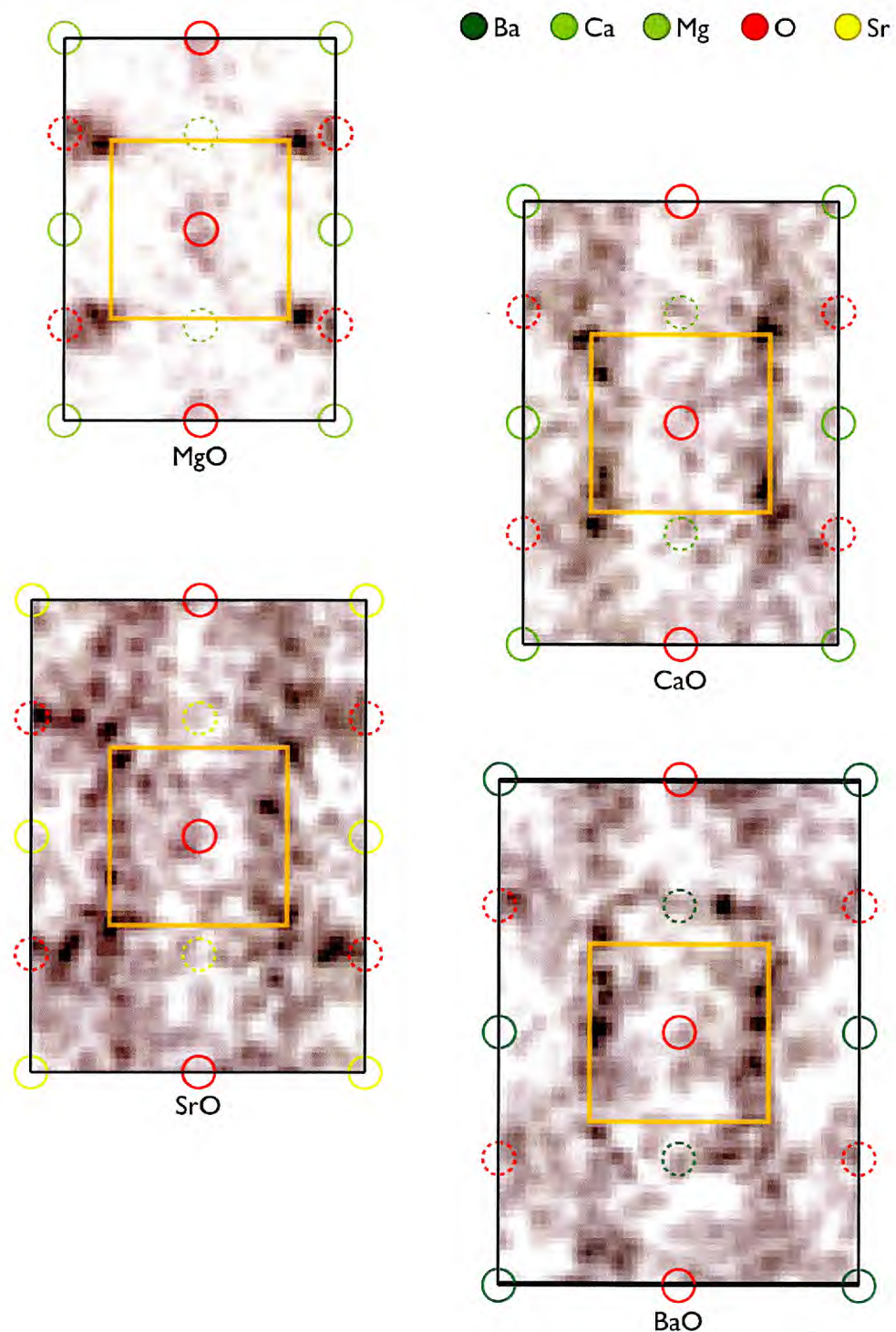
Figure 5.28: Oxygen Surface concentration maps for MW glass (110) interfaces. An orange box, with side length equal to that of an SiO_4 tetrahedron has been overlaid on the plot.

map. From this, it can be seen that the position of oxygen atoms, belonging to furrow bridging tetrahedra, correspond well with regions of high oxygen concentration found in the oxygen layer above this interface. Furrow bridging was not seen, to any great extent, at interfaces with CaO, SrO and BaO. It seems likely therefore that the difference between the MgO pattern and those of CaO, SrO and BaO can be attributed to the occurrence of furrow bridging at this interface.

In the discussion of the modifier distribution at the MW glass MgO-(110) interface (section 4.5.3) it was noted that the position of modifiers close to the interface corresponded to Mg sites had the ceramic continued. In other words, the modifiers above the surface formed what appeared to be a partially occupied layer of the MgO's cation sublattice. The MgO concentration map suggests that something similar occurred for the oxygen atoms in the glass close to the interface. The concentration map showed that oxygen atoms were found sitting (in the *xy* plane at least) at locations which would be occupied by anions in a subsequent layer of the MgO structure.

From analysis of the oxygen density profile (figure 5.8), it was found that oxygen atoms sat, on average, 1.6Å from the interface, a value which is quite close to the MgO-(110) layer spacing (1.5Å). This suggests that, not only did the structure of the glass close to this interface mimic MgO's cation sublattice but also the anion sublattice. In other words, above the MgO-(110) interface, a partially occupied layer of the MgO structure existed in the glass (albeit with Na and Li atoms replacing Mg atoms). This is particularly significant as, unlike the mobile modifier species, oxygen atoms in the glass were strongly bound to silicon and boron atoms. In order to create the MgO-like layer in the glass, cooperative rearrangement of the Si, O and B would have been required.

5.3 Discussion

The data presented over the preceding pages showed that, close to the glass-ceramic interfaces, structural modification of the glass network took place as a response to the ceramic:
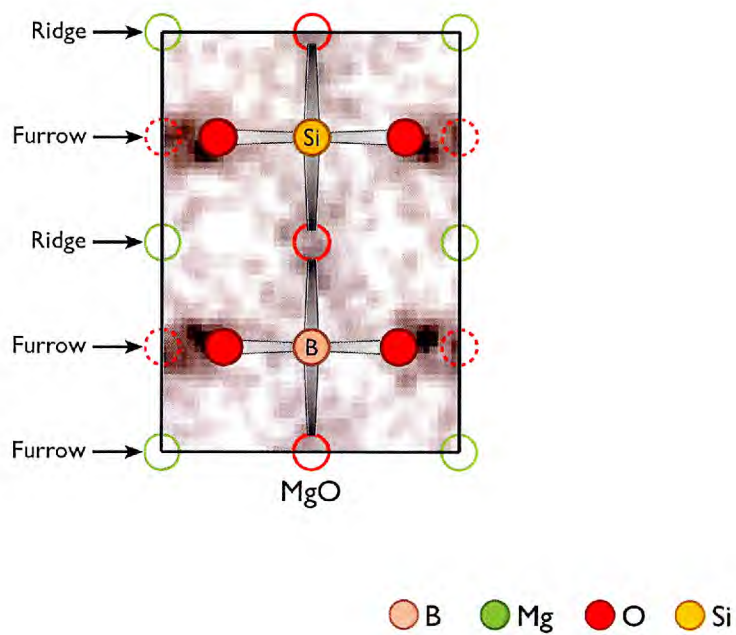
Figure 5.29: A silicate (top) and borate tetrahedron (bottom) in furrow bridging configuration superimposed onto the MW glass MgO-(110) concentration map.

- In the immediate vicinity of the interface, anions sitting in the ceramic's surface contributed to borate and silicate polyhedra. This behaviour was found to be more prevalent at (110) than (100) interfaces (it is not clear if this is responsible for the greater stability of (110) interfaces).

- A little further from the interface, a densified layer mostly containing oxygen atoms was found. This suggested an association between the oxygen atoms in the borate and silicate units close to the interface and the ceramic surface.

- Extending further into the glass, periodic and alternating layers of boron/silicon and oxygen were seen. Their presence suggested that partial ordering of the glass close to the interface had taken place.

The following discussion proposes mechanisms by which the interfacially induced changes to the glass network might have taken place.

5.3.1   Possible Reasons for Density Oscillations

The silicate and borate polyhedra in the layer of glass at the glass-ceramic interface were found to favour alignments where one of their facets (a triangle containing three anions) was parallel to the glass-ceramic interface. A layer of tetrahedra aligned in this manner could account for two oxygen and one boron/silicon layer in the glass close to the interface. However, the density profiles for the network formers near the glass-ceramic interfaces showed evidence for layers extending a significant distance into the glass. As an example, oscillations were still clearly detectable over 10Å from the MW glass MgO-(100) interface (see figure 5.4). Somehow, the ceramic was affecting the structure of the glass at a considerable distance from the interface. Two possible mechanisms by which this could have occurred were considered:

1. Periodicity in the electric field above the ceramic.

2. A localised mechanism based on layering similar to that seen in epitaxial growth, where the arrangement of atoms is influenced by the structure of underlying atomic layers.

Electrostatic Field

The effect of the electric field, above the ceramic's surface was considered as a possible cause for the layering of the glass structure. Experimentally it has been shown that glasses can be poled through the application of an electric field; the application of an electric field across a sodium silicate glass at high temperature caused Na^+ enrichment at the cathode [133]. This structure was maintained after the glass was cooled and the field was withdrawn. The electrostatic field caused by the ceramic might also be expected to cause periodic changes to the glass structure.

In terms of the periodicity observed in the glass near to the ceramic, if the ceramic's electric field gradient varied as a function of distance along the z-axis it would be expected that cations would move towards regions of positive electric field gradient and anions towards regions of negative field gradient. Segregation of this kind could then account for the alternating layers of cations and anions seen in the glass' density profiles. In order to test this hypothesis, the electric fields above the (100) and (110) surfaces of MgO were mapped.

The electric field was mapped using the following procedure. For each surface, MgO supercells were created. For the (1 0 0) surface this was $3 \times 3 \times 3$ unit cells in size. That for the (1 1 0) surface had dimensions of $3 \times 3 \times 2$. These cell sizes were chosen to have the same thickness as the ceramic blocks used in the glass-ceramic simulations. Static energy minimisation was performed on the supercells. The electric field was then measured in a grid pattern above the surface by placing a +1 point charge at each position the measuring the potential energy gradient at that point. The grid ranged from one angstrom above to three layer spacings above the surface (along the z axis) and had a 0.1 Å resolution. These calculations were performed using version three of the GULP code [134–136].

A series of slices were taken along [100] through the electric field above each surface, the component of the electric field vector acting along the z axis was plotted as a series of contour plots in figures 5.30 and 5.31 for (100) and (110) respectively. As might be expected, at both surfaces, the field strength above oxygen atoms was positive and above magnesium atoms was negative. Moving away from each atom, the field strength decayed quickly with distance from

the surface. In all the contour plots, there was no evidence for periodicity along the z axis. This means that the periodic layering of the glass was not caused by oscillations in the electrostatic field caused by the ceramic.

Templating

It is possible that the layering observed at the glass ceramic interfaces occurred through a templating mechanism. The layer of glass closest to the glass-ceramic interfaces considered, showed evidence of partial ordering. This ordered layer may have acted as a template for layers further from the interface: layers further from the interface could inherit some of the ceramic surface's structure at second hand through interactions with the ordered layer of glass at the interface.

An example of a process where layers of material inherit the structure of an underlying substrate is epitaxial growth. This process, which is often used to generate thin films in the semiconductor industry, involves gradually depositing atoms onto a substrate (normally from the vapour phase) [137]. Layers form as the atoms are adsorbed onto the substrate. Further layers then form on top of these deposited layers. As each layer is deposited its structure is related to the previously deposited layer, which in turn are related to the structure of the original substrate. In effect each layer acts as a blueprint for the following layer. Although the glass was not deposited onto the ceramic surface in the same way as in epitaxial growth, propagation of the ceramic phase's order into the glass structure may have ocurred by a similar layering process.

In most of the glass-ceramic systems considered, the ceramic phase caused alignment of borate and silicate polyhedra close to the interface (see section 5.2.2). Anions in these polyhedra were constrained to form a partial oxygen layer parallel to the interface. The effect of this constraint on borate and silicate tetrahedra is to cause their faces or edges to sit parallel to the interface leading to the formation of a layer in which many of the borate and silicate polyhedra had common alignments.

In addition it was shown in section 5.2.2 that network forming species became associated with particular sites at the ceramic surface. For instance, Si and B atoms tended to sit over anion sites

Figure 5.30: Slices taken through the electric field above {100} surface of MgO (slices are in the *bc* plane).
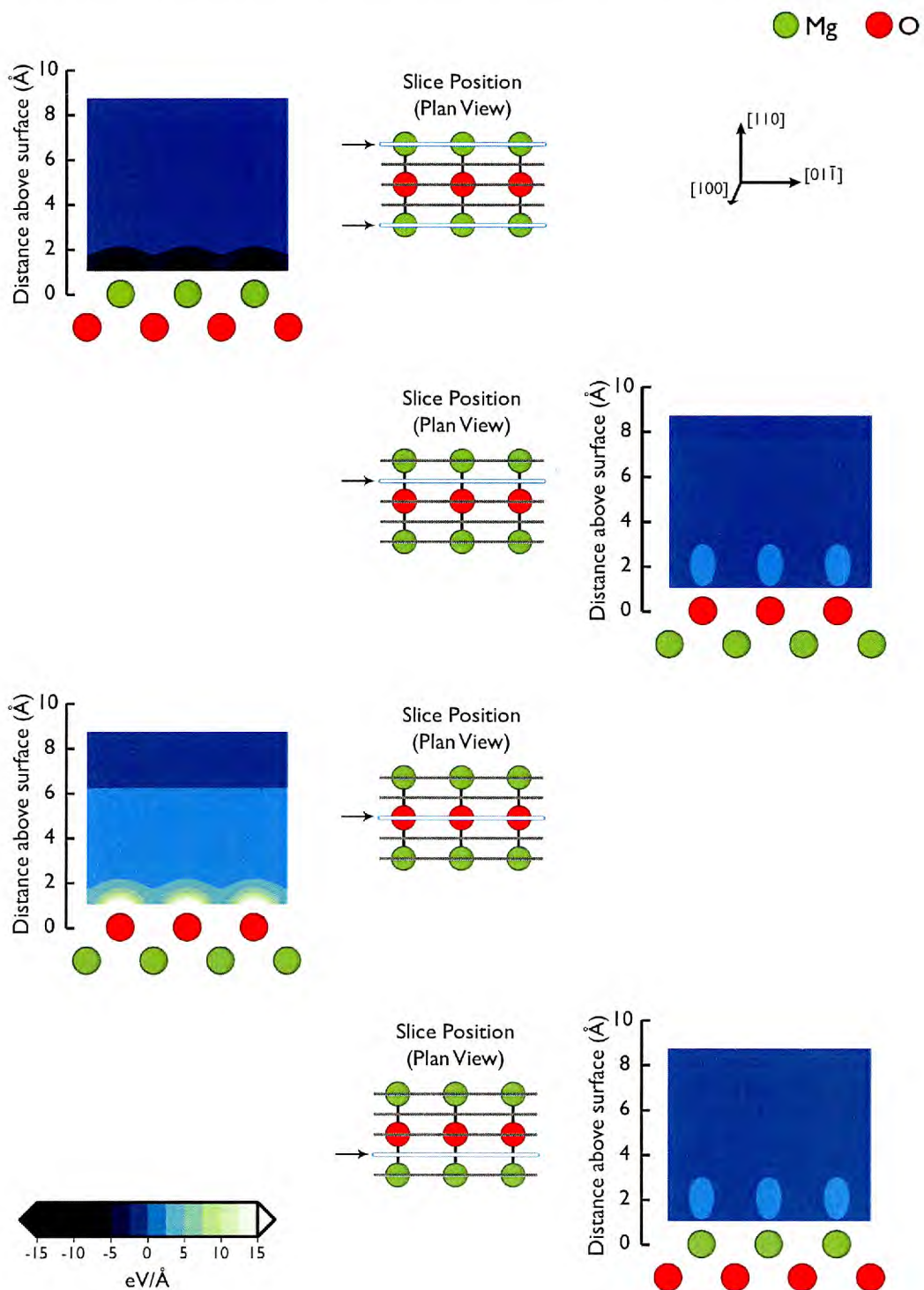
Figure 5.31: Contour plots showing slices taken through the electric field above the {110} surface of MgO (slices are in the (100) plane).

whereas glass anions were associated with cation sites at MgO interfaces, and with ceramic interstices at the CaO, SrO and BaO interfaces. The regular arrangement of sites at the crystal surface meant that, the glass polyhedra in a layer near the interface were partly arranged on a grid. Compared to the bulk glass, the layer of glass near the interface was relatively ordered and had taken on much of the character of a ceramic surface.

The constraints imposed by the ceramic surface would be expected to limit the amount by which silicate and borate polyhedra in the ordered layer close to the interface could relax to accommodate the bulk glass. Instead, the silicate and borate polyhedra in the glass adjacent to this constrained layer would be expected to adopt similar orientations to those in the constrained layer, in order to continue the corner sharing glass network. In this way, some of the constraints imposed by the ceramic on the glass near the interface would be propagated through the glass. This could then continue, layer by layer, as glass units partly aligned themselves to the previous layer.

5.3.2   Lack of Periodicity in SiO_2

Density oscillations were found in the oxygen density profiles of all the interfacial systems considered, with one notable exception: the interface between SiO_2 and MgO-(100). This is interesting as the SiO_2 glass did not contain network modifiers.

The formation of densified layers of oxygen and silicon at the MgO-(100) interfaces of the SiO_2+Na and SiO_2+Na+Li glasses indicated that some order had been imparted to the glass' silicate network at these interfaces. By comparison, the SiO_2 MgO-(100) interface showed no such ordering.

Although some silicate tetrahedra shared an anion with the MgO surface, the alignment of tetrahedral edges along $< 110 >$ witnessed at other MgO-(100) interfaces did not occur. A prerequisite of layering via the templating mechanism proposed above is the formation of an ordered layer of tetrahedra close to the interface. In the ordered layers seen at other interfaces, the position of tetrahedra became correlated to the surface, taking on preferred orientations which were related to the structure of the ceramic surface. Without this ordering templating

and therefore layering could not occur.

Of the glasses considered, the SiO_2 composition had the most polymerised network; the majority of silicate units shared bridging oxygens with another four tetrahedra. This high degree of polymerisation would be expected to limit the glass' conformational freedom. It seems likely that this lack of freedom prevented the alignment of tetrahedral edges along the $< 110 >$ directions of the MgO surface. As each tetrahedron was highly connected, alignment would require the concerted motion of many, interconnected tetrahedra. It seems therefore that the SiO_2 network was too constrained to allow its tetrahedra to explore conformational space and find the favourable low energy orientations seen at other MgO-(100) interfaces. In the absence of a layer of partially ordered glass, templating and layering could not take place.

Chapter 6

Pyrochlore: A Ceramic Wasteform

$A_2B_2O_7$ pyrochlores are a class of ceramic materials which have been suggested as hosts for the long term storage of high level nuclear waste. Several compositions with the pyrochlore and closely related disordered fluorite crystal structures have shown excellent radiation tolerance to heavy ion bombardment [138,139]. Unfortunately, there is a paucity of published experimental data describing the effects of irradiation on the dimensional stability of these materials. In an effort to rectify this situation, the following chapter presents the results of a systematic study which attempted to predict the volume change experienced by a series of rare-earth pyrochlore materials when amorphised or otherwise disordered so as to mimic the effects of irradiation.

The transformation of pyrochlore to disordered fluorite can also be thermally induced. In the second part of this chapter, predictions for the order to disorder transformation temperature for a series of zirconate pyrochlores will be presented. This also has implications to wasteform design as, at least initially, the radioactive species in the waste generate considerable heat. This may induce an order disorder transformation, though this may also aid in recovery from radiation damage events.

6.1   Pyrochlore's Crystal Structure

Pyrochlore occurs naturally as a mineral which has the following chemical formula $(NaCa)(NbTa)O_6F/OH$. Technologically, however, pyrochlore usually refers to materials with the formula $A_2B_2O_7$ (where A and B are cations). There are about 150 ternary oxides with a $A_2B_2O_7$ stoichiometry and a structure closely related to the pyrochlore mineral [140]. These exist in two general forms; the (3+, 4+) and (2+, 5+) pyrochlores which have the chemical formulae of $A_2^{3+}B_2^{4+}O_7$ and $A_2^{2+}B_2^{5+}O_7$ respectively [141]. The results presented in this chapter pertain to (3+, 4+) pyrochlores.

The full cubic pyrochlore unit cell is shown in figure 6.1 and has the $Fd\bar{3}m$ space group. If the unit cell origin is chosen to coincide with a B^{4+} cation [1] the atom positions, described using Wyckoff notation are as follows [143]:

Species	Wyckoff Positions
A^{3+}	$16d$
B^{4+}	$16c$
O^{2-}	$48f, 8b$

In pyrochlore the large A^{3+} cations sit on $16d$ sites within distorted cubic polyhedra and are coordinated by eight oxygen atoms. The small B^{4+} cations on the $16c$ site form corner sharing sheets of distorted BO_6 octahedra, in three and six membered rings parallel to the (111) plane [14]. In the anion sublattice, oxygen atoms at the $48f$ site are coordinated by two B^{4+} and two A^{3+} cations, whilst those at $8b$ are tetrahedrally coordinated by A^{3+} cations.

---

[1]origin choice 2 from the *International Tables For X-Ray Crystallography* [142]
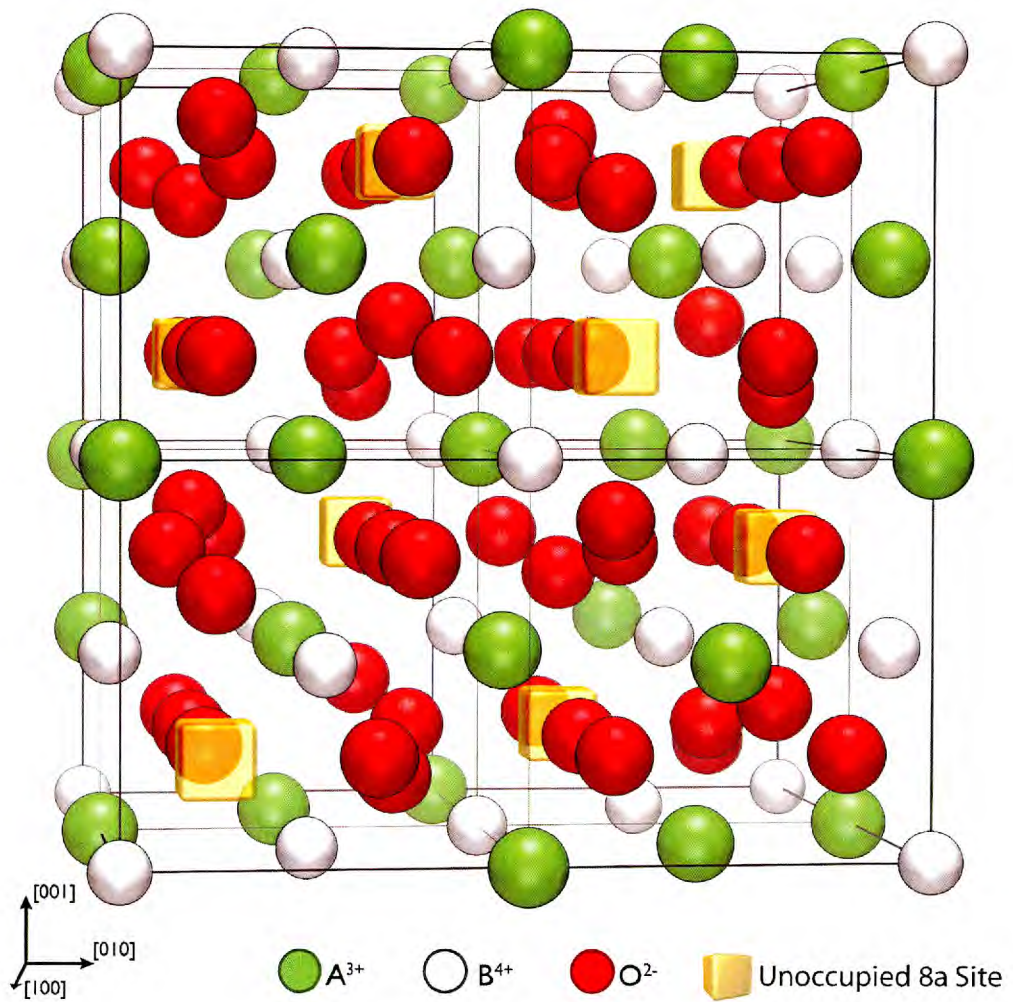
Figure 6.1: The full $A_2B_2O_7$ unit cell (subdivisions for fluorite related 1/8 cell are also highlighted).

6.1.1 Pyrochlore and its Relationship to Fluorite

The structure of pyrochlore is closely related to that of $B^{4+}O_2^{2-}$ fluorites. This similarity is demonstrated in figure 6.2 where $\frac{1}{8}$ of the full pyrochlore cell (figure 6.2a) is compared with the full fluorite cell (figure 6.2b). From these diagrams it can be seen that, in effect, pyrochlore is a fluorite in which half the B^{4+} cations have been replaced with A^{3+} and the $8a$ site is unoccupied in order to maintain charge neutrality.

The oxygen atoms in figure 6.2a were shown at their ideal, unrelaxed positions to allow better comparison with the fluorite structure (this corresponds to a $48f$ oxygen positional parameter of 0.375). In reality there is significant relaxation of the surrounding ions towards the unoccupied $8a$ site [144]. This is illustrated in figure 6.3, which shows the relaxed structure of $La_2Zr_2O_7$ (which has a $48f$ positional parameter of 0.333 [139]).

6.1.2 Pyrochlore, Defects and Disorder

As the sizes of the A and B cations become more similar, $A_2B_2O_7$ stoichiometric compositions with the pyrochlore structure can exhibit an order-disorder transformation to an oxygen deficient, disordered fluorite structure [140]. In the disordered state, A cations sit on B sites and vice versa. Disordering also occurs on the anion sublattice where the normally unoccupied $8a$ oxygen site becomes partially occupied with the formation of vacancies on the $48f$ and $8b$ anion sites. There also exists a threshold in the A:B radius ratio beyond which $A_2B_2O_7$ compositions no longer exhibit the ordered cubic pyrochlore structure, even after lower temperature anneals for extended periods. Broadly speaking, in terms of the A:B radius ratio, the pyrochlore stability range extends between 1.46 (e.g. $Gd_2Zr_2O_7$) and 1.78 (e.g. $Sm_2Ti_2O_7$) [138]. Figure 6.4 shows the extent of the pyrochlore and defect fluorite phase fields. The boundaries of these regions were determined from computer simulations by Minervini *et al.* [145]. In the lower right hand corner, a region containing compositions that are found as disordered fluorites is shown. Moving towards the top left corner, a region containing cubic pyrochlore compositions is shown. The region indicated in the top left hand corner contains compounds which have been observed experimentally to form non-cubic phases; the precise bounds of this region
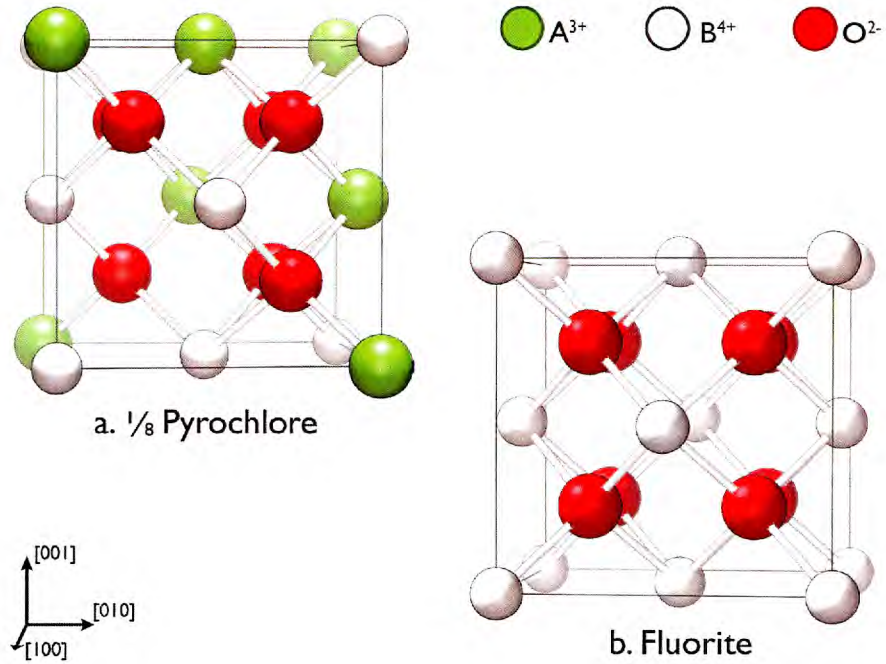
Figure 6.2: The pyrochlore structure can be thought of as an oxygen deficient fluorite.
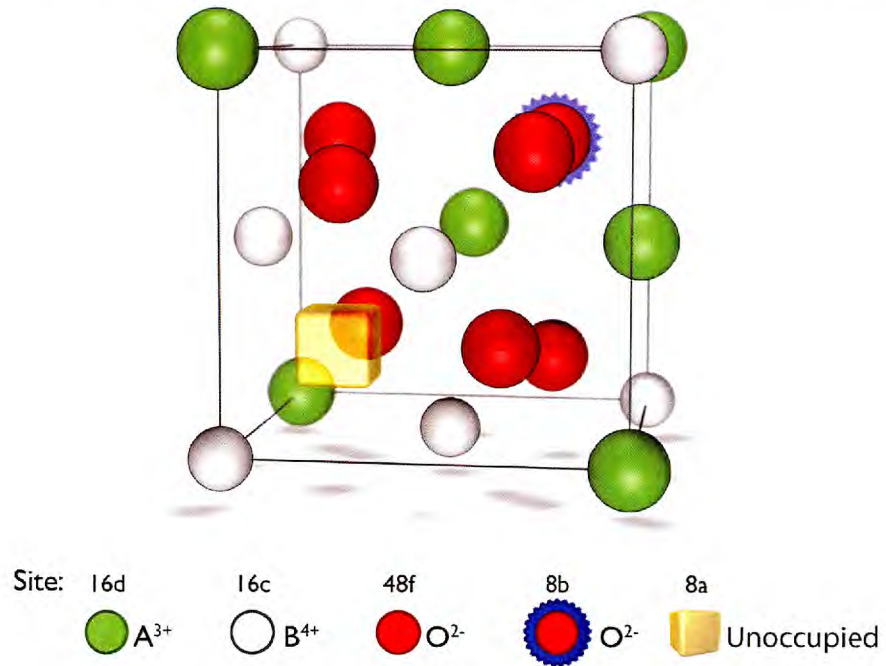
Figure 6.3: One eighth of the full pyrochlore unit cell, showing relaxation of anions towards unoccupied 8a site.

are unknown. Next to the disordered fluorite region, several compositions have been found to exhibit the δ-phase structure [146][2].

For specific compositions, the change from ordered pyrochlore to disordered fluorite can be thermally activated. Above a critical temperature, the pyrochlore structure can spontaneously transform to become disordered fluorite. Compositions which undergo this transformation are often located close to the pyrochlore-fluorite phase boundary and include $Gd_2Zr_2O_7$. A list of experimentally determined transformation temperatures is listed in table 6.1 for zirconate and hafnate pyrochlores. From these it can be seen that the transition temperature decreases as A, B cation size mismatch decreases. By comparison, no thermally induced order disorder transformation has been seen in rare-earth titanate pyrochlores [14].

A knowledge of the disordered state is also critical to understanding the radiation tolerance behaviour of pyrochlore and its related oxides. Bombardment of materials using beams of heavy ions (such as Pb^+ or Kr^+) is often used to simulate the effects of radiation damage due to α decay. Lian et al. have shown that ordered $Gd_2Zr_2O_7$ undergoes a transformation to disordered fluorite when bombarded by 1.5 MeV Xe^+ ions [152]. Even though the ion dose was estimated to have caused 34 displacements per atom (dpa), the disordered $Gd_2Zr_2O_7$ structure remained crystalline and did not amorphise. Other zirconate pyrochlores have also been reported as showing good radiation tolerance; having first transformed to disordered fluorite, $Sm_2Zr_2O_7$ and $Nd_2Zr_2O_7$ resisted amorphisation under bombardment at high ion fluences [139]. Furthermore, Sickafus et al. have demonstrated that $Er_2Zr_2O_7$ remains crystalline even at a dose of 140 dpa (5×10^{16} ions/cm^2 by 350 keV Xe^+ at room temperature) [141, 153]. To put these figures into context, $Gd_2Ti_2O_7$ amorphised at a dose of 0.18 dpa [152], $Er_2Ti_2O_7$ at 0.25 dpa whilst $Lu_2Ti_2O_7$ was slightly more tolerant at 0.51 dpa [154]. It must be highlighted that, although they show worse radiation tolerance than zirconate pyrochlores, these titanate ceramics are still considered radiation tolerant when compared with most ceramics.

Sickafus et al. [141] argue that the cation antisite defect formation energy can be used to predict radiation damage behaviour. As cation antisite defects are an unavoidable consequence of

---

[2]$A_4B_3O_{12}$ δ-phase materials are rhombohedral materials (exhibiting the $R\bar{3}$ space-group), that are structurally similar to pyrochlore. [147]
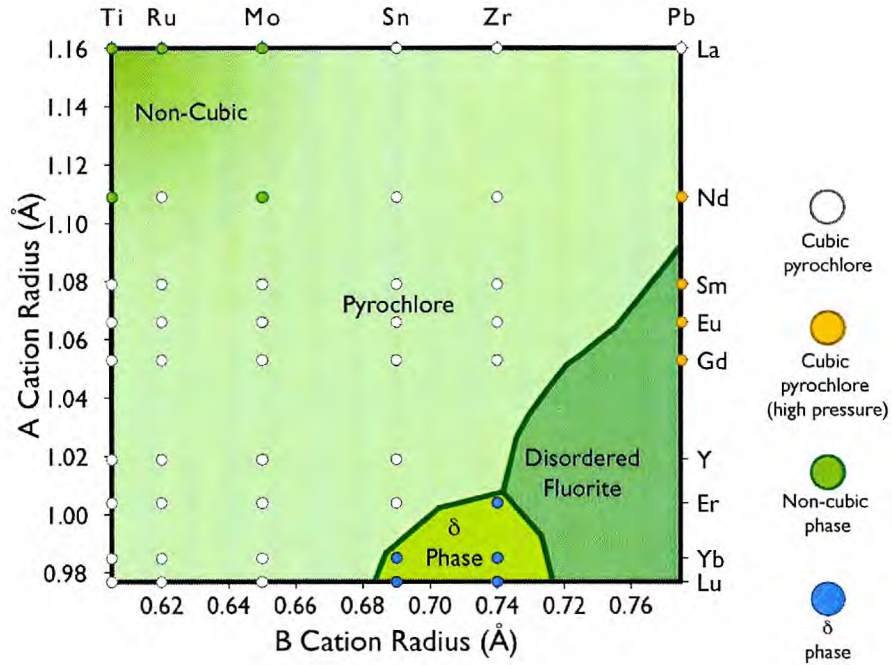
Figure 6.4: Pyrochlore stability map showing the extent of different phase fields predicted by Minervini [145], this is overlaid with points showing where experimentally observed pyrochlore compositions [140].

System	Order-Disorder Temperature (K)	Ref.
$Gd_2Zr_2O_7$	1803	[148]
$Sm_2Zr_2O_7$	2273	[148]
$Nd_2Zr_2O_7$	2573	[148]
$Tb_2Hf_2O_7$	2423	[149]
$Gd_2Hf_2O_7$	2623	[149]
$Eu_2Hf_2O_7$	2723	[150]
$Sm_2Hf_2O_7$	2823	[151]

Table 6.1: Experimentally determined order-disorder transformation temperatures for hafnate and zirconate pyrochlores.

displacive radiation environments, it is argued that those compounds with large defect forma-
tion energies would be expected to undergo destabilisation of their crystal structures and then
amorphisation (due to the larger retained energy). In Kröger Vink notation (see reference [155]
for details) the cation antisite formation reaction can be expressed as:

$$A_A^\times + B_B^\times \longrightarrow A_B' + B_A^\bullet \qquad (6.1)$$

An extensive set of atomic scale computer simulations were conducted by Minervini *et al.*
to determine the isolated cation antisite defect formation energies for a wide range of rare
earth pyrochlores [141, 145]. As might be expected, this showed that antisite formation was
energetically expensive in those compounds in which the *A* cation was much larger than the
B cation (i.e. a large *A* : *B* radius ratio). These compounds would be expected to amorphise
under irradiation whereas compositions with more similar radii would be more robust. These
findings correspond well with available ion bombardment results [139, 141, 152, 154].

In simple terms, it is thought that, compositions which tolerate the cation disorder associ-
ated with becoming a defective fluorite, can also tolerate the additional disorder imparted by
the displacive radiation effects caused by α-decay. As a result, compositions sitting close to
the pyrochlore-fluorite phase boundary exhibit good radiation tolerance. Pyrochlores with a
stronger tendency towards cation ordering, such as the titanate series, show a greater propen-
sity for amorphisation in displacive radiation environments.

As the level of disorder increases in the cation sublattice, the $8b$ and $48f$ oxygen sites become
more and more crystallographically equivalent. As a consequence of this, Wilde and Cat-
low [156] found that the presence of disordering in the cation sublattice dramatically reduced
the formation energy of Frenkel defects through:

$$A_A^\times + B_B^\times + O_O^\times \longrightarrow A_B' + B_A^\bullet + V_{O(48f)}^{\bullet\bullet} + O_{i(8a)} \qquad (6.2)$$
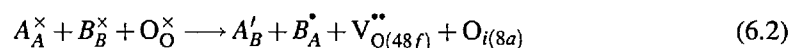
This is an interesting result as it shows that disordering of the cation lattice encourages an-
ion disordering. The work of Minervini [145] confirmed this view and further indicated that

clustering of cation antisite and oxygen Frenkel defects was important. Over the range of compositions considered, the energy of the defect reaction given in equation 6.2 was 3–6 eV when defect association was not considered. This energy fell by approximately 1 eV when clustering was introduced. This shows that it is important to consider defect associations when modelling disorder in pyrochlore and its related phases.

6.2 Volume Change

As a general rule, radiation induced volume change in immobilised nuclear waste is undesirable. For instance in a multi-barrier containment system [11], large volume increases could breech the canisters into which the immobilised waste had been placed. Alternatively, localised volume changes could lead to large internal strain within a material, causing microcracking and increased waste dissolution rates [138]. Along with chemical durability, thermal stability and radiation tolerance, dimensional stability is therefore an important selection criterion for nuclear waste materials. In an effort to help inform materials selection, the following section presents predictions for radiation induced volume change in pyrochlore and related oxides. Simulations were performed that considered transformations between pyrochlore, disordered fluorite and an amorphous state for a wide range of pyrochlore compositions.

Swelling can be defined as the dose dependent volume change a material experiences on irradiation (where dose is the number of α decay events per unit mass). For pyrochlore related materials this can be expressed as [138]:

$$\frac{\Delta V(d)}{V_0} = f_C \frac{\Delta V_C(d)}{V_0} + f_A \frac{\Delta V_A(d)}{V_0} + \frac{V_{EX}(d)}{V_0} \qquad (6.3)$$

where:

d	=	Radiation dose
V_0	=	Original volume of pyrochlore
$\Delta V(d)$	=	Overall volume change

f_C =   Crystalline fraction of material, by mass

f_A =   Amorphous fraction of material, by mass

$\Delta V_C(d)$ =   Volume change of crystalline component of irradiated material

$\Delta V_A(d)$ =   Volume change of amorphous component of irradiated material

$V_{EX}(d)$ =   Volume of extended void like microstructures

As radiation dose increases, the volume of the material tends also to increase [138]. This can be caused by an increase in the material's amorphous fraction or an increasingly disordered pyrochlore lattice. Beyond a critical dose however, the volume change levels off and increasing dose does not yield increased swelling. Depending on composition, this normally occurs when the material has either fully amorphised or become fully disordered. The aim of the current work was to calculate this saturation volume change and hence produce "worst-case" predictions for swelling under repository conditions. For this reason, the volume of pyrochlore compositions, amorphised using a melt-quench method were calculated to produce values for $\frac{\Delta V_A}{V_0}$. Similarly the volume change experienced on going from ordered pyrochlore to disordered fluorite were calculated to give values for $\frac{\Delta V_C}{V_0}$. Under typical actinide immobilisation conditions $V_{EX}(d)$ is negligible for most pyrochlore compositions [138]. For this reason volume changes due to void, pore and bubble formation and micro-cracking were not considered.

6.2.1 Volume Change on Becoming 100% Disordered

Two methods were used to calculate the volume of pyrochlore on becoming a fully disordered fluorite. In the first, the relaxation volumes, for defect clusters representing 100% disorder were calculated. The second represented disorder using large supercells, which were relaxed using isobaric molecular dynamics. The exact details of these different methodologies are described below. Volume changes on going from ordered pyrochlore to disordered fluorite and to the amorphous state were calculated for each of the unique pairs of A and B cations in table 6.2. In addition, the volume change on going from disordered fluorite to the amorphous state was calculated.

A^{3+} Cations	La, Nd, Sm, Eu, Gd, Y, Er, Yb, Lu
B^{4+} Cations	Ti, Ru, Mo, Sn, Zr, Pb

Table 6.2: Compositions for which volume changes were calculated.

Defining 100% Disorder

On undergoing disorder, A^{3+} ions can move from their original $16c$ sites onto $16d$ sites. This is accompanied by the movement of B^{4+} from $16d$ to $16c$ sites. In a fully disordered fluorite, 50% of A sites would be occupied by B cations and 50% B sites would be occupied by A cations. This is expressed in terms of site occupancies for the $16c$ and $16d$ sites in table 6.3.

Applying the same treatment to the anion lattice: there are 64 sites on which oxygen atoms can sit (i.e. $48f$, $8b$ and the normally unoccupied $8a$ site). Again, if it is assumed that there is an equal chance that any anion species can occupy any site available to it, then the 56 oxygen atoms in the full pyrochlore unit cell would be uniformly distributed amongst the 64 available anion sites in the fully disordered state. In other words, the anion occupancy for each oxygen site becomes $56/64 = \frac{7}{8}$ as summarised in table 6.3.

Species	Site	Site Occupancy
A^{3+}	$16c$	0.5
	$16d$	0.5
B^{4+}	$16c$	0.5
	$16d$	0.5
O^{2-}	$8a$	0.875
	$8b$	0.875
	$48f$	0.875

Table 6.3: Site occupancies for fully disordered fluorite.

Relaxation Volume Calculation using Mott-Littleton Method

The first method used to calculate the volume change on going from pyrochlore to fluorite involved using static energy minimisation to calculate the volume change experienced when a small area of disorder, represented by a cluster of point defects, was introduced into the perfect pyrochlore lattice. The change in volume due to these defects (the so called defect volume) can be obtained from defect energies calculated using the Mott-Littleton method, as described by Grimes *et al.* [157] for the spinel system and originally described by Catlow *et al.* [158]. In this method, defect volumes (V_p) are obtained from the following relationship:

$$V_p = -K_T V_0 \left(\frac{df}{dV} \right)_T \tag{6.4}$$

where:

V_p = Defect volume $(\text{\AA}^3)$

K_T = Isothermal compressibility $(\text{\AA}^3 \text{eV}^{-1})$

V_0 = Pyrochlore unit cell volume $(\text{\AA}^3)$

$\left(\frac{df}{dV} \right)_T$ = Isothermal variation of free energy with cell volume $(\text{eV\AA}^{-3})$

Isothermal compressibility, K_T, is obtained by taking the reciprocal of bulk modulus (K). For a cubic material this is [159]:

$$K_T = \frac{3}{(c_{11} + 2c_{12})} \tag{6.5}$$

where c_{ij} are members of the material's elastic constant tensor. Values of c_{ij} and hence K_T were obtained from constant pressure simulations of the perfect pyrochlore lattice. Values for V_0 were also obtained from these calculations.

The value of $\left(\frac{df}{dc}\right)_T$ (where c is lattice parameter) was obtained for each pyrochlore composition using a finite difference method. Cluster defect formation energies (f) were calculated for a series of lattice parameters, by performing constant volume calculations. The values of c chosen for these simulations were taken either side of the constant pressure lattice parameter obtained from perfect lattice energy minimisation. In practice lattice parameters 1% and 2% above and below the constant pressure lattice parameter were used. Including the constant pressure value, this gave five values for defect energy and lattice parameter per system. Finally, $\frac{df}{dc}$ was obtained by plotting f against c and taking the gradient of the data's line of best fit. The Mott-Littleton calculations were performed using the CASCADE code [80].

The observant reader will have noticed that in equation 6.4, defect volume was calculated from $\frac{df}{dV}$, however the procedure described in the previous paragraph gives $\frac{df}{dc}$. For this reason, defect volumes were calculated using the following modified form of equation 6.4:

$$V_p = -\frac{cK_T}{3}\frac{df}{dc} \tag{6.6}$$

Defect clusters were chosen to represent a fully disordered pyrochlore with the site occupancies listed in table 6.3. To obtain a site occupancy of 0.5 for A cations on B sites, $8 \times A'_B$ antisite defects are required and $8 \times B^{\bullet}_A$ are required on the B sites.

In terms of anion defects, $\frac{1}{8}$ of the $48f$ sites, are unoccupied, meaning that $6 \times V^{\bullet\bullet}_{O(48f)}$ are required. In the same way, one $8b$ oxygen vacancy is required to account for the partial occupancy of this site. Conversely, seven interstitial defects are required on the $8b$ site to represent an occupancy of $\frac{7}{8}$. In summary, the point defects required to represent a disordered fluorite are as follows:

$$8 \times A'_B$$
$$8 \times B'_A$$
$$6 \times V^{\bullet\bullet}_{O(48f)}$$
$$1 \times V^{\bullet\bullet}_{O(8b)}$$

$$7 \quad \times \quad O''_{i(8a)}$$
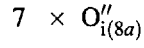
As described earlier, Minervini *et al.* showed that defect clustering must be taken into account when modelling disorder in pyrochlore related oxides [145]. She found that the most stable cluster configuration in $A_2B_2O_7$ pyrochlore was made up of an anion Frenkel defect and two cation antisite defects in nearest neighbour positions:

$$\left\{ A'_B : B^{\bullet}_A : V^{\bullet\bullet}_{O(48f)} : O''_{i(8a)} \right\}^{\times} \tag{6.7}$$
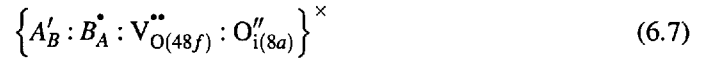
Henceforth this cluster will be referred to as cluster A. The full complement of point defects listed above cannot, however, be arrived at with this cluster alone. A maximum of six of these clusters can be used in the pyrochlore cell before excess $V^{\bullet\bullet}_{O(48f)}$ defects are introduced. A second cluster (cluster B) was introduced which comprised of the defects remaining after six instances of cluster A had been accounted for:

$$\left\{ 2A'_B : 2B^{\bullet}_A : V^{\bullet\bullet}_{O(8b)} : O''_{i(8a)} \right\}^{\times} \tag{6.8}$$
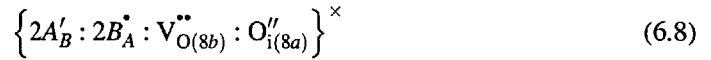
The defect volumes associated with the lowest energy configurations of clusters A and B were calculated for each pyrochlore composition. From these, the overall volume changes on going from ordered pyrochlore to disordered fluorite were calculated thus:

$$\frac{\Delta V_C}{V_0} = \frac{6 \times V_{clusterA} + V_{clusterB}}{V_0} \tag{6.9}$$

where $V_{clusterA}$ and $V_{clusterB}$ are the defect volumes for cluster A and cluster B respectively.

Supercell Calculations

In addition to the cluster calculations described in the previous section, disordered supercells were created (as described below) then equilibrated using isobaric molecular dynamics. The

volume of a disordered fluorite was obtained from the size of the cell averaged over the data collection stages of equilibration.

A $3 \times 3 \times 3$ pyrochlore supercell containing 2376 atoms was used as the starting point from which disordered cells were generated. The initial dimensions of the simulation cell were determined from the results of static energy minimisation of the pyrochlore structure.

A simple model for disorder was assumed. For each composition, the A^{3+} and B^{4+} ions were assigned randomly to the available 16c and 16d sites. A similar procedure was employed on the oxygen sub-lattice, where anions were distributed not only to the 48f and 8b sites occupied in pyrochlore but also to the normally unoccupied 8a site. The resulting supercell was then equilibrated using the following series of molecular dynamics runs:

1. Molecular dynamics performed for 7.5ps at 1500K in the canonical (NVT) ensemble.

2. NPT equilibration at 1500K.

3. NPT quench to 1200K.

4. NPT equilibration at 1200K.

5. NPT quench to 900K.

6. NPT equilibration at 900K.

7. NPT quench to 600K.

8. NPT data collection at 600K.

9. NPT quench to 300K.

10. NPT equilibration and data collection at 300K.

The quench steps listed above were achieved by an iterative procedure where temperature was reduced in 10K steps with 0.1ps of molecular dynamics being performed at each temperature. Equilibration stages were 7.5ps long and during the data collection steps, cell volume was sampled at 0.05ps intervals. All dynamics runs used a timestep of 1fs.

Temperature was maintained during dynamics calculations by using the Nosé-Hoover thermostat. Isobaric simulation steps used the anisotropic Hoover barostat and were performed with 0Pa of applied pressure. This barostat allowed both cell volume and shape to vary during molecular dynamics. Both the thermostat and barostat had a relaxation time of 0.5ps. Calculations were performed using version 2.14 of the DL_POLY simulation code [160].

For each composition, five randomised fluorite super-cells were examined. The results presented later are the average of these five structures. As each $3 \times 3 \times 3$ supercell contained 27 pyrochlore cells, this effectively meant that 135 disordered pyrochlore cells were sampled for each composition. In practice, the energies of the five different randomised cells were found to be very similar. For example, the average total energy at 300K for the five $Gd_2Ti_2O_7$ cells was 272.8 eV per $A_2B_2O_7$ formula unit and only had a standard deviation of 0.04 eV. Similarly, the average energy of the five disordered $Gd_2Zr_2O_7$ cells was 262.4 eV per formula unit, and had a standard deviation of 0.05 eV.

In addition MD derived V_0 values were calculated for each composition by performing 7.5ps of NPT equilibration at 300K on an ordered $3 \times 3 \times 3$ pyrochlore cell.

6.2.2 Volume Change on Becoming Amorphous

Amorphous structures were created from $3 \times 3 \times 3$ pyrochlore supercells using a melt-quench method. The melt-quench 'recipe' was as follows:

1. 15ps NVT randomisation stage at 7000K (9000K for titanates).

2. NVT quench to 5000K.

3. NPT quench to 1500K.

4. NPT equilibration for 7.5ps at 1500K.

5. NPT equilibration at 1500K.

6. NPT quench to 1200K.

7. NPT equilibration at 1200K.

8. NPT quench to 900K.

9. NPT equilibration at 900K.

10. NPT quench to 600K.

11. NPT data collection at 600K.

12. NPT quench to 300K.

13. NPT equilibration and data collection at 300K.

The details of the quench and equilibration stages were the same as those used during the simulation of the disordered structures described above and is similar to that used when creating the silicate and borosilicate glasses described in earlier chapters (see chapter 2). With the exception of $A_2Ti_2O_7$ compositions the initial randomisation stage of the melt-quench process was performed at a temperature of 7000K. However, certain titanate compositions failed to amorphise at this temperature, as a consequence, the titanates were heated to 9000K. All the structures resulting from melt-quenches were examined using molecular visualisation to confirm that they had amorphised. As before volumes were sampled every 0.05ps at 300K during the data collection stage of the simulation.

Pair Potentials

As with the glass simulations presented earlier, short range atomic interactions between ions in the pyrochlore system were described using classical pair-potentials. A slightly different potential form was employed than with the glass systems; pair interactions were described using the Buckingham potential [161]:

$$\phi_{short} = A \exp\left(\frac{-r_{ij}}{\rho}\right) + \frac{C_{ij}}{r_{ij}^6} \qquad (6.10)$$

where A, ρ and C are parameters specific to pairs of interacting species. As before, ϕ_{short} was the potential energy between a pair of ions (i and j) separated by r_{ij}. Electrostatic forces were calculated using the Ewald sum [64].

The potentials used during both the molecular dynamics and Mott-Littleton volume calculations were based on those by Cleave [146]. These used partial charges of -1.7, $+2.55$ and $+3.4$ for the O, A and B ions respectively. The values of A, ρ and C used can be found in table 6.4.

6.2.3 Volume Change Predictions

Having obtained volumes for pyrochlore compositions in the ordered, disordered and amorphous states, it was possible to calculate the volume change associated with moving between from one state to another. The following state changes were calculated: pyrochlore to amorphous, fluorite to amorphous and pyrochlore to fluorite. These were obtained simply by taking the volume difference between each state. For example, the volume change on going from pyrochlore to amorphous was calculated by subtracting the volume of the pyrochlore cell from the volume of the amorphous simulation cell. The volume change was then expressed as a percentage of the original state (in this case as a percentage of the original pyrochlore cell size).

As shown earlier (section 6.1.1), the fluorite unit cell is comparable with $\frac{1}{8}$ of the full pyrochlore cell; the lattice parameter of the fluorite cell being half that of the equivalent pyrochlore structure. The dimensions of a $2 \times 2 \times 2$ fluorite supercell are therefore directly comparable to those of the equivalent pyrochlore unit cell. The volume changes that follow, were calculated against this comparable cell. For example, the volume change, on going from pyrochlore to disordered fluorite is the volume change between a full pyrochlore cell and a cell containing eight fluorite unit-cells.

Interacting Species	A (eV)	ρ (Å)	C (eV Å^6)
$Er^{2.55+}$–$O^{1.7-}$	2103.60	0.3097	17.55
$Eu^{2.55+}$–$O^{1.7-}$	2172.45	0.3168	20.59
$Gd^{2.55+}$–$O^{1.7-}$	2165.40	0.3158	19.90
$La^{2.55+}$–$O^{1.7-}$	2306.26	0.3263	23.25
$Lu^{2.55+}$–$O^{1.7-}$	2069.99	0.3067	16.87
$Mo^{3.4+}$–$O^{1.7-}$	1901.50	0.3011	0.00
$Nd^{2.55+}$–$O^{1.7-}$	2205.88	0.3206	22.59
$O^{1.7-}$–$O^{1.7-}$	4870.00	0.2670	77.00
$Pb^{3.4+}$–$O^{1.7-}$	2005.10	0.3203	19.50
$Ru^{3.4+}$–$O^{1.7-}$	1883.39	0.2954	0.00
$Sm^{2.55+}$–$O^{1.7-}$	2179.20	0.3181	21.28
$Sn^{3.4+}$–$O^{1.7-}$	1945.41	0.3099	13.66
$Ti^{3.4+}$–$O^{1.7-}$	1865.80	0.2946	0.00
$Y^{2.55+}$–$O^{1.7-}$	2107.60	0.3109	17.51
$Yb^{2.55+}$–$O^{1.7-}$	2075.26	0.3076	16.57
$Zr^{3.4+}$–$O^{1.7-}$	1953.80	0.3109	5.10

Table 6.4: Short range pair potential parameters: Partial charge model.

Contour plots

Contour plots provide a convenient way for elucidating the trends in smoothly varying sets of related data. As a consequence, contour maps were used to show the results of the volume change calculations. These were constructed by ordering B^{4+} cation radius along the x-axis whilst the A^{3+} radii were ordered along the y-axis. The material property of interest (i.e. volume change predictions) were shown in the contour plots by levels of varying colour. Hot colours represented high values and cold colours, low values. Points at which simulations had been performed were indicated using white circles overlaid onto the plot. The filled regions were bounded by contour lines connecting values with the same property value. All cation radii were taken from Shannon [118]; VIII coordinate radii were used for the A^{3+} cations and VI coordinate radii were used for the B^{4+} cations. Values falling between simulation results were obtained using a spline based interpolation scheme [162]. All contour maps were made using the Generic Mapping Tools computer package [163].

Volume Changes Associated with Irradiation Processes

Contour plots showing volume change on going from ordered pyrochlore to the amorphous state and from fluorite to amorphous are shown in figures 6.5 and 6.6 respectively. Two methods were used to calculate the volume change from pyrochlore to fluorite. The results of the supercell method appear in figure 6.7 whilst those calculated using the cluster method are given in figure 6.8.

The general trend, observed in all the contour plots, shows volume change decreasing from the top left to the bottom right of the contour plots. In other words, volume change tended to decrease as B cation radius increased and A cation radius decreased (a decrease in $A:B$ cation radius ratio). In terms of the magnitude of change, the fluorite to amorphous results yielded the largest variation, with volume changes ranging from $\sim 10\%$ in $La_2Ti_2O_7$ to 2% for $Lu_2Pb_2O_7$. The pyrochlore to fluorite transformation yielded a smaller range and the fluorite to amorphous volume changes were almost independent of composition showing only a $\sim 2\%$ variation across the compositional range considered.
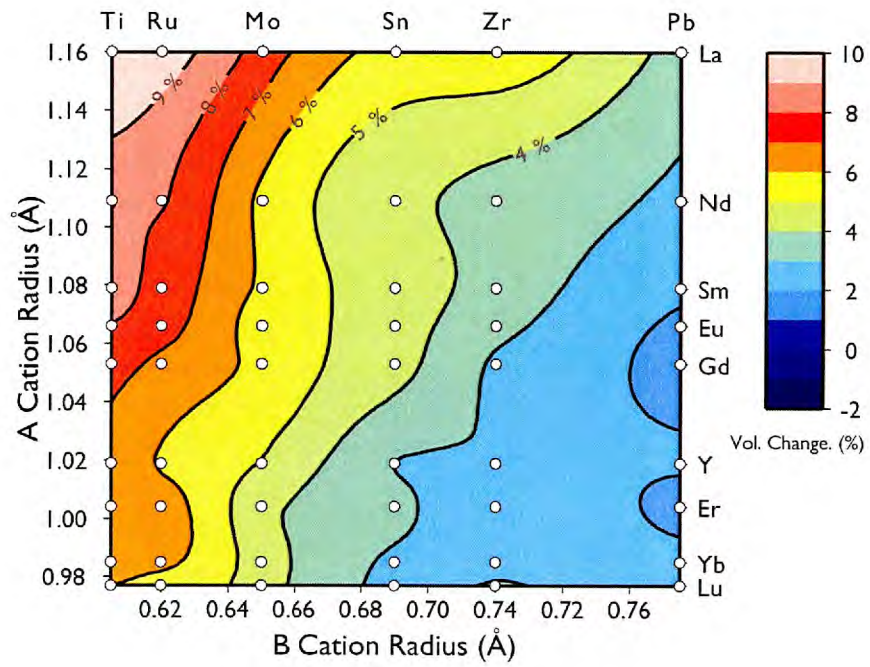
Figure 6.5: Volume change between ordered pyrochlore and amorphous state, calculated from MD results.
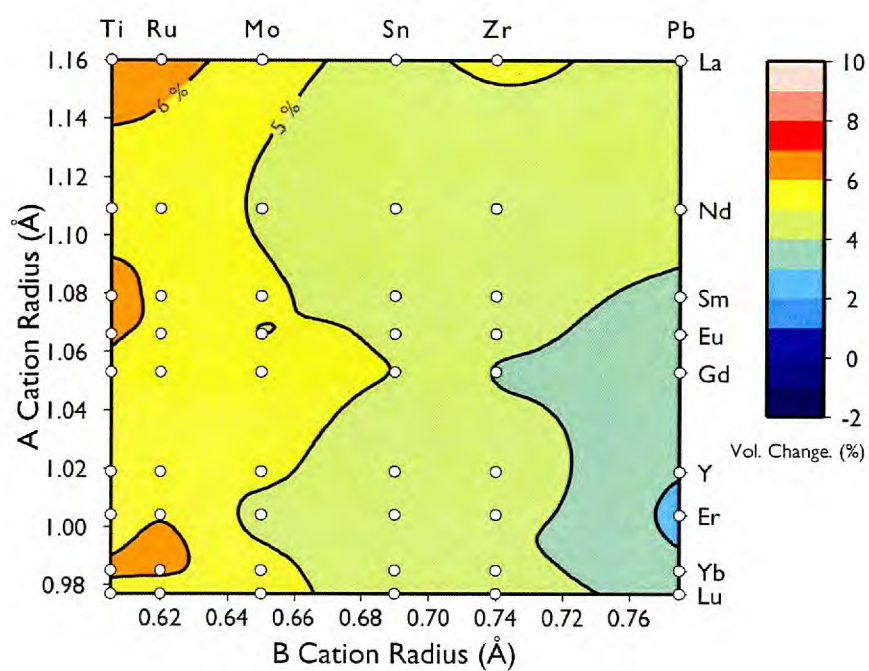
Figure 6.6: Volume change on going from disordered fluorite to amorphous state, calculated from MD results.
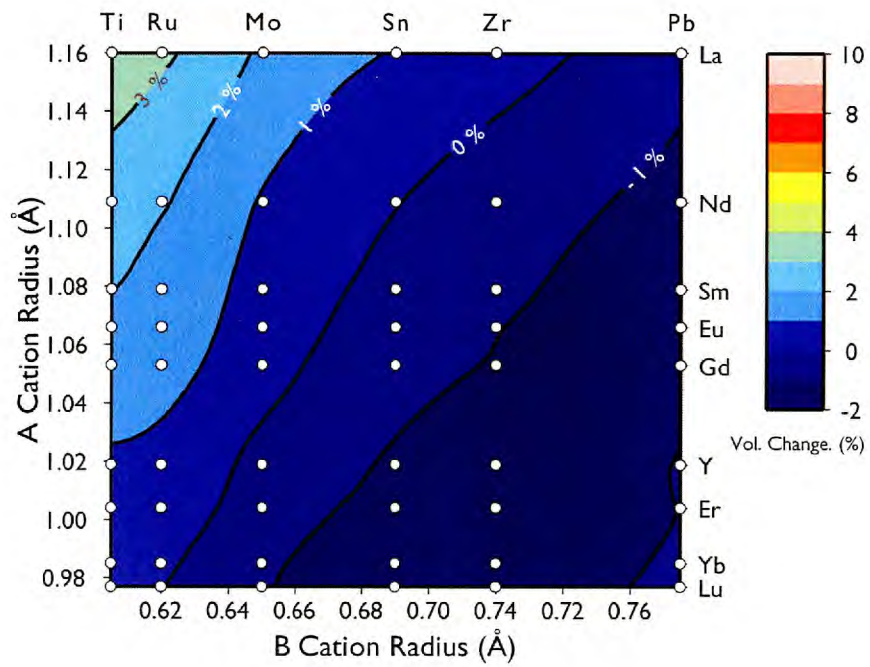
Figure 6.7: Volume change between ordered pyrochlore and disordered fluorite, calculated from MD results.

As few experimental values for volume change have been published for the compositions considered, reasonable comparison of the values calculated here with published values was difficult. Ewing *et al.* [138] have however, quoted an experimentally determined volume change of 5.85% for $Gd_2Ti_2O_7$ on going from pyrochlore to becoming amorphous at a temperature of 350K. This compares to the value calculated here of 7.5% at 300K which is an over-estimation of 1.7%. This assumes, of course, that the material measured by Ewing *et al.* was indeed 100% amorphous with no residual ordered fraction.

It is possible that the high quench rate (1×10^{14} K/s) used during the melt-quench procedure could also account for this difference. A high quench rate leads to an amorphous state with a high fictive temperature [20, 164]. The fast quench rate leads to some of the attributes of a material's high temperature structure being preserved at room temperature. As atoms in a high temperature structure tend to have less efficient packing, amorphous systems which have been quenched rapidly tend to have larger volumes than those which have been quenched more slowly. As a result, it is perhaps not surprising that this method slightly over-estimates the volume of the amorphous state. In order to test this hypothesis, an amorphous $Gd_2Ti_2O_7$ structure was created using a slower quench rate of 1×10^{13} K/s. This was an order of magnitude slower than that used for the other quenches and had the desired effect in reducing the predicted pyrochlore to amorphous volume change by 1.4%. Unfortunately, longer quench times lead to longer simulation times. With the available computational resource and the large number of compositions examined, it was not possible to run simulations at the slower quench rate for all compositions. The level of over estimation should be the same for all the amorphous volumes, as such the general trends in this data should be valid (see section 7.3). Volumes obtained from molecular dynamics for the fluorite and pyrochlore supercells were not quenched, therefore the volume changes obtained from these results are expected to have a smaller error.

The volume changes predicted by the supercell method (figure 6.7) suggest that there is essentially no volume change for the zirconates on going from pyrochlore to fluorite. By comparison, the titanates showed significant volume increases, ranging from over 3% for $La_2Ti_2O_7$ to around 0.5% for $Lu_2Ti_2O_7$. These changes were however, somewhat lower, than those observed for the transformation from pyrochlore to amorphous.

The volume change results may suggest a reason why certain materials undergo a transformation to fluorite before amorphising. The overall volume change on going from pyrochlore to fluorite, then from fluorite to the amorphous state is equal to that experienced when amorphising directly from ordered pyrochlore.

Comparison of Supercell and Cluster Methodologies

The pyrochlore to fluorite volume change results obtained using the supercell (figure 6.7) and cluster (figure 6.8) methods show a good level of agreement. The same general trend is seen in the contour plots generated via both methodologies, and if viewed side by side, the contour lines in both figures are parallel. The level of agreement obtained between the two sets of data is gratifying given the quite different methodologies used. This cross validation should engender some confidence in predictions made from these results.

Although in good general agreement, some differences are apparent between the two sets of results. The contour lines were more closely spaced in the cluster results suggesting that pyrochlore to fluorite volume change was more sensitive to the $A:B$ cation radius ratio than predicted by the supercell method. This difference means that as $A:B$ ratio increased towards the titanates, volume change predictions from the cluster model increase more rapidly than the supercell values. This led to a 1–2% difference at large $A:B$ ratios. Both models, however, predict a position for the technologically significant 0% contour that corresponds, approximately, to the edge of the disordered fluorite phase field shown in figure 6.4.

What could account for the differences observed between the supercell and cluster methods? In the supercell model, the thermal motion of atoms was considered explicitly. As the name suggests, the static energy minimisation procedure used during cluster calculations, does not consider thermal motion. In effect structures are relaxed at a temperature of 0K. The volume of the pyrochlore and fluorite systems would be expected to increase with temperature as they both have positive thermal expansion coefficients. If the difference between thermal expansion coefficients for the fluorite and pyrochlore phases decreased as a function of composition on moving from the zirconates, to the titanates, the volume changes predicted by the supercell
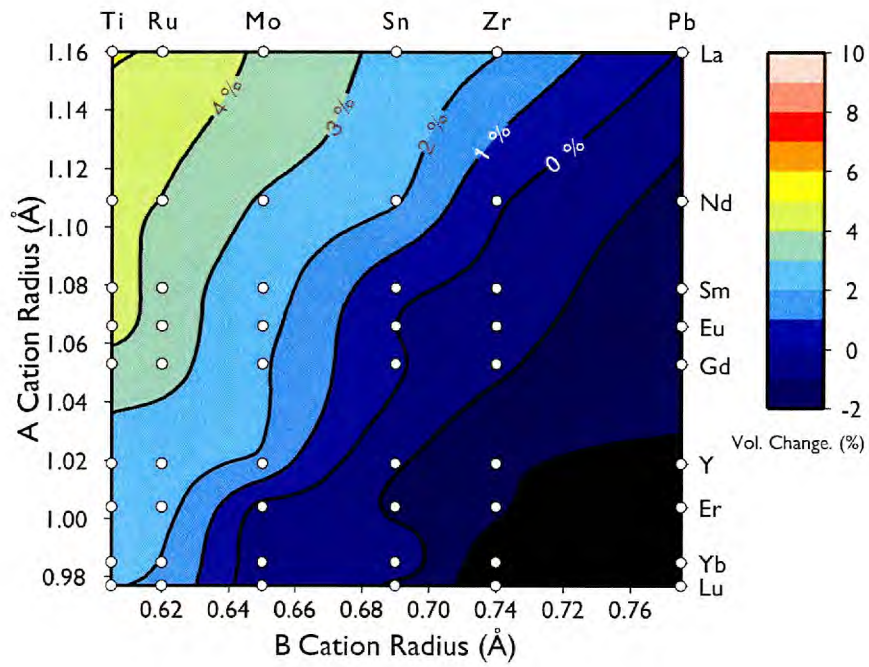
Figure 6.8: Volume change between ordered pyrochlore and disordered fluorite, calculated from Mott-Littleton defect energies.

method would be smaller. This could help explain the divergence between the two models, but clearly more work is necessary to verify this hypothesis.

The other main difference between the supercell and cluster models was in the way they represented disorder. The cluster used during Mott-Littleton calculations represented the lowest energy configuration for the defects in each cluster. By comparison, disorder was introduced into the supercells using a simpler, probabilistic approach. Atoms were assigned at random to available sites without consideration as to which configurations were more thermodynamically likely. Given the relatively low equilibration temperature it is unlikely that localised, high energy defect configurations, would have had a chance to anneal out of the structure during equilibration (particularly on the cation sublattice). This would mean that the volume changes predicted by the supercell method are likely to have been for systems with higher internal energy than those represented by the cluster method. If this was the case however, it might be expected that the volume change predictions for the titanate compositions would be higher than the cluster predictions. As discussed earlier, the titanates are more sensitive to lattice disorder than the zirconate pyrochlores. Therefore, if they contained high energy defect configurations, it is possible that this would manifest itself in terms of higher lattice strain and thus large order-disorder volume changes. Instead, it was the cluster method that predicted larger values for these compositions. This suggests that the simple disorder model adopted for the supercell calculations, was not to blame for the divergence between the two models.

Volume Change in Relation to Irradiation Stability

How can the volume change results be interpreted in terms of the irradiation stability of the different compositions? As previously mentioned (see section 6.1.2), Sickafus *et al.* argued that the internal energy of formation for a cluster (similar to cluster A), could be used to predict the radiation tolerance of a pyrochlore material [141]. Those materials, found to have low disorder energies (and hence good radiation tolerance), coincide with those compositions which showed little or no overall volume change on becoming disordered fluorite. Similarly, those materials which have previously shown large defect energies (see refs. [141, 145, 165]) correspond to compositions in which a transformation to a disordered fluorite causes significant volume in-

creases and would therefore induce significant lattice strain. This means that on becoming disordered, the penalty imposed by the change in internal energy and by the increase in lattice strain makes it more difficult for these materials to tolerate the disordered fluorite state, as a consequence it is possible that this makes it more difficult for them to tolerate disordering by displacive radiation events.

In conclusion, if volume change is considered as a materials selection criterion for nuclear waste materials, those materials close to the 0% contour of the pyrochlore to fluorite contour plot (figure 6.7) should be favoured. Under irradiation these compositions would be expected to show good dimensional stability. In addition, compositions close to this contour, such as $Gd_2Zr_2O_7$, have already been shown to display good radiation tolerance. It is also interesting that the 0% contour sits close to the pyrochlore to fluorite phase transition. This suggests that the small volume changes and good radiation tolerance of these compositions is due to their structural similarity to the parent fluorite phase rather than anything specific to the pyrochlore structure.

6.3 Predicting Pyrochlore to Disordered Fluorite Transformation Temperature

It has been established experimentally that at high temperatures, some pyrochlore compounds undergo a transformation from ordered pyrochlore to disordered fluorite whilst others remain as pyrochlore until they melt [140]. On transforming to disordered fluorite, the properties of the material can change. For instance thermal conductivity can decrease as disorder increases [166], whilst oxide ion conductivity can see large increases [167]. In high temperature applications, such as fuel cells and thermal barrier coatings for gas turbine engines, it is useful to know at what temperature any order-disorder transformation might occur. Previously, Stanek and Grimes [168] described an Arrhenius type relationship between the formation energy (f) for a defect cluster containing cation antisite and oxygen Frenkel pairs and the order-disorder transformation temperature (T_{OD}):

$$\ln(f) = m \times \frac{-1}{T_{OD}} + c \qquad (6.11)$$

This takes the form of a straight line with gradient, m, and an intercept with the dependent axis of c. Using experimental values for T_{OD} (see table 6.1), and defect energies from Mott-Littleton calculations it was possible to establish values for m and c that allowed predictions for T_{OD} to be made by extrapolating from the existing experimental data. An Arrhenius model was chosen by Stanek and Grimes [169] as they assumed that the transformation to disordered fluorite was governed by a diffusion process.

A similar approach has been used here to predict order-disorder temperatures for zirconate pyrochlores. In the same way as Stanek and Grimes [168], a small area of the disordered lattice was represented using a cluster of point defects consisting of both oxygen Frenkel and cation antisite defects in nearest neighbour positions (i.e. cluster A from the Mott-Littleton defect volume calculations in section 6.2.1). It is assumed that the internal energy to form this small section of disorder was representative of the disorder in a defect fluorite as a whole.

In order to allow direct comparison of the current results with those of Stanek and Grimes [168], the same set of pair potentials was employed during defect calculations. These were based on Minervini's potentials from refs. [145] and [165]. The potential parameters used are given in table 6.5. In contrast to the potential set used during the volume calculations of section 6.2, formal charges of -2, $+3$ and $+4$ were assigned to the O, A and B ions. Calculations were performed using both the CASCADE and GULP codes.

Order-disorder transformation temperature predictions made using the $\ln f \propto -\frac{1}{T_{OD}}$ relationship (equation 6.11) are plotted in figure 6.9 along with Stanek and Grimes' earlier hafnate results (from ref. [168]). Using the experimentally determined order-disorder temperatures for $Nd_2Zr_2O_7$, $Sm_2Zr_2O_7$ and $Gd_2Zr_2O_7$, given in table 6.1, it was possible to plot $\ln f$ vs. $-\frac{1}{T_{OD}}$. A trend line was then constructed through these points, using a least squares fit. Having established the gradient (m) and intercept (c), it was possible to use equation 6.11 to predict T_{OD} from cluster formation energies for compositions with unknown transformation temperatures. The predictions resulting from this are given in table 6.7 and the defect energies used in their

Interacting Species	A (eV)	ρ (Å)	C (eV Å^6)
Er^{3+}–O^{2-}	1739.91	0.3399	15.55
Eu^{3+}–O^{2-}	1925.71	0.3403	20.59
Gd^{3+}–O^{2-}	1885.75	0.3399	20.34
La^{3+}–O^{2-}	2088.89	0.3460	23.25
Lu^{3+}–O^{2-}	1618.80	0.33849	16.27
Mo^{4+}–O^{2-}	1223.97	0.3470	0.00
Nd^{3+}–O^{2-}	1995.20	0.3430	23.95
O^{2-}–O^{2-}	9547.96	0.2192	32.00
Pb^{4+}–O^{2-}	1640.34	0.3507	19.50
Ru^{4+}–O^{2-}	1215.78	0.3441	0.00
Sm^{3+}–O^{2-}	1944.44	0.3414	21.49
Sn^{4+}–O^{2-}	1414.32	0.3479	13.66
Ti^{4+}–O^{2-}	2131.04	0.3088	8.986
Y^{3+}–O^{2-}	1766.40	0.33849	19.43
Yb^{3+}–O^{2-}	1649.80	0.3386	16.57
Zr^{4+}–O^{2-}	1502.11	0.3477	5.10

Table 6.5: Short range pair potential parameters for formal charge model used to predict order-disorder temperature.

calculation, in table 6.6.

6.3.1 Comparison of f vs T_{OD} and $\ln f$ vs $-\frac{1}{T_{OD}}$ models

Equation 6.11 relates defect energy to transformation temperature through an Arrhenius type equation. It is by no means clear that this provides a better fit to experimental transformation temperatures than a simple linear model in which defect energy is assumed to be proportional to T_{OD}:

$$f = mT_{OD} + c \qquad (6.12)$$

where m and c are the gradient and intercept of a straight line linking defect energy (f) to transformation temperature (T_{OD}). Using this relationship, values for m and c were once more established from a least squares fit to the experimental transformation temperatures in table 6.1. The predictions made using the linear model are plotted in figure 6.10 and compared with those made with the Arrhenius model in table 6.7.

The residual error between predicted T_{OD} values and known experimental transformation temperatures were calculated in an effort to show which of the linear and Arrhenius models best described the order-disorder transformation and are given in table 6.8. For the hafnate pyrochlores the average error was 18K for the linear model and 22K for the Arrhenius model. The average error for the zirconates was 33K and 64K for the linear and Arrhenius models respectively (these compare with the ±50K error quoted for experimental transformation tem-

System	Defect Energy (eV)
$Nd_2Zr_2O_7$	3.81
$Sm_2Zr_2O_7$	3.58
$Eu_2Zr_2O_7$	3.46
$Gd_2Zr_2O_7$	3.34
$Tb_2Zr_2O_7$	3.22
$Dy_2Zr_2O_7$	3.06
$Y_2Zr_2O_7$	2.97

Table 6.6: Defect energies used to predict order-disorder transformation temperatures.
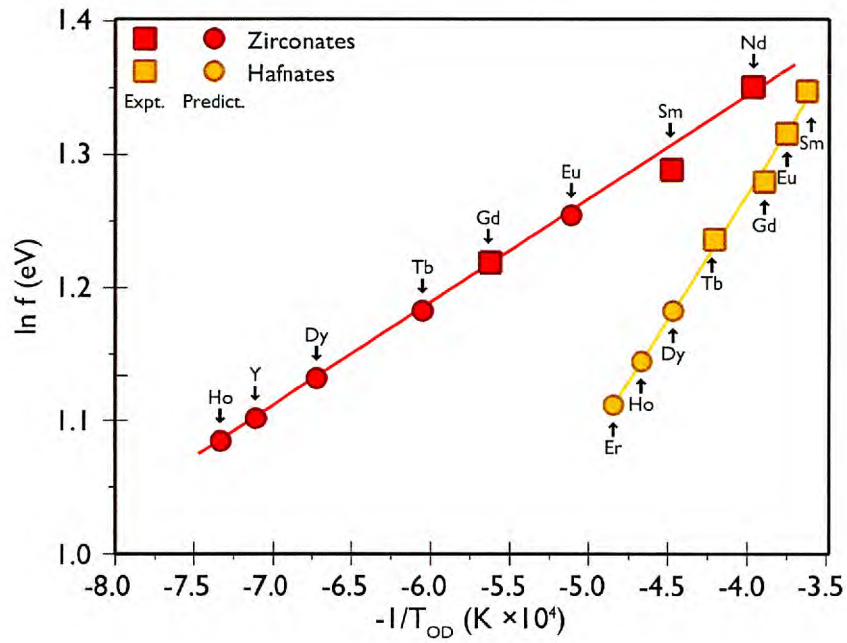
Figure 6.9: Plot of $\ln(f)$ vs. $-\frac{1}{T}$ (hafnate data taken from [168]).
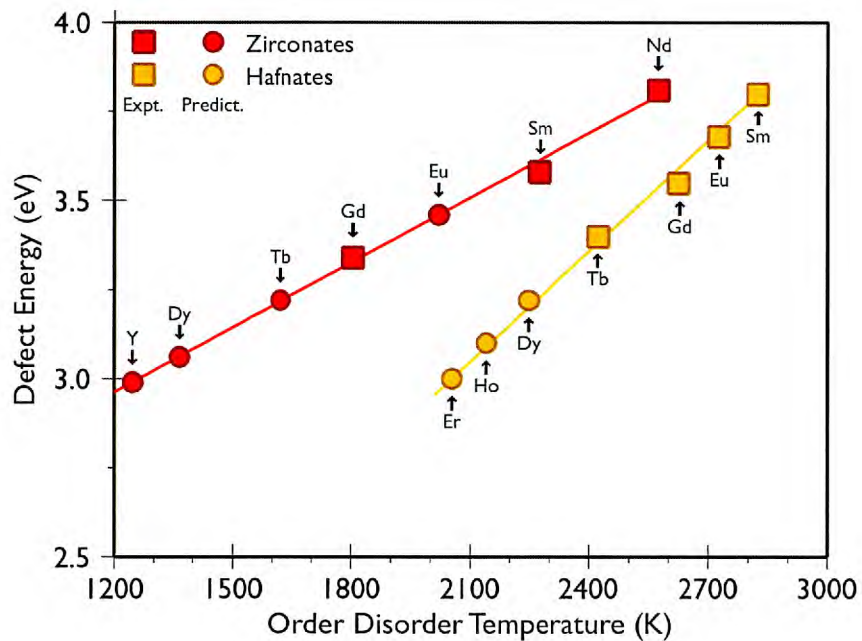
Figure 6.10: Predicted order-disorder transformation temperatures for zirconate and hafnate pyrochlores. Linear model. (hafnate data taken from [168]).

	Order Disorder Temperature (K)	
System	f vs. T_{OD}	$\ln f$ vs. $-\frac{1}{T_{OD}}$
$Ho_2Zr_2O_7$	1132	1378
$Y_2Zr_2O_7$	1214	1422
$Dy_2Zr_2O_7$	1362	1506
$Tb_2Zr_2O_7$	1625	1675
$Eu_2Zr_2O_7$	2020	1989
$Er_2Hf_2O_7$	2052	2100
$Ho_2Hf_2O_7$	2150	2179
$Dy_2Hf_2O_7$	2269	2280

Table 6.7: Order disorder temperatures predicted from defect energies using linear and $\ln f$ vs $-1/T$ models, (hafnate data from [168], for compositions whose transformation temperatures have not been established experimentally).

peratures). In both cases, the linear model fitted the experimental transformation temperatures better than the Arrhenius model. For this reason, predictions made from the linear model were used in the discussion that follows. It must be noted however, that the linear model has been chosen on an empirical basis, clearly further work that established the physical processes underlying the order-disorder transformation, should be carried out (see 7.3).

6.3.2 $Eu_2Zr_2O_7$

Phase diagrams published for the ZrO_2-Eu_2O_3 system suggest the existence of a pyrochlore phase field [170]. The bounds of this field, however, are hypothetical with no order-disorder transformation temperature indicated (see figure 6.11). In addition, this composition is bounded by $Gd_2Zr_2O_7$ and $Sm_2Zr_2O_7$ in the plot of f vs. T_{OD} in figure 6.7, both of which have experimentally verified transformation temperatures. Structurally, these pyrochlores are also similar to $Eu_2Zr_2O_7$: Gd, Eu and Sm have ionic radii of 1.053, 1.066 and 1.079Å respectively [118]. Their 48f positional parameters are also very similar all having values about 0.333 [171]. It seems likely therefore that this composition will undergo a transformation from an ordered pyrochlore to disordered fluorite at around the predicted value of 2020K.
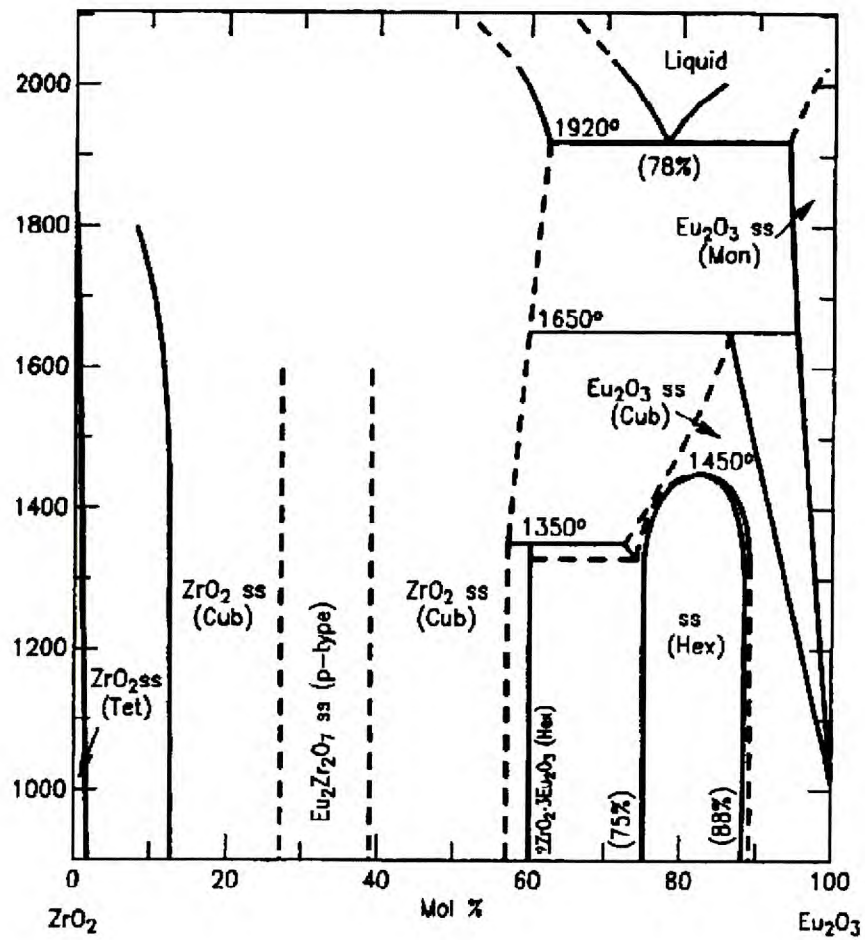
Figure 6.11: ZrO$_2$-Eu$_2$O$_3$ phase diagram reproduced from [170].

	Order Disorder Temperature (K)				
System	Experiment	f vs. T_{OD}	$\pm$	$\ln f$ vs. T_{OD}	$\pm$
$Gd_2Zr_2O_7$	1803	1823	20	1821	18
$Sm_2Zr_2O_7$	2273	2217	56	2184	89
$Nd_2Zr_2O_7$	2573	2595	22	2658	85
$Tb_2Hf_2O_7$	2423	2444	21	2439	16
$Gd_2Hf_2O_7$	2623	2592	31	2584	39
$Eu_2Hf_2O_7$	2723	2721	4	2720	5
$Sm_2Hf_2O_7$	2823	2838	15	2851	29

Table 6.8: Residual values for linear and $\ln f$ vs $-1/T$, T_{OD} values predicted by each model are compared with experimental values.

As Tb^{3+} is only 0.01Å smaller[3] than Gd^{3+} and the predicted transformation temperature for $Tb_2Zr_2O_7$ (1622K) lies close to that of the known transformation temperature of $Gd_2Zr_2O_7$ this composition may also be worthy of further investigation.

The pyrochlore stability map in figure 6.4 shows that $Ho_2Zr_2O_7$, $Dy_2Zr_2O_7$ and $Y_2Zr_2O_7$ have not been seen as ordered pyrochlores even under conditions of high pressure synthesis [140]. The low predicted transformation temperatures for these compounds (1132, 1214 and 1362K respectively) support this finding. The low temperatures indicate that the activation energy for disorder would be sufficiently low for ordering not to occur (even if it were possible to form these $A_2B_2O_7$ compositions).

The transformation temperatures plotted in figure 6.10 also suggest another interesting possibility; the predictions for $Dy_2Hf_2O_7$, $Ho_2Hf_2O_7$ and $Er_2Hf_2O_7$ were close enough to the experimental value for $Gd_2Zr_2O_7$ that it may be possible to observe these compositions as ordered pyrochlores.

---

[3]Calculated from +3 VIII coordinated Shannon radii [118]

Publications

Predictions for volume changes between the pyrochlore, disordered fluorite and amorphous states from section 6.2 appear in:

M.J.D Rushton, C.R. Stanek, A.R. Cleave, B.P. Uberuaga, K.E. Sickafus and R.W. Grimes, "Simulation of defects processes in fluorite and fluorite related oxides: implications for radiation tolerance", *Nuclear Instruments and Methods in Physics Research Section B*, 2006 *In Press* .

The discussion of order-disorder transformation temperatures given in section 6.3 has been published in the Journal of Materials research as follows: M.J.D. Rushton, R.W. Grimes, C.R. Stanek and S. Owens, "Predicted pyrochlore to fluorite disorder temperature $A_2Zr_2O_7$ compositions", *Journal of Materials Research*, vol. 19, p. 1603, 2004.

.

Chapter 7

Suggestions for Further Work

The following chapter, provides suggestions on how the glass, glass-ceramic and pyrochlore work contained in this thesis could be extended.

7.1 Glass Simulations

In section 3.5.2, Voronoi tessellations were generated for simulated glass systems. These were used to establish connectivity between the alkali atoms in these glasses; this information was then used to define the alkali distribution in terms of a network structure. As migration of alkali atoms through glasses is thought to proceed via a hopping mechanism (in which atoms jump between neighbouring sites) it was argued that each network edge represented a possible path along which a migratory hop could occur. It was then argued that analysis of the connectivity and length of paths in these networks could be used to predict the efficiency of alkali migration through the glass and hence glass durability.

Defining a glass' alkali distribution as a network is potentially a very powerful technique. In effect it makes a link between the structure of a glass and some of its dynamic properties. As it stands, however, this technique is largely untested. Further research must therefore be carried out to determine if intrinsic properties of networks (describing connectivity and path lengths),

are physically significant to alkali migration. As further work, alkali network predictions must be tested. This could be achieved as follows: a series of model glass structures could be created comprising of alkali and mixed alkali compositions. Predictions for the relative migration behaviour of atoms in these model systems could then be made using the Voronoi cell method. These predictions would then be tested using molecular dynamics simulations, from which the rate of alkali ion migration could be calculated. This could be partnered by an experimental programme in which the same series of glasses could be generated, allowing migration of alkali atoms to be measured and compared with the model predictions.

Reverse Monte Carlo (RMC) provides a useful technique for generating model glass structures that provide excellent agreement with experimental data. RMC can also be used to refine the structure of simulated glasses generated using molecular dynamics, to give a better level of agreement with experiment [93]. A disadvantage of the traditional RMC technique is that it creates static structures (although a hybrid technique that combines RMC and MD has been suggested [40]). As the migration of alkali atoms is a dynamic process RMC cannot be applied to its study. This is unfortunate because RMC can generate structures that match experiment better than molecular dynamics alone. Assuming it is valid, the Voronoi cell method could be used to make predictions for alkali migration from static models of the sort generated by RMC.

The MW and MW+Al+Mg glass compositions used during the simulation of glass ceramic interfaces were closely related to those used in commercial vitrification processes [11]. The effects of nuclear waste on these systems has however, not been considered explicitly by this work. The effect of waste elements on the structure of glasses should be considered in future. This could yield useful information that would help improve the design of future wasteforms.

7.2 Glass Ceramic Interfaces

Techniques similar to those used to generate the results shown in chapters 4 and 5 could be adapted to consider the effects of waste elements on glass ceramic interfaces. With suitable pair-potentials there is no practical reason why the quench with ceramic technique could not be used to simulate waste bearing simulated glass-ceramic systems. These systems could then

be examined to answer a number of interesting questions.

Glass-ceramic composite wasteforms are sometimes used to immobilise high level nuclear waste [11]. Computer simulations could be used to determine whether certain elements partition to the ceramic or the glass phase in these materials. Using a technique similar to that employed here, energies could be calculated for glass-ceramic systems where the waste elements were, in the first instance, dispersed in the glass phase, and in the second instance in the ceramic phase. The energy difference between the two systems could then be used to see if the waste would rather sit in the glass or ceramic phase. Systematic calculations of this sort for different glass and ceramic compositions could highlight regions of compositional interest. This information could then be used to optimise the composition of glass-ceramic composites used for nuclear waste containment.

Self irradiation of nuclear wasteforms by the radionuclides they contain is a concern when considering a wasteform's long-term performance [11]. Molecular dynamics has been used to successfully simulate the effects of α-particle radiation on the structure of nuclear waste glass compositions [172]. It has also been used to study the performance of ceramic wasteforms under α irradiation [173]. Similarly, molecular dynamics could be used to study the way in which glass-ceramic interfaces react to the type of ballistic damage caused by α-particles. The damage (and recovery processes) associated with primary knock-on atoms approaching the interface at different angles and with different energies could be examined. This could show if these damage processes encouraged or discouraged devitrification of waste glasses.

In section 4.3.3 it was found that the potential model employed for glass and glass-ceramic simulations, gave lattice energies for MgO, CaO, SrO and BaO that were significantly lower than those obtained experimentally. Although the potentials predicted glass and ceramic structures consistent with the available experimental data, the difference in lattice energy indicates that this potential set could be improved. As further work, an improved set of pair potentials should be derived that not only correctly predicts structural properties but also lattice and surface energies for both glass and ceramic materials.

The analyses in chapters 4 and 5 focused on the structure of the ceramic and glass close to

glass-ceramic interfaces. As further work it would be interesting to consider the effects of interfaces on dynamic processes in the glass and ceramic phase adjacent to the interface. It was found that often quite profound structural changes had occurred in the systems examined. In particular, at most interfaces the concentration of alkali species in the glass proximal to the interface was enhanced. Further analysis showed that at the interface, alkali atoms sat above particular crystallographic sites in the ceramic's surface leading to partial ordering of the glass. The mobility of alkali species in the glass is much higher than the network formers (e.g. Si, O and B). It is likely that the interfacially induced ordering of these mobile species would have changed their mobility in comparison to the bulk glass. For instance, alkali atoms might be quite tightly bound to sites at the ceramic surface decreasing their mobility. Alternatively, the ordered arrangement of alkali ions at the interface might allow diffusion to occur more rapidly (as the diffusion pathways would be straighter and less tortuous) the same may be true for segregated fission products. Examination of long timescale MD simulations would allow the dynamic behaviour of alkali atoms close to simulated glass ceramic interfaces to be compared with those in the bulk glass. Bearing in mind that long timescale techniques are dominated by the fastest process, the migration of alkalis may occur on a timescale that is too small to allow significant acceleration of the simulation.

The enhancement of alkali ions adjacent to glass-ceramic interfaces led to their depletion for a small region further from the interface (see section 4.5.1). Longer equilibration times might show that this depletion region disappeared as diffusion of alkali atoms from the bulk glass into this region occurred. Long MD runs of this kind would be worthwhile as they would show whether or not this depletion region was a characteristic of glass ceramic interfaces or a temporary response to the enhanced alkali concentration at the interface.

In section 4.3.2 it was found that interfaces containing MW+Al+Mg glass consistently showed lower interfacial energies than equivalent interfaces with the MW glass composition. Unfortunately, it was found that the small number of Mg and Al atoms in the MW+Al+Mg glass made it difficult to obtain reasonable statistics for these species. As a result, it was not possible to determine the effects of adding Al and Mg to the MW glass interfaces. As further work, larger systems containing more particles could be created. This would allow statistics to be obtained from a significant sample of Mg and Al atoms, without changing the composition of the glass.

Additionally, glass compositions could be created allowing the individual effects of Al and Mg to be observed. Glass ceramic interfaces for MW glass with Al (but not Mg) could be examined to see if the interface's energy decreased due to the polymerising effect of Al. Similar simulations for MW glass with Mg (but not Al) would show if the energy decrease could be attributed to the network modifying effects of Mg.

Ravishankar et al. [174] have reported that faceting of a ceramic may occur at a glass-ceramic interface. Droplets of anorthite liquid (a calcium aluminosilicate) were cooled rapidly on the surface of alumina. These were then etched away using HF acid. In regions that had been underneath droplets, faceting of the ceramic surface was observed. The work presented in this thesis considers the planar (100) and (110) terminating surfaces of rocksalt compositions. It is possible that faceting of the surface could help lower the energy of glass-ceramic interfaces. A future study could look at whether surface faceting also lowered interfacial energies at glass-rocksalt interfaces. In addition, it would be interesting to see if the densified layers found parallel to planar interfaces (described in chapter 5), also occurred at a non planar, faceted surfaces.

In section 4.3.1, a general trend was observed whereby, interfacial energy could be linked to the ceramic component's surface energy for the MW glass series of interfaces. Ceramic surfaces with large surface energies had smaller interfacial energies, whilst smaller surface energies indicated larger interfacial energies. This is interesting, however, to properly establish any trend between surface energy and interfacial energy, more interfacial systems would need to be considered. If such a link could be established, a knowledge of surface energy could, potentially be used to predict interfacial properties.

Density oscillations were found in the glass adjacent to glass ceramic interfaces. These oscillations took the form of decaying sinusoidal wave. In section 5.2.1, a function of the following form was used to describe these oscillations:

$$\rho(r) = A \cdot \exp[-b(r-s)] \cdot \cos\left[\frac{2\pi}{\lambda}(r-s)\right] + d$$

The exponential component of this expression was used to represent the attenuation in the amplitude of the density oscillations as the distance from the interface increased. However, the choice of an exponential form to describe the decaying amplitude was rather arbitrary. Work

should be done in establishing the underlying physical processes that determine the rate of density oscillation decay (as a function of distance from the interface). It may be that this is related to the dielectric behaviour of the glass close to the interface (which would be expected to vary depending on the interface), if so, a decay function proportional to $\frac{1}{r^2}$ (where r is the distance to the interface) might be expected.

7.3 Pyrochlore

Volume change predictions were calculated for pyrochlore compositions on going from an ordered pyrochlore to an amorphous state (see chapter 6). Volumes for the amorphous state were calculated by using a melt-quench procedure (see chapter 2). It was found that, when compared to the limited amount of experimental data available, the amorphous volumes predicted by this method were too large. As a test, a lower quench rate (1×10^{13} compared to 1×10^{14} Ks^{-1}) was used for the $Gd_2Ti_2O_7$ system. The amorphous volume change predicted using this lower quench rate was found to be much closer to the experimental value. This suggests that, in order to improve the pyrochlore to amorphous volume change predictions, all of the other pyrochlore compositions examined should be obtained using this lower quench rate.

It has been found that certain rare-earth $A_2B_2O_7$ compositions exhibit the delta phase structure rather than pyrochlore [146]. For completeness therefore, volume changes between pyrochlore, defect-fluorite and the delta phase should be calculated.

The predictions for volume changes occurring between the pyrochlore and defect-fluorite structures were obtained using two distinct methodologies. In the first, volumes were obtained for the pyrochlore and fluorite states using molecular dynamics in conjunction with large supercells. In the second, clusters of point defects were used to represent a small portion of the disordered fluorite lattice from which volume changes were obtained. In general both, the supercell and cluster models predicted the same variation for volume changes as a function of composition. In particular, both methods predicted that pyrochlore compositions near the pyrochlore-defect fluorite phase boundary would show very small volume increases on becoming disordered. However, as the $A:B$ cation radius ratio increased on moving from the zirconate

to titanate pyrochlores, the level of agreement between the two models decreased. For titanate compositions, the cluster model predicted larger volume changes than the supercell method. This behaviour was unexpected (for the reasons given in section 6.2.3). The difference between the two models could be accounted for by a difference in thermal expansion coefficient between the zirconate and titanate series. Alternatively, this may indicate that the low energy nearest neighbour defect clusters employed in the cluster method, did not represent the lowest energy defect configuration for these materials. Further investigations should be performed to establish why the two models did not agree. It would be enlightening to compare the thermal expansion coefficients for the zirconate and titanate series of compositions. In addition, defect clusters that take in, not only nearest neighbour but next nearest neighbour configurations should be considered, to see if a lower energy defect configuration exists.

Amorphous structures were generated for pyrochlore materials by performing a melt-quench. At the end of each quench, computer visualisation was used to establish that each material had amorphised and had not retained the crystalline structure used as the starting point of the quench. The amorphous structure of the pyrochlore was not however characterised further. The details of the amorphised pyrochlore structures should be examined. For instance, the coordination environments of the A and B cations in the amorphous state could be compared to those in the pyrochlore crystal. It would be interesting to see if the local order of the crystal was maintained in the amorphous state (as is the case in vitreous silica).

In section 6.3, predictions were made for pyrochlore to defect fluorite transformation temperatures. In order to make these predictions, a correlation was established between the formation energy for a cluster of isolated defects and experimentally determined order-disorder transformation temperatures. Once this had been achieved, calculated defect energies were used to predict order-disorder temperatures for compositions where an experimental value was not available. It was established that a linear relationship between defect energy and transformation temperature gave a better fit to experimental data, than an Arrhenius type expression that had been used previously [168]. The basis for choosing this linear model was empirical. Work should be carried out to establish the basic physics governing the order-disorder transformation and to help justify the choice of a linear model. This could, in theory, be achieved by performing molecular dynamics on pyrochlore and disordered fluorite supercells. Energies

could be obtained for each structure by performing a series of MD equilibration runs, gradually increasing the temperature at each stage. The energy obtained for the pyrochlore and fluorite structures could be compared at each temperature: the point at which the fluorite cell gives a lower energy, would define the order-disorder temperature.

Pyrochlore glass-composites have been proposed as nuclear wasteforms [37, 38], in which radionuclides would be contained in the pyrochlore phase which would then be dispersed in a glass matrix (to provide a further barrier between the waste atoms and the biosphere). Ruthenium lead pyrochlores have also been observed [175] to form in lead borosilicate glasses containing Ru additions. This is of interest as RuO_2 accounts for 7.8 wt% of the calcine obtained from the reprocessing of magnox nuclear fuel [10]. It was always the intention of the work presented here, to consider pyrochlore-glass interfaces using the same techniques employed for the glass-rocksalt interfaces. Unfortunately, time constraints did not allow this to happen. However, a study of the interfaces between borosilicate glass and pyrochlore ceramics would help lead to a better understanding of these materials and should be carried out as further work. The volume changes predicted for pyrochlore materials in section 6.2, could also be applied to the study of glass-pyrochlore composites. Large pyrochlore volume changes could lead to microcracking of the glass matrix and have implications for wasteform durability by providing pathways for the ingress of water into the material.

Chapter 8

Conclusions

The aim of the work presented in this thesis was to model glass, ceramic and glass-ceramic materials relevant to the immobilisation of nuclear waste. To this end simulations were performed which allowed the atomic scale structure of glass and glass-ceramic interfaces to be studied. In addition, order-disorder transformations and associated volume changes were considered for pyrochlore and pyrochlore related materials.

8.1   Glass and Glass Ceramics

In chapter 3, simulated silicate, alkali silicate, borosilicate and aluminoborosilicate glass systems were generated by performing a simulated quench from the molten state. These systems were compared with experimentally determined structural data which showed there was a good level of agreement between experimental and model systems. The experimental radial distribution function for vitreous SiO_2 was compared with that obtained from the simulated glass. This showed, using Wright's reliability index [82], that the model system was within 8% of the experimental structure. The bond angle distribution for the silicate glasses was also compared with experiment and showed a similar level of agreement. The speciation of the borosilicate glasses was also compared with experimental values, again this showed that the simulation method had replicated the main structural features well.

246

For the alkali silicate and mixed alkali silicate glasses, the distribution of network modifying species was examined. Each glass system was partitioned using the Voronoi tessellation [102]. This was used to determine the coordination environment of the alkali atoms in the system. From this it was determined that significant aggregation of alkali species took place in a manner consistent with Greaves' modified random network theory [21].

With respect to the alkali distribution in the simulated mixed alkali glass compositions (i.e. SiO_2+Na+Li, MW and MW+Al+Mg glasses) it was found that, when considered as a whole, the alkali distribution was very similar to that seen in a single alkali, sodium silicate glass. In other words, considerable alkali aggregation was also observed in the mixed-alkali glasses. Extensive intermixing of the Li and Na species present in the mixed alkali glasses was observed. In addition, the alkali species in these glasses were predicted to favour coordination environments in which they had heterogeneous alkali neighbours (i.e. Li atoms tended to have Na neighbours). The extent to which this is an active process, rather than a consequence of the random distribution of alkali atoms in the glass also needs to be investigated.

Nearest neighbour alkali sites (defined using the Voronoi construct), were used to define networks of interconnected alkali sites. These were then used to predict the migration behaviour of alkali atoms in the SiO_2+Na, SiO_2+Na+Li, MW and MW+Al+Mg glasses. The SiO_2+Na glass was found to contain contiguous Na clusters which spanned the entire simulation cell. This indicated that this glass had exceeded its percolation threshold and would exhibit rapid alkali migration. The extensive intermixing of alkali sites in SiO_2+Na+Li, MW and MW+Al+Mg was predicted to reduce the ability of alkali species to migrate through these glasses. This view is consistent with the theory that a heterogeneous site blocking mechanism is responsible for the mixed alkali effect observed in oxide glasses.

8.1.1 Glass Ceramic Interfaces

The structure of glass-ceramic interfaces were predicted for several glass ceramic interfaces. Interfaces were generated between the (100) surface of MgO and SiO_2, SiO_2+Na, SiO_2+Na+Li, MW and MW+Al+Mg glass compositions. In addition, for the MW and MW+Al+Mg glasses

interfaces with CaO, SrO and BaO were studied. A comparison was also made between the (110) and (100) interfaces between MW glass and MgO, CaO, SrO and BaO.

Interfacial energies were defined for all the interfaces considered. These showed that, for the MW glass, (110) surfaces were stabilised by the glass-ceramic interface to a greater degree than equivalent (100) surfaces.

For both the (100) and (110) MW glass interfaces it was found that the interfacial energy increased with ceramic cation radius between MgO and SrO. Unexpectedly, a drop in interfacial energy was found as the ceramic cation radius increased between SrO and BaO. These trends were also observed for the (100) interfaces between MgO, CaO, SrO and BaO and the MW+Al+Mg glass.

The alkali distribution at glass ceramic interfaces was examined. Increased alkali concentrations adjacent to the interface were observed in most of the simulated glass-ceramic systems. As an example, a Li concentration ten times that found in the equivalent bulk glass was found adjacent to the interface of MgO (100) and MW glass. The level of interfacial alkali enhancement decreased with increasing ceramic cation radius. This was attributed to a decrease in the number of anion sites found in the ceramic surface as the lattice parameter increased from MgO to BaO.

Alkali atoms sitting at (100) interfaces sat in positions directly above anion sites in the ceramic surface. At (110) interfaces alkali atoms sat over furrows in the ceramic surface, above cations in the second layer of the ceramic block. Alkali atoms at interfaces between glasses and the MgO ceramic, sat in positions which represented cation sites in the next layer of the MgO lattice (if the lattice had continued). In effect a layer of the MgO cation sublattice, partially occupied by alkali atoms, was formed in the glass adjacent to MgO interfaces.

At the interfaces between the (100) surface of MgO and the SiO_2+Na, SiO_2+Na+Li, MW and MW+Al+Mg glasses, oxygen atoms in the glass adjacent to the interfaces tended to sit over cation sites in the ceramic's surface. At the same interfaces, the glass cations near the interface were associated with anion sites in the surface. In effect silicate tetrahedra aligned one of their edges along the ceramic's < 110 > vector, parallel to the plane of the interface.

By comparison, the borate and silicate polyhedra at the interfaces between the (100) surfaces of CaO, SrO, BaO and the MW and MW+Al+Mg glasses tended towards different orientations. Whilst glass cations adjacent to these interfaces tended to sit above anion sites in the glass surface, anions did not sit directly above ceramic cations (as observed at MgO-(100) interfaces). Instead, glass sat above interstitial sites in the (100) ceramic surface. This change in behaviour between MgO and the other rocksalt compositions, was attributed to the nearest neighbour cation separation in the ceramic surface being approximately equal to the tetrahedral edge lengths of borate and silicate tetrahedra, but larger in CaO, SrO and BaO.

For the MW glass interfaces between MgO, CaO, SrO and BaO, the effect of the ceramic's terminating surface on the glass' network was examined and the (100) and (110) surfaces were compared. At (110) interfaces, a substantial number of silicate and borate polyhedra were found to contain oxygen atoms from the ceramic surface. At the (100) interfaces, borate polyhedra also showed this behaviour, whilst only relatively few silicate tetrahedra shared a vertex with (100) ceramic surfaces.

Glass anions adjacent to the MW glass, MgO (110) interface formed a layer in which the atoms occupied positions consistent with the subsequent layer of the ceramic block (had it formed). Adjacent to the interface, therefore, a partially occupied layer that mimicked a layer of the ceramic was formed in the glass.

The alignment of borate and silicate polyhedra, along preferred directions at the (100) and (110) interfaces was found to induce the formation of densified layers in the glass parallel to the interface. These layers extended a substantial distance into the glass, indicating that the interface had induced partial ordering in the glass network. A templating mechanism has been proposed to account for the formation of these layers.

Layering was not observed for the interface between SiO_2 and MgO-(100) ceramic. The lack of conformational freedom in SiO_2 (due to the highly polymerised nature of this glass) seems to have prevented the alignment of silicate tetrahedra along preferred directions in the crystal's surface. This lack of concerted alignment by the tetrahedra at the interface, prevented templating and the formation of subsequent densified layers in the glass further from the interface.

This indicates that depolymerisation of the glass network is required before layering of a glass close to a glass-ceramic interface can take place.

8.2 Pyrochlore

Atomic scale computer simulations were used to study order-disorder transformations in rare-earth pyrochlore and pyrochlore related materials. Volume change predictions were made for $A_2B_2O_7$ compositions on undergoing transformations from pyrochlore to disordered fluorite and amorphous states (again generated by quenching the liquid). For the transformation to disordered fluorite, predicted volume changes decreased as $A{:}B$ cation radius ratio decreased. A similar trend was observed for the transformation from pyrochlore to the amorphous state. By comparison, the volume change on transforming from a disordered fluorite to the amorphous state was predicted to be largely independent of composition.

Dimensional stability is a desirable property for a nuclear wasteform. Pyrochlore compositions which do not show a volume increase on transforming to the disordered or amorphous states, are potentially of great technological significance. $A_2B_2O_7$ compositions close to the pyrochlore-disordered fluorite phase boundary were predicted to show small volume increases on undergoing the transformation to disordered fluorite or even to the amorphous state.

Certain $A_2B_2O_7$ compositions which exhibit the pyrochlore structure at room temperature, undergo a transformation to become a disordered fluorite at a certain temperature, whilst others stay as pyrochlore until they melt. In section 6.3, predictions for this transformation temperature were made for a series of zirconate pyrochlores. Of particular interest is the transformation temperature of 2020K, proposed for $Eu_2Zr_2O_7$. The predicted transformation temperature for $Tb_2Zr_2O_7$ (1622K) was found to lie close to that of the experimentally known temperature of $Gd_2Zr_2O_7$, as a result, this composition would also be worth investigating experimentally.

Bibliography

[1] "The energy challenge energy review report 2006," Technical Report, Department of Trade and Industry, 2006.

[2] "BP statistical review of world energy 2005," Technical Report, BP plc., 2005.

[3] "Managing the nuclear legacy: A strategy for action," Technical Report, Secretary of State for Trade and Industry, July 2002 2002.

[4] "Annual plan 2005/06," Technical Report, Nuclear Decommissioning Authority, 2005.

[5] *Directive on the limitation of emissions of certain pollutants into the air from large combustion plants 2001/80/EC*. European Parliament and Council, 2001.

[6] "Kyoto protocol: Status of ratification," Technical Report, United Nations, 2005.

[7] "Report on the national greenhouse gas inventory data from annex I parties for the period 1990-2001," Technical Report FCCC/SBSTA/2003/14, United Nations: Subsidiary Body for Scientific and Technological Advice, 2003.

[8] P. D. Wilson, ed., *The Nuclear Fuel Cycle*. Oxford: Oxford University Press, 1996.

[9] I. Hore-Lacy, *Nuclear Electricity*. Uranium Information Centre Ltd., 7th ed., 2003.

[10] I. W. Donald, B. L. Metcalfe, and R. N. J. Taylor, "The immobilization of high level radioactive wastes using ceramics and glasses," *Journal of Materials Science*, vol. 32, p. 5851, 1997.

[11] M. I. Ojovan and W. E. Lee, *An Introduction to Nuclear Waste Immobilisation*. Amsterdam: Elsevier, 2005.

[12] "Long-lived legacy: managing high-level and transuranic waste at the DOE nuclear weapons complex," Technical Report OTA-BPO-83, U.S. Congress office of technology assessment, 1991.

[13] W. J. Weber, R. C. Ewing, and W. Lutze, "Crystalline ceramics: waste forms for the disposal of weapons plutonium," Technical Report PNL-SA-26437, U.S. Department of Energy, 1995.

[14] R. C. Ewing, W. J. Weber, and F. W. Clinard, "Radiation effects in nuclear waste forms for high-level radioactive waste," *Progress in Nuclear Energy*, vol. 20, p. 63, 1995.

[15] H. Rawson, *Properties and Applications of Glass*, vol. 3 of *Glass Science and Technology*. Amsterdam: Elsevier, 1980.

[16] Y.-M. Chiang, D. Birnie III, and W. D. Kingery, *Physical Ceramics: Principles for Ceramic Science and Engineering*. New York: John Wiley & Sons, 1997.

[17] R. W. G. Wyckoff, "Chapter IV: Structures of the compounds RX_2," in *Crystal Structures*, vol. 1, New York: Interscience Publishers, 2nd ed., 1963.

[18] A. C. Wright, "Neutron and X-ray amorphography," in *Experimental Techniques of Glass Science* (C. J. Simmons and O. H. El-Bayoumi, eds.), p. 205, The American Ceramic Society, 1993.

[19] W. Zachariasen, "The atomic arrangement in glass," *Journal of the American Chemical Society*, vol. 54, p. 3844, 1932.

[20] R. H. Doremus, *Glass Science*. New York: John Wiley & Sons, 1973.

[21] G. N. Greaves, A. Fontaine, P. Lagarde, D. Raoux, and S. J. Gurman, "Local structure of silicate glasses," *Nature*, vol. 293, p. 611, 1981.

[22] G. N. Greaves, "EXAFS and the structure of glass," *Journal of Non-Crystalline Solids*, vol. 71, p. 203, 1985.

[23] G. N. Greaves, W. Smith, E. Giulotto, and E. Pantos, "Local structure, microstructure and glass properties," *Journal of Non-Crystalline Solids*, vol. 222, p. 13, 1997.

[24] G. N. Greaves, "Structure and ionic transport in disordered silicates," *Mineralogical Magazine*, vol. 64, p. 441, 2000.

[25] G. N. Greaves, N. T. Barrett, G. M. Antonini, F. R. Thornley, B. T. M. Willis, and A. Steel, "Glancing-angle X-ray absorption spectroscopy of corroded borosilicate glass surfaces containing uranium," *Journal of the American Chemical Society*, vol. 111, p. 4313, 1989.

[26] J. O. Isard, "The mixed alkali effect in glass," *Journal of Non-Crystalline Solids*, vol. 1, p. 235, 1969.

[27] N. J. Kreidl, "Inorganic glass-forming systems," in *Glass Science and Technology: Glass Forming Systems* (D. R. Uhlmann and N. J. Kreidl, eds.), vol. 1, p. 105, New York: Academic Press, 1983.

[28] J. Krogh-Moe, "Structural interpretation of melting point depression in the sodium borate system," *Physics and Chemistry of Glasses*, vol. 3, no. 4, p. 101, 1962.

[29] J. Zhong and P. J. Bray, "Change in boron coordination in alkali borate glasses and mixed alkali effects as elucidated by NMR," *Journal of Non-Crystalline Solids*, vol. 111, p. 67, 1989.

[30] P. J. Bray and J. G. O'Keefe, "Nuclear magnetic resonance investigations of the structure of alkali borate glasses," *Physics and Chemistry of Glasses*, vol. 4, p. 37, 1963.

[31] P. K. Abraitis, F. R. Livens, J. E. Monteith, J. S. Small, D. P. Trivedi, D. J. Vaughan, and R. A. Wogelius, "The kinetics and mechanisms of simulated British magnox waste glass dissolution as a function of pH, silicic acid activity and time in low temperature aqueous systems," *Applied Geochemistry*, vol. 15, no. 9, pp. 1399–1416, 2000.

[32] B. G. Parkinson, D. Holland, M. E. Smith, A. P. Howes, and C. R. Scales, "The effect Cs_2O additions on HLW wasteform glasses," *Journal of Non-Crystalline Solids*, vol. 351, p. 2425, 2005.

[33] H. Eckert, "Structural characterization of noncrystalline solids and glasses using solid state NMR," *Progress in NMR Spectroscopy*, vol. 24, p. 159, 1992.

[34] M. Jiricka, P. Hrma, and J. D. Vienna, "The effect of composition on spinel crystals equilibrium in low-silica high-level waste glasses," *Journal of Non-Crystalline Solids*, vol. 319, p. 280, 2003.

[35] J. Alton, T. J. Plaisted, and P. Hrma, "Kinetics of growth of spinel crystals in a borosilicate glass," *Chemical Engineering Science*, vol. 57, p. 2503, 2002.

[36] R. Hand, "Molybdenum in glasses containing vitrified nuclear waste," *Glass technology*, vol. 46, no. 2, p. 121, 2005.

[37] A. A. Digeos, J. A. Valdez, K. E. Sickafus, S. Atiq, R. W. Grimes, and A. R. Boccaccini, "Glass matrix/pyrochlore phase composites for nuclear wastes encapsulation," *Journal of Materials Science*, vol. 38, p. 1597, 2003.

[38] A. R. Boccaccini, S. Atiq, and R. W. Grimes, "Hot-pressed glass matrix composites containing pyrochlore phase particles for nuclear waste encapsulation," *Advanced Engineering Materials*, vol. 5, p. 501, 2003.

[39] J. M. Delaye, "Modeling of multicomponent glasses: a review," *Current Opinion in Solid State and Materials Science*, vol. 5, p. 451, 2001.

[40] R. L. McGreevy, "Reverse Monte Carlo modelling," *Journal of Physics of Condensed Matter*, vol. 13, p. R877, 2001.

[41] R. L. McGreevy and P. Zetterström, "Reverse Monte Carlo modelling of network glasses: useful or useless?," *Journal of Non-Crystalline Solids*, vol. 293–295, p. 297, 2001.

[42] I. Newton, *Principia: mathematical principles of natural philosophy, a new translation by I. Bernard Cohen*. Los Angeles: University of California Press, 1999.

[43] M. P. Allen and D. J. Tildesley, *Computer Simulation of Liquids*. Oxford : Clarendon, 1987.

[44] L. V. Woodcock, C. A. Angell, and P. Cheeseman, "Molecular dynamics studies of the vitreous state: Simple ionic systems and silica," *Journal of Chemical Physics*, vol. 65, p. 1565, 1976.

[45] M. E. Garcia, E. Webb III, and S. H. Garofalini, "Molecular dynamics simulations of V_2O_5/Li_2SiO_3 interface," *Journal of the Electrochemical Society*, vol. 145, p. 2155, 1998.

[46] M. E. Garcia and S. H. Garofalini, "Molecular dynamics simulation of the effect of crystal orientation on lithium-ion diffusion at the V_2O_5/Li_2SiO_3 interface," *Journal of the Electrochemical Society*, vol. 146, p. 840, 1999.

[47] W. C. Swope, H. C. Andersen, P. H. Berens, and K. R. Wilson, "A computer simulation method for the calculation of equilibrium constants for the formation of physical clusters of molecules: applications to small water clusters," *Journal of Chemical Physics*, vol. 76, p. 637, 1982.

[48] L. Verlet, "Computer "experiments" on classical fluids. I. thermodynamical properties of Lennard-Jones molecules," *Physical Review*, vol. 159, no. 1, p. 98, 1967.

[49] H. C. Andersen, "Molecular-dynamics simulations at constant pressure and-or temperature," *Journal of Chemical Physics*, vol. 72, no. 4, pp. 2384–2393, 1980.

[50] S. Nosé, "A molecular dynamics method for simulations in the canonical ensemble," *Molecular Physics*, vol. 52, pp. 255–268, 1984.

[51] S. Nosé, "A unified formulation of the constant temperature molecular-dynamics methods," *Journal of Chemical Physics*, vol. 81, no. 1, pp. 511–519, 1984.

[52] W. G. Hoover, "Canonical dynamics: Equilibrium phase-space distributions," *Physical Review A*, vol. 31, pp. 1695–1697, 1985.

[53] P. H. Hünenberger, "Thermostat algorithms for molecular dynamics simulations," *Advances in Polymer Science*, vol. 173, pp. 105–149, 2005.

[54] M. Born, *Atomtheorie des Festen Zustandes,*. Leipzig: Teubner, 1923.

[55] S. Tsuneyuki, M. Tsukada, and H. Aoki, "First-principles interatomic potential of silica applied to molecular dynamics," *Physical Review Letters*, vol. 61, no. 7, p. 869, 1988.

[56] B. van Beest and G. Kramer, "Force fields for silicas and aluminophosphates based on ab initio calculations," *Physical Review Letters*, vol. 64, no. 16, p. 1955, 1990.

[57] J. E. Lennard-Jones, "Cohesion," *The Proceedings of the Physical Society*, vol. 43, p. 461, 1931.

[58] P. Dauber-Osguthorpe, V. A. Roberts, D. J. Osguthorpe, J. Wolff, M. Genest, and A. T. Hagler, "Structure and energetics of ligand binding to proteins: Escherichia coli dihydro-folate reductase-trimethoprim, a drug-receptor system," *Proteins: Structure, Function, and Genetics*, vol. 4, p. 31, 1988.

[59] S. Lifson, A. T. Hagler, and P. Dauber-Osguthorpe, "Consistent force field studies of intermolecular forces in hydrogen-bonded crystals. I. carboxylic acids, amides, and the C=O...H- hydrogen bonds," *Journal of the American Chemical Society*, vol. 101, p. 5131, 1979.

[60] A. T. Hagler, S. Lifson, and P. Dauber-Osguthorpe, "Consistent force field studies of in-termolecular forces in hydrogen-bonded crystals. 2. a benchmark for the objective com-parison of alternative force fields," *Journal of the American Chemical Society*, vol. 101, p. 5122, 1979.

[61] O. L. Anderson and P. Andreatch, "Pressure derivatives of elastic constants of single-crystal MgO at 23° and -195.8°," *Journal of the American Ceramic Society*, vol. 49, p. 404, 1966.

[62] D. K. Smith and H. R. Leider, "Low-temperature expansion of LiH, MgO and CaO," *Journal of Applied Crystallography*, vol. 1, p. 246, 1968.

[63] W. G. Burgers, "Röntgenographische untersuchung des verhaltens von BaO-SrO-gemischen beim glühen," *Zeitschrift für Physik A Hadrons and Nuclei*, vol. 80, p. 352, 1933.

[64] P. P. Ewald, "Die berechnung optischer und elektrostatischer gitterpotentiale," *Annalen der Physik*, vol. 64, pp. 253–87, 1921.

[65] C. Kittel, *Solid State Physics*. New York: John Wiley & Sons, 1953.

[66] *Accelrys DISCOVER Molecular Simulation Program v2002.1*. Accelrys, 2002.

[67] A. Abbas, J. M. Delaye, D. Ghaleb, and G. Calas, "Molecular dynamics study of the structure and dynamic behavior at the surface of a silicate glass," *Journal of Non-Crystalline Solids*, vol. 315, p. 187, 2003.

[68] A. N. Cormack, J. Du, and T. R. Zeitler, "Alkali ion migration mechanisms in silicate glasses probed by molecular dynamics simulations," *Physical Chemistry Chemical Physics*, vol. 4, p. 3193, 2002.

[69] J. M. Roderick, D. Holland, A. P. Howes, and C. R. Scales, "Density-structure relations in mixed-alkali borosilicate glasses by 29Si and 11B MAS-NMR," *Journal of Non-Crystalline Solids*, vol. 293-295, pp. 746–751, 2001.

[70] O. V. Mazurin and M. V. Streltsina, *Handbook of glass data. Part A, Silica glass and binary silicate glasses.* Amsterdam ; Oxford: Elsevier, 1983.

[71] H. Doweidar, "The density of alkali silicate glasses in relation to the microstructure," *Journal of Non-Crystalline Solids*, vol. 194, pp. 155–162, 1996.

[72] A. A. Megahed, "Density of mixed alkali glasses," *Physics and chemistry of glasses*, vol. 40, p. 130, 1999.

[73] M. Montorsi, M. C. Menziani, C. Leonelli, and A. N. Cormack, "The sodium-alumino silicate glasses: A molecular dynamic study," *Molecular Engineering*, vol. 8, p. 427, 1999.

[74] C. Webb, "MPs fight against car 'death-traps'," *The Times (London)*, 16th August 1986.

[75] S. H. Garofalini and P. Shadwell, "Molecular dynamics simulations of cathode / glass interface behavior: effect of orientation on phase transformation, Li migration, and interface relaxation," *Journal of Power Sources*, vol. 89, p. 190, 2000.

[76] N. F. Mott and M. J. Littleton, "Conduction in polar crystals I. electrolytic conduction in solid salts," *Transactions of the Faraday Society*, vol. 34, p. 485, 1938.

[77] A. B. Lidiard, "The Mott-Littleton method: An introductory survey," *Journal of the Chemical Society Faraday Transactions 2*, vol. 85, p. 341, 1989.

[78] J. H. Harding, "Computer simulation of defects in ionic solids," *Reports on Progress in Physics*, vol. 53, p. 1403, 1990.

[79] C. R. A. Catlow, "Computer simulation studies of transport in solids," *Annual Reviews in Materials Science*, vol. 16, p. 517, 1986.

[80] M. Leslie, "SERC Daresbury laboratory report," Technical Report DL-SCI-TM31T, Daresbury Laboratory UK, 1982.

[81] C. Hammond, *The Basics of Crystallography and Diffraction*. IUCr Texts on Crystallography 3, Oxford: Oxford University Press, 1997.

[82] A. C. Wright, "The comparison of molecular dynamics simulation with diffraction experiments," *Journal of Non-Crystalline Solids*, vol. 159, p. 264, 1993.

[83] D. I. Grimley, A. C. Wright, and R. N. Sinclair, "Neutron scattering from vitreous silica IV. time-of-flight diffraction," *Journal of Non-Crystalline Solids*, vol. 119, p. 49, 1990.

[84] E. Lorch, "Neutron diffraction by germania, silica and radiation-damaged silica glasses," *Journal of Physics C: Solid State Physics*, vol. 2, p. 229, 1969.

[85] E. Lorch, "Conventional and elastic neutron diffracttion from vitreous silica," *Journal of Physics C: Solid State Physics*, vol. 3, p. 1314, 1970.

[86] "Neutron scattering lengths and cross sections of the elements and their isotopes," *Neutron News*, vol. 3, p. 29, 1992.

[87] A. N. Cormack and B. Park, "Proceedings of the international conference "thermodynamics and chemical structure of melts and glasses": Molecular dynamics simulations of silicate glasses and melts," *Glass Physics and Chemistry*, vol. 27, p. 28, 2001.

[88] H. Poulsen, J. Neuefeind, H.-B. Neumann, J. Schneider, and M. Zeidler, "Amorphous silica studied by high energy X-ray diffraction," *Journal of Non-Crystalline Solids*, vol. 188, p. 63, 1995.

[89] R. L. Mozzi and B. E. Warren, "The structure of vitreous silica," *Journal of Applied Crystallography*, vol. 2, p. 164, 1969.

[90] X. Yuan and A. N. Cormack, "Si–O–Si bond angle and torsion angle distribution in vitreous silica and sodium silicate glasses," *Journal of Non-Crystalline Solids*, vol. 319, p. 31, 2003.

[91] L. Gladden, "Structure and dynamics of 4-2 coordinated glasses," in *The Physics of Non-Crystalline Solids* (L. D. Pye, W. LaCourse, and H. Stevens, eds.), p. 91, Taylor & Francis, 1992.

[92] J. Neuefeind and K.-D. Liss, "Bond angle distribution in amorphous germania and silica," *Berichte der Bunsen-Gesellschaft Physical Chemistry*, vol. 100, p. 1341, 1996.

[93] M. G. Tucker, D. A. Keen, M. T. Dove, and K. Trachenko, "Refinement of the Si-O-Si bond angle distribution in vitreous silica," *Journal of Physics of Condensed Matter*, vol. 17, p. S67, 2005.

[94] F. Mauri, A. Pasquarello, B. G. Pfrommer, Y. Young-Gui, and S. G. Louie, "Si-O-Si bond-angle distribution in vitreous silica from first-principles ^{29}Si NMR analysis," *Physical Review B: Rapid Communications*, vol. 62, p. R4768, 2000.

[95] G. Kramer, N. P. Farragher, B. van Beest, and R. A. van Santen, "Interatomic force fields for silicas, aluminophosphates and zeolites: Derivation based on ab initio calculations," *Physical Review B*, vol. 43, p. 506B, 1991.

[96] G. Henderson, "A Si K-edge EXAFS/XANES study of sodium silicate glasses," *Journal of Non-Crystalline Solids*, vol. 183, p. 43, 1995.

[97] N. Zotov and H. Keppler, "The structure of sodium tetrasilicate glass from neutron diffraction reverse Monte Carlo simulations and Raman spectroscopy," *Physics and Chemistry of Minerals*, vol. 25, p. 259, 1998.

[98] K. Budwhani and S. Feller, "A density model for the lithium, sodium and potassium borosilicate glass systems," *Physics and Chemistry of Glasses*, vol. 36, p. 183, 1995.

[99] W. J. Dell, P. J. Bray, and S. Z. Xiao, "^{11}B NMR studies and structural modeling of $Na_2O–B_2O_3–SiO_2$ glasses of high soda content," *Journal of Non-Crystalline Solids*, vol. 58, p. 1, 1983.

[100] Y. H. Yun and P. J. Bray, "Nuclear magnetic resonance studies of the glasses in the system $Na_2O-B_2O_3-SiO_2$," *Journal of Non-Crystalline Solids*, vol. 27, p. 363, 1978.

[101] B. C. Bunker, D. R. Tallant, R. J. Kirkpatrick, and G. L. Turner, "Multinuclear nuclear magnetic resonance and raman investigation of sodium borosilicate glass structures," *Physics and Chemistry of Glasses*, vol. 31, p. 30, 1990.

[102] J. O'Rourke, *Computational Geometry in C*. Cambridge University Press, 2nd ed., 1998.

[103] F. Aurenhammer, "Voronoi diagrams – a survey of a fundamental geometric data structure," *ACM Computing Surveys*, vol. 23, p. 345, 1991.

[104] E. Wigner and F. Seitz, "On the constitution of metallic sodium," *Physical Review*, vol. 43, p. 804, 1933.

[105] J. M. Delaye and D. Ghaleb, "Dynamic processes during displacement cascades in oxide glasses: A molecular-dynamics study," *Physical Review B*, vol. 61, p. 14481, 2000.

[106] J. M. Delaye and D. Ghaleb, "Volume change origin in glasses subjected to ballistic collisions: Molecular dynamics simulations," *Nuclear Instruments and Methods in Physics Research Section B*, vol. 191, p. 10, 2002.

[107] C. B. Barber, D. P. Dobkin, and H. Huhdanpaa, "The quickhull algorithm for convex hulls," *ACM Transactions of Mathermatical Software*, vol. 22, p. 469, 1996.

[108] W. J. Weber, "Radiation effects in nuclear waste glasses," *Nuclear Instruments and Methods in Physics Research Section B*, vol. 32, p. 471, 1988.

[109] B. Boizot, G. Petite, D. Ghaleb, N. Pellerin, F. Fayon, B. Reynard, and G. Calas, "Migration and segregation of sodium under β-irradiation in nuclear glasses," *Nuclear Instruments and Methods in Physics Research Section B*, vol. 166-167, p. 500, 2000.

[110] B. Boizot, N. Ollier, F. Olivier, G. Petite, D. Ghaleb, and E. Malchukova, "Irradiation effects in simplified nuclear waste glasses," *Nuclear Instruments and Methods in Physics Research Section B*, vol. 240, p. 146, 2005.

[111] N. Ollier, T. Charpentier, B. Boizot, and G. Petite, "A structural approach by MAS NMR spectroscopy of mechanisms occurring under β-irradiation in mixed alkali aluminoborosilicate glasses," *Journal of Physics: Condensed Matter*, vol. 16, p. 7625, 2004.

[112] A. N. Cormack and J. Du, "Sodium ion migration mechanisms in silicate glasses probed by molecular dynamics simulations," *Journal of Non-Crystalline Solids*, vol. 323, p. 147, 2003.

[113] J. Habasaki, I. Okada, and Y. Hiwatari, "MD study of mixed-alkali effect in terms of the potential surface in the lithium-potassium metasilicate glass," *Journal of Non-Crystalline Solids*, vol. 208, p. 181, 1996.

[114] S. Balasubramanian and K. J. Rao, "Molecular dynamics investigation of structure and transport in the $K_2O-2SiO_2$ system using a partial charge based model potential," *Journal of Physical Chemistry*, vol. 98, p. 10871, 1994.

[115] A. Hagberg, D. Schult, and P. Swart, *NetworkX – A Python package for the creation, manipulation, and study of the structure, dynamics, and functions of complex networks.* http://networkx.lanl.gov, 2006.

[116] J. Ellson, E. R. Gansner, E. Koutsofios, S. C. North, and G. Woodhull, "Graphviz and dynagraph – static and dynamic graph drawing tools," in *Graph Drawing Software* (M. Junger and P. Mutzel, eds.), pp. 127–148, Springer-Verlag, 2003.

[117] B. Hayes, "Graph theory in practice: Part I," *American Scientist*, vol. 88, p. 9, 2000.

[118] R. D. Shannon, "Revised effective ionic radii and systematic studies of interatomic distances in halides and chalcogenides," *Acta Crystallographica*, vol. A32, p. 751, 1976.

[119] J. D. Bass, "Elasticity of minerals, glasses, and melts," in *Mineral Physics and Crystallography: A Handbook of Physical Constants* (T. J. Ahrens, ed.), p. 45, Washington DC: American Geophysical Union, 3 ed., 1995.

[120] H. D. B. Jenkins and H. K. Roobottom, "Lattice energies," in *CRC Handbook of Chemistry and Physics, Internet Version* (D. R. Lide, ed.), Boca Raton: Taylor and Francis, 86 ed., 2006.

[121] W. Mackrodt, "Atomistic simulation of oxide surfaces," *Physics and Chemistry of Minerals*, vol. 15, p. 228, 1988.

[122] C. D. Valentin, R. Ferullo, R. Binda, and G. Pacchioni, "Oxygen vacancies and peroxo groups on regular and low-coordinated sites of MgO, CaO, SrO and BaO surfaces," *Surface Science*, vol. 600, p. 1147, 2006.

[123] "Physical constants of inorganic compounds," in *CRC Handbook of Chemistry and Physics, Internet Version 2007* (D. R. Lide, ed.), pp. 4–43, Boca Raton, Florida: Taylor and Francis, 87 ed., 2006.

[124] C. Levelut, A. Faivre, R. Le Parc, B. Champagnon, J.-L. Hazemann, and J.-P. Simon, "In situ measurements of density fluctuations and compressibility in silica glasses as a function of temperature and thermal history," *Physical Review B*, vol. 72, p. 224201, 2005.

[125] H. Sillescu, "Heterogeneity at the glass transition: a review," *Journal of Non-Crystalline Solids*, vol. 243, p. 81, 1999.

[126] W. Humphrey, A. Dalke, and K. Schulten, "VMD - visual molecular dynamics," *Journal of Molecular Graphics*, vol. 14, p. 33, 1996.

[127] D. J. Bacon and W. F. Anderson, "A fast algorithm for rendering space filling molecule pictures," *Journal of Molecular Graphics*, vol. 6, p. 219, 1988.

[128] E. A. Merritt and M. E. Murphy, "Raster3D version 2.0: A program for photorealistic molecular graphics," *Acta Crystallographica D*, vol. 50, p. 869, 1994.

[129] E. A. Merritt and D. J. Bacon, "Raster3D: Photorealistic molecular graphics," *Methods in Enzymology*, vol. 277, p. 505, 1997.

[130] K. Levenberg, "A method for the solution of certain problems in least squares," *Quarterly Applied Mathematics*, vol. 2, p. 164, 1944.

[131] D. W. Marquardt, "An algorithm for least-squares estimation of nonlinear parameters," *Journal of the Society for Industrial and Applied Mathematics*, vol. 11, p. 431, 1963.

[132] T. Williams and C. Kelley, "gnuplot version 4.0," 2004.

[133] Y. Quiquempois, A. Kudlinski, and G. Martinelli, "Zero-potential condition in thermally poled silica samples: evidence of a negative electric field outside the depletion layer," *Journal of the Optical Society of America B*, vol. 22, p. 598, 2005.

[134] J. D. Gale, "GULP - a computer program for the symmetry adapted simulation of solids," *Journal of the Chemical Society Faraday Transactions*, vol. 93, p. 629, 1997.

[135] J. D. Gale, "Empirical potential derivation for ionic materials," *Philosophical Magazine B*, vol. 73, p. 3, 1996.

[136] J. D. Gale and A. Rohl, "The general utility lattice program," *Molecular Simulation*, vol. 29, p. 291, 2003.

[137] H. Okumura, S. Misawa, and S. Yoshida, "Epitaxial growth of cubic and hexagonal GaN on GaAs by gas-source molecular-beam epitaxy," *Applied Physics Letters*, vol. 59, p. 1058, 1991.

[138] R. C. Ewing, W. J. Weber, and J. Lian, "Nuclear waste disposal – pyrochlore ($A_2B_2O_7$): Nuclear waste form for the immobilisation of plutonium and "minor" actinides," *Journal of Applied Physics*, vol. 95, p. 5949, 2004.

[139] J. Lian, X. T. Zu, K. V. G. Kutty, J. Chen, L. M. Wang, and R. C. Ewing, "Ion-irradiation-induced amorphization of $La_2Zr_2O_7$ pyrochlore," *Physical Review*, vol. 66, p. 054108, 2002.

[140] M. A. Subramanian, G. Aravamudan, and G. V. Subba Rao, "Oxide pyrochlores – a review," *Progress in Solid State Chemistry*, vol. 15, no. 2, pp. 55–143, 1983.

[141] K. E. Sickafus, L. Minervini, R. W. Grimes, J. A. Valdez, M. Ishimaru, F. Li, K. J. McClellan, and T. Hartmann, "Radiation tolerance of complex oxides," *Science*, vol. 289, p. 748, 2000.

[142] N. F. M. Henry and K. Lonsdale, eds., *International Tables for X-ray crystallography: Symmetry Groups*, vol. 1. Birmingham: Kynoch Press, 1952.

[143] R. W. G. Wyckoff, "Chapter IXD: Compounds $R_xM_yX_7$," in *Crystal Structures*, pp. 439–440, New York: Interscience Publishers, 2nd ed., 1965.

[144] E. Aleshin and R. Roy, "Crystal chemistry of pyrochlore," *Journal of the American Ceramic Society*, vol. 45, p. 18, 1962.

[145] L. Minervini and R. W. Grimes, "Disorder in pyrochlore oxides," *Journal of the American Ceramic Society*, vol. 83, p. 1873, 2000.

[146] A. Cleave, *Atomic Scale Simulations for Wasteform Applications*. PhD thesis, Department of Materials, Imperial College London, 2006.

[147] A. Bogicevic, C. Wolverton, G. M. Crosbie, and E. B. Stechel, "Defect ordering in aliovalently doped cubic zirconia from first principles," *Physical Review B*, vol. 64, p. 014106, 2001.

[148] D. Michel, M. Perez y Jorba, and R. Collongues, "Study by raman spectroscopy of order-disorder phenomena occurring in some binary oxides with fluorite-related structures," *Journal of Raman Spectroscopy*, vol. 5, p. 163, 1976.

[149] A. Shevchenko, L. M. Lopato, and L. V. Nazarenko *Inorganic Materials*, vol. 20, p. 1615, 1984.

[150] E. R. Andrievskaya, L. M. Lopato, A. Shevchenko, and V. P. Smirnov *Inorganic Materials*, vol. 33, p. 835, 1997.

[151] E. R. Andrievskaya and L. M. Lopato, "Interaction in the HfO_2-Y_2O_3-La_2O_3 and HfO_2-Y_2O_3-Sm_2O_3 systems at 1250-2800°," in *Solid Solid Phase Transformations, Proceedings of the International Conference of Solid-Solid Phase Transformations in Inorganic Materials* (W. C. Johnson, ed.), (Farmington, Pennsylvania), Minerals Metals and Materials Society, 1994.

[152] J. Lian, L. M. Wang, S. X. Wang, J. Chen, L. A. Boatner, and R. C. Ewing, "Nanoscale manipulation of pyrochlore: New nanocomposite ionic conductors," *Physical Review Letters*, vol. 87, p. 145901, 2001.

[153] K. E. Sickafus, L. Minervini, R. W. Grimes, J. A. Valdez, and T. Hartmann, "A comparison between radiation damage accumulation in oxides with pyrochlore and fluorite structures," *Radiation Effects and Defects in Solids*, vol. 155, p. 133, 2001.

[154] J. Lian, L. Wang, J. Chen, K. Sun, R. C. Ewing, J. M. Farmer, and L. A. Boatner, "The order-disorder transition in ion-irradiated pyrochlore," *Acta Materialia*, vol. 51, p. 1493, 2003.

[155] F. A. Kröger and H. J. Vink, *Solid State Physics - Advances in Research and Applications*. New York: Academic Press, 1957.

[156] P. J. Wilde and C. R. A. Catlow, "Defects and diffusion in pyrochlore structured oxides," *Solid State Ionics*, vol. 112, p. 173, 1998.

[157] R. W. Grimes, D. J. Binks, and A. B. Lidiard, "The extent of zinc oxide solution in zinc chromate spinel," *Philosophical Magazine A*, vol. 72, p. 651, 1995.

[158] C. R. A. Catlow, J. Corish, P. W. M. Jacobs, and A. B. Lidiard, "The thermodynamics of characteristic defect parameters," *Journal of Physics C: Solid State Physics*, vol. 14, p. L121, 1981.

[159] J. C. Anderson, K. D. Leaver, R. D. Rawlings, and J. M. Alexander, *Materials Science*. London: Chapman & Hall, 4th ed., 1990.

[160] W. Smith, C. Yong, and P. Rodger, "DL_POLY: Application to molecular simulation," *Molecular Simulation*, vol. 28, p. 385, 2002.

[161] R. A. Buckingham, "The classical equation of state of gaseous helium, neon and argon," *Proceedings of the Royal Society A*, vol. 168, p. 264, 1938.

[162] W. H. F. Smith and P. Wessel, "Gridding with continuous curvature splines in tension," *Geophysics*, vol. 55, p. 293, 1990.

[163] P. Wessel and W. H. F. Smith, "Free software helps map and display data," *EOS Transactions of the American Geophysical Union*, vol. 72, p. 441, 1991.

[164] A. Q. Tool, "Relation between inelastic deformability and thermal expansion of glass in its annealing range," *Journal of the American Ceramic Society*, vol. 29, p. 240, 1946.

[165] C. R. Stanek, L. Minervini, and R. W. Grimes, "Nonstoichiometry in $A_2B_2O_7$ pyrochlores," *Journal of the American Ceramic Society*, vol. 85, p. 2792, 2002.

[166] P. K. Schelling, S. R. Phillpot, and R. W. Grimes, "Optimum pyrochlore compositions for low thermal conductivity," *Philosophical Magazine Letters*, vol. 84, p. 127, 2004.

[167] J. B. Goodenough, "Oxide-ion electrolytes," *Annual Reviews in Materials Research*, vol. 33, p. 91, 2003.

[168] C. R. Stanek and R. W. Grimes, "Prediction of rare-earth $A_2Hf_2O_7$ pyrochlore phases," *Journal of the American Ceramic Society*, vol. 85, p. 2139, 2002.

[169] R. W. Grimes, "Personal communication - explanation to why an Arrhenius type equation was chosen to predict order-disorder temperature from defect energies.," 2006.

[170] S. S. Kiparisov, R. A. Belyaev, A. I. Belyakov, V. V. Kondarenko, V. P. Vyskubov, V. G. Kozlov, S. A. Kuznetsov, and L. P. Melikhova *Inorg. Mater.*, vol. 12, p. 1393, 1976.

[171] L. Minervini, R. W. Grimes, Y. Tabira, R. L. Withers, and K. E. Sickafus, "The oxygen positional parameter in pyrochlores and its dependence on disorder," *Philosophical Magazine A*, vol. 82, p. 123, 2002.

[172] A. Abbas, Y. Serruys, D. Ghaleb, J. M. Delaye, B. Boizot, B. Reynard, and G. Calas, "Evolution of nuclear glass structure under α-irradiation," *Nuclear Instruments and Methods in Physics Research Section B*, vol. 166-167, p. 445, 2000.

[173] K. Trachenko, M. T. Dove, and E. K. H. Salje, "Atomistic modelling of radiation damage in zircon," *Journal of Physics: Condensed Matter*, vol. 13, p. 1947, 2001.

[174] N. Ravishankar, S. R. Gilliss, and C. B. Carter, "Glass and metals on crystalline oxides," *Journal of the European Ceramic Society*, vol. 23, p. 2777, 2003.

[175] K. Adachi and H. Kuno, "Decomposition of ruthenium oxides in lead borosilicate glass," *Journal of the American Ceramic Society*, vol. 80, p. 1055, 1997.